WILEY-VCH

Ernst O. Göbel and Uwe Siegner

The New International System of Units (SI)

Quantum Metrology and Quantum Standards

The New International System of Units (SI)

The New International System of Units (SI)

Quantum Metrology and Quantum Standards

Ernst O. Göbel and Uwe Siegner

WILEY-VCH

Authors

Prof. Dr. Ernst O. Göbel
Physikalisch-Technische Bundesanstalt
Emeritus
Oscar-Fehr-Weg 16
38116 Braunschweig
Germany

Prof. Dr. Uwe Siegner
Physikalisch-Technische Bundesanstalt
Bundesallee 100
38116 Braunschweig
Germany

All books published by **Wiley-VCH** are carefully produced. Nevertheless, authors, editors, and publisher do not warrant the information contained in these books, including this book, to be free of errors. Readers are advised to keep in mind that statements, data, illustrations, procedural details or other items may inadvertently be inaccurate.

Library of Congress Card No.:
applied for

British Library Cataloguing-in-Publication Data
A catalogue record for this book is available from the British Library.

Bibliographic information published by the Deutsche Nationalbibliothek
The Deutsche Nationalbibliothek lists this publication in the Deutsche Nationalbibliografie; detailed bibliographic data are available on the Internet at <http://dnb.d-nb.de>.

© 2019 Wiley-VCH Verlag GmbH & Co. KGaA, Boschstr. 12, 69469 Weinheim, Germany

All rights reserved (including those of translation into other languages). No part of this book may be reproduced in any form – by photoprinting, microfilm, or any other means – nor transmitted or translated into a machine language without written permission from the publishers. Registered names, trademarks, etc. used in this book, even when not specifically marked as such, are not to be considered unprotected by law.

Print ISBN: 978-3-527-34459-8
ePDF ISBN: 978-3-527-81451-0
ePub ISBN: 978-3-527-81449-7
oBook ISBN: 978-3-527-81448-0

Cover Design SCHULZ Grafik-Design, Fußgönheim, Germany
Typesetting SPi Global, Chennai, India
Printing and Binding

Printed on acid-free paper

10 9 8 7 6 5 4 3 2 1

Contents

Foreword

The International System of Units (*Système International d'Unités,* SI) provides the basis for internationally harmonized measurements that are indispensable for scientific, economic, and social progress. The SI was established in the Metre Convention, which was signed in 1875 and presently has 60 Signatory States as well as 42 Associate States and Economies, who together represent more than 97% of the world economy. It is thus the cornerstone of global trade and quality infrastructure. Since 1875, the SI has been continuously advanced by the organs of the Metre Convention: the General Conference on Weight and Measures (*Conférence Générale des Poids et Mesures*, CGPM) and the International Committee for Weights and Measures (*Comité International des Poids et Mesures*, CIPM), including its Consultative Committee for Units (CCU) and the International Bureau of Weights and Measures (*Bureau International des Poids et Mesures*, BIPM), a scientific institute in Sèvres near Paris.

In 2018, the evolution of the SI took a quantum leap forward: in a landmark decision in November 2018, the 26th CGPM voted to fundamentally revise the SI by abandoning all physical artifacts, material properties, and measurement descriptions used to date to define the kilogram/mole, the kelvin, and the ampere, respectively. On 20 May 2019, the revised SI, which is defined by fixing the numerical values of seven "defining constants," will come into force. Among these are fundamental constants such as the Planck constant, the speed of light in vacuum, and the elementary charge, which together form the fine-structure constant α. The units will thus be independent of space and time with a relative accuracy below 10^{-17} per year, according to the state-of-the-art experiments on the constancy of α. The revised SI guarantees long-term stability and realization of the units anywhere in the known universe with ever-increasing accuracy as technology develops, thus opening the door to innovation in science, industry, and technology.

This book provides a complete review of the revised SI. The definition of units based on the defining constants is examined alongside the realization of the units, which often incorporates the most recent progress in quantum technologies. The book explains and illustrates the physics and technology behind the definitions and their impact on measurements, emphasizing the decisive role quantum metrology has played in the revision. It also reviews what progress based on quantum metrology is anticipated. The book is thus indispensable and highly topical – indeed, it is urgently needed in order to

communicate the background and consequences of the revised SI to the broad scientific community and to other interested readers, including lecturers and teachers.

The authors are well qualified for this undertaking. Both have extensive experience and an excellent track record in metrology: Ernst Göbel was president of PTB, the national metrology institute of Germany, for more than 16 years. He was also a member of the CIPM for more than 15 years and served as its president from 2004 to 2010. Uwe Siegner joined the PTB in 1999, working on metrological applications of femtosecond laser technology and on electrical quantum metrology. He has been the head of the electricity division of PTB since 2009. Both authors are experienced university lecturers; in fact, this book is based on lectures they have given at the Technische Universität Braunschweig.

I have studied the book with great interest and pleasure, and I wish the same to a broad readership.

Braunschweig
November 2018

Prof. Dr. Joachim Ullrich
President of PTB, Vice President of CIPM,
President of the Consultative Committee for Units (CCU)

Preface

The General Conference on Weights and Measures (*Conférence Générale des Poids et Mesures*, CGPM) is the governing body of the Metre Convention. The CGPM rules the International System of Units (*Système International d'Unités*), the SI, which provides the basis for all measurements worldwide. At its 26th meeting in November 2018, the CGPM decided that all SI units would be based on seven "defining constants," among them fundamental constants of nature, such as the Planck constant, the speed of light in vacuum, and the elementary charge. To a significant extent, quantum metrology has provided the scientific foundation for this revolutionary change of the system of measurement units. The essence of quantum metrology is to base measurements on counting of discrete quanta.

The concept of some indivisible discrete single particles that are the basic building blocks of all matter goes back to philosophers many centuries BCE. In particular, the Greek philosopher *Demokrit* and his students specified the idea of *atoms* (from the Greek *àtomos*) as the base elements of all matter.

These concepts found support in natural science beginning in the eighteenth century. This was particularly driven by chemistry (e.g. *A. Lavoisier*, *J. Dalton*, and *D. Mendeleev*), kinetic gas theory (e.g. *J. Loschmidt* and *A. Avogadro*), and statistical physics (e.g. *J. Stefan*, *L. Boltzmann*, and *A. Einstein*).

The discovery of the electron by *J.J. Thomson* (1897) and the results of the scattering experiments by *J. Rutherford* and his coworkers (1909) opened a new era in physics, based on their conclusions that atoms are not indivisible but instead composite species. In the atomic model developed by *N. Bohr* in 1913, the atom consists of electrons carrying a negative elementary charge ($-e$) and a tiny nucleus which carries almost all the mass of an atom composed of positively charged ($+e$) protons and electrically neutral neutrons. In Bohr's model, the electrons in an atom can only occupy discrete energy levels, consistent with the experimental findings of atomic spectroscopy.

In the standard model of modern particle physics, electrons are in fact elementary particles belonging to the group of leptons. Protons and neutrons are composite particles composed of fractionally charged elementary particles, named quarks, which are bound together by the strong force.

In the last 50 years or so, scientists have learned to handle single quantum objects, for example, atoms, ions, electrons, and Cooper pairs, not least due to the tremendous progress in laser physics and nanotechnology. This progress has also laid the base for "quantum metrology." The paradigm of quantum metrology

is to base measurements on the counting of discrete quanta (e.g. charge or magnetic flux quanta). In contrast, in classical metrology, the values of continuous variables are determined. Proceeding from classical to quantum metrology, the measurement of real numbers is replaced by counting of integers.

The progress in quantum metrology stimulated the discussion about a revision of the SI more than 10 years ago. In particular, it was recognized early on that quantum metrology would allow a new definition of the base units of the SI in terms of constants of nature. This concept was implemented by the decision of the CGPM in November 2018 to revise the SI and to base it on seven defining constants. This book describes this new SI, which will be used from 20 May 2019, its definitions and the underlying physics and technology.

The discrete nature of a physical system is sometimes obvious, for example, by counting cycles when microwave or optical transitions between discrete energy states in atoms or ions are considered. The discrete quantum character of solid-state systems is less obvious because their single-particle energy spectra are quasi-continuous energy bands. Discrete quantum entities can then result from collective effects called macroscopic quantum effects.

The paradigm of quantum metrology becomes particularly obvious when the new definition of the electrical units (ampere, volt, and ohm) is considered. We, therefore, give a more comprehensive description of the underlying solid-state physics and the relevant macroscopic quantum effects. For example, we partly summarize the textbook knowledge and deduce results starting from general principles in Chapter 4 where we introduce superconductivity, the Josephson effect, and quantum interference phenomena in superconductors.

This book addresses advanced students, research workers, scientists, practitioners, and professionals in the field of modern metrology as well as a general readership interested in the foundations of the new SI definition. However, we consider this book as an overview that shall not cover all subjects in the same detail as it covers the electrical units. For further reading, we refer to the respective literature.

This book is based on the previous book by the same authors "Quantum Metrology: Foundation of Units and Measurements," however, reorganized and revised by including the final wording of the new SI definitions and the final values of the defining constants as decided by the 26th CGPM. The differences between the previous and the present SI are highlighted. Further, the individual chapters are updated by including latest results and progress.

This book would not have been possible without the support of many colleagues and friends. We would like to especially mention Stephen Cundiff (JILA, now University of Michigan), Wolfgang Elsäßer (University of Darmstadt), Peter Michler (University Stuttgart), and Alfred Leitenstorfer (University Konstanz)

as well as our PTB colleagues Franz Ahlers, Peter Becker, Ralf Behr, Bernd Fellmuth, Joachim Fischer, Christian Hahn, Frank Hohls, Oliver Kieler, Johannes Kohlmann, Stefan Kück, Andre Müller, Ekkehard Peik, Klaus Pierz, Hansjörg Scherer, Piet Schmidt, Sibylle Sievers, Lutz Trahms, Stephan Weyers, and Robert Wynands. We are also grateful for the technical support provided by Alberto Parra del Riego and Jens Simon. We further acknowledge the support of the Wiley-VCH staff members.

Braunschweig
December 2018

Ernst O. Göbel and Uwe Siegner

List of Abbreviations

2DEG	two-dimensional electron gas
AGT	acoustic gas thermometer/thermometry
AIST	National Institute of Advanced Industrial Science and Technology (National Metrology Institute of Japan)
APD	avalanche photo diode
BIPM	International Office for Weights and Measures (*Bureau International des Poids et Mesures*)
CBT	Coulomb blockade thermometer/thermometry
CCC	cryogenic current comparator
CCEM	Consultative Committee for Electricity and Magnetism
CCL	Consultative Committee for Length
CCM	Consultative Committee for Mass
CCT	Consultative Committee for Temperature
CCU	Consultative Committee for Units
CERN	European Organization for Nuclear Science
CGPM	General Conference on Weights and Measures (*Conférence Générale des Poids et Mesures*)
CIPM	International Committee for Weights and Measures (*Comité International des Poids et Mesures*)
CIPM MRA	CIPM mutual recognition arrangement
CODATA	International Council for Science: Committee on Data for Science and Technology
CVD	chemical vapor deposition
CVGT	constant volume gas thermometer/thermometry
DBT	Doppler broadening thermometer/thermometry
DCGT	dielectric constant gas thermometer/thermometry
ECG	electrocardiography
EEG	electroencephalography
EEP	Einstein's equivalence principle
FQHE	fractional quantum Hall effect
GUM	guide to the expression of uncertainties in measurements
HEMT	high electron mobility transistor
IAC	international Avogadro coordination
IDMS	isotope dilution mass spectroscopy
IERS	International Earth Rotation and Reference Systems Service

INRIM	National Institute of Metrology of Italy (*Istituto Nazionale di Ricerca Metrologia)*
ISO	International Organization for Standards
ITS	international temperature scale
JNT	Johnson noise thermometer/thermometry
KRISS	Korea Research Institute of Standards and Science
LED	light emitting diode
LNE	French Metrology Institute (*Laboratoire National de Métrologie et d'Essais*)
MBE	molecular beam epitaxy
MCG	magnetocardiography
MEG	magnetoencephalography
METAS	Federal Institute of Metrology, Switzerland
MOCVD	metalorganic chemical vapor deposition
MODFET	modulation-doped field-effect transistor
MOS	metal-oxide-semiconductor
MOSFET	metal-oxide-semiconductor field-effect transistor
MOT	magneto-optical trap
MOVPE	metalorganic vapor-phase epitaxy
MSL	Measurement Standards Laboratory of New Zealand
NBS	National Bureau of Standards
NEXAFS	near-edge absorption fine structure
NIM	National Institute of Metrology (National Metrology Institute of China)
NININ	normal metal/insulator/normal metal/insulator/normal metal
NIST	National Institute of Standards and Technology (National Metrology Institute of the United States)
NMIJ	National Metrology Institute of Japan
NMR	nuclear magnetic resonance
NPL	National Physics Laboratory (National Metrology Institute of the United Kingdom)
NRC	National Research Council, Canada
NV	nitrogen vacancy
OM	optical molasses
PLTS	provisional low temperature scale
PMT	photomultiplier tube
PTB	Physikalisch-Technische Bundesanstalt (National Metrology Institute of Germany)
PTR	Physikalisch-Technische Reichsanstalt (former National Metrology Institute of Germany)
QED	quantum electrodynamics
QHE	quantum Hall effect
QMT	quantum metrology triangle
QVNS	quantized voltage noise source
RCSJ	resistively and capacitively shunted junction
RHEED	reflection high-energy electron diffraction
RIGT	refractive index gas thermometer/thermometry

rms	root-mean-square
RT	radiation thermometry
SEM	scanning electron microscopy
SET	single-electron transport
SI	International System of Units (*Système International d'Unités*)
SINIS	superconductor/insulator/normal metal/insulator/superconductor
SIS	superconductor/insulator/superconductor
SNS	superconductor/normal metal/superconductor
SNT	shot noise thermometer
SOI	silicon-on-insulator
SPAD	single-photon avalanche diode
SQUID	superconducting quantum interference device
TAI	international atomic time (*temps atomique international*)
TES	transition-edge sensor
TEM	transmission electron microscope
TPW	triple point of water
ULCA	ultrastable low-noise current amplifier
UME	TÜBITAK Ulusal Metroloji Enstitüsü
UV	ultraviolet
UTC	coordinated universal time
XRCD	X-ray crystal density
XRF	X-ray fluorescence
XPS	X-ray photoelectron spectroscopy
XXR	X-ray reflectometry
YBCO	yttrium barium copper oxide

1

Introduction

Metrology is the science of measurement including all theoretical and experimental aspects, in particular, the experimental and theoretical investigations of uncertainties in measurement results. According to Nobel Prize Winner *J. Hall*, "metrology truly is the mother of science" [1].

Metrology is almost as old as humankind. When people began to exchange goods, they had to agree on commonly accepted standards as a base for their trade. Indeed, many of the ancient cultures such as China, India, Egypt, Greece, and the Roman Empire had a highly developed measurement infrastructure. Examples are the Nippur cubit from the third millennium BCE found in the ruins of a temple in Mesopotamia and now exhibited in the archeology museum in Istanbul and the famous Egyptian royal cubit as the base length unit for the construction of pyramids. However, the culture of metrology faded during the Middle Ages when many different standards were in use. In Germany, for instance, at the end of the eighteenth century, 50 different standards for mass and more than 30 standards for length were used in different parts of the country. This, of course, had been a barrier to trade and led to abuse and fraud. It was then during the French Revolution that the *French Académie des Sciences* took the initiative to define standards independent of the measures taken from the limbs of royal representatives. Instead, their intent was to base the standards on stable quantities of nature available for everyone at all times. Consequently, in 1799, the standard for length was defined as the ten millionth part of the quadrant of the earth, and a platinum bar was fabricated to represent this standard (*Mètre des Archives*). Subsequently, the kilogram, the standard of mass, was defined as the mass of one cubic decimeter of pure water at the temperature of its highest density at 3.98 °C. This can be seen as the birth of the metric system, which, however, at that time was not generally accepted through Europe or even in France. It was only with the signature of the Metre Convention in 1875 by 17 signatory countries that the metric system based on the meter and the kilogram received wider acceptance [2]. At the time of this writing, the Metre Convention was signed by 60 states with another 42 states being associated with the General Conference on Weights and Measures *(Conférence Générale des Poids et Mesures, CGPM)* (as of November 2018). At the General Conferences, following the first one in 1889, the system of units was continuously extended. Finally, at the 11th CGPM in 1960, the previous SI (*Système International*

The New International System of Units (SI): Quantum Metrology and Quantum Standards,
First Edition. Ernst O. Göbel and Uwe Siegner.
© 2019 Wiley-VCH Verlag GmbH & Co. KGaA. Published 2019 by Wiley-VCH Verlag GmbH & Co. KGaA.

d'Unités) (see Section 2.2) with the kilogram, second, meter, ampere, kelvin, and candela as base units was defined. The mole, unit of amount of substance, was added at the 14th CGPM in 1971. Within the SI, the definition of some units has been adopted according to progress in science and technology; for example, the meter was defined in 1960 based on the wavelength of a specific emission line of the noble gas krypton. But then, in 1983, it was replaced by the distance light travels in a given time and by assigning a fixed value to the speed of light in vacuum. Similarly, the second, originally defined as the ephemeris second, was changed by the 13th CGPM and defined via an electronic transition in the Cs isotope 133. Thus, in the previous SI, the meter and the second were defined by constants of nature. In the present revised SI, as accepted by the 26th CGPM in 2018, all units are based on constants of nature [3–7]. In fact, in this context, single quanta physics has a decisive role as will be outlined in this book.

We shall begin with introducing some basic principles of metrology in Chapter 2. We start in Section 2.1 by repeating some basic facts related to measurement and discuss the limitations for measurement uncertainty. The present SI is then presented in Section 2.2. The previous definitions of the respective units are also given for comparison.

Chapter 3 treats the realization of the present definition of the second employing atomic clocks based on the hyperfine transition in the ground state of ^{133}Cs applying thermal beams and laser-cooled atoms, respectively.

Chapter 4 is devoted to superconductivity and its utilization in metrology. Because of its prominent role for electrical metrology, we introduce superconductivity, the Josephson effect, magnetic flux quantization, and quantum interference. By means of the Josephson effect, the volt (the unit for the electrical potential difference) is traced back to the Planck constant and the elementary charge as realized in today's most precise voltage standards. We further discuss magnetic flux quantization and quantum interference allowing the realization of quantum magnetometers (superconducting quantum interference devices) with unprecedented resolution and precision.

The underlying solid-state physics and the metrological application of the quantum Hall effect are discussed in Chapter 5. In the present SI, the unit of electric resistance, ohm, is traced back to the Planck constant and the elementary charge by the quantum Hall effect.

In Chapter 6, we describe the physics of single-electron transport devices, which allow the realization of the unit of electric current, the ampere, according to its present definition based on the elementary charge and frequency. We further discuss the so-called metrological triangle experiment aimed to prove the consistency of the present realizations of the volt, ampere, and ohm.

Chapter 7 is then devoted to the present definition of the kilogram and the mole based on, respectively, the Planck constant and the Avogadro constant. We present the Kibble balance and the silicon single-crystal experiment, which have been seminal for the precise determination of the Planck constant and are now primary realizations of the kilogram replacing the International Kilogram Prototype (IKP).

Various experiments that have contributed to the precise determination of the value of the Boltzmann constant and that are potential realizations of the unit of thermodynamic temperature, kelvin, are described in Chapter 8.

In Chapter 9, we take an even further look into the future of the SI when we discuss optical clocks, which may in due time cause a change of the defining constant for the unit of time, the second, resulting in an improved realization. Further, we discuss the prospect of single-photon emitters for a possible new definition of radiometric and photometric quantities, for example, for (spectral) irradiance and luminous intensity.

In an outlook in Chapter 10, we finally discuss a few examples how the present definitions of the SI pave the way to bring quantum metrology and quantum technology to the "workbench," thereby considerably improving the quality of measurements for industry, science, and society.

References

1 Hall, J. (2011). Learning from the time and length redefinition, and the metre demotion. *Philos. Trans. R. Soc. London, Ser. A* 369: 4090–4108.

2 For a review on the development of modern metrology see e.g.: Quinn, T. and Kovalevsky, J. (2005). The development of modern metrology and its role today. *Philos. Trans. R. Soc. London, Ser. A* 363: 2307–2327.

3 Discussion Meeting issue "The new SI based on fundamental constants", organized by Quinn, T. (2011). *Philos. Trans. R. Soc. London, Ser. A* 369: 3903–4142.

4 Mills, I.M., Mohr, P.J., Quinn, T.J. et al. (2006). Redefinition of the kilogram, ampere, kelvin and mole: a proposed approach to implementing CIPM recommendation 1 (CI-2005). *Metrologia* 43: 227–246.

5 BIPM (2019). Draft of the ninth SI-Brochure. https://www.bipm.org/utils/en/pdf/si-revised-brochure/Draft-SI-Brochure-2018.pdf (accessed November 2018).

6 Fischer, J. and Ullrich, J. (2016). The new system of units. *Nat. Phys.* 12: 4–7.

7 Stenger, J. and Ullrich, J.H. (2016). Units based on constants: the redefinition of the international system of units. *Annu. Rev. Condens. Matter Phys.* 7: 35–59.

2

Some Basics

2.1 Measurement

Measurement is a physical process to determine the value or magnitude of a quantity. The quantity value can be calculated as follows:

$$Q = \{q\} \cdot [Q] \tag{2.1}$$

where $\{q\}$ is the numerical value and $[Q]$ the unit (see Section 2.2). The unit is thus simply a particular example of a quantity value. Equation (2.1) also applies for Q being a constant. If the numerical value of a constant is fixed, it defines the unit because their product must be equal to the quantity value, Q. This is the underlying concept of the present SI.

Repeated measurements of the same quantity, however, will generally result in slightly different results. In addition, systematic effects that impact the measurement result must be considered. Thus, any measurement result **must** be completed by an uncertainty statement. This measurement uncertainty quantifies the dispersion of quantity values being attributed to a measurand, based on the information used. Measurement uncertainty comprises, in general, many components. Some of the components may be evaluated by type A evaluation of measurement uncertainty from the statistical distribution of quantity values from a series of measurements and can be characterized by standard deviations. The other components, which may be evaluated by type B evaluation of measurement uncertainty, can also be characterized by standard deviations, evaluated from probability density functions based on experience or other information. For the evaluation of uncertainties in measurements, an international agreed guide has been published jointly by ISO and the *Bureau International des Poids et Mesures* (BIPM), the ***G**uide to the Expression of **U**ncertainty in **M**easurement* (GUM) [1–3]. Generally, precision measurements are those with smallest measurement uncertainty.

2.1.1 Limitations of Measurement Uncertainty

One might tend to believe that measurement uncertainty can be continuously decreased as more efforts are put in the respective experiment. However, this is not the case since there are fundamental as well as practical limitations for measurement precision. The fundamental limit is a consequence of the Heisenberg

The New International System of Units (SI): Quantum Metrology and Quantum Standards,
First Edition. Ernst O. Göbel and Uwe Siegner.
© 2019 Wiley-VCH Verlag GmbH & Co. KGaA. Published 2019 by Wiley-VCH Verlag GmbH & Co. KGaA.

uncertainty principle of quantum mechanics, and the major practical limit is due to noise.

2.1.1.1 The Fundamental Quantum Limit

Note that throughout this book, we use the letter f to denote technical frequencies and the Greek letter ν to denote optical frequencies.

The Heisenberg uncertainty principle is a fundamental consequence of quantum mechanics stating that there is a minimum value for the physical quantity action, H:

$$H_{\min} \approx h \tag{2.2}$$

where h is the Planck constant. Action has the dimensions of energy multiplied by time and its unit is joule seconds. From the Heisenberg uncertainty principle, it follows that conjugated variables, such as position and momentum or time and energy, cannot be measured with ultimate precision at a time. For example, if Δx and Δp are the standard deviation for position, x, and momentum, p, respectively, the inequality relation holds ($\hbar = h/2\pi$):

$$\Delta x \Delta p \geq \frac{1}{2}\hbar \tag{2.3}$$

Applied to measurement, the argument is as follows: during a measurement, information is exchanged between the measurement system and the system under consideration. Related to this is an energy exchange. For a given measurement time, τ, or bandwidth of the measurement system, $\Delta f = 1/\tau$, the energy extracted from the system is limited according to Eq. (2.2) [4]:

$$E_{\min} \cdot \tau = \frac{E_{\min}}{\Delta f} \approx h \tag{2.4}$$

Let us now consider, for example, the relation between inductance, L, and, respectively, magnetic flux, Φ, and current, I (see Figure 2.1). The energy is given by $E = (1/2)LI^2 = (1/2)(\Phi^2/L)$, and consequently,

$$I_{\min} \approx \sqrt{\frac{2h}{\tau \cdot L}}; \quad \Phi_{\min} \approx \sqrt{\frac{2h \cdot L}{\tau}} \tag{2.5}$$

These relations are also depicted in Figure 2.1. The gray area corresponds to the regime that is accessible by measurement. Note that this is a heuristic approach that does not consider a specific experiment. Nevertheless, it may provide useful conclusions on how to optimize an experiment. For instance, if an ideal coil (without losses) is applied to measure a small current, inductance should be large (e.g. $L = 1$ H, $\tau = 1$ s, and then $I_{\min} = 3.5 \times 10^{-17}$ A). If instead the coil is applied to measure magnetic flux, L should be small (e.g. $L = 10^{-10}$ H, $\tau = 1$ s, and then $\Phi_{\min} = 4 \times 10^{-22}$ V s $= 2 \times 10^{-7} \times \Phi_0$, where $\Phi_0 = h/2e$ is the flux quantum $= 2.067 \times 10^{-15}$ V s).

Similarly, for a capacitor with capacitance, C, the energy is given by

$$E = \frac{1}{2}Q^2/C = \frac{1}{2}U^2 \cdot C \tag{2.6}$$

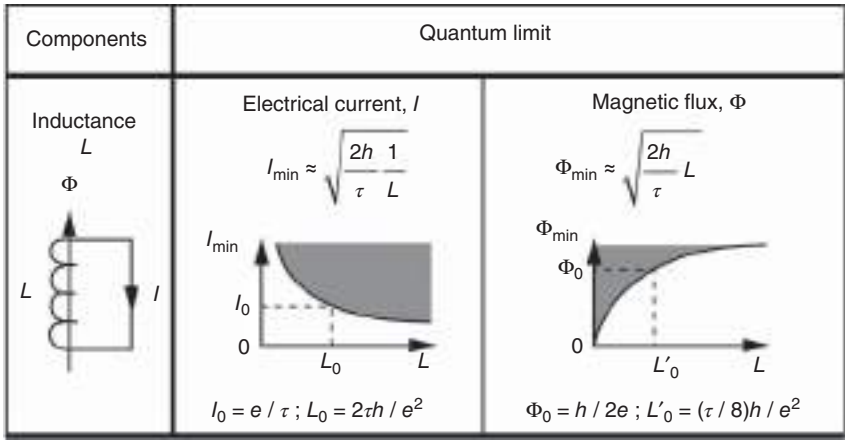

Figure 2.1 Components and quantities considered (left) and the minimum current, I_{min}, and the minimum magnetic flux, Φ_{min}, versus inductance, L, for an ideal coil. Source: Kose and Melchert 1991 [4]. Reproduced with permission of John Wiley and Sons.

and thus,

$$Q_{min} \approx \sqrt{\frac{2h \cdot C}{\tau}}; \quad U_{min} \approx \sqrt{\frac{2h}{\tau \cdot C}}. \tag{2.7}$$

Finally, for a resistor with resistance, R, the energy is given by

$$E = I^2 \cdot R \cdot \tau = \frac{U^2}{R} \cdot \tau \tag{2.8}$$

and thus, for the minimum current and voltage, respectively, we obtain

$$I_{min} \approx \frac{1}{\tau} \cdot \sqrt{\frac{h}{R}}; \quad U_{min} \approx \frac{1}{\tau} \cdot \sqrt{h \cdot R} \tag{2.9}$$

2.1.1.2 Noise

In this chapter, we briefly summarize some aspects of noise theory. For a more detailed treatment of this important and fundamental topic, the reader is referred to, for example, [5].

Noise limits the measurement precision in most practical cases. The noise power spectral density, $P(T,f)/\Delta f$, can be approximated by (Planck formula)

$$\frac{P(T,f)}{\Delta f} = h \cdot f + \frac{h \cdot f}{e^{hf/kT} - 1} \tag{2.10}$$

where f is the frequency, k the Boltzmann constant, and T the temperature. Two limiting cases can be considered as follows.

(i) *Thermal noise (Johnson noise) ($kT \gg hf$)*:

$$\frac{P_{th}(T)}{\Delta f} = k \cdot T \tag{2.11}$$

According to this "Nyquist relation," the thermal noise power spectral density is independent of frequency (white noise) and increases linearly with

temperature. Thermal noise was first studied by Johnson [6]. It reflects the thermal agitation of, for example, carriers (electrons) in a resistor.

(ii) *Quantum noise ($hf \gg kT$)*:

$$\frac{P_{\mathrm{qu}}(f)}{\Delta f} = h \cdot f \tag{2.12}$$

The quantum noise power spectral density in this limit is determined by the zero point energy, hf, and is independent of temperature and increases linearly with frequency.

Thermal noise dominates at high temperatures and low frequencies (see Figure 2.2). The transition frequency, $f_{\mathrm{c}}(T)$, where both contributions are equal depends on temperature and is given by

$$f_{\mathrm{c}}(T) = \frac{kT}{h} \cdot \ln 2 \tag{2.13}$$

This transition frequency amounts to 4.3 THz at $T = 300$ K and 60.6 GHz at the temperature of liquid He at $T = 4.2$ K.

The thermal noise in an electrical resistor at temperature T generates under open circuit or short circuit, respectively, a voltage or current with effective values:

$$U_{\mathrm{eff}} = \sqrt{\frac{\langle u^2(t)\rangle}{\Delta f}} = \sqrt{4kT \cdot R} \tag{2.14}$$

$$I_{\mathrm{eff}} = \sqrt{\frac{\langle i^2(t)\rangle}{\Delta f}} = \sqrt{4kT/R} \tag{2.15}$$

To reduce thermal noise, the detector equipment should be cooled to low temperatures. Decreasing the temperature from room temperature (300 K)

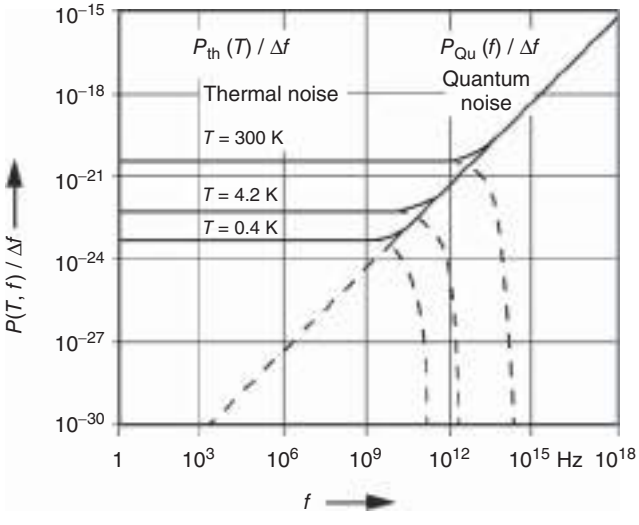

Figure 2.2 Noise power spectral density, $P(T,f)/\Delta f$, versus frequency for different temperatures. Source: Kose and Melchert 1991 [4]. Reproduced with permission of John Wiley and Sons.

to liquid He temperature (4.2 K) reduces the thermal noise power by a factor of about 70. In addition, both thermal and quantum noise can be reduced by reducing the bandwidth, that is, by integrating over longer times, τ. This, however, requires stable conditions during the measurement time, τ. Unfortunately, however, other noises may be observed such as shot noise and at low frequencies the so-called $1/f$ noise.

(iii) *Shot noise*: Shot noise originates from the discrete nature of the species carrying energy (e.g., electrons, photons). It was first discovered by Schottky [7] when studying the fluctuations of current in vacuum tubes. Shot noise is observed when the number of particles is small such that the statistical nature describing the occurrence of independent random events is described by the Poisson distribution. The Poisson distribution transforms into a normal (Gaussian) distribution as the number of particles increases. At low frequencies, shot noise is white; that is, the noise spectral density is independent of frequency and, in contrast to thermal noise, also independent of temperature. The shot noise spectral density of an electric current, S^{el}, at sufficiently low frequencies is given by

$$S^{\mathrm{el}} = 2eI \tag{2.16}$$

where I is the average current. Similarly, for a monochromatic photon flux, we have the shot noise spectral density of photon flux, S^{opt},

$$S^{\mathrm{opt}} = 2h\nu P \tag{2.17}$$

where $h\nu$ is the photon energy and P the average power.

(iv) *Low-frequency noise (1/f noise)*: $1/f$ noise (sometimes also called pink noise or flicker noise) occurs widely in nature but might have quite different origins. More precisely, the relation between noise power spectral density and frequency is often given by

$$\frac{P(f)}{\Delta f} \propto 1/f^{\beta} \quad (0.5 \leq \beta \leq 2) \tag{2.18}$$

with β usually close to 1. In contrast to thermal or quantum noise, the noise power of $1/f$ noise decreases with increasing frequency (by 3 dB per octave of frequency). Figure 2.3 shows, for example, the noise power spectral density measured for a superconducting quantum interference device (SQUID) magnetometer versus frequency.

2.2 The SI (Système International d'Unités)

According to the decision of the 26th meeting of the *Conférence Générale des Poids et Mesures* (CGPM), the present system of units is set up by seven defining constants, namely, the frequency of the radiation corresponding to the transition between the two hyperfine levels of the ground state of the cesium 133 atom ($\Delta\nu_{\mathrm{Cs}}$), the Planck constant (h), the velocity of light in vacuum (c), the elementary charge (e), the Boltzmann constant (k), the Avogadro constant (N_{A}), and the

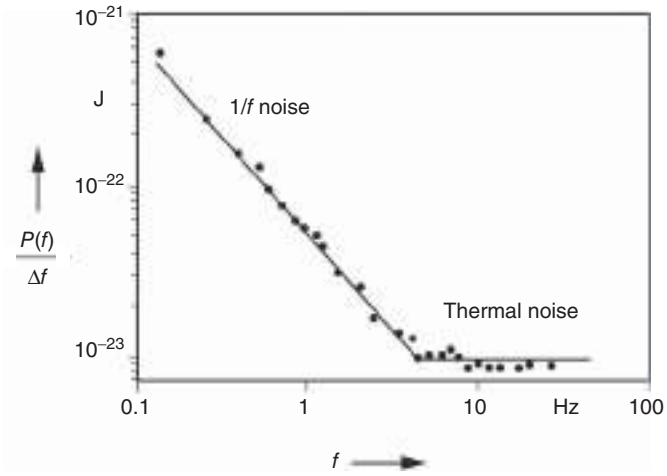

Figure 2.3 Noise power spectral density as measured for a SQUID magnetometer versus frequency. Source: Kose and Melchert 1991 [4]. Reproduced with permission of John Wiley and Sons.

luminous efficacy of monochromatic radiation of frequency 540×10^{12} Hz (K_{cd}) [8].

The respective wording together with the numerical values of the defining constants based on the 2017 CODATA evaluation [9, 10] is presented in the recent edition of the SI brochure [11] and it reads as follows:

> The International System of Units, the SI, is the system of units in which
>
> - the unperturbed ground state hyperfine transition frequency of the caesium 133 atom $\Delta\nu_{Cs}$ is 9 192 631 770 Hz,
> - the speed of light in vacuum c is 299 792 458 m/s,
> - the Planck constant h is $6.626\,070\,15 \times 10^{-34}$ J s,
> - the elementary charge e is $1.602\,176\,634 \times 10^{-19}$ C,
> - the Boltzmann constant k is $1.380\,649 \times 10^{-23}$ J/K,
> - the Avogadro constant N_A is $6.022\,140\,76 \times 10^{23}$ mol^{-1},
> - the luminous efficacy of monochromatic radiation of frequency 540×10^{12} hertz K_{cd} is 683 lm/W.

These seven constants set the scale of the entire SI (Figure 2.4), and they are all needed to fully define it. These numerical values do not exhibit uncertainty and have been chosen to ensure continuity between the previous and present SI. These definitions of the present SI disconnect the definition of a unit from its realization, thus leaving room for improved realizations as science and technology advance. The nature of the constants is quite different, ranging from fundamental constants such as the Planck constant, h, and the speed of light in vacuum, c, to a technical constant such as the luminous efficacy, K_{cd}. The set of the seven defining constants has been chosen such that they provide a most fundamental, stable,

Figure 2.4 Illustration of the base units of the SI and their defining constants. Source: Courtesy of PTB.

and universal reference and simultaneously allow for practical realizations with smallest uncertainties [11]. All physical artifacts are abandoned in the present SI.

The previous SI consisted of 7 base units and 22 derived units with specific names. A formal distinction between the base units and derived units does not exist in the present SI, however, is maintained since it is historically established and proven to be useful and in particular to maintain consistency with international written standards such as the ISO/IEC 80000 series. The system is called coherent, which means that the derived units are given as a product of powers of the base units with only "1" as the numerical factor (e.g., for the derived unit for energy, joule, we have $1\,\mathrm{J} = 1\,\mathrm{m}^2\,\mathrm{kg}\,\mathrm{s}^{-2}$). Consequently, numerical equations do have the same format as quantity equations.

Now we briefly describe the present (and the previous) seven base units: second, meter, kilogram, kelvin, ampere, mole, and candela. In the present definition, one of the seven defining constants is explicitly assigned to each base unit as described in the following sections. For further reading, we refer to the SI brochure of the BIPM [11].

2.2.1 The Second: Unit of Time

The unit second was originally defined as the 86 400th part of the duration of a mean solar day. However, at the 11th CGPM in 1960, after it had been shown that the rotation of the earth was not stable, the second was referred to the duration of the tropical year in 1900 (ephemeris second). In 1967 [12], however, the definition of the second was changed and no longer based on an astronomic timescale but refers to the frequency of electromagnetic radiation of a magnetic dipole transition in the hyperfine split $|F = 3, m_F = 0\rangle \leftrightarrow |F = 4, m_F = 0\rangle$ ground state $6^2\mathrm{S}_{1/2}$ of the isotope ^{133}Cs (for the energy level scheme of ^{133}Cs; see Figure 3.3). The definition of the second is unchanged in the present SI and is still defined via the hyperfine transition frequency in ^{133}Cs, $\Delta\nu_{\mathrm{Cs}}$, which is now one of the

defining constants of the SI. According to the SI-Brochure [11], the wording for the definition of the second is as follows:

> The second, symbol s, is the SI unit of time. It is defined by taking the fixed numerical value of the caesium frequency $\Delta\nu_{Cs}$, the unperturbed ground-state hyperfine transition frequency of the caesium 133 atom, to be 9 192 631 770 when expressed in the unit Hz, which is equal to s^{-1}.

This definition implies the exact relation $\Delta\nu_{Cs} = 9\,192\,631\,770$ Hz. Inverting this relation gives an expression for the unit second in terms of the value of the defining constant $\Delta\nu_{Cs}$:

$$1\ \text{Hz} = \frac{\Delta\nu_{Cs}}{9\,192\,631\,770} \quad \text{or} \quad 1\ \text{s} = \frac{9\,192\,631\,770}{\Delta\nu_{Cs}} \tag{2.19}$$

The second is equal to the duration of 9 192 631 770 periods of the radiation corresponding to the transition between the two hyperfine levels of the unperturbed ground state of the ^{133}Cs atom [11].

The wording in the present SI is intended to make it clear that the definition refers to an isolated cesium atom unperturbed by any external field such as electric and magnetic fields and black body radiation. This wording thus defines the idealized value of the Cs hyperfine transition frequency and defines the "proper time" valid for any gravitational potential [13]. For the provision of a coordinated timescale, the signals of different primary clocks in different locations are combined, which must be corrected for relativistic frequency shifts.

In the previous SI, the definition of the second read as follows:

> The second is the duration of 9 192 631 770 periods of the radiation corresponding to the transition between the two hyperfine levels of the ground state of the caesium 133 atom.

Despite the different wording, the definitions in the previous and the present SI are identical.

By this definition of the second, it had been ensured that at the time of the definition the new "atomic clock second" did agree with the ephemeris second. To keep the astronomic timescale and the atomic timescale (coordinated universal time (UTC)) identical, leap seconds are added (or subtracted) to the international atomic time (TAI) occasionally whenever their difference becomes larger than 0.9 s. Up to today, 27 leap seconds have been added to UTC since 1972 (see also [14]). The responsibility for adding or subtracting leap seconds lies with the International Earth Rotation and Reference Systems Service (IERS), and changing the procedure by taking much longer time intervals for coordinating these two timescales is under discussion.

The definition of the second is put into praxis, that is, realized, as metrologists use to say, by atomic clocks. The basic concept of atomic clocks is to lock the frequency of a local oscillator to the frequency of an electronic resonance of the respective atom, which in the classical Cs atomic clocks lies in the microwave regime. The two different versions of primary Cs atomic clocks currently in use

operate with a thermally generated beam of Cs atoms and laser-cooled Cs atoms, respectively, which are described in detail in Chapter 3.

2.2.2 The Meter: Unit of Length

The definition of the meter is also unchanged in the present SI and based on the defining constant speed of light in vacuum [11].

> The metre, symbol m, is the SI unit of length. It is defined by taking the fixed numerical value of the speed of light in vacuum c to be 299 792 458 when expressed in the unit m s^{-1}, where the second is defined in terms of the caesium frequency $\Delta\nu_{Cs}$.

One meter is defined as the length of the path traveled by light in vacuum during a time interval of 1/299 792 458 of a second [11].

Thus

$$1\ \mathrm{m} = (c/299\,792\,458)\ \mathrm{s} \approx 30.663\,319\frac{c}{\Delta\nu_{Cs}} \tag{2.20}$$

Since 1983, the following definition had been used for the meter in the previous SI:

> The metre is the length of the path traveled by light in vacuum during a time interval of 1/299 792 458 of a second.
> It follows that the speed of light in vacuum is exactly 299 792 458 m/s, $c_0 = 299\,792\,458$ m/s.

Though customary in astronomy to measure distances in the path length light travels in a given time (e.g. light-year), it is not very convenient for daily life purposes. Therefore, the Consultative Committee for Length (CCL) of the International Committee for Weights and Measures (CIPM) recommended three different procedures to realize the meter:

(i) According to its definition by measuring the distance light travels within a certain time interval.
(ii) Via radiation sources (in particular lasers) with known wavelength (or frequency). A list of respective radiation sources (Mise en Pratique) is published by the CCL and frequently updated [15–17].
(iii) Via the vacuum wavelength, λ, of a plane electromagnetic wave with frequency f. The wavelength is obtained according to $\lambda = c/f$.

According to procedures (ii) and (iii), interferometry can then be applied to calibrate the length of a gauge block [18]. Gauge blocks made of metals or ceramics exhibit two opposing precisely flat, parallel surfaces. For calibration of its length, the gauge block is wrung on an auxiliary platen forming one of the end mirrors of a modified Michelson interferometer (Twyman–Green interferometer, Kösters comparator). Since interference can be obtained from both end surfaces of the gauge block, its length can be measured in terms of the wavelength of the radiation used by counting the interference orders. Iodide-stabilized He–Ne lasers

are often applied for this purpose. For the highest precision, the interferometer is placed in vacuum to avoid uncertainties due to the refractive index of air. In addition, the temperature must be precisely known and stable. In any case, the frequency (and hence the wavelength) of the respective laser must be known in terms of the frequency of the Cs hyperfine transition frequency, $\Delta\nu_{\mathrm{Cs}}$, which defines the second. Today, these many orders of frequency are bridged by optical frequency combs. This technique for which *T. Hänsch* and *J. Hall* were awarded the 2005 Nobel Prize in physics can be considered as a gear, which transfers the microwave frequency of the Cs atomic clock into the visible and adjacent spectral regimes. The name "optical frequency comb" refers to the emission spectrum of mode-locked lasers generating ultrafast (fs) laser pulses. Femtosecond frequency combs are discussed in more detail in Section 9.1.1.

At present, the meter can be realized according to recommendations (ii) and (iii) of the CCL with a relative uncertainty of the order of 10^{-11}, and gauge calibrations can reach fractional uncertainties as low as 10^{-8} [18, 19].

2.2.3 The Kilogram: Unit of Mass

The definition of the kilogram reads as follows [11]:

> The kilogram, symbol kg, is the SI unit of mass. It is defined by taking the fixed numerical value of the Planck constant h to be $6.626\,070\,15 \times 10^{-34}$ when expressed in the unit J s, which is equal to kg m^2 s^{-1}, where the metre and the second are defined in terms of c and $\Delta\nu_{\mathrm{Cs}}$.

This definition implies the exact relation $h = 6.626\,070\,15 \times 10^{-34}\,\mathrm{kg\,m^2\ s^{-1}}$. Inverting this relation gives an exact expression for the kilogram in terms of the three defining constants h, $\Delta\nu_{\mathrm{Cs}}$, and c [11]:

$$1\,\mathrm{kg} = (h/6.626\,070\,15 \times 10^{-34})\,\mathrm{m^{-2}\,s} \approx 1.475\,5214 \times 10^{40} h\,\Delta\nu_{\mathrm{Cs}}/c^2 \tag{2.21}$$

The techniques for realization of the kilogram according to its definition (Kibble balance and Avogadro experiment) are described in Chapter 7.

Before the redefinition, the kilogram had been defined since the first CGPM in 1889 by the international platinum/iridium prototype (IKP) (Figure 2.5) stored in the premises of the BIPM in Sévres in the suburban of Paris. At the third CGPM in 1901, this definition was confirmed by the following statement:

> The kilogram is the unit of mass; it is equal to the mass of the international prototype of the kilogram.

It followed that the mass of the IKP had always been 1 kg exactly, $m(\mathrm{IKP}) \equiv 1\,\mathrm{kg}$. However, due to the inevitable accumulation of contaminants on its surfaces, the international prototype is subject to reversible surface contamination that approaches 1 µg per year in mass. For this reason, the CIPM declared that, pending further research, the reference mass of the international prototype is that immediately after cleaning and washing by a specific method

Figure 2.5 The Pt/Ir kilogram prototype as stored at the Bureau International des Poids et Mesures (BIPM). Source: Courtesy of BIPM.

(see Section 7.1). This reference mass was then used to calibrate national standards of platinum/iridium alloy or stainless steel.

However, comparisons of the prototype with its copies during the 2nd and 3rd verification around 1946 and 1990, respectively, appeared to indicate that there might also be some irreversible change in its mass, which indeed had been the major driving force for the new definition of mass and the other SI units [20] (see Chapter 7).

2.2.4 The Ampere: Unit of Electric Current

The ampere is defined in the present SI as follows [11]:

> The ampere, symbol A, is the SI unit of electric current. It is defined by taking the fixed numerical value of the elementary charge e to be $1.602\,176\,634 \times 10^{-19}$ when expressed in the unit C, which is equal to A s, where the second is defined in terms of $\Delta\nu_{\mathrm{Cs}}$.

This definition implies the exact relation $e = 1.602\,176\,634 \times 10^{-19}$ A s. Inverting this relation gives an exact expression for the unit ampere in terms of the defining constants e and $\Delta\nu_{\mathrm{Cs}}$ [11]:

$$1\ \mathrm{A} = \left(\frac{e}{1.602\,176\,634 \times 10^{-19}} \right) \mathrm{s}^{-1} \approx 6.789\,687 \times 10^{8}\ \Delta\nu_{\mathrm{Cs}} e \qquad (2.22)$$

The effect of this definition is that 1 A is the electric current corresponding to the flow of $1/(1.602\,176\,634 \times 10^{-19})$ elementary charges per second.

In the previous SI, the ampere was defined at the ninth CGPM in 1948 as follows:

> The ampere is that constant current which, if maintained in two straight parallel conductors of infinite length, of negligible circular cross-section, and placed 1 metre apart in vacuum, would produce between these conductors a force equal to 2×10^{-7} N m^{-1} of length.

This definition fixed the value of μ_0, the permeability of vacuum or magnetic constant, according to Faraday's law to exactly $4\pi \times 10^{-7}$ H m^{-1}.

A realization of the ampere precisely according to this definition obviously had not been possible. Closest to its definition, the ampere was realized by the so-called current balances, where the force between two coils passed by a given current is balanced by gravitational force. This allows realization of the ampere with an uncertainty of order 10^{-6}. Alternatively, the ampere had been reproduced (not realized!) according to Ohm's law through the units V_{90} and Ω_{90} resulting in the non-SI unit A_{90}. V_{90} and Ω_{90} had been represented, respectively, by the Josephson and quantum Hall effect (see Chapters 4 and 5). In the present SI, the ampere can be **realized** by the quantum Hall effect and Josephson effect since the SI volt and the SI ohm now can be realized by the Josephson and quantum Hall effect. Alternatively, the ampere can be realized through single-electron transport devices (see Chapter 6).

2.2.5 The Kelvin: Unit of Thermodynamic Temperature

The definition of the kelvin is as follows [11]:

> The kelvin, symbol K, is the SI unit of thermodynamic temperature. It is defined by taking the fixed numerical value of the Boltzmann constant k to be $1.380\,649 \times 10^{-23}$ when expressed in the unit J K^{-1}, which is equal to kg m^2 s^{-2} K^{-1}, where the kilogram, metre and second are defined in terms of h, c and $\Delta\nu_{Cs}$.

This definition implies the exact relation $k = 1.380\,649 \times 10^{-23}$ kg m^{2}s^{-2}K^{-1}. Inverting this relation gives an exact expression for the kelvin in terms of the defining constants k, h, and $\Delta\nu_{Cs}$ [11]:

$$1\ \mathrm{K} = \left(\frac{1.380\,649}{k}\right) 10^{-23}\ \mathrm{kg\,m^2\,s^{-2}} \approx 2.266\,6653\,\frac{\Delta\nu_{Cs} h}{k} \tag{2.23}$$

One kelvin is equal to the change of thermodynamic temperature that results in a change in thermal energy kT by $1.380\,649 \times 10^{-23}$ J.

The previous definition of the unit of thermodynamic temperature had been decided at the 10th CGPM in 1954 by choosing the triple point of water as the basic fix point and assigning the temperature of 273.16 K to it. The name kelvin,

however, was only accepted at the 13th CGPM in 1967/1968. The definition of the kelvin in the previous SI is as follows:

> The kelvin, unit of thermodynamic temperature, is the fraction 1/273.16 of the thermodynamic temperature of the triple point of water.
> It follows that the thermodynamic temperature of the triple point of water is exactly 273.16 K, $T_{\mathrm{TPW}} = 273.16\,\mathrm{K}$.

However, since the triple-point temperature depends on the isotopic composition of the water, the CIPM at its 2005 meeting affirmed that

> This definition refers to water having the isotopic composition defined exactly by the following amount of substance ratios: 0.000 155 76 mol of ^{2}H per mole of ^{1}H, 0.000 379 9 mol of ^{17}O per mole of ^{16}O, and 0.002 005 2 mol of ^{18}O per mole of ^{16}O. (Vienna Standard Mean Ocean Water).

Additionally, the triple-point temperature is affected by impurities dissolved. Nonetheless, the triple-point temperature had been realized especially in constructed triple-point cells with a reproducibility of 2×10^{-7} in the previous SI.

Since in the present SI the kelvin is defined by fixing the numerical value of the Boltzmann constant, k, instead of the triple point of water, T_{TPW}, the latter must be determined experimentally with an uncertainty assigned to its value. At the time of adopting the present definition, T_{TPW} was equal to 273.16 K with a relative standard uncertainty of less than 1×10^{-6} based on measurements of k made prior to the redefinition.

Primary thermometers allow the realization of the kelvin at any temperature in the present SI based on the defining constant k and a well-understood physical system whose temperature may be derived from traceable measurements of other quantities such as volume, pressure, speed of sound (see Chapter 8). Primary thermometers were already used in the previous SI to determine temperatures other than the triple-point temperature (T_{TPW}) using the best-known value of the Boltzmann constant. They were also used to determine the Boltzmann constant at the triple-point temperature prior to the redefinition resulting in the fixed value of k (see Chapter 8).

However, primary thermometers are difficult to use. Therefore, a practical international temperature scale (ITS) has been defined as decided by the CGPM in 1990 [21]. This ITS-90 is still used in the present SI and is supposed to be as close as possible to the thermodynamic temperature scale. The ITS is defined and represented by several fix points and respective measurement procedures to interpolate between these fix points. It is valid with fix points such as the triple points of hydrogen, neon, oxygen, argon, mercury, and water (of course) and melting points of gallium and other metals such as indium and copper (at 1357 K). The ITS-90 presently extends from 0.65 K up to the highest temperature accessible by radiation thermometry applying Planck's law. For temperatures in the range of 1 K to 0.902 mK also, a practical temperature scale on the base of the melting pressure curve of ^{3}He has been defined, the provisional low temperature scale, PLTS 2000 [21].

Because of the way temperature scales used to be defined, it remains common practice to express a thermodynamic temperature, symbol T, in terms of its difference from the reference temperature $T_0 = 273.15\,\mathrm{K}$, the ice point. This difference is called the Celsius temperature, symbol t, which is defined by the quantity equation: $t = T - T_0$. The unit of Celsius temperature is the degree Celsius, symbol °C, which is by definition equal in magnitude to the kelvin. A difference or interval of temperature may be expressed in kelvins or in degrees Celsius (13th CGPM, 1967/68).

2.2.6 The Mole: Unit of Amount of Substance

The quantity used to quantify the amount of elements or chemical compounds taking part in a chemical reaction is called amount of substance. This quantity is proportional to the number of elementary units of a sample with the proportionality constant being the same universal constant for all samples. The constant that relates the number of entities, $N(X)$, to the amount of substance, $n(X)$, is called the Avogadro constant, N_A, $N(X) = N_A \cdot n(X)$.

The unit of amount of substance is the mole [11]:

> The mole, symbol mol, is the SI unit of amount of substance. One mole contains exactly $6.022\,140\,76 \times 10^{23}$ elementary entities. This number is the fixed numerical value of the Avogadro constant, N_A, when expressed in the unit mol^{-1} and is called the Avogadro number. The amount of substance, symbol n, of a system is a measure of the number of specified elementary entities. An elementary entity may be an atom, a molecule, an ion, an electron, any other particle or specified group of particles.

This definition implies the exact relation $N_A = 6.022\,140\,76 \times 10^{23}\ \mathrm{mol}^{-1}$. Inverting this relation gives an exact expression for the mole in terms of the defining constant N_A:

$$1\ \mathrm{mol} = \left(\frac{6.022\,140\,76 \times 10^{23}}{N_A}\right) \tag{2.24}$$

The mole is defined as the amount of substance of a system that contains $6.022\,140\,76 \times 10^{23}$ specified elementary entities.

The previous definition of the mole fixed the value of the molar mass of carbon 12, $M(^{12}\mathrm{C})$ to be exactly 0.012 kg/mol [11]:

> 1) The mole is the amount of substance of a system which contains as many elementary entities as there are atoms in 0.012 kg of carbon 12; its symbol is "mol."
> 2) When the mole is used, the elementary entities must be specified and may be atoms, molecules, ions, electrons, other particles, or specified groups of such particles.
>
> It follows that the molar mass of carbon 12 is exactly $12\,\mathrm{g\ mol}^{-1}$, $M(^{12}\mathrm{C}) = 12\,\mathrm{g\ mol}^{-1}$.

In this definition, it was understood that unbound atoms of carbon 12, at rest and in their ground state, are referred to. In the present SI, $M(^{12}\mathrm{C})$ is no longer known exactly and must be determined experimentally. The value chosen for N_A is such that at the time of adopting the present definition of the mole, $M(^{12}\mathrm{C})$ was equal to 0.012 kg/mol with a relative standard uncertainty of less than 1×10^{-9} [11].

The molar mass of any atom or molecule X may still be obtained from its relative atomic mass from the equation

$$M(X) = A_\mathrm{r}(X)\,[M(^{12}\mathrm{C})/12] = A_\mathrm{r}(X)\,M_\mathrm{u} \tag{2.25}$$

and the molar mass of any atom or molecule X is also related to the mass of the elementary entity $m(X)$ by the relation

$$M(X) = N_\mathrm{A} m(X) = N_\mathrm{A} A_\mathrm{r}(X) m_\mathrm{u} \tag{2.26}$$

In these equations, M_u is the molar mass constant, equal to $M(^{12}\mathrm{C})/12$, and m_u is the unified atomic mass constant, equal to $m(^{12}\mathrm{C})/12$. They are related by the Avogadro constant through the relation

$$M_\mathrm{u} = N_\mathrm{A} m_\mathrm{u} \tag{2.27}$$

The realization of the mole is done by primary measurement techniques (e.g. gravimetry, coulombmetry, or isotope dilution mass spectroscopy) with specified measurands and uncertainties traced back to the SI [22].

2.2.7 The Candela: Unit of Luminous Intensity

The candela is a photometric unit defining the value of luminous intensity at the maximum of the spectral response of human eyes for daylight seeing, $V(\lambda)$, at a wavelength of about 555 nm corresponding to a frequency of 540×10^{12} Hz. The definition of the candela in the present SI is identical to the one in the previous SI, yet the wording is modified to be consistent with the other units [11]:

> The candela, symbol cd, is the SI unit of luminous intensity in a given direction. It is defined by taking the fixed numerical value of the luminous efficacy of monochromatic radiation of frequency 540×10^{12} Hz, K_cd, to be 683 when expressed in the unit $\mathrm{lm\,W^{-1}}$, which is equal to $\mathrm{cd\,sr\,W^{-1}}$, or $\mathrm{cd\,sr\,kg^{-1}\,m^{-2}\,s^3}$, where the kilogram, metre and second are defined in terms of h, c and $\Delta\nu_{\mathrm{Cs}}$.

This definition implies the exact relation $K_\mathrm{cd} = 683\,\mathrm{cd\,sr\,kg^{-1}\,m^{-2}\,s^3}$ for monochromatic radiation of frequency $\nu = 540 \times 10^{12}$ Hz. Inverting this relation gives an exact expression for the candela in terms of the defining constants K_cd, h, and $\Delta\nu_{\mathrm{Cs}}$ [11]:

$$1\,\mathrm{cd} = \left(\frac{K_\mathrm{cd}}{683}\right)\mathrm{kg\,m^2\,s^{-3}\,sr^{-1}} \approx 2.614\,830 \times 10^{10} (\Delta\nu_{\mathrm{Cs}})^2 h K_\mathrm{cd} \tag{2.28}$$

Table 2.1 List of all units with special name and symbol.

Name	Symbol	Derivation from defining constants	Defining constant(s)
Base units			
Second	s	$1\ \mathrm{s} = 9\,192\,631\,770/\Delta\nu_{\mathrm{Cs}}$	$\Delta\nu_{\mathrm{Cs}}$
Meter	m	$1\ \mathrm{m} \approx 30.663\,319\ c/\Delta\nu_{Cs}$	c, $\Delta\nu_{\mathrm{Cs}}$
Kilogram	kg	$1\ \mathrm{kg} \approx 1.475\,5214 \times 10^{40}\ h\Delta\nu_{\mathrm{Cs}}/c^2$	h, c, $\Delta\nu_{\mathrm{Cs}}$
Kelvin	K	$1\ \mathrm{K} \approx 2.266\,6653\ \Delta\nu_{\mathrm{Cs}}h/k$	k, h, $\Delta\nu_{\mathrm{Cs}}$
Ampere	A	$1\ \mathrm{A} \approx 6.789\,687 \times 10^8\ \Delta\nu_{\mathrm{Cs}}e$	e, $\Delta\nu_{\mathrm{Cs}}$
Mole	mol	$1\ \mathrm{mol} = 6.022\,140\,76 \times 10^{23}/N_A$	N_{A}
Candela	cd	$1\ \mathrm{cd} \approx 2.614\,830 \times 10^{10}\ (\Delta\nu_{\mathrm{Cs}})^2 h\ K_{cd}$	K_{cd}, h, $\Delta\nu_{\mathrm{Cs}}$

	Symbol	Derivation	Expressed in base units	Defining constant(s)
Derived units				
Hertz	Hz	1/s	s^{-1}	$\Delta\nu_{\mathrm{Cs}}$
Newton	N	$\mathrm{kg(m/s^2)}$	$\mathrm{kg\,m\,s^{-2}}$	h, c, $\Delta\nu_{\mathrm{Cs}}$
Pascal	Pa	$\mathrm{N/m^2}$	$\mathrm{kg\,m^{-1}\,s^{-2}}$	h, c, $\Delta\nu_{\mathrm{Cs}}$
Joule	J	N m	$\mathrm{kg\,m^2\,s^{-2}}$	h, c, $\Delta\nu_{\mathrm{Cs}}$
Watt	W	J/s	$\mathrm{kg\,m^2\,s^{-3}}$	h, c, $\Delta\nu_{\mathrm{Cs}}$
Volt	V			e, h, $\Delta\nu_{\mathrm{Cs}}$
Ohm	Ω			e, h
Coulomb	C	A s	A s	e
Farad	F	C/V		e, h, $\Delta\nu_{\mathrm{Cs}}$
Siemens	S	A/V		e, h
Weber	Wb	ϕ_0		e, h
Tesla	T	$\mathrm{Wb/m^2}$		e, h, c, $\Delta\nu_{\mathrm{Cs}}$
Henry	H	Wb/A		e, h, $\Delta\nu_{\mathrm{Cs}}$
Degree Celsius	°C	K − 273.15	K	k
Radian	rd		$\mathrm{m\,m^{-1}}$	c, $\Delta\nu_{\mathrm{Cs}}$
Steradian	sr		$\mathrm{m^2\,m^{-2}}$	c, $\Delta\nu_{\mathrm{Cs}}$
Lumen	lm	cd sr	cd sr	K_{cd}
Lux	lx	$\mathrm{lm/m^2}$	$\mathrm{cd\,sr\,m^{-2}}$	c, $\Delta\nu_{\mathrm{Cs}}$, K_{cd}
Becquerel	Bq	1/s	s^{-1}	$\Delta\nu_{\mathrm{Cs}}$
Gray	Gy	J/kg	$\mathrm{m^2\,s^{-2}}$	c, $\Delta\nu_{\mathrm{Cs}}$
Sievert	Sv	J/kg	$\mathrm{m^2\,s^{-2}}$	c, $\Delta\nu_{\mathrm{Cs}}$
Katal	kat	mol/s	$\mathrm{mol\,s^{-1}}$	N_{A}, $\Delta\nu_{\mathrm{Cs}}$

The justification as one of the base units in the previous and present SI had been, and still is, the immense economic importance of the quantitative characterization of illuminating light sources.

The previous definition had been set by the 16th CGPM in 1979:

> The candela is the luminous intensity, in a given direction, of a source that emits monochromatic radiation of frequency 540×10^{12} Hz and that has a radiant intensity in that direction of 1/683 watt per steradian.
> It follows that the spectral luminous efficacy for monochromatic radiation of frequency of 540×10^{12} Hz is exactly 683 lm W^{-1}, $K = 683$ lm $W^{-1} = 683$ cd sr W^{-1}.

2.2.8 Summary: Base and Derived Units of the SI

To conclude Section 2.2, Table 2.1 summarizes the present definition of the 7 base units and the 22 derived units with given names.

Note that the derivation of a derived unit is not always unambiguous. For example, the joule and watt can be derived from mechanical or electrical units. In Table 2.1, we have chosen to express the joule and, in turn, the watt by mechanical units. Moreover, the traceability of a derived unit to the defining constants of the SI is not always unambiguous either. The given sets of defining constants are the choice of the authors. We have chosen to link the electrical units to e and h only, whenever this is possible. Consequently, for the unit of magnetic flux, weber, we have chosen the flux quantum, Φ_0, for the derivation instead of Vs. This selection highlights the importance of the electrical quantum effects that involve e and h (see Chapters 4–6 for the details).

We finally state that the previous SI has proven to be most successful in providing the base for a harmonized, comparable, and traceable measurement system worldwide. Yet, the present SI is conceptually superior since it rests totally on constants of nature, which on the level required for present and near future metrology requirements are independent on space and time. So, all physical artifacts are abandoned. It further gives freedom to choose the experiments or techniques to realize the respective unit, and, therefore, improved techniques as well as advances in science can be considered and implemented at any time without changing the definition. In a nutshell, the present SI is universal, highly stable, and open to scientific and technical innovation.

References

1 BIPM GUM: Guide for the Expression of Uncertainties in Measurement https://www.bipm.org/en/publications/guides/gum.html (accessed November 2018).

2 Siebert, B.R.L. and Sommer, K.D. (2010). Uncertainty. In: *Handbook of Metrology*, vol. 2 (ed. M. Gläser and M. Kochsiek), 415–462. Weinheim: Wiley-VCH Verlag GmbH.

3 Weise, K. and Wöger, W. (1999). *Meßunsicherheit und Messdatenauswertung*. Weinheim: Wiley-VCH Verlag GmbH (in German).
4 Kose, V. and Melchert, F. (1991). *Quantenmaße in der elektrischen Meßtechnik*. Weinheim: Wiley-VCH Verlag GmbH (in German).
5 van der Ziel, A. (1954). *Noise*. Prentice-Hall; Vasilescu, G. (2005). *Electronic Noise and Interfering Signals: Principals and Applications*. Berlin, Heidelberg, New York: Springer.
6 Johnson, J.B. (1928). Thermal agitation of electricity in conductors. *Phys. Rev.* 32: 97–109.
7 Schottky, W. (1918). Über spontane Stromschwankungen in verschiedenen Elektrizitätsleitern. *Ann. Phys.* 57: 541–567 (in German).
8 BIPM Resolution 1 of the 26th CGPM. https://www.bipm.org/utils/common/pdf/CGPM-2018/26th-CGPM-Resolutions.pdf (accessed November 2018).
9 Newell, D.B., Cabiati, F., Fischer, J. et al. (2018). The CODATA 2017 values for *h,e,k*, and N_A for the revision of the SI. *Metrologia* 55: L12–L15.
10 Mohr, P.J., Newell, D.B., Taylor, B.N., and Tiesinga, E. (2018). Data and analysis for the CODATA 2017 special fundamental constants adjustment. *Metrologia* 55: 125–146.
11 BIPM (2019). Draft of the ninth SI-Brochure. http://www.bipm.org/utils/en/pdf/si-revised-brochure/Draft-SI-Brochure-2018.pdf (accessed November 2018).
12 BIPM (1967). Resolution 1 of the 13th CGPM, https://www.bipm.org/en/CGPM/db/13/1/ and *Metrologia* 4(1), 41–45 (accessed November 2018).
13 see e.g. Bauch, A. (2017). Atomare Definition der Zeiteinheit 1967–2017. *PTB-Mitteilungen* 127 (3): 13–28 (in German).
14 BIPM (2018). Resolution 2 of the 26th CGPM. https://www.bipm.org/utils/common/pdf/CGPM-2018/26th-CGPM-Resolutions.pdf (accessed November 2018).
15 Quinn, T.J. (2003). Practical realization of the definition of the metre, including recommended radiations of other optical frequency standards. *Metrologia* 40: 103–132.
16 BIPM. http://www.bipm.org/en/publications/mises-en-pratique/standard-frequencies.html (accessed November 2018).
17 Riehle, F., Gill, P., Arias, F., and Robertsson, L. (2018). The CIPM list of recommended frequency standard values: guidelines and procedures. *Metrologia* 55: 188–200.
18 see e.g.Schödel, R. (2009). *Handbook of Optical Metrology; Principals and Applications* (ed. T. Yoshizawa), 365–390. CRC Press.
19 Schödel, R., Walkov, A., Zenker, M. et al. (2012). A new ultra precision interferometer for absolute length measurements down to cryogenic temperatures. *Meas. Sci. Technol.* 23: 094004 (19 pp).
20 Mills, I.M., Mohr, P.J., Quinn, T.J. et al. (2005). Redefinition of the kilogram: a decision whose time has come. *Metrologia* 42: 71.
21 https://www.bipm.org/en/committees/cc/cct/publications-cc.html (accessed November 2018).
22 Appendix 2 of the SI broschure. https://www.bipm.org/utils/en/pdf/SIApp2_mol_en.pdf (accessed November 2018).

3

Realization of the SI Second: Thermal Beam Cs Clock, Laser Cooling, and the Cs Fountain Clock

This chapter describes the currently used common versions of Cs atomic clocks to realize the unit of time, the second, according to its present (and previous) definition.

We begin by recalling a few basics about the characterization of frequency standards and the nomenclature of electronic states in atoms. Next, we describe the "classical" Cs clock operating with a thermally generated beam of Cs atoms. Subsequently, we present the methods for laser cooling and trapping of neutral atoms, which laid the base for the realization of the Cs fountain clock discussed at the end of this chapter. Laser cooling is also indispensable for the so-called optical clocks, which we discuss in Section 9.1.

To start, let us recall some basic quantities to characterize frequency standards. The quality of a frequency standard is quantified by its accuracy and frequency stability or, vice versa, its uncertainty and frequency instability. The accuracy of a frequency standard characterizes how well the output of a clock agrees with the SI definition of the second. Different systematic effects may be the cause for differences in the instantaneous frequency output with respect to the nominal transition frequency of the unperturbed individual atom such as finite temperature, external magnetic or electric fields. A careful estimate of the uncertainty of a clock considering all possible contributions thus is of utmost importance for primary clocks that claim highest accuracy and stability. The evaluation of the frequency stability, which reflects statistical (noise) fluctuations of the output frequency of a standard, could, in principle, follow the standard statistical procedure by computing, for example, the standard deviation of a series of clock readings relative to a perfect or much better clock. However, this would result in misleading conclusions in some cases. Consider, for instance, a very stable clock with a constant frequency offset. In this case, the standard deviation incorrectly would assign a high instability to the standard, and, even worse, the standard deviation would increase with time. Therefore, clocks and their frequency standards are usually characterized by the so-called Allan deviation and its square, the Allan variance, respectively [1], as discussed briefly in the following text.

Consider the output voltage of a frequency standard

$$U(t) = U_0 \sin(2\pi\nu(t) \cdot t) = U_0 \sin(2\pi\nu_0 \cdot t + \varphi(t)) \tag{3.1}$$

where U_0 is the amplitude (which we have assumed to be stable), $\nu(t)$ the instantaneous frequency, ν_0 the nominal frequency, and $\varphi(t)$ the instantaneous phase.

The New International System of Units (SI): Quantum Metrology and Quantum Standards,
First Edition. Ernst O. Göbel and Uwe Siegner.
© 2019 Wiley-VCH Verlag GmbH & Co. KGaA. Published 2019 by Wiley-VCH Verlag GmbH & Co. KGaA.

The relative frequency deviation, also called fractional frequency, is then given by

$$y(t) \equiv \frac{\nu(t) - \nu_0}{\nu_0} = \frac{1}{2\pi\nu_0}\frac{\mathrm{d}\varphi}{\mathrm{d}t} \tag{3.2}$$

the relative frequency drift by

$$\dot{y}(t) \equiv \frac{\mathrm{d}}{\mathrm{d}t}y(t) \tag{3.3}$$

and the normalized phase fluctuation by

$$x(t) \equiv \frac{\varphi(t)}{2\pi\nu_0} \tag{3.4}$$

If the timescale is divided into contiguous sections with width τ, the mean relative frequency deviation in section n, $\overline{y_n(\tau)}$, is given by

$$\overline{y_n(\tau)} = \frac{1}{\tau}\int_{t_n}^{t_n+\tau} y(t)\,\mathrm{d}t. \tag{3.5}$$

The fluctuation of the instantaneous frequency of a clock, that is, its stability or instability, is characterized by the two-sample variance, also called Allan variance:

$$\sigma_y^2(\tau) = \frac{1}{2}\langle(\overline{y_{n+1}} - \overline{y_n})^2\rangle \tag{3.6}$$

For a finite series of measurements, this can be approximated by

$$\sigma_y^2(\tau) = \frac{1}{2(k-1)}\sum_{n=1}^{k-1}(\overline{y_{n+1}} - \overline{y_n})^2 \tag{3.7}$$

where k, the number of samples taken, must be sufficiently large to achieve high significance.

The Allan standard deviation, $\sigma_y(\tau)$, is defined as the square root of the Allan variance. A double logarithmic plot of $\sigma_y(\tau)$ versus τ allows to identify possible causes of instability. If, for example, shot noise (white frequency noise) is the dominating contribution, $\sigma_y(\tau)$ decreases like $\tau^{-1/2}$, for $1/f$ frequency noise $\sigma_y(\tau)$ turns constant at higher τ and may even increase again, for example, if frequency drift is present.

For white frequency noise, the Allan standard deviation scales as

$$\sigma_y(\tau) \propto \frac{1}{Q}\frac{1}{(S/N)}\tau^{-1/2} \tag{3.8}$$

where Q, the line quality factor, $Q = \nu/\Delta\nu$, is given by the frequency of the transition, ν, with respect to its measured linewidth, $\Delta\nu$, and S/N is the signal-to-noise ratio.

A more elaborated discussion of the properties of frequency standards can be found in [2].

Next, we recall a few basics about the nomenclature of electronic states in atoms, since this will repeatedly encounter us throughout the book.

Let us take the ground state of the Cs atom "$6^2S_{1/2}$" as an example. The first number, 6, indicates the main quantum number. The capital letter, S, gives the angular momentum in units of $\hbar = h/2\pi$, where S, P, D, F, and so on stand for,

respectively, 0, 1, 2, 3, 4, and so on. The small number on the upper left stands for the multiplicity, which is given by $(2\mathbf{S}+1)$, where $\mathbf{S}$ is the resulting electron spin of the atom in units $\hbar$. The lower right number finally corresponds to the total angular momentum of the atom, $\mathbf{J} = \mathbf{L} + \mathbf{S}$ (for Russell–Saunders coupling). For the notation of a specific quantum state, we shall use the $\langle bra|ket\rangle$ notation. Note that for optical dipole transitions, we have the selection rules $\Delta J = 0, \pm 1$ with the exception that $|0\rangle \rightarrow |0\rangle$ transitions are also forbidden.

3.1 The Thermal Beam Cs Clock

The setup of a Cs atomic clock with a thermally generated atom beam is schematically shown in Figure 3.1. In these clocks, the Cs atoms are generated by evaporating Cs in an oven. The atoms in this "thermal beam" are then state selected with respect to their quantum state by an inhomogeneous magnetic field, the polarizer (Stern–Gerlach technique). Alternatively, optical pumping can be applied for state selection. Subsequently, the atoms enter a microwave Ramsey resonator where the resonant transition between the two hyperfine states is induced.

The method of separated oscillatory fields applied here has been first proposed by Ramsey [3, 4] in the frame of atomic beam magnetic resonance spectroscopy. As shown in Figure 3.1, the microwave interaction regime is not a homogeneous microwave cavity but instead is split into two separated interaction regimes (each of width l) separated by an interaction-free regime of length L. The major result

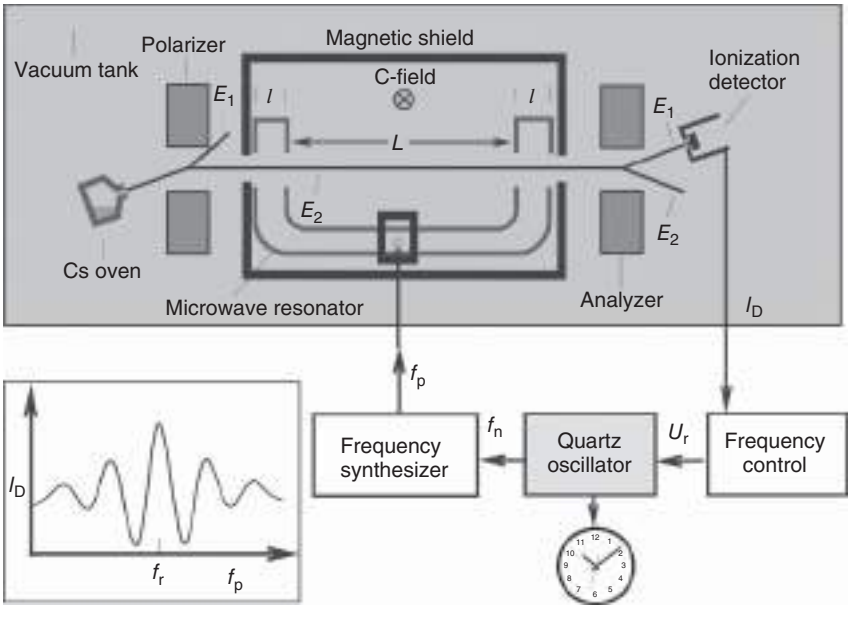

Figure 3.1 Schematic representation of a "thermal" Cs atomic clock. In the lower left, a section of a Ramsey resonance curve is shown. I_D is the current of the ionization detector. Source: Courtesy of A. Bauch, PTB.

of this arrangement is to increase the effective interaction time between the atom and the microwave, which thus according to the Heisenberg uncertainty relation results in a respective decrease in the linewidth of the resonant transition. The Ramsey technique has several advantages even compared to a single interaction zone of the same total length $2l + L$. For example, the linewidth is narrower (by a factor of 0.6), the requirements on the homogeneity of the magnetic field are considerably relaxed, and the first-order Doppler effect is absent provided the phase difference of the microwave field in the two sections is constant [4–6].

There are different approaches to describe phenomenologically the action of the Ramsey resonator. One is in terms of coherent interaction of the atoms with the microwave field by two subsequent $\pi/2$ pulses in the two regions. When the frequency of the microwave field exactly matches the Cs hyperfine frequency splitting of the $|F = 3, m_F = 0\rangle$ and $|F = 4, m_F = 0\rangle$ states, the atoms are placed by the $\pi/2$ pulse in a superposition with equal probability for both states. This state then can evolve freely with a frequency corresponding to the energy difference of these two states and enter the second interaction zone. Since the phase evaluation has been dictated by the microwave field in the first zone, the interaction with the second $\pi/2$ pulse is fully coherent (provided no phase relaxation occurs during the free travel), that is, after the interaction in the second zone, the probability of finding the atom in either state ($F = 3$ or $F = 4$) depends on the phase of the rf field with respect to the atomic oscillator. Thus, as the frequency of the rf field is changed, the number of atoms in either state oscillates, giving rise to the Ramsey interference. Alternatively, the action of the Ramsey arrangement can be described in analogy to an optical double-slit experiment [5]. A calculation of the transition probability, $P(\tau)$, for monochromatic atoms and $T \gg \tau$, where T is the time traveled freely between the two interaction sections, $T = L/\mathrm{v}$ (v is the velocity), and τ is the interaction time with the microwave field in each section, $\tau = l/\mathrm{v}$, yields [6]

$$P(\tau) = \frac{1}{2}\sin^2 b\tau(1 + \cos(\omega_{\mu\mathrm{W}} - \omega_{\mathrm{HF}})T + \varphi) \tag{3.9}$$

where $\omega_{\mu\mathrm{W}}$ is the angular frequency of the microwave field and ω_{HF} is the angular frequency of the hyperfine splitting, b is the Rabi frequency, $b = \mu B_{\mu\mathrm{W}}/\hbar$ (μ is the magnetic dipole moment and $B_{\mu\mathrm{W}}$ the amplitude of the microwave magnetic field), and φ is the phase difference between the two microwave fields in the two interaction sections. As a function of the detuning, $\delta = \omega_{\mu\mathrm{W}} - \omega_{\mathrm{HF}}$, Eq. (3.9) describes an interference structure as shown in Figure 3.2, the central part of which is also shown in Figure 3.1.

Equation (3.9) is valid for a given velocity of the atoms, and although the central peak of the Ramsey fringes does not exhibit first-order Doppler broadening, the fringe pattern is smeared out at larger detuning because of the velocity distribution, causing the so-called Ramsey pedestal.

Finally, as shown in Figure 3.1, the atoms leaving the Ramsey resonator pass a second state-selecting magnet (analyzer) and hit a detector with its signal intensity proportional to the number of atoms that have undergone a resonance transition. In addition, a small constant magnetic field (C field) is applied to split the otherwise energetically degenerated m_F states to excite only the

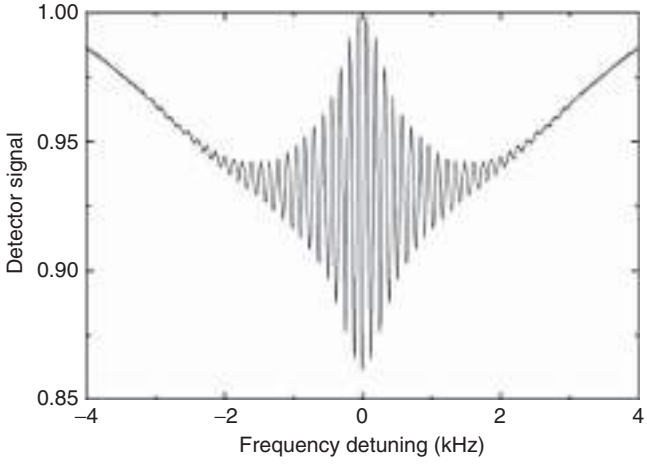

Figure 3.2 Measured Ramsey fringe pattern for the PTB's CS1 thermal beam clock. The curve appears upside down compared to the result of Eq. (3.9) due to the special operation configuration of PTB CS1. Source: Courtesy of A. Bauch, R. Wynands, PTB.

$|F = 3, m_F = 0\rangle \leftrightarrow |F = 4, m_F = 0\rangle$ transitions. Yet, the magnetic field-induced (quadratic) shift of the $m_F = 0$ states must be accounted for. The detector signal is then used through a feedback loop to stabilize the oscillator to the clock transition frequency. The relative uncertainty for these thermal beam clocks with magnetic state selection is of the order of 10^{-14} or slightly below as, for example, for the PTB's CS1 with a relative uncertainty of 8×10^{-15} [7]. Slightly smaller uncertainties have been achieved using optical pumping for state selection and laser-induced fluorescence for detection [8, 9].

We further note that meanwhile chip-scale atomic clocks based on microfabricated vapor cells with alkali atoms (usually ^{87}Rb) had been developed at the National Institute of Standards and Technology (NIST) and have become commercially available (see, for example, [10]).

Limiting factors for both clock accuracy and frequency stability of the realization of the second by the thermal Cs clock are the second-order (relativistic) Doppler effect and the limited interaction time regardless of the application of the Ramsey scheme (always assuming that the intrinsic, recombination lifetime-limited linewidth is much narrower). Both scale with the velocity of the atoms, v (for the second-order Doppler effect, which is a consequence of the relativistic time dilatation, we have $\Delta\nu/\nu = (1/2)(\mathrm{v}/c)^2$, which, at room temperature, [$\mathrm{v} \sim 100\,\mathrm{m/s}$] is of the order of 10^{-13}). Thus, the ultimate choice would be to use atoms with lower velocity. The first proposal in this sense by Zacharias (see, for example, [11]) was to use a vertical geometry with one microwave interaction regime where the atoms are launched upward and still interact with the microwave twice, first when flying upward and second when falling due to the action of gravity. The transit time would again be determined by the velocity of the atoms, and thus, a considerable increase in interaction time could be expected for the slowest atoms within the thermal distribution. Yet, the early approaches failed due to the weakness of the signal. However, with

the progress of laser cooling techniques, the concept was successfully realized in the fountain clocks (see Section 3.3).

Finally, since a clock is more than a frequency standard, validation of a clock needs at least a second clock to compare with. In fact, clock comparisons are at the heart of clock metrology as briefly mentioned at the end of Section 9.1.5.

3.2 Techniques for Laser Cooling and Trapping of Atoms

Laser irradiation as a method for cooling atoms and ion gases was first proposed by Hänsch and Schawlow [12] and Wineland and Dehmelt [13] in 1975, respectively. Cooling of atoms or ions relies on the presence of a strong allowed optical transition, as it is the case in Cs, for example, for the $6^2S_{1/2}$ to $6^2P_{3/2}$ transition (see Figure 3.3). However, cooling and trapping techniques differ for an ensemble of atoms or single ions. We briefly describe the cooling and trapping techniques of neutral atoms relevant for the Cs fountain clock, that is, Doppler and sub-Doppler cooling as well as optical molasses and magneto-optical traps.

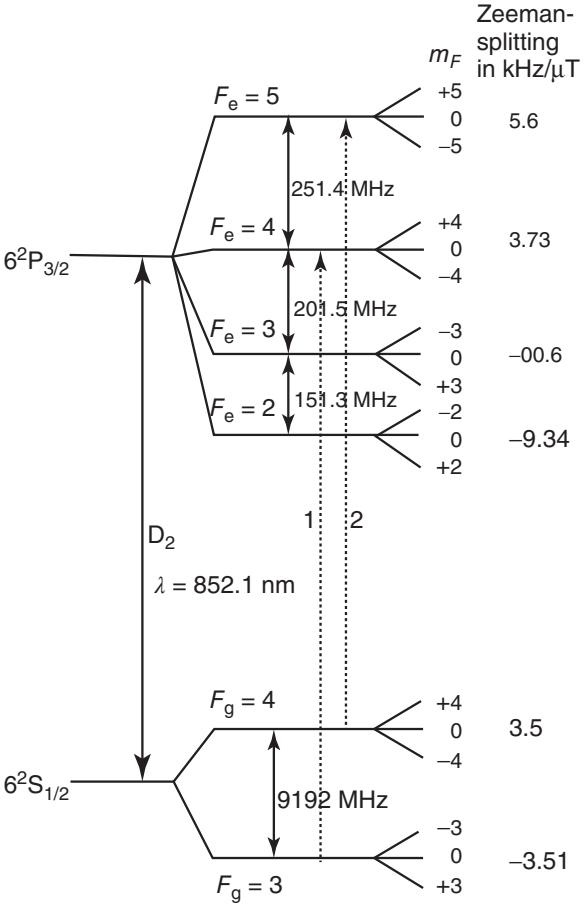

Figure 3.3 Energy-level scheme of the lower states in ^{133}Cs. Source: Göbel and Siegner 2005 [14]. Reproduced with permission of John Wiley & Sons.

Cooling and trapping of ions as well as trapping of neutral atoms in optical lattices are described in Chapter 9. For a more detailed reading on techniques and application of laser cooling, the reader is referred to [15–19].

3.2.1 Doppler Cooling, Optical Molasses, and Magneto-Optical Traps

If an atom gas with a given temperature and hence velocity distribution – in thermal equilibrium, this is a Maxwell–Boltzmann distribution – is irradiated by a laser with wavelength λ, slightly tuned to the red with respect to the resonance transition, only atoms with the "right" velocity opposing the laser beam are able to absorb a photon, as the frequency is shifted by the proper amount due to the Doppler effect. With the absorption process, a recoil momentum $\hbar k = {}^{h}/_{\lambda}$ pointing along the propagation direction of the incoming laser is transferred to the atom. As the atom recombines back into its ground state by emission of a photon, again it will receive a recoil momentum. However, since the emission will be in a random direction, in repeating absorption and emission processes, the "emission" recoil momentum averages out to zero but not the "absorption" momentum. Thus, consequently, the velocity of the atoms traveling toward the incoming laser beam will be lowered, and due to thermalization by scattering among each other, the entire atom gas will become cooler maintaining approximately a Maxwell–Boltzmann distribution. However, as the atom gas cools, the Doppler shift will be reduced, and, eventually, the incoming laser will not be in resonance anymore. This problem can be overcome in two ways: (i) tune (sweep) the laser frequency [20] or (ii) change the resonance frequency, for example, by applying a DC magnetic field due to the Zeeman effect [21]. The Zeeman method requires, however, that the shifts of the ground and excited states be different as it is the case for the cooling transition in Cs. In this case, the field can gradually be changed along the path of the atoms, thus always keeping a subset of atoms in resonance (Zeeman slower). A limit for this cooling procedure is set by the natural (homogeneous) linewidth, $\Delta\nu = 1/(2\pi T)$ (T is the excited-state phase relaxation time) of the resonance transition, resulting in a minimum temperature achievable by Doppler cooling in a two-level system of [22]

$$T_{\mathrm{D}} = \frac{h\Delta\nu}{2k_{\mathrm{B}}} \tag{3.10}$$

Consider next two laser beams opposing each other and are still detuned slightly to the red. Then for each atom, there is a laser beam, which travels in the opposite direction as the atom (for the one-dimensional case to which we restrict the discussion for the moment). The atomic resonance frequency is shifted toward the laser frequency of the opposing beam such that absorption can take place. Thus, there is a resulting force decelerating the atoms. With three intersecting pairs of orthogonal laser beams as illustrated in Figure 3.4, the so-called optical molasses (OM) can be realized. The name "optical molasses" reflects the fact that the motion of atoms is like a particle (or body) in a viscous medium. Note, however, that an OM does not provide a trap for atoms, since there is no restoring force for atoms leaving the center of the intersecting laser

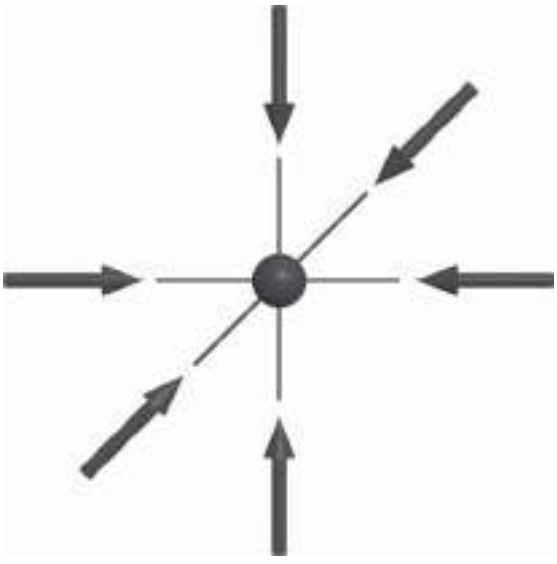

Figure 3.4 Laser beam arrangement for an optical molasses. Source: Göbel and Siegner 2005 [14]. Reproduced with permission of John Wiley & Sons.

beams. Trapping and cooling of atoms are realized by magneto-optical traps (MOTs).

In an MOT, the combined action of a spatially inhomogeneous magnetic field and laser light performs both cooling and trapping. It requires for the resonance transition being involved that the angular momentum of the ground state, J_g, and the excited state, J_e, differ by one unit, $J_e = J_g + 1$, that is, $J_g = 0$ and $J_e = 1$ in the simplest case as, for example, for ^{40}Ca and ^{88}Sr (see Chapter 9). Taking this simplest case, the action of a DC magnetic field, B, will leave the ground state, $J_g = 0$, unaffected, while the excited state, $J_e = 1$, splits into $2J_e + 1 = 3$ substates with $m_J = 0, -1$, and $+1$, respectively. The energy of the $m_J = 0$ state is almost independent of the magnetic field strength, whereas the energies of the $m_J = \pm 1$ vary linearly with the magnetic field:

$$\Delta E = \pm g_J \mu_B B \tag{3.11}$$

where g_J is the Landé factor and μ_B the Bohr magneton. Optical transitions between the ground state to the $m_J = +1$ and $m_J = -1$ excited state can be induced by σ^+ and σ^- circular polarized light, respectively.

Next we consider a magnetic field that varies linearly along the z direction like $B_z(z) = bz$ from a center at $z = 0$ and two counter propagating laser beams of opposite circular polarization, σ^+ and σ^-, respectively, slightly tuned to the red with respect to the $J_g \rightarrow J_e$, $m_J = 0$ transition as shown in Figure 3.5. Atoms traveling from $z = 0$ to the right opposing the σ^- laser beam will have their energy level $m_J = -1$ shifted toward the laser frequency, resulting in an increase in absorption. Conversely, for the σ^+ laser beam, the absorption even further decreases, and which results in cooling. But in contrast to the OM, we now have a redriving force toward the center at $z = 0$ due to the spatial gradient of the magnetic field. On the other side, the same arguments hold with the role of the σ^+ and σ^- beam reversed. A three-dimensional (3D) trap consequently can be realized similarly

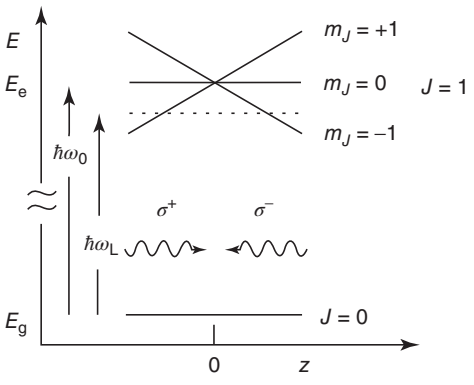

Figure 3.5 Energy levels and laser beam arrangement in a (1D) MOT. Riehle 2004 [2]. Reproduced with permission of John Wiley & Sons.

to the OM (see Figure 3.4) but now with three pairs of opposing laser beams with opposite circular polarization [23]. The magnetic field with properties as required is a quadrupole field that is usually generated by a pair of Helmholtz coils with the opposite direction of the electric current ("anti-Helmholtz coils").

3.2.2 Cooling Below the Doppler Limit

Cooling well below the Doppler limit was observed first by Bill Phillips's group at the NIST in Gaithersburg, where in a sodium gas, they measured temperatures as low as $T = 43\,\mu K$ while the Doppler limit was at $T_D = 240\,\mu K$ [24]. As subsequently shown by Dalibad and Cohen-Tannoudji [25], this is due to the multilevel character of the alkali atoms combined with a spatially varying light field. Although in the meantime different schemes for sub-Doppler cooling (see, e.g. in [15–19]) have been demonstrated, we shall briefly describe only Sisyphus cooling. This mechanism is based on the standing-wave pattern generated by opposing laser beams (in the z direction) with the same wavelength but orthogonal linear (lin ⊥ lin) polarization. In this standing-wave pattern, the polarization state varies spatially with a period corresponding to the wavelength of the laser beams. The polarization changes across half a wavelength are shown in Figure 3.6a. Starting,

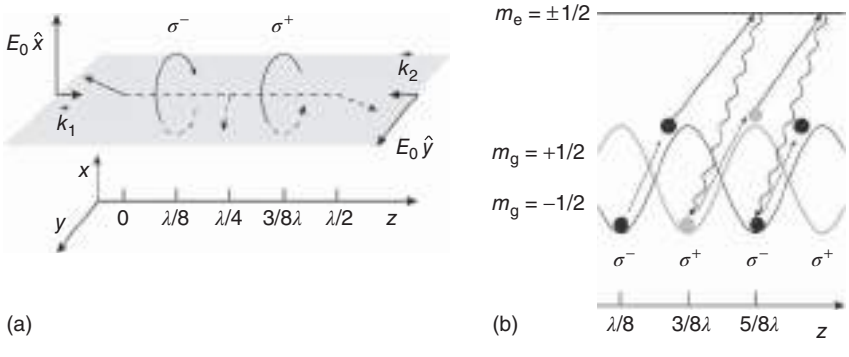

Figure 3.6 Illustration of Sisyphus cooling. (a) The polarization along the z direction in a "lin ⊥ lin" standing-wave configuration. (b) The corresponding light shift of the $m_g = +1/2$ and $m_g = -1/2$ ground state. Riehle 2004 [2]. Reproduced with permission of John Wiley & Sons.

for example, at $z = 0$, where we have a resulting linear polarization under 45° with respect to the incoming beams, the polarization changes to σ^- circular polarization at $z = \lambda/8$ then becomes linear again at $z = \lambda/4$, and subsequently changes to σ^+ circular polarization at $z = 3/8\lambda$ and so forth. An atom with a $J = 1/2$ ground state will experience a spatially varying shift of its $m_g = -1/2$ and $m_g = +1/2$ states due to the Stark effect as shown in Figure 3.6b. Consider an atom at the $z = \lambda/8$ position, where the polarization is σ^-, traveling along the z direction. While moving forward, it has to climb up the hill at the expense of its kinetic energy. At the top of the hill at $z = 3/8\lambda$, the polarization has changed to σ^+, resulting in strong transitions into the excited state $m_e = +1/2$ ($\Delta m = +1$) from where the atom can recombine in either the $m_g = -1/2$, 0, or $+1/2$ state, resulting in a net transfer of atoms from the $m_g = -1/2$ into the $m_g = +1/2$ state where it ends up in the potential minimum. Moving forward, it has to climb up the potential hill again, and as it reaches the top at $z = 5/8\lambda$, it will be pumped by the σ^- light back into the $m_g = -1/2$ state and the process is repeated again. In principle, cooling could proceed until the recoil limit for atoms with total mass M

$$T = \frac{(\hbar k)^2}{2k_B M} \tag{3.12}$$

is reached (k is the wave vector of the laser light, while the Boltzmann constant is denoted by k_B in this section). This fundamental limit is set by the spontaneous emission of a single photon, that is, the momentum transferred by the last photon emitted before the final temperature is reached.

3.3 The Cs Fountain Clock

The Cs fountain clock [26] relies on the same principle as the "thermal beam" Cs clock described in Section 3.1, that is, the $|F = 3, m_F = 0\rangle \rightarrow |F = 4, m_F = 0\rangle$ hyperfine microwave transition of the ^{133}Cs ground state, $\Delta\nu_{Cs}$, is the reference transition according to the definition of the second, and a Ramsey scheme is applied for the interrogation of the Cs atoms with the rf field. However, in the fountain clock laser-cooled Cs atoms are used with a velocity (about 1 cm/s) that is much lower than that of the Cs atoms in the thermal beam (of order 100 m/s). The interaction time increases accordingly, resulting in a considerably reduced linewidth. The setup of a Cs fountain clock is schematically shown in Figure 3.7. It consists of three major parts: the preparation zone, the detection zone, and the microwave interaction zone. The Cs atoms are released into the cooling chamber of the preparation zone from a Cs reservoir held at a constant temperature close to room temperature and a partial pressure of some 10^{-6} Pa. Laser cooling is achieved in an MOT in combination with an OM (sometimes only an OM is used). The cloud of Cs atoms with about 10^7–10^8 atoms is cooled below the Doppler limit to temperatures of order 1 μK. The strong dipole-allowed $|6^2S_{1/2}, F_g = 4\rangle$ to the $|6^2P_{3/2}, F_e = 5\rangle$ transition (labeled 2 in Figure 3.3) is used for laser cooling. However, since during the cooling cycle some atoms also relax – though ideally forbidden – into the $|F_g = 3\rangle$ state, in addition to the cooling laser beams, a repumping laser (labeled 1 in Figure 3.3 is required to pump these atoms back

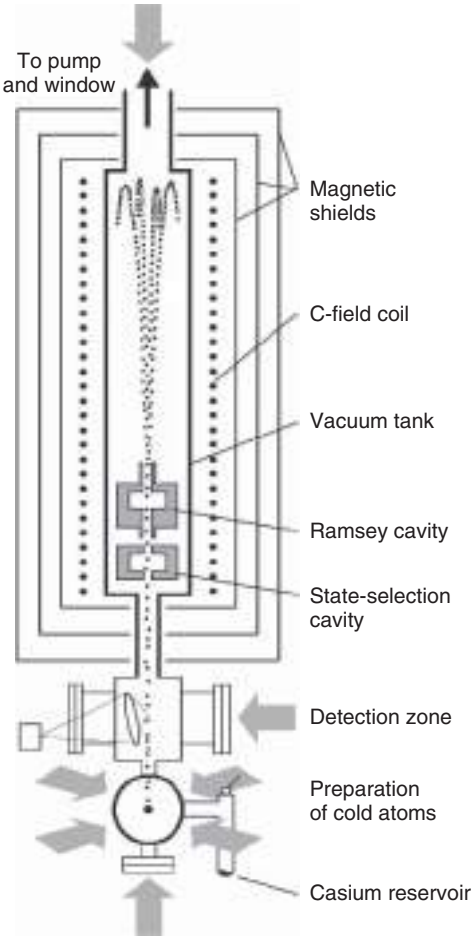

Figure 3.7 Schematic setup (simplified) of an atomic fountain clock. Source: Courtesy of R. Wynands, PTB.

into the $|F_g = 4\rangle$ state via the $|F_e = 4\rangle$ state. At the end of the cooling phase, a moving OM is generated by slightly detuning the vertical laser beams. If the upward-pointing laser beam is detuned to the blue by an amount $\delta\nu$ and vice versa the downward-pointing laser to the red by the same amount, the resulting interference pattern moves upward (moving molasses) and the atom cloud is accelerated to velocities of typically several meters per second. When subsequently all laser beams are turned off, the atoms fly on into the microwave resonator after passing the detection zone and the state selection cavity. As the atoms enter the state selection cavity, they are in the $|F_g = 4\rangle$ state with nine $|m_F\rangle$ states ($m_F = -4, -3, \ldots, +4$) equally populated. In the state selection cavity, atoms are transferred from the $|F_g = 4, m_F = 0\rangle$ state into the $|F_g = 3, m_F = 0\rangle$ state by applying a microwave pulse tuned at the clock transition frequency, and subsequently, all other atoms that remained in the $|F_g = 4\rangle$ state are pushed away by a laser beam tuned to the $|F_g = 4\rangle \rightarrow |F_e = 5\rangle$ transition. Thus, only $|F_g = 3, m_F = 0\rangle$ atoms enter the Ramsey cavity where the clock transition is excited as described in Section 3.1. The interaction time is now given by the time of flight of

the atoms up to their apogee, where due to gravitational force they come to rest and subsequently fall back down to the cavity. This time of flight ($T = 2\sqrt{2h/g}$) for an $h \sim 1$ m apogee above the cavity is of the order 1 s, which consequently determines the repetition rate for the entire cycle. During the flight, the atomic cloud will expand according to its thermal velocity, and thus, only a fraction of the atoms will hit the aperture of the Ramsey resonator and undergo the second Ramsey transition. However, as the atoms are cooled below the Doppler limit, this spread for a $T = 1$ μK cloud is small such that about 50% of the atoms again enter the interaction regime. If the atoms had been cooled to the Doppler limit only ($T = 125$ μK), this fraction would have been reduced to about 1%. Finally, the atoms after leaving the microwave section pass through the detection zone where the number of atoms in the $|F_g = 4\rangle$ and $|F_g = 3\rangle$ states is detected separately by laser-induced fluorescence [27]. The detection zone has to be viewed as three spatially subsequent zones. In the first part, the atoms pass a standing-wave laser field exciting the $|F_g = 4\rangle \rightarrow |F_e = 5\rangle$ transition. Relaxation into the $|F_g = 4\rangle$ state results in the emission of fluorescence.

Repeating this process many times (cycling) results in a fluorescence signal, which can be detected by a photodetector with its overall signal strength being proportional to the number of atoms originally in the $|F_g = 4\rangle$ state. Under this first detection stage, the atoms in the $|F_g = 4\rangle$ state are then pushed away by a strong unidirectional laser beam again tuned to the $|F_g = 4\rangle \rightarrow |F_e = 5\rangle$ transition so that only $|F_g = 3\rangle$ atoms reach the third zone. There, they are pumped in a standing-wave field into the $|F_g = 4\rangle$ state, and then again, the cycling transition is used with the fluorescence signal now being proportional to the number of $|F_g = 3\rangle$ atoms entering the zone. The entire cycle from cooling to detection is summarized in Figure 3.8.

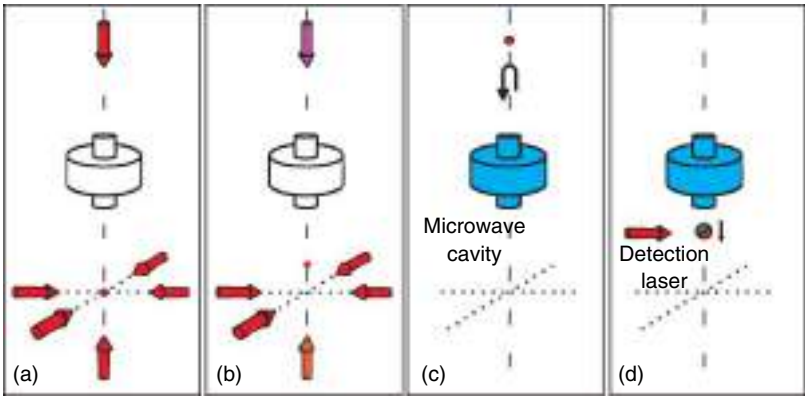

Figure 3.8 Principle of operation of the atomic fountain clock illustrating the essential four steps in a measurement cycle: (a) preparation of the cloud of cold atoms, (b) launch of the cloud toward the microwave cavity and subsequent passage through the state selection cavity and Ramsey cavity, (c) free flight and turnaround of the cloud and subsequent second passage through the Ramsey cavity, and (d) detection of the number of atoms in the $|F_g = 3\rangle$ and $|F_g = 4\rangle$ states, respectively. Source: Courtesy of R. Wynands, PTB.

As a major result, the Cs fountain clock has improved the stability and accuracy of the realization of the second by roughly 1 order of magnitude compared to the thermal beam Cs clock [28–34]. Resulting values for the Allan standard deviation as low as $\sigma_y(\tau) = 2.5 \times 10^{-14}\ (\tau/s)^{-1/2}$ and fractional uncertainties of 1.71×10^{-16} [34] have been reported. Consequently, the scale unit of the International Atomic Time (TAI) scale is presently dominated by frequency calibration reports by fountain clocks operated in national metrology institutes [34, 35].

In addition, fountain clocks operating in a continuous mode, rather than the previously described pulse mode, have been developed [36, 37]. Further, there has been realized a ^{87}Rb fountain frequency standard at the SYRTE laboratory in Paris [38] and at Penn State University [39] as well as a dual fountain clock, simultaneously using cesium and rubidium atoms also at SYRTE [40].

At the end of this section dealing with microwave clocks and frequency standards, hydrogen maser must be mentioned because of its excellent short-term stability (Allan standard deviation $<10^{-14}$ at 1 s of averaging time) and its use in timing laboratories as the so-called flywheel to increase the short-time stability of the timescales. The hydrogen maser is based on transitions between the two $|F = 1, m_F = 0\rangle$ and $|F = 0, m_F = 0\rangle$ ground states of the hydrogen atom at 1.42 GHz. From a beam of atoms, the $|F = 1, m_F = 0\rangle$ and $|F = 1, m_F = 1\rangle$ states are selected by a Stern–Gerlach magnet and transferred into a storage bulb inside a microwave cavity resonant with a transition frequency of 1.42 GHz. All atoms in the other ground states $|F = 1, m_F = -1\rangle$ and $|F = 0, m_F = 0\rangle$ do not reach the storage bulb. Thus, a population inversion exists, resulting in stimulated emission of the $|F = 1, m_F = 0\rangle \rightarrow |F = 0, m_F = 0\rangle$ transition, and self-sustaining maser oscillation may build up. A small antenna can pick up this oscillation (active hydrogen maser). In contrast, in the passive hydrogen maser, a microwave signal at the resonance frequency is amplified by the population-inverted hydrogen atom gas.

For further description and discussion of the properties of active and passive hydrogen masers, the reader is referred to [2].

References

1 Allan, D.W. (1966). Statistics of frequency standards. *Proc. IEEE* 54: 221–230.
2 Riehle, F. (2004). *Frequency Standards*. Wiley-VCH: Weinheim.
3 Ramsey, N.F. (1950). A molecular beam resonance method with separated oscillating fields. *Phys. Rev.* 78: 695–699.
4 Ramsey, N.F. (1990). Experiments with separated oscillatory fields and hydrogen masers. *Rev. Mod. Phys.* 62: 541–552.
5 Wynands, R. (2009). *Time in Quantum Mechanics*, Lecture Notes on Physics, vol. 2 and 789 (ed. G. Muga, A. Ruschhaupt and A. del Campo), 363–418. Berlin, Heidelberg: Springer-Verlag.
6 Vanier, J. and Audo, C. (2005). The classical caesium beam frequency standard: fifty years later. *Metrologia* 42: S31–S42.
7 Bauch, A. (2005). The PTB primary clocks CS1 and CS2. *Metrologia* 42: S43–S54.

8 Makdissi, A. and de Clercq, E. (2001). Evaluation of the accuracy of the optically pumped caesium beam primary frequency standard of BNM-LPTF. *Metrologia* 38: 409–425.

9 Hasegawa, A., Fukuda, K., Kajita, M. et al. (2004). Accuracy evaluation of optically pumped primary frequency standard CRL-O1. *Metrologia* 41: 257–262.

10 Kitching, J. (2018). Chip scale atomic devices. *Appl. Phs. Rev.* 5: 031302-1-38.

11 Kasevich, M.A., Riis, E., Chu, S., and DeVoe, R.G. (1989). Atomic fountains and clocks. *Opt. News* 15 (12): 31–32.

12 Hänsch, T. and Schawlow, A. (1975). Cooling of gases by laser radiation. *Opt. Commun.* 13: 68–69.

13 Wineland, D. and Dehmelt, H. (1975). Proposed 1014 $\delta\nu < \nu$ laser fluorescence spectroscopy on Ti+ mono-ion oscillator. *Bull. Am. Phys. Soc.* 20: 637.

14 Göbel, E.O. and Siegner, U. (2005). *Quantum Metrology: Foundation of Units and Measurements*. Weinheim: Wiley-VCH, 2018.

15 Campbell, G.K. and Phillips, W.D. (2011). Ultracold atoms and precise time standards. *Philos. Trans. R. Soc. London, Ser. A* 369: 4078–4089.

16 Metcalf, H.J. and van der Straten, P. (1999). *Laser Cooling and Trapping*. New York, Berlin, Heidelberg: Springer-Verlag.

17 Phillips, W.D. (1989). Laser cooling and trapping of neutral atoms. *Rev. Mod. Phys.* 70: 721–741.

18 Chu, S. (1998). The manipulation of neutral particles. *Rev. Mod. Phys.* 70: 685–706.

19 Cohen-Tannoudji, C. (1998). Manipulation of atoms with photons. *Rev. Mod. Phys.* 70: 707–720.

20 Letokhov, V.S., Minogin, V.G., and Pavlik, B.D. (1976). Cooling and trapping of atoms and molecules by a resonant laser field. *Opt. Commun.* 19: 72–75.

21 Phillips, W. and Metcalf, H. (1982). Laser deceleration of an atomic beam. *Phys. Rev. Lett.* 48: 596–599.

22 Lett, P.D., Phillips, W.D., Rolston, S.L. et al. (1989). Optical molasses. *J. Opt. Soc. Am. B* 6: 2084–2107.

23 Raab, E.L., Prentiss, M., Cable, A. et al. (1987). Trapping of neutral atoms with radiation pressure. *Phys. Rev. Lett.* 59: 2631–2634.

24 Lett, P.D., Watts, R.N., Westbrook, C.I. et al. (1988). Observation of atoms laser cooled below the Doppler limit. *Phys. Rev. Lett.* 61: 169–172.

25 Dalibad, J. and Cohen-Tannoudji, C. (1989). Laser cooling below the Doppler limit by polarization gradients: simple theoretical models. *J. Opt. Soc. Am. B* 6: 2023–2045.

26 For review see e.g.:Wynands, R. and Weyers, S. (2005). Atomic fountain clock. *Metrologia* 42: S64–S79.

27 Weyers, S., Bauch, A., Hübner, U. et al. (2000). First performance results of PTB's atomic caesium fountain and a study of contributions to its frequency instability. *IEEE Trans. Ultrason. Ferroelectr. Freq. Control* 47: 432–437.

28 Bize, S., Laurent, P., Abgrall, M. et al. (2004). Advances in atomic fountains. *C.R. Phys.* 5: 829–843.

29 Guéna, J., Abgrall, M., Rovera, D. et al. (2012). Progress in atomic fountains at LNE-SYRTE. *IEEE Trans. Ultrason. Ferroelectr. Freq. Control* 59: 391–410.

30 Heavner, T.P., Donley, E.A., Levi, F. et al. (2014). First accuracy evaluation of NIST-F2. *Metrologia* 51: 174–182.

31 Szymaniec, K., Park, S.E., Marra, G., and Chalupczak, W. (2010). First accuracy evaluation of the NPL-CsF2 primary frequency standard. *Metrologia* 47: 363–376.

32 Domnin, Y.S., Baryshev, V.N., Boyko, A.I. et al. (2013). The MTsR-F2 fountain-type cesium frequency standard. *Meas. Tech.* 55: 1155–1162.

33 Levi, F., Calonico, D., Calosso, C.E. et al. (2014). Accuracy evaluation of ITCsF2: a nitrogen cooled caesium fountain. *Metrologia* 51: 270.

34 Weyers, S., Gerginov, V., Kazda, M. et al. (2018). Advances in the accuracy, stability, and reliability of the PTB primary fountain clocks. *Metrologia* 55 (6): 789–805.

35 BIPM (2019). Circular T. https://www.bipm.org/jsp/en/TimeFtp.jsp (accessed February 2019).

36 Dudle, G., Mileti, G., Joyet, A. et al. (2000). An alternative cold cesium frequency standard: the continuous fountain. *IEEE Trans. Instrum. Meas.* 47: 438–442.

37 Jallageas, A., Devenoges, L., Petersen, M. et al. (2018). First uncertainty evaluation of the FoCS-2 primary frequency standard. *Metrologia* 55: 366–385.

38 Bize, S., Sortais, Y., Santos, M.S. et al. (1999). High-accuracy measurement of the 87 Rb ground-state hyperfine splitting in an atomic fountain. *Europhys. Lett.* 45: 558–564.

39 Fertig, C. and Gibble, K. (1999). Laser cooled 87 Rb clock. *IEEE Trans. Instrum. Meas.* 48: 520–523.

40 Guéna, J., Abgrall, M., Clairon, A., and Bize, S. (2014). Contributing to TAI with a secondary representation of the SI second. *Metrologia* 51: 108–120.

4

Flux Quanta, Josephson Effect, and the SI Volt

The elementary charge e and the Planck constant h are defining constants of the present SI. Their fixed numerical values determine the SI value of the flux quantum, which is an elementary excitation in superconductors. Superconductivity is a macroscopic quantum effect, which is observed in certain solid-state systems at low temperatures. The superconducting state can be described by a single wave function, which extends over macroscopic distances in real space. The composite quasiparticles that occupy the macroscopic quantum state are bosonic Cooper pairs consisting of two electrons, which are weakly bound to each other. If a superconducting ring is placed in a magnetic field, the magnetic flux penetrating the ring is found to be quantized in integer multiples of the flux quantum.

Quantum metrology and quantum standards take advantage of Cooper pairs and flux quanta. The tunneling of Cooper pairs between two superconductors is called the Josephson effect [1]. This phenomenon links the macroscopic physical quantity voltage to the counting of flux quanta per time interval. Thereby, the SI unit volt is realized due to the link to the defining constants e and h. Josephson voltage standards, the realization of the SI volt, and metrology based on Josephson voltage standards are addressed in Section 4.1.

In Section 4.2, we discuss that flux quanta can also be used to implement quantum-based magnetic measurements. The ratio between the magnetic flux and the flux quantum determines the outcome of interference effects in superconducting quantum interference devices (SQUIDs). This interference allows highly sensitive measurements of magnetic flux and, in turn, results in measurements of magnetic field and magnetic moment. The measurements are linked to the flux quantum. The chapter is concluded by a brief introduction to the realization of the tesla, the SI unit of the magnetic flux density, by nuclear magnetic resonance (NMR).

4.1 Josephson Effect and Quantum Voltage Standards

4.1.1 Basics of Superconductivity

The physical properties of superconductors are the basis of the phenomena treated in this chapter. Therefore, we introduce the basic physics of superconductors in this section. Superconductivity was discovered by the Dutch physicist

The New International System of Units (SI): Quantum Metrology and Quantum Standards,
First Edition. Ernst O. Göbel and Uwe Siegner.
© 2019 Wiley-VCH Verlag GmbH & Co. KGaA. Published 2019 by Wiley-VCH Verlag GmbH & Co. KGaA.

Heike Kamerlingh Onnes in 1911 after he had succeeded in liquefying ^{4}He in 1908. For his achievements in low-temperature physics, *Kamerlingh Onnes* received the Nobel Prize in physics in 1913. Superconductivity is the disappearance of electric resistance below a critical temperature T_c and expulsion of magnetic fields from the interior of a superconducting material (Meissner–Ochsenfeld effect; see Section 4.2.1). *Kamerlingh Onnes* discovered superconductivity when he studied the temperature dependence of the resistance of mercury (Hg), which has a critical temperature $T_c = 4.2$ K. Subsequently, superconductivity was found in other metals, such as tin (Sn, $T_c = 3.7$ K), lead (Pb, $T_c = 7.2$ K), and niobium (Nb, $T_c = 9.5$ K).

After several classical or semiclassical approaches to describe superconductivity [2, 3], superconductivity was quantum mechanically described by Bardeen et al. in 1957 [4, 5]. In 1972, *John Bardeen*, *Leon. N. Cooper*, and *John Robert Schrieffer* received the Nobel Prize in physics for their "BCS theory."

The basic concept of the BCS theory involves the formation of Cooper pairs from electrons close to the Fermi surface and their condensation into a macroscopic quantum state described by a single wave function. Cooper pairs consist of two electrons with opposite spin S and wave vector $\mathbf{k}$, resulting in $S = 0$, $\mathbf{k} = 0$, and a total charge $e_S = -2e$ if e denotes the elementary charge. In classical low-temperature superconductors, the attractive force to bind two electrons is mediated by the electron–phonon interaction, which overcomes the repulsion of the negatively charged electrons. We note, however, that the BCS theory is independent of the nature of the attractive force between the electrons.

The Cooper pairs are separated in energy from the single-particle electron states by an energy gap $2\Delta(T)$. With increasing temperature, $\Delta(T)$ decreases from $\Delta(T = 0) = 1.76kT_c$ (k Boltzmann constant) to zero at T_c according to

$$\Delta(T) = \Delta(T = 0)\sqrt{\cos\left(\frac{\pi}{2}\left(\frac{T}{T_c}\right)^2\right)} \tag{4.1}$$

The continuous decrease in the order parameter, Δ, is characteristic of a second-order phase transition. At any temperature, superconductivity is unstable against external magnetic fields and disappears at some critical magnetic field strength, different for type I and II superconductors. Moreover, superconductivity breaks down in electric fields that cause a potential drop over the superconductor comparable to its energy gap $2\Delta(T)$.

For the forthcoming discussion of the Josephson effect, the key element is the wave function ψ, which describes the macroscopic quantum state of a superconductor according to the BCS theory. The wave function can be written as

$$\psi = \sqrt{n_S}e^{i\theta} \tag{4.2}$$

with $n_S = \psi\psi^*$ being the density of Cooper pairs, where the asterisk indicates the complex conjugate, and θ the phase of the macroscopic wave function.

The BCS theory describes metallic low-temperature superconductors, on which today's most advanced applications in metrology are based. For completeness, we like to mention that in 1986 *Georg Bednorz and Alexander Müller* at the IBM laboratories in Rüschlikon discovered superconductivity in a perovskite

ceramic material (a Ba–La–Cu oxide) at a temperature of 35 K [6]. In 1987, they received the Nobel Prize in physics for this discovery. Their work set a starting point for intense research in the so-called high-temperature superconductors with the most prominent cuprate material being yttrium barium copper oxide (YBCO). YBCO was the first material in which superconductivity was observed at a critical temperature $T_c = 93$ K above the temperature of liquid nitrogen [7]. An impressively high critical temperature of $T_c = 133$ K has been achieved with a Hg–Ba–Ca–Cu–O-based cuprate [8]. The theoretical description of high-T_c superconductors is still a matter of discussion. Yet, it seems clear that the CuO planes and the precise oxygen content play a decisive role.

Iron-based materials (so-called pnictides, e.g., $Sm(O_{1-x}F_x)FeAs$) with critical temperatures up to $T_c = 55$ K have been discovered [9]. Even though their critical temperatures are still considerably lower than those of cuprates, mechanical properties of some oxygen-free pnictides, such as $SrFe_2As_2$, are superior to those of brittle cuprates. This property may allow easier fabrication of, for example, cables.

4.1.2 Basics of the Josephson Effect

The Josephson effect was theoretically predicted by *Brian D. Josephson* in 1962 [1]. It refers to the tunneling of Cooper pairs without resistance between two superconductors, which are separated by a thin tunnel barrier. This arrangement, called the Josephson junction, is schematically shown in Figure 4.1.

A key element of a Josephson junction is the tunnel barrier, which can be an insulator, a normal metal, or a semiconductor. Its thickness is typically a few nanometers, chosen to be large enough to prevent direct exchange of Cooper pairs. On the other hand, the barrier is thin enough to allow the macroscopic wave function ψ_1 of superconductor 1 to couple to superconductor 2, and vice versa. Such a barrier is said to provide a weak link. The coupling is a purely quantum mechanical phenomenon. It reflects the fact that a quantum mechanical wave function does not end abruptly at the edge of a sample or structure but leaks into the neighboring region, where it decays exponentially.

The supercurrent of Cooper pairs across the tunnel barrier is determined by the time-dependent Schrödinger equation. More specifically, two separate equations must be written for superconductors 1 and 2, which read in short notation

$$i\hbar\frac{\partial\psi_{1,2}(t)}{\partial t} = E_{1,2}\psi_{1,2}(t) + K\psi_{2,1} \tag{4.3}$$

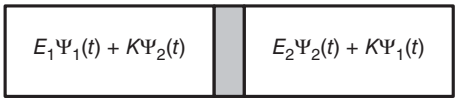

Figure 4.1 Schematic drawing of a Josephson junction. Two superconductors are separated by a thin tunnel barrier (gray) with a typical thickness of a few nanometers. Ψ_i is the wave function and E_i the energy of superconductor *i*. With *K*, we denote the coupling constant, which depends on the barrier thickness and height. Source: Göbel and Siegner [10]. Reproduced with permission of John Wiley & Sons.

The coupling constant K describes the quantum mechanical coupling between the superconductors and, hence, couples the two equations. If an external voltage U is applied across the junction, the energies E_1 and E_2 denote the potentials of superconductors 1 and 2, respectively, arising from the voltage. Thus, $|E_2 - E_1| = 2eU$. If the two superconductors are identical, the voltage drop is symmetric, $E_2 = eU$ and $E_1 = -eU$.

Solving the coupled Schrödinger equation (4.3) with an ansatz for the wave functions according to Eq. (4.2) shows that the Cooper pair densities n_1 and n_2 of superconductors 1 and 2, respectively, are time dependent. The time dependence results in a Cooper pair current

$$I_S(t) \propto \frac{\partial}{\partial t} n_1(t) = -\frac{\partial}{\partial t} n_2(t) \tag{4.4}$$

given by

$$I_S(t) = I_{S\max} \sin(\theta_1(t) - \theta_2(t)) \tag{4.5}$$

In this equation, $I_{S\max}$ is the critical current, which is proportional to the coupling constant K, and $\theta_i(t)$ is the phase of the wave function of the superconductor labeled i. The time evolution of the Cooper pair current is determined by the time evolution of the phase terms. The time dependence of the phase difference

$$\varphi(t) = \theta_1(t) - \theta_2(t) \tag{4.6}$$

is given by

$$\frac{\partial \varphi(t)}{\partial t} = \frac{2e}{\hbar} U \tag{4.7}$$

Equations (4.5) and (4.7) are called the Josephson equations, and the prefactor $2e/h$ (not $2e/\hbar$) is known as the Josephson constant K_J. Its inverse, $h/2e$, is the flux quantum Φ_0. Combining Eqs. (4.5) through Eq. (4.7), we obtain for the tunnel current of Cooper pairs (or Josephson current)

$$I_S(t) = I_{S\max} \sin\left(\frac{2e}{\hbar} \int_0^t U(\tau) \mathrm{d}\tau + \varphi_0\right) \tag{4.8}$$

The constant phase φ_0 is the integration constant determined by the initial conditions of the experiment. In the following section, we analyze the predictions of Eq. (4.8) for different types of external voltages across a Josephson junction.

4.1.2.1 AC and DC Josephson Effect

If a constant DC voltage $U \neq 0$ is applied across a Josephson junction, the Cooper pair current amounts to

$$I_S(t) = I_{S\max} \sin\left(\frac{2e}{\hbar} U \cdot t + \varphi_0\right) \tag{4.9}$$

Thus, $I_S(t)$ is a high-frequency AC current with angular frequency $\omega_J = 2eU/\hbar$ and frequency $f_J = 2eU/h$. Equation (4.9) describes the so-called AC Josephson effect, that is, the conversion of voltage to frequency. The temporal average of the AC Josephson current is zero since it contains no DC contribution.

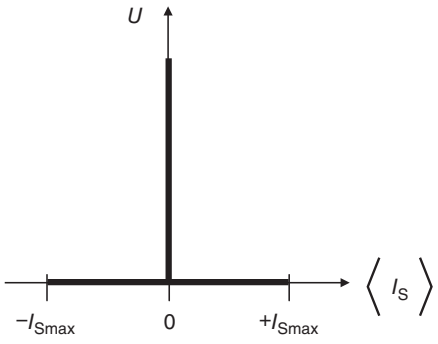

Figure 4.2 Voltage–current characteristic of an ideal Josephson junction illustrating the DC and AC Josephson effects. The current axis shows the time-averaged current. Source: Göbel and Siegner [10]. Reproduced with permission of John Wiley & Sons.

If no voltage is applied, $U = 0$, a DC Cooper pair current is generated whose magnitude and direction depend on the constant phase term φ_0. For $\varphi_0 \neq 0$, a current flows without voltage drop, which is called the DC Josephson effect. For the ideal Josephson junction treated so far, the DC and AC Josephson effects are illustrated in Figure 4.2, in which the voltage is plotted versus the time-averaged current.

4.1.2.2 Mixed DC and AC Voltages: Shapiro Steps

The essence of Josephson voltage standards becomes apparent if a mixed voltage containing DC and AC contributions is inserted in Eq. (4.8). We write this mixed voltage as

$$U(t) = U + u_{\mathrm{M}} \cos(\omega_{\mathrm{M}} t) \tag{4.10}$$

where ω_{M} is the angular frequency of the AC part. For the Josephson current one then finds

$$I_{\mathrm{S}}(t) = I_{\mathrm{Smax}} \sum_{n=-\infty}^{\infty} (-1)^n J_n \left(\frac{2eu_{\mathrm{M}}}{\hbar\omega_{\mathrm{M}}} \right) \sin((\omega_{\mathrm{J}} - n\omega_{\mathrm{M}})t + \varphi_0) \tag{4.11}$$

where J_n is the Bessel function of order n. Equation (4.11) shows that the Josephson junction carries a DC Cooper pair current whenever $\omega_{\mathrm{J}} - n\omega_{\mathrm{M}} = 0$ holds, that is, if

$$U_n = n\frac{h}{2e} f_{\mathrm{M}} = \frac{nf_{\mathrm{M}}}{K_{\mathrm{J}}} \tag{4.12}$$

where n is an integer. The discrete voltages U_n are called Shapiro steps, named after *Sidney Shapiro* who first experimentally observed them in 1963 [11]. The integer n is the step number. Figure 4.3 illustrates the voltage–current characteristic.

From a physical point of view, the Shapiro steps U_n are the result of the frequency modulation of the AC Josephson current with frequency ω_{J} by the applied AC voltage with frequency ω_{M}. This frequency modulation generates sidebands, among which DC terms are found for $\omega_{\mathrm{J}} - n\omega_{\mathrm{M}} = 0$. In the context of quantum metrology, Eq. (4.12) can be interpreted such that the DC voltage is given by the number of flux quanta transported through the Josephson junction per time

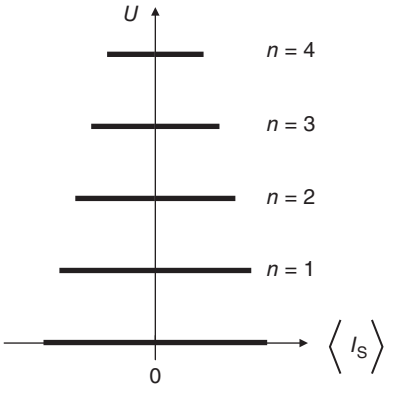

Figure 4.3 Voltage–current characteristic of an ideal Josephson junction for the application of a mixed voltage illustrating the generation of quantized voltages. The current axis shows the time-averaged current. Source: Göbel and Siegner [10]. Reproduced with permission of John Wiley & Sons.

interval. Here, the Josephson junction acts as an ideal frequency–voltage converter, which can be viewed as the inverse of the AC Josephson effect discussed in Section 4.1.2.1. Finally, from the viewpoint of the present SI, Eq. (4.12) links the voltage to the defining constants e and h.

4.1.3 Basic Physics of Real Josephson Junctions

When proceeding from ideal Josephson junctions, which have been dealt with in Section 4.1.2, to real ones, other current contributions must be taken into account. In addition to the Cooper pair current I_S, a displacement current I_C must be considered due to the finite capacitance C of the junction. Moreover, an unpaired-electron tunnel current I_N flows across the junction at finite temperatures. The treatment of real Josephson junctions should also consider that a current bias is applied in experiments on Josephson junctions. These considerations are taken into account by the resistively and capacitively shunted junction (RCSJ) model proposed by Stewart and McCumber [12, 13]. The RCSJ model describes the real Josephson junction by the electric circuit of Figure 4.4. In this parallel circuit, the bias current I_{bias} is split into the Cooper pair current I_S of an ideal Josephson junction, the displacement current I_C through the capacitance C, and the unpaired-electron current I_N, which is expressed as the current through an ohmic resistance R. Thus, for finite temperatures below T_c, the RCSJ model yields the following equation for the dynamic behavior of a real Josephson junction:

$$I_{bias}(t) = I_{Smax}\sin(\varphi(t)) + \frac{U}{R} + C\frac{dU}{dt} \tag{4.13}$$

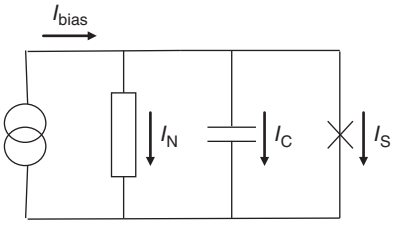

Figure 4.4 RCSJ model to describe a real Josephson junction accounting for displacement (I_C) and unpaired-electron (I_N) currents. Source: Göbel and Siegner [10]. Reproduced with permission of John Wiley & Sons.

The RCSJ model is useful to distinguish between two different types of real Josephson junctions – junctions that show either hysteretic or nonhysteretic dynamic behavior. This becomes apparent if in a linear approximation to Eq. (4.13), the term $\sin(\varphi)$ is replaced by φ, the Josephson inductance $L_\mathrm{J} = \hbar/(2eI_\mathrm{Smax})$ is introduced, and the Josephson equation (4.7) is used to replace U by the time derivative of φ, resulting in the equation of an RLC oscillator. Using the general expression for the eigenfrequency of an RLC oscillator, the eigenfrequency or plasma frequency of a real Josephson junction can be written as

$$f_\mathrm{P} = \frac{1}{2\pi\sqrt{L_\mathrm{J}C}} = \sqrt{\frac{eI_\mathrm{Smax}}{\pi hC}}. \tag{4.14}$$

The quality factor of an RLC oscillator, which is defined as the ratio between its eigenfrequency and the full width at half maximum of its resonance, is given by

$$Q = 2\pi f_\mathrm{P} RC \tag{4.15}$$

For the description of a real Josephson junction in the frame of the RCSJ model, the so-called McCumber parameter, β_C, is introduced as the square of the quality factor:

$$\beta_\mathrm{C} = Q^2 = 2e\frac{I_\mathrm{Smax}R^2C}{\hbar} \tag{4.16}$$

The McCumber parameter is used to distinguish between hysteretic and nonhysteretic junctions. If $\beta_\mathrm{C} > 1$ holds, the junction is underdamped and shows the hysteretic behavior illustrated in Figure 4.5a,b. If only a DC bias current is applied, the supercurrent increases till the critical current is reached for increasing bias. For higher bias currents, the junction switches to the normal conducting state, and the voltage–current characteristic approaches the normal-state resistance. If the bias current is decreased again, hysteretic behavior is observed.

If microwave excitation is added to the DC bias current, different Shapiro steps can be observed, which overlap around zero bias current. As discussed in more detail in Section 4.1.4.2, this behavior is used to realize Josephson voltage standards, which generate fixed DC voltages. The current range, over which a constant-voltage step extends, and the observed step number depend on the applied microwave power. Metastable Shapiro steps are observed for certain ranges of microwave power and modulation frequency ω_M. Beyond these ranges, the Josephson junction shows chaotic behavior [14]. Underdamped junctions satisfying the relation $\beta_\mathrm{C} > 1$ are realized if the tunnel barrier is an insulator with a large resistance R and for a finite capacitance C of the junction, as shown by Eq. (4.16). This type of Josephson junction is often referred to as the superconductor/insulator/superconductor (SIS) junction.

Overdamped Josephson junctions satisfy the relation $\beta_\mathrm{C} \leq 1$. They can be realized by lowering the junction resistance using a normal metal (N) or a combination of a normal metal and insulating layers as tunnel barrier. These junctions are referred to as superconductor/normal metal/superconductor (SNS) and superconductor/insulator/normal metal/insulator/superconductor (SINIS) junctions, respectively. As illustrated in the lower part of Figure 4.5, overdamped junctions

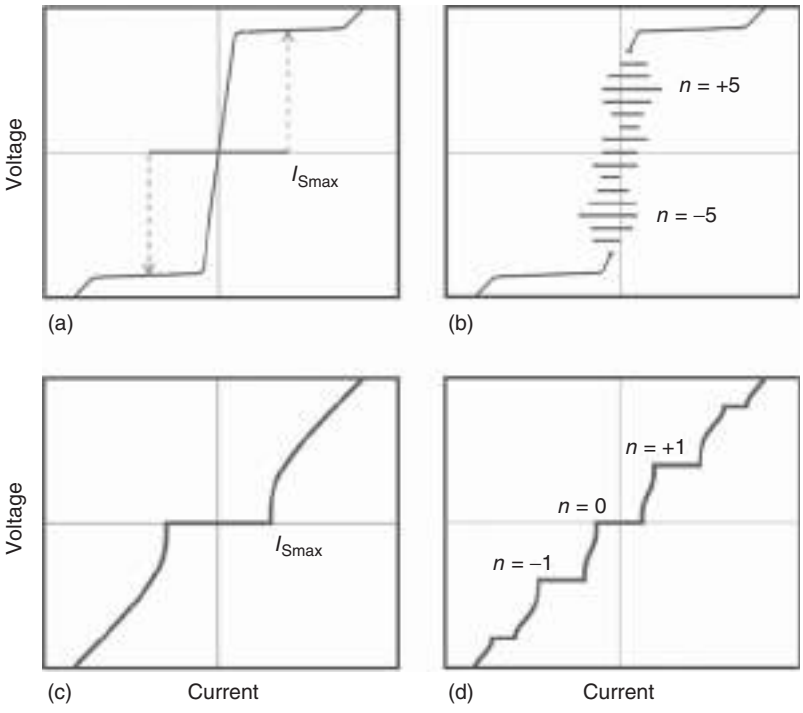

Figure 4.5 Schematic voltage–current characteristic of real Josephson junctions. Upper part: hysteretic (underdamped) junctions. Lower part: nonhysteretic (overdamped) junctions. Left-hand side: behavior if only a DC bias current is applied. Right-hand side: behavior for excitation with microwaves in addition to the DC bias current. Note that the characteristic of hysteretic (underdamped) junctions is observed when microwave power and DC bias are tuned and the different voltages generated during the tuning are superimposed. Source: Courtesy of PTB.

exhibit nonhysteretic behavior. In particular, for excitation with microwaves, an unambiguous relation between the DC bias current and the voltage step number is obtained. This feature provides the basis for the development of programmable binary Josephson voltage standards and pulse-driven AC Josephson voltage standards, which are discussed in Sections 4.1.4.3 and 4.1.4.4, respectively.

An in-depth analysis of the physics of real Josephson junctions can be found, for example, in Refs. [15–18].

4.1.4 Josephson Voltage Standards

The Josephson effect links the voltage to frequency, the defining constants e and h, and an integer, as shown in Eq. (4.12). Since the frequency can be realized with extremely high precision with atomic clocks (nowadays with a relative uncertainty smaller than 10^{-15}; see Chapter 3), Eq. (4.12) bears the potential for the very precise generation of voltages. Moreover, in the 1960s, it was already experimentally demonstrated that the Josephson effect itself was highly reproducible at the level of one part in 10^8 [19]. Subsequent measurements demonstrated even better reproducibility up to the level of parts in 10^{16} [20] and parts in 10^{19} [21].

These findings prompted substantial efforts to construct voltage standards based on the Josephson effect. The main obstacle encountered was the small magnitude of the voltage generated by a single Josephson junction even for frequencies in the gigahertz range. For example, the voltage of the lowest Shapiro step is only 145 μV at a frequency of 70 GHz. Therefore, a considerable amount of work was spent on the development of arrays of Josephson junctions. A Josephson array is a series circuit of many junctions, in which the voltages of the junctions add up to reach practical voltage levels up to 10 V, as required for a voltage standard. Three different types of Josephson voltage standards can be distinguished:

- Standards with SIS Josephson junctions for the generation of fixed DC voltages
- Programmable binary Josephson voltage standards for the generation of variable DC voltages and simple time-dependent voltage waveforms
- Pulse-driven AC Josephson voltage standards for the generation of arbitrary time-dependent voltage waveforms.

In Section 4.1.4, we review the technology of these Josephson voltage standards, the main ideas that advanced their development, and their present state of the art. Their impact on metrology is discussed in Section 4.1.5. More details of the development of Josephson voltage standards are presented in several review papers. The interested reader is referred to, for example, Refs. [22–24].

4.1.4.1 General Overview: Materials and Technology of Josephson Arrays

A single Josephson junction generates voltages in the submillivolt range. Therefore, the voltages of thousands or tens of thousands junctions must be added up in a series circuit to obtain practical voltage levels. To this end, integrated circuits are fabricated using thin film technology, including sputter deposition of superconducting layers and dielectrics, patterning by photo or electron-beam lithography, and etching.

In the 1980s, integrated Josephson arrays were based on lead/lead alloy technology [25]. Yet, this technology did not provide the required long-term stability since lead alloys can be damaged by humidity and thermal cycling between room temperature and low temperatures. Niobium proved to be a better choice of the superconducting material of an array of Josephson junctions. This metal combines chemical stability with a large critical temperature of 9.5 K. Niobium can easily be covered with aluminum serving as a normal metal, which even has a stable natural oxide that can be used to form an insulating layer. Thus, Nb/Al/Al oxide technology [26] provides all ingredients required to fabricate SIS and SINIS Josephson arrays. For the fabrication of SNS Josephson arrays, niobium can be combined with, for example, PdAu [27] or NbSi [28]. Therefore, niobium is presently chosen as the superconducting material for Josephson voltage standards. Niobium standards can be operated at the temperature of liquid helium, that is, 4.2 K. Operation at a higher temperature around 10 K becomes feasible with NbN arrays [29]. The higher temperature allows the NbN arrays to be operated in cryocoolers. The high-temperature superconductor cuprate materials have not yet led to a breakthrough in voltage standards since their inhomogeneity precludes the development of highly integrated circuits with many uniform Josephson junctions.

The choice of material determines the operating margins of a Josephson array. The maximum frequency (named characteristic frequency), f_c, at which the array can be operated, is limited by the so-called characteristic voltage V_c according to

$$f_c = V_c \frac{2e}{h} \tag{4.17}$$

The characteristic voltage V_c is given by the critical current and the normal-state resistance:

$$V_c = I_{Smax} R \tag{4.18}$$

The critical current depends on the critical current density j_{Smax} of the superconducting material. Only in theory the critical current $I_{Smax} = j_{Smax} A$ can be adjusted at will by adjusting the area A of the Josephson junction for a given material with given critical current density j_{Smax}. In practice, if the area A is increased, the size of the Josephson array increases, which compromises the uniformity of the junctions across the array and complicates the microwave design. Thus, to obtain the desired output voltage of a Josephson array, the driving frequency, number of junctions, step number, material parameters, and dimensions must be chosen carefully. In the following sections, we discuss in more detail how these constraints are dealt with for the different types of Josephson voltage standards.

As a concluding remark regarding general technological aspects, we address microwave issues. The design of a Josephson array must be chosen such that all junctions are excited by almost the same microwave power. To this end, the Josephson junctions are embedded in high-frequency transmission lines, such as low-impedance microstrip lines or 50 Ω coplanar waveguides and coplanar striplines. Measures must be taken to avoid reflections and the formation of standing waves. The number of Josephson junctions, which a single microwave transmission line can accommodate, is limited by the attenuation of the microwave power along the line. The transmission line must not be too long since otherwise power losses become too large. This constraint limits the number of Josephson junctions per line. To excite many junctions equally with microwaves, several microwave branches can be operated in parallel. The microwave is split, and the resulting partial waves are fed into different branches. Microwave components for power splitting are routinely available for sinusoidal microwaves with a narrow frequency spectrum.

4.1.4.2 SIS Josephson Voltage Standards

SIS Josephson voltage standards are used to generate fixed DC voltages up to 10 V. Their development started in the 1980s, and they were the first Josephson standards that substantially impacted metrology. Nowadays, they are routinely used by national metrology institutes around the world to realize and maintain the DC voltage scale. SIS Josephson voltage standards have been commercialized and are also used by calibration laboratories in industry.

The development of SIS Josephson voltage standards was advanced by two ideas. The first one was the suggestion to take advantage of the overlapping Shapiro steps of the hysteretic SIS Josephson junctions around zero bias current [30]. This concept eliminates the need to bias different junctions individually,

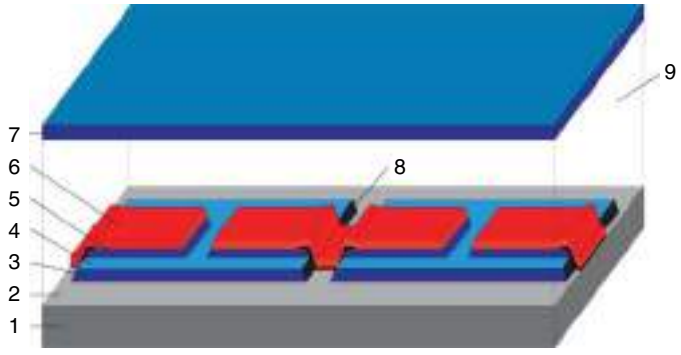

Figure 4.6 Schematic layout of an SIS Nb/Al–Al_2O_3/Nb Josephson array. Shown are four junctions embedded in a microstrip line whose ground plate is seen at the top of the structure. (1) Silicon substrate; (2) sputtered Al_2O_3 layer, typical thickness 30 nm; (3) niobium tunnel electrode, 170 nm; (4) Al_2O_3 barrier, 1.5 nm, fabricated by thermal oxidation of an Al layer; (5) niobium tunnel electrode, 85 nm; (6) wiring layer, 400 nm; (7) niobium ground plane, 250 nm; (8) Nb oxide edge protection, 80 nm. The Nb ground plane (7) rests on a 2-μm-thick Si oxide dielectric layer (9). Source: Courtesy of J. Kohlmann, PTB.

which facilitates the integration of many Josephson junctions in a series array. The second important idea was to embed the junctions in a high-frequency transmission line to ensure uniform microwave excitation.

In 1984, the first Josephson array providing 1 V output was demonstrated. The array was based on lead/lead alloy technology and a microstrip line was employed to distribute the microwave power [25]. Later, Nb/Al/Al oxide technology has been used to fabricate SIS Josephson arrays for the generation of DC voltages of 10 V. The typical current step width is some tens of microamperes. In most designs, microstrip lines are chosen as high-frequency transmission lines. A schematic layout of such an array is shown in Figure 4.6. Thanks to the large normal-state resistance of the SIS junctions, the characteristic voltage is so large that driving frequencies f of 70 GHz can be applied. The SIS Josephson arrays can be operated on higher-order Shapiro steps. For typical parameters, such as $f = 70$ GHz and step number $n = 5$, 14 000 junctions are sufficient to obtain 10 V output.

Figure 4.7 shows a photograph of a 10 V Josephson array fabricated by the Physikalisch–Technische Bundesanstalt (PTB). The Josephson chip is mounted

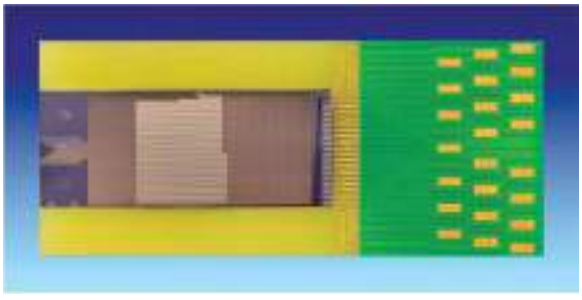

Figure 4.7 Photograph of a 10 V Josephson array mounted onto a chip carrier. The size of the array is 24 mm by 10 mm. Source: Courtesy of PTB.

onto a chip carrier. The fin-line-taper antenna, seen on the left-hand side, is coupled to a waveguide (not shown), through which the microwave is transmitted to the Josephson array. For operation, the complete array is immersed into liquid helium. DC measurements with SIS Josephson voltage standards are treated in Section 4.1.5.1.

4.1.4.3 Programmable Binary Josephson Voltage Standards

For some DC measurements, it is advantageous to quickly switch between different DC voltage levels. Moreover, many important measurements in electrical metrology involve AC voltages. A prime example is the measurement of electric power and energy at the line frequency of 50 or 60 Hz of the power grid. Conventionally, the AC volt (and also the AC ampere) is realized and disseminated using thermal converters. In a thermal converter, the heat generated by an AC electrical quantity is compared to the heat produced by its DC counterpart, which can be determined with high precision. This calorimetric approach yields the root-mean-square (rms) value of the AC quantity. Thermal converters can measure the rms value of AC voltages ranging from millivolts to kilovolts and over the frequency range from 10 Hz to several MHz with relative uncertainties as good as one part in 10^6. Unlike thermal converters, AC Josephson voltage standards have the potential to determine the complete waveform of an AC voltage with high precision. Moreover, they hold promise to establish quantum-based measurements of other electrical quantities, such as impedance and electric power, and quantum-based characterization of measuring instruments, such as analog–digital converters. Consequently, since the 1990s, efforts have been made to harness the Josephson effect and its high reproducibility for AC voltage metrology.

The simplest implementation of a Josephson standard with AC measurement capabilities is the programmable binary Josephson voltage standard. Its operation is based on the rapid and reliable switching between different Shapiro steps. Hysteretic SIS Josephson junctions are not suited to implement this concept due to their ambiguous voltage–current characteristic, that is, due to the overlap of the voltage steps. This property precludes reliable switching between Shapiro steps. Therefore, nonhysteretic Josephson junctions are used to realize programmable binary Josephson voltage standards. Varying the DC bias current, the $n = 0$, 1, or -1 Shapiro step can be addressed in these junctions (see Figure 4.5).

We consider an array of nonhysteretic SNS or SINIS Josephson junctions. If $m(t)$ is the number of junctions activated at the time t, that is, with step number $n \neq 0$, the time-dependent output voltage of the array is

$$U(t) = nm(t)K_J^{-1}f \tag{4.19}$$

Usually, the Shapiro step number n is ± 1. As for SIS Josephson arrays, f is assumed to be the constant frequency of a sinusoidal microwave. The schematic layout of a programmable binary Josephson array is depicted in Figure 4.8. The array is divided into $N + 1$ segments with 2^0, 2^1, 2^2, …, 2^N Josephson junctions. The segments can be addressed individually. If each junction generates a voltage U_1, any voltage between $-(2^{N+1} - 1)U_1$ and $+(2^{N+1} - 1)U_1$ can be generated with a resolution given by U_1. For a typical frequency of 15 GHz, U_1 is

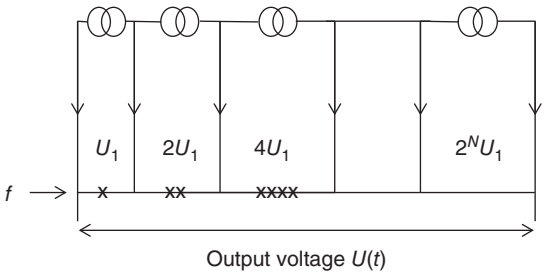

Figure 4.8 Schematic layout of a binary divided programmable Josephson array. Each of the bold X represents a single Josephson junction delivering a voltage U_1. The numbers of junctions per segment form a binary sequence. Each segment has its own power supply, which provides the bias current to select the Shapiro step number $n = 1, -1$ (or 0 to deactivate the segment). Source: Göbel and Siegner [10]. Reproduced with permission of John Wiley & Sons.

31 μV. The programmable binary Josephson array can be considered a multibit digital-to-analog converter. Figure 4.9 shows a stepwise approximated 50 Hz sine wave with 16 steps per period as an example of a temporally varying voltage generated with a programmable Josephson array.

The fabrication of programmable binary Josephson arrays entails technological challenges not encountered with SIS arrays. Programmable arrays are operated on the step number $n = \pm 1$, rather than on a step number $n > 1$ as SIS arrays. Therefore, the number of Josephson junctions needs to be increased to achieve the same voltage level as with an SIS array that is driven at the same frequency. Other constraints arise regarding the choice of the driving frequency. The product of critical current I_{Smax} and normal-state resistance R of an SNS array is usually smaller than that of SIS arrays. Consequently, the characteristic voltage and the driving frequency are reduced, as seen from Eqs. (4.17) and (4.18). The

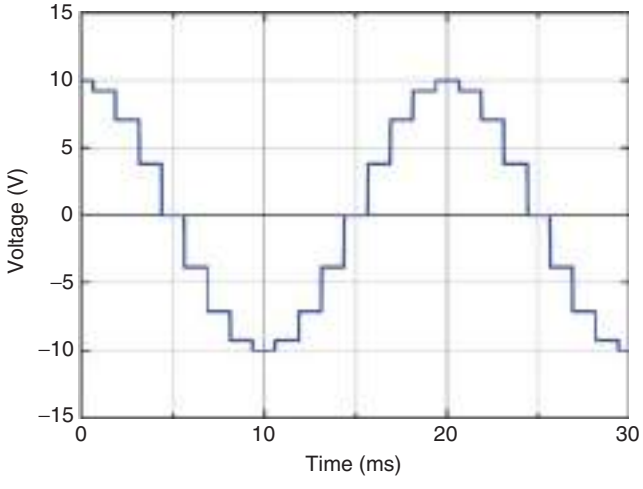

Figure 4.9 Stepwise approximated 50 Hz sine wave generated by a programmable binary Josephson voltage standard. Source: Courtesy of R. Behr, PTB.

decrease in the driving frequency must be compensated by a further increase in the number of junctions. The first practical programmable binary 1 V array of the SNS type contained 32 768 junctions with PdAu barriers and was operated at 16 GHz [27]. Later, programmable binary 10 V arrays for operation at 16–20 GHz were designed and fabricated by the National Institute of Standards and Technology (NIST, USA) and the National Institute of Advanced Industrial Science and Technology (AIST, Japan) [29, 31]. Such arrays consist of 300 000 junctions. With increasing number of junctions, uniformity of junctions across an array is more difficult to achieve. Moreover, the microwave design becomes more complicated since a larger number of microwave branches must be operated in parallel.

To reduce the required number of junctions, the PTB developed SINIS arrays based on Nb/Al/Al oxide technology. This technology allows the $I_{\mathrm{Smax}}R$ product to be tuned for operation at 70 GHz. In 2007, the PTB presented a programmable binary 10 V SINIS array with "only" 70 000 junctions [32]. Yet, the fabrication yield of these SINIS arrays was rather low due to their thin, only 1–2-nm-thick, and damage-prone Al oxide insulating layers. Therefore, the PTB and NIST jointly developed NbSi as an alternative barrier material [28]. NbSi barriers have a thickness on the order of 10 nm and are less damage prone. Moreover, $\mathrm{Nb}_x\mathrm{Si}_{1-x}$ allows large $I_{\mathrm{Smax}}R$ products to be realized when the Nb content is tuned close to the metal–insulator transition at $x = 11\%$. Nowadays, the PTB employs NbSi as barrier material for programmable 10 V arrays. The arrays have a current step width of 1 mA or larger and can reliably be operated at 70 GHz thanks to the large $I_{\mathrm{Smax}}R$ product.

This brief rundown shows that the fabrication of programmable binary Josephson standards with 10 V output is a mature technology nowadays. These voltage standards are commercially available and are used for calibration and testing in industry (see Section 4.1.5). At national metrology institutes, programmable binary Josephson arrays with 20 V output have also been demonstrated [33, 34].

A key element of programmable binary Josephson standards is the programmable current source used to individually address the binary segments of the array. In principle, stepwise approximations of any waveform can be generated. In practice, the switching time of the current source must be considered, that is, the time required to change the bit pattern that is inputted to the Josephson array. This time together with the number of voltage levels, which is chosen to approximate one cycle of the output waveform, limits the frequency of the output voltage. For example, for a typical switching time of 2 µs, corresponding to a rate of 500 kHz, the maximum frequency of the output voltage is limited to the 10 kHz range considering that each cycle of the output waveform is composed of several tens of voltage levels.

When settled on a voltage level, the output of a programmable binary Josephson array has the same high reproducibility as achieved with an SIS Josephson standard, which generates a fixed DC voltage. Yet, during the switching between two voltage levels, the output voltage of the programmable Josephson array is not determined by Eq. (4.19). It is given by the so-called transients whose amplitude and shape are not exactly known. The transient regime can be limited to a time window of less than 100 ns using modern electronics with rise times in

the 10 ns range. Nonetheless, the transients compromise the uncertainty of rms measurements with programmable binary Josephson arrays. The effect of the transients increases with the number of switching events per time, that is, with the number of voltage levels per cycle and the frequency of the output voltage. Consequently, the frequency is limited to the kilohertz range. In Section 4.1.5, we discuss in more detail how the transients affect different types of measurements.

4.1.4.4 Pulse-Driven AC Josephson Voltage Standards

Programmable binary Josephson standards are not perfect AC voltage sources since they allow only stepwise approximations of waveforms to be generated and suffer from the undefined transients. This shortcoming has motivated work on a conceptually different approach toward AC voltage generation with Josephson standards. This approach is known as pulse-driven AC Josephson voltage standard and is also implemented with nonhysteretic Josephson junctions.

The basic idea of pulse-driven AC Josephson standards is to vary the frequency f, at which the Josephson array is driven, while the number m of activated Josephson junctions is kept fixed. Yet, simulations based on the RCSJ model show that this approach faces severe limitations if a sinusoidal microwave drive is considered. Stable operation of a nonhysteretic Josephson array, that is, a sufficiently large current step width, is obtained only for frequencies close to the characteristic frequency (see Eqs. (4.17) and (4.18)) for sinusoidal excitation [35, 36]. However, frequency tuning over a wide range can be realized if a train of sufficiently short current pulses is used to drive the Josephson array [36, 37]. The output voltage of a pulse-driven AC Josephson array with m junction is then given by

$$U(t) = nmK_J^{-1} f_R(t) \tag{4.20}$$

In this equation, $f_R(t)$ is the repetition frequency of the pulse train, that is, the inverse of the temporal spacing between successive pulses. The integer n is the step number, which is usually ± 1. Stable operation is obtained if the width of the individual pulses is shorter than the inverse of the characteristic frequency [36]. The repetition frequency $f_R(t)$ can then be tuned between zero and the characteristic frequency.

The basic physics of pulse-driven operation is seen considering the effect of a single current pulse. Each current pulse induces a phase change of $2\pi n'$ across the Josephson junction [38]. This phase change corresponds to the generation of a voltage pulse with an area of n' flux quanta $\Phi_0 = h/(2e) = K_J^{-1}$ according to Eq. (4.7). If this process is repeated at the frequency $f_R(t)$, a voltage according to Eq. (4.20) is obtained with $n = n'$. The voltage is determined by the number of flux quanta transferred through the Josephson junctions per time.

Pulse pattern generators are used to drive the Josephson arrays. These current sources allow the generation of various current pulse sequences and, thereby, the variation of the repetition frequency $f_R(t)$. Since the repetition frequency can be arbitrarily varied in time, pulse-driven AC Josephson standards can generate arbitrary waveforms. In particular, they can generate pure sinusoidal voltages without undefined transient contributions. The corresponding spectrum consists of a single narrow line at the fundamental frequency and does not contain higher harmonics. The fundamental frequency can be varied from DC to megahertz.

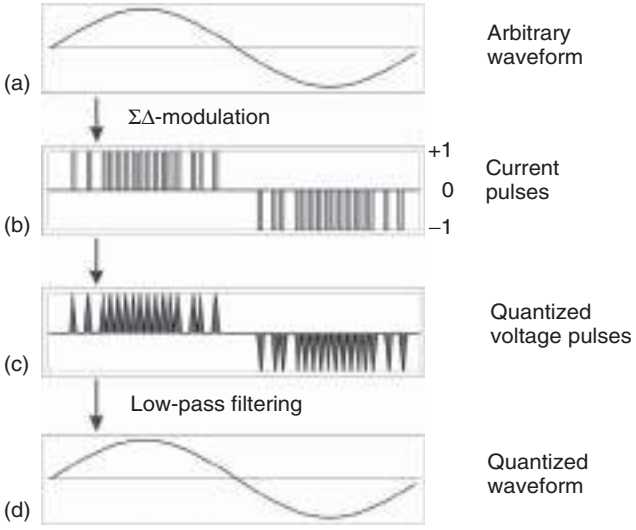

Figure 4.10 Scheme of the generation of a quantized waveform with arbitrary shape using a pulse-driven Josephson array, shown for the example of a sine wave. The arbitrary waveform (a) is encoded in a pulse train with a ΣΔ converter, whose code controls the output of a pulse pattern generator. The pulse pattern generator outputs the current pulse sequence shown in (b). The current pulses drive a Josephson array, which generates voltage pulses having the area of the flux quantum Φ_0 (c). Low-pass filtering produces the quantized waveform of (d) according the Eq. (4.20). Source: Courtesy of O. Kieler, PTB.

To generate an arbitrary waveform, a ΣΔ converter is generally used to encode the waveform in a train of short current pulses with variable pulse separation. Figure 4.10 shows the operation principle for a sine wave. Note that the voltage pulses generated by the pulse-driven Josephson array (Figure 4.10c) have the area of the flux quantum Φ_0. The quantized waveform of Figure 4.10d is obtained by low-pass filtering of the voltage pulses of Figure 4.10c. The filtering removes quantization noise.

Before we comment on the experimental results achieved with pulse-driven AC Josephson standards, we review some technological aspects. Various pulse pattern generators are commercially available with repetition rates up to 65 GHz and the capability to output bipolar current pulse sequences. The use of bipolar current pulses allows truly alternating voltages to be generated. If no bipolar pulse pattern generator is available, the output of a unipolar pulse pattern generator can be combined with a sinusoidal microwave to produce a bipolar current pulse train. Yet, this scheme involves the sensitive synchronization of the two signals, which compromises the stability of the pulse drive. Pulse pattern generators with up to eight synchronized channels can be used to operate several pulse-driven Josephson arrays in parallel so that their outputs can be combined [39].

Nonhysteretic Josephson junctions of the SNS type with typical characteristic frequencies on the order of 10 GHz are used for pulse-driven Josephson voltage standards. The maximum repetition frequency of the train of current pulses can then be chosen to be of the same order as the characteristic frequency of the

junctions. NbSi barriers are employed in most pulse-driven Josephson standards [40–42].

The microwave design of pulse-driven Josephson voltage standards involves issues not encountered with SIS or programmable Josephson standards. These issues result from the broadband spectrum of the current pulses. The pulse spectrum extends from DC to beyond the maximum repetition frequency, that is, to several tens of gigahertz. Ordinary microwave splitters do not support such a large bandwidth. It is then not possible to operate several array branches in parallel driven by the output of a single current source. The operation of only a single branch limits the number of Josephson junctions in an array. This is due to the attenuation of the high-frequency components of the pulse spectrum along the array. The attenuation precludes the use of an arbitrarily large number of junctions even if the area of each junction is reduced as compared to programmable array designs. This constraint restricts the output voltage of a pulse-driven Josephson array.

There are several options to increase the output voltage. To operate more Josephson junctions per array, stacks of two [40, 41], three [42], or four Josephson junctions can be fabricated. The scanning electron microscope image of Figure 4.11 shows quadruple stacks of Nb/NbSi/Nb Josephson junctions fabricated at the PTB.

Moreover, the output voltages of several arrays can be combined. For example, a total output voltage of 275 mV rms was achieved by combining the outputs of two pulse-driven arrays with 6400 junctions per array [39]. The arrays were driven by two synchronized current pulse trains [39]. This approach was the key to achieving a practical voltage level of 1 V rms after several years of engineering work. The NIST combined the output of four arrays to this end [43, 44]. In total, the four arrays contained either 25 600 Josephson junctions operated at the Shapiro step $n = 2$ [43] or twice as many junctions operated at $n = 1$ [44]. The PTB combined the output of eight arrays with overall 63 000 junctions (operated at $n = 1$)

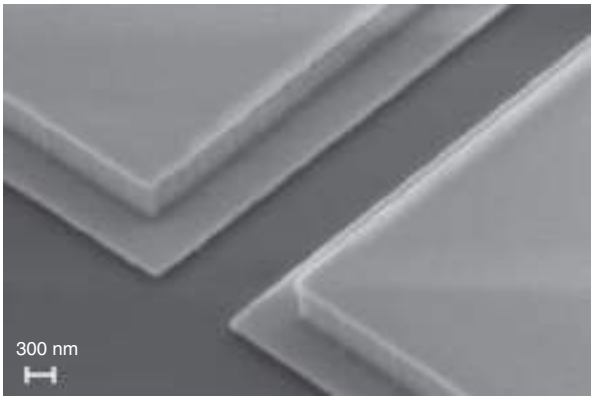

Figure 4.11 Scanning electron microscope image showing part of a Josephson array with quadruple stacks of Nb/NbSi/Nb junctions. The NbSi barriers appear dark while the niobium appears lighter. The image was taken at an intermediate step of the fabrication process and does not show all details of a complete Josephson array. Source: Courtesy of O. Kieler, PTB.

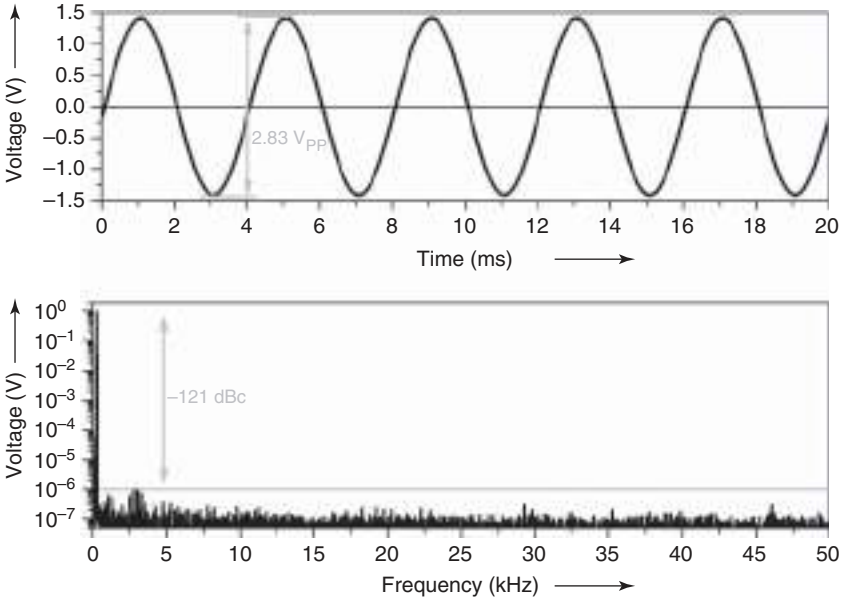

Figure 4.12 Sine wave with a frequency of 250 Hz, synthesized combining the outputs of eight pulse-driven Josephson arrays with overall 63000 (Nb/NbSi/Nb) junctions: (upper panel) temporal waveform and (lower panel) spectrum. The peak–peak amplitude is 2.83 V corresponding to 1 V rms. The spectrum demonstrates that higher harmonics are suppressed by at least −121 dBc. Source: Courtesy of O. Kieler, PTB.

to obtain 1 V rms [42]. Figure 4.12 shows a sinusoidal voltage with a frequency of 250 Hz generated with eight pulse-driven Josephson arrays connected in series. The peak–peak amplitude is 2.83 V corresponding to 1 V rms. The quality of the waveform is demonstrated by the spectrum which shows that higher harmonics are suppressed by at least −121 dBc.

The practical disadvantage of the aforementioned schemes is that each array requires a separate current pulse source, which is synchronized to all other current pulses sources. Therefore, broadband microwave splitters, the so-called Wilkinson dividers, have been introduced [45, 46]. With this technology, 51 200 Josephson junctions could be driven by a single current pulse source to generate 1 V rms [46]. Moreover, 2 V rms could be achieved with four synchronized current pulse sources, which drove two 1 V chips with overall eight Josephson arrays [45].

Optoelectronic schemes are an alternative to drive several Josephson arrays with a single source of electric current pulses [38]. In this approach, electric current pulses are converted into optical pulses with optoelectronic techniques (electrically driven optical modulators, lasers). The optical pulse train is duplicated with optical power splitters. The power splitting yields several synchronized optical pulse trains, which are then converted into synchronized electric current pulse trains with suitable photodetectors.

The accuracy of the voltage quantization achievable with a pulse-driven Josephson array has been tested by comparing its output to that of a programmable

Josephson voltage standard. At a frequency of 500 Hz and an rms value of 104 mV, the fundamental frequency components of the two systems were found to agree within an uncertainty of three parts in 10^7 [47]. Sine waves generated with two pulse-driven Josephson arrays were found to agree within an uncertainty of three parts in 10^8 at a voltage level of approximately 10 mV [41]. Recently, the comparison of a 1 V pulse-driven Josephson standard and a programmable Josephson standard yielded agreement at a level of one part in 10^8 [48]. Thus, pulse-driven Josephson voltage standards provide arbitrary waveforms with high precision.

Concluding this section, we note that the technology of pulse-driven AC Josephson voltage standards has considerably matured in recent years. Further technological improvements can be expected. In fact, at the time of writing, pulse-driven AC Josephson voltage standards with 4 V output and first implementations of optoelectronic driving schemes had been presented at conferences. Applications of pulse-driven Josephson standards in metrology are reviewed in Section 4.1.5.3. At the time of writing, first steps were taken to commercialize the technology and, therefore, many more applications can be expected in the future.

4.1.5 Metrology with Josephson Voltage Standards

Josephson standards have made tremendous impact on voltage measurements. In the present International System of Units, SIS or programmable binary Josephson voltage standards are routinely used by national metrology institutes to realize and disseminate the SI volt linked to the defining constants e and h. Details are given in Section 4.1.5.1. Already in the previous SI, Josephson standards were used to set up a conventional volt scale. In Section 4.1.5.2, the now abrogated conventional volt is treated and the changes to voltage metrology are highlighted that resulted from the implementation of the present SI in 2019. These changes resemble those in resistance metrology, which are discussed in Section 5.4.2.

Programmable binary and pulse-driven Josephson standards are also used to perform AC measurements. The measured AC electrical quantities include voltages and impedance ratios among others. Moreover, pulse-driven AC Josephson standards are employed in Johnson noise thermometry to realize and disseminate the SI kelvin (see Section 8.1.5). AC measurements with Josephson voltage standards are treated in Section 4.1.5.3. Finally, it is worth mentioning that Josephson voltage standards are essential components of Watt balances (also named Kibble balances) used to realize the SI kilogram, discussed in detail in Chapter 7.

4.1.5.1 DC Voltage, the SI Volt

The Josephson effect allows quantized voltages to be realized, which depend only on the defining constants e and h, an integer, and a frequency. The frequency can be realized with extremely high precision with atomic clocks (with a relative uncertainty smaller than 10^{-15} as discussed in Chapter 3). Moreover, the effect itself is highly reproducible at the level of parts in 10^{16} [20] or even parts in 10^{19} [21], as already mentioned. In fact, an important argument in support of selecting the Planck constant h as a defining constant was to harness the full potential of

the Josephson effect (and the quantum Hall effect, see Chapter 5) for metrology; see the more detailed discussion in Section 7.1.

Consequently, the Josephson effect is the prime choice for the realization of the SI volt. The relative uncertainty of this SI volt realization can be inferred from comparisons at practical voltage levels of 1 and 10 V and is a few parts in 10^{10} or better [49]. Note that the reproducibility tests mentioned earlier were performed with only a few Josephson junctions and were not affected by the uncertainty of the frequency. To fully harmonize voltage metrology worldwide, the Consultative Committee for Electricity and Magnetism (CCEM) of the Meter Convention recommends the use of the following value of the Josephson constant, which has been calculated to 15 significant digits from the defining constants e and h introduced in Section 2.2 [50]

$$K_{\mathrm{J}} = 483\,597.848\,416\,984\ \mathrm{GHz\ V^{-1}} \tag{4.21}$$

The choice of 15 significant digits allows one to quote accurate voltage values even if the uncertainty of voltage comparisons can be further reduced by some orders of magnitude below the present state of the art of approximately 10^{-10}.

Either SIS or programmable binary Josephson voltage standards are used to realize the SI volt and to calibrate secondary voltage standards, such as Zener diodes. For calibration, the output voltage of a Josephson standard at liquid helium temperature is compared to the output of the secondary standard at room temperature. For this purpose, a compensation technique is used where the difference of the two voltages is measured with a sensitive nanovoltmeter that serves as a null detector. To fine-tune the Josephson voltage, the driving frequency of the Josephson standard can be slightly adjusted.

For an absolute measurement, the frequency is referenced to an atomic clock standard. Thermal voltages arise from the temperature difference between the Josephson standard and the room temperature part of the measurement setup. However, they can be compensated by reversing the polarity of the Josephson voltage and the voltage of the secondary standard. Programmable binary Josephson standards allow faster polarity reversal as SIS Josephson standards. The faster polarity switching increases the amount of data that can be taken per time interval and, thus, reduces the measurement uncertainty. Moreover, programmable Josephson standards allow measurement procedures involving several DC voltages to be automated. Of course, calibrations in the DC regime are not affected by the ill-defined transients.

The impact of Josephson standards on voltage metrology becomes fully obvious when the realization of the volt in the previous SI is considered. Before the implementation of the present SI in 2019, the SI volt was realized using a so-called voltage balance [51] and a calculable capacitor [52]. The calculable capacitor yielded an SI value of the capacitance traceable to the meter. Using this value, the voltage balance compared the electrostatic force to the gravitational force, thereby realizing the SI volt with a relative uncertainty of a few parts in 10^7 [53]. Thus, the realization of the SI volt with Josephson voltage standards in the present SI is a substantial improvement over the previous realization of the SI volt, which did not involve Josephson standards.

4.1.5.2 The Conventional Volt in the Previous SI

Already in the 1980s, it was realized that voltage metrology could be significantly harmonized using the highly reproducible Josephson effect. Since the prime goal of metrology is to ensure worldwide uniformity of measurements, steps were taken to base voltage measurements on the use of the Josephson effect, highly precise frequency measurements, and a fixed, agreed-upon value of the Josephson constant K_J. In 1987, the General Conference of the Meter Convention (*Conférence Générale des Poids et Mesures*, CGPM) instructed the International Committee for Weights and Measures (*Comité International des Poids et Measures*, CIPM) to recommend a value of the Josephson constant K_J, which should be used when analyzing Josephson measurements [54]. In 1988, the CIPM recommended a value that was determined using the best experimental data available at that time and should be used from 1 January 1990 [55]. This conventional value or agreed-upon value was denoted by $K_{J\text{-}90}$. $K_{J\text{-}90}$ was introduced together with the conventional value of the von Klitzing constant $R_{K\text{-}90}$ (see Section 5.4.2) and was given by

$$K_{J\text{-}90} = 483\,597.9\ \text{GHz V}^{-1} \tag{4.22}$$

To ensure the compatibility of $K_{J\text{-}90}$ and the then valid SI value of K_J, $K_{J\text{-}90}$ was assigned a conventional relative uncertainty of four parts in 10^7.

In close analogy to the resistance case of Section 5.4.2, the relation

$$U_{90} = \frac{nf}{K_{J\text{-}90}} \tag{4.23}$$

established a new, highly reproducible voltage scale U_{90}. In Eq. (4.23), $K_{J\text{-}90}$ could be treated as a constant with zero uncertainty since no comparison to SI quantities was made. Equation (4.23) provided a representation of the unit volt, namely, the conventional volt or volt$_{90}$, yet not a realization of the volt according to the definition of the SI. The non-SI unit volt$_{90}$ was disseminated and used in electrical metrology from 1990 to the implementation of the present SI on 20 May 2019. The superior reproducibility of the Josephson effect reduced the uncertainty of voltage measurements based on $K_{J\text{-}90}$ to a few parts in 10^{10} or better [49].

The conventional value of the Josephson constant $K_{J\text{-}90}$ has been abrogated in the present SI (as well as the conventional value of the von Klitzing constant $R_{K\text{-}90}$; see Section 5.4.2) [56]. The disseminated electrical units are now fully coherent with the SI. Since K_J of Eq. (4.21) and $K_{J\text{-}90}$ of Eq. (4.22) are slightly different, voltage-related quantities underwent a small discontinuous change when the present SI was implemented. The relative change was approximately 1.067×10^{-7} [56]. Reference [56] instructed users of electrical metrology how to deal with this change and ensured a seamless transition from the previous SI to the present one.

4.1.5.3 AC Measurements with Josephson Voltage Standards

Programmable binary Josephson voltage standards were the first type of Josephson standard used to measure AC electrical quantities. This was because their high output voltage of 10 V facilitated high-precision measurements already before 2010. The application of pulse-driven Josephson standards was limited to measurements at low voltages till their output could be increased to

the 1 V level around 2015. This field is rapidly evolving at present. In this section, we give an overview of the most important AC measuring techniques with Josephson voltage standards starting with programmable Josephson standards and progressing to pulse-driven standards.

An important AC measurement is realized by the so-called AC quantum voltmeter, which is intended to measure the waveform of an unknown periodic AC voltage [57, 58]. To this end, a programmable Josephson standard is used to synthesize an AC reference voltage, which is synchronized and phase locked to the unknown voltage. The difference between the reference and the unknown voltage is measured with a sampling voltmeter, which serves as a null detector. This concept is similar to the DC voltage calibration described in Section 4.1.5.1, in which also the difference between reference and measurand is nulled. AC quantum voltmeters can be operated in the audio frequency range. Thanks to the sampling technique, the output of the programmable Josephson array is only used as reference if the array has settled on a quantized voltage step. Data taken during the switching are discarded. This temporal gating suppresses the adverse effect of the transients. The achievable uncertainty depends on the frequency and complexity of the unknown waveform. For a simple approximation of a sinusoidal voltage (consisting of only four levels), an uncertainty of parts in 10^9 was demonstrated at frequencies below 400 Hz [22].

The AC quantum voltmeter has been demonstrated with 10 V programmable Josephson standards [59, 60]. This was an important step toward commercialization, which has already been accomplished using 10 V Josephson technology [59, 61, 62]. Commercial AC quantum voltmeters achieve uncertainties of less than one part in 10^6 for measurements of AC voltages up to 1 kHz [61]. Operation of 10 V programmable Josephson standards in cryogen-free cryocoolers has also been demonstrated [62, 63]. Cryocooler operation is an important feature for the use of commercial AC quantum voltmeters for calibration and testing in industry [62].

In Ref. [64], it has been suggested to combine an AC quantum voltmeter with standard resistors to enable automated measurements of DC and AC resistances and currents. The current measurements are based on measurements of the voltage drop over a known resistor. Resistance measurements can be accomplished with potentiometric methods involving a known standard resistor.

The concept of the AC quantum voltmeter was also used to develop a quantum-based standard of electric power [65]. Another approach toward a quantum-based power standard involves the use of analog–digital converters that are characterized using a programmable Josephson standard [66, 67]. Electric power standards reach uncertainties on the order of 10^{-6} limited by the uncertainty of their voltage and current transformers.

Various approaches are reported in the literature to use programmable Josephson standards for measurements of rms values, for example, for the calibration of thermal converters. A comprehensive summary can be found, for example, in Ref. [22]. Measurements of rms values are affected by the transients, which, so far, has limited the achievable uncertainty to parts in 10^7 even under the most favorable measuring conditions [68].

Programmable Josephson voltage standards have also been used for the measurement of impedance ratios with impedance bridges. The idea of the bridge measurement is to adjust the ratio of two voltages such that the voltages drive the same current through the two impedances whose ratio is to be determined. A null detector monitors the balancing of the bridge. If the bridge is balanced, the impedance ratio is given by the voltage ratio. In conventional bridges, the voltage ratio is manually adjusted using inductive voltage dividers. As an alternative, the two voltages can be generated by two programmable Josephson voltage standards [69]. Such a Josephson impedance bridge offers the advantage that the balancing can be automated over a frequency range from some tens of hertz to several kilohertz, which substantially facilitates the calibration of impedances. The effect of the transients can be sufficiently suppressed in bridge measurements of like impedances. To this end, a square wave is generated by the programmable Josephson standards and phase-locked detection is used at the fundamental frequency of this wave [70]. Thereby, the higher harmonics of the fast transients do not affect the measurement. Impedance bridges with programmable Josephson voltage standards reach approximately the same uncertainties as obtained with manually operated conventional bridges if like impedances are compared. For example, for the measurement of two 10 kΩ resistors, an uncertainty of a few parts in 10^8 was demonstrated [69]. The ratio of two 100 pF capacitors was determined with uncertainties in the range of 10^{-8}–10^{-7} depending on frequency [22]. More recent work investigated the measurement of 100 to 10 pF capacitance ratios [71]. Agreement was found between measurements with conventional impedance bridges and bridges with programmable Josephson standards at an uncertainty level of 10^{-7}–10^{-6} depending on frequency [71]. The comparison of unlike impedances, for example, capacitances and AC resistances, is more challenging. This is because the balancing condition of impedance bridges depends on frequency for unlike impedances. If the bridge is balanced at one frequency, it is not at other frequencies. Therefore, programmable Josephson voltage standards with their fast transients and complex spectra do not lend themselves well to bridge measurements of unlike impedances.

Applications of pulse-driven Josephson standards often exploit the possibility to generate voltages with well-defined spectra, for example, a single tone corresponding to a sinusoidal wave. This property is used in impedance bridges for unlike impedances. Reference [72] reports a Josephson impedance bridge with two pulse-driven Josephson standards, which can compare any two impedances (resistance/capacitance, resistance/inductance, and inductance/capacitance). The bridge can be operated from 1 to 20 kHz, and relative uncertainties well below one part in 10^6 can be achieved [72]. An important measurement in electrical metrology links capacitance to a quantum Hall resistance standard, thereby realizing the SI farad (see Section 5.4.4). The measurement requires a quadrature bridge, that is, an impedance bridge that compares capacitance to AC resistance. Reference [73] reports a Josephson impedance bridge with two pulse-driven Josephson standards, which compares a 10 nF capacitance standard with a quantum Hall resistance standard with an uncertainty of 1.4 parts in 10^8.

Apart from impedance metrology, pulse-driven Josephson voltage standards were used for the calibration of thermal converters with pure sinusoidal voltage at

different frequencies [74]. Such measurements of rms values greatly benefit from the absence of undefined voltage transients. Other measurements of electronic components include nanovoltmeters and lock-in amplifiers [75]. The nonlinearity of electronic components was investigated with multitone spectra generated by a pulse-driven Josephson standard [76]. More applications in electronic testing are likely to develop as pulse-driven Josephson voltage standards become commercially available. This development is supported by the possibility to operate pulse-driven Josephson standards in cryogen-free cooling systems [45, 77].

Beyond electrical metrology, pulse-driven Josephson voltage standards are used in Johnson noise thermometry to realize and disseminate the SI kelvin. The Josephson standard is used to generate a calculable pseudonoise voltage waveform whose power is compared to the thermal noise power of a resistor [78]. The method can be implemented with voltage amplitudes below 1 μV [78]. Johnson noise thermometry with pulse-driven Josephson voltage standards has substantially contributed to the determination of the Boltzmann constant in the previous SI and the redefinition of the kelvin [79–81]. Details can be found in Chapter 8.

4.2 Flux Quanta and SQUIDs

In Section 4.1, the flux quantum $\Phi_0 = h/(2e) \approx 2 \times 10^{-15}$ V s was introduced and shown to provide the basis of the realization of the SI unit volt. In this section, we discuss that flux quanta also enable extremely sensitive measurements of magnetic quantities using SQUIDs. In SQUIDs, the physics of Josephson junctions combines with the physics of flux quantization in a superconducting ring. Flux quantization refers to the fact that the smallest amount of magnetic flux that can be maintained in a superconducting ring is given by the flux quantum. Moreover, the magnetic flux threading a superconducting ring is always an integer multiple of the flux quantum, very much like an isolated amount of charge is an integer multiple of the elementary charge *e*. Flux quantization is indeed the rationale for considering $\Phi_0 = h/(2e)$ a quantum entity rather than a simple combination of two fundamental constants.

The first SQUID was demonstrated in 1964 [82], only two years after *Brian D. Josephson* had published his seminal paper about supercurrents in superconducting tunnel structures [1]. SQUID technology has substantially matured since then. Nowadays, SQUIDs are commercially available and used in various applications from biomagnetism to nondestructive material testing and geophysics. For a comprehensive, in-depth treatment of SQUID physics, technology, and applications, the interested reader is referred to specialized monographs and review articles (e.g., [16, 83–85]). In Section 4.2, we focus on the basics of SQUIDs in the context of quantum metrology and on selected applications in measurement.

4.2.1 Superconductors in External Magnetic Fields

A SQUID consists of a superconducting ring, which is interrupted by one or two Josephson junctions and threaded by magnetic flux. Therefore, we introduce the reader to the physics of superconducting structures in external magnetic

fields before discussing SQUIDs in Section 4.2.2. To do so, we start with bulk superconductors in Section 4.2.1.1 and then proceed to superconducting rings to introduce the concept of flux quantization in Section 4.2.1.2. Finally, we discuss single Josephson junctions in external magnetic fields in Section 4.2.1.3.

4.2.1.1 Meissner–Ochsenfeld Effect

The Meissner–Ochsenfeld effect refers to the observation that a magnetic field does not penetrate deeply into a superconductor. The effect was first observed by *Walther Meissner* and *Robert Ochsenfeld* at the Physikalisch–Technische Reichsanstalt, the predecessor of the PTB, in 1933 [86].

To describe a superconductor in a magnetic field and, in particular, the Meissner–Ochsenfeld effect, we start from very general grounds, namely, from the quantum mechanical electric current density, $\mathbf{j}_S(\mathbf{r})$. The electric current density is obtained by multiplying the probability current density and the charge of the Cooper pair $e_S = -2e$. The electric current density can then be written as

$$\mathbf{j}_S(\mathbf{r}) = \frac{e_S\hbar}{2m_S i}\left[\Psi^*(\mathbf{r})grad\Psi(\mathbf{r}) - \Psi(\mathbf{r})grad\Psi^*(\mathbf{r})\right] - \frac{e_S^2}{m_S}\mathbf{A}(\mathbf{r})\Psi^*(\mathbf{r})\Psi(\mathbf{r}) \tag{4.24}$$

with

$$\Psi(\mathbf{r}) = \sqrt{n_S(\mathbf{r})}e^{i\theta(\mathbf{r})} \tag{4.25}$$

being the macroscopic quantum mechanical wave function of the BCS theory according to Eq. (4.2). The mass of the Cooper pair is denoted by m_S. As usual, $\mathbf{A}(\mathbf{r})$ is the vector potential of the magnetic flux density $\mathbf{B}(\mathbf{r})$, that is,

$$\mathbf{B}(\mathbf{r}) = \text{rot}\,\mathbf{A}(\mathbf{r}) \tag{4.26}$$

holds. While the Josephson effect is determined by the temporal variation of the phase difference φ, spatial variations will turn out to be important for the description of superconductors in magnetic fields. Therefore, the spatial dependence of all quantities is explicitly noted in the above equations. Inserting Eq. (4.25) in Eq. (4.24) yields

$$\mathbf{j}_S(\mathbf{r}) = \frac{n_S e_S^2}{m_S}\left[\frac{\hbar}{e_S}grad\,\theta\,(\mathbf{r}) - \mathbf{A}(\mathbf{r})\right] \tag{4.27}$$

Taking the curl of either side and keeping in mind that the curl of any gradient field vanishes, we obtain

$$\text{rot}\,\mathbf{j}_S(\mathbf{r}) = -\frac{1}{\mu_0\lambda^2}\mathbf{B}(\mathbf{r}) \tag{4.28}$$

with

$$\lambda^2 = \frac{m_S}{\mu_0 n_S e_S^2} \tag{4.29}$$

μ_0 is the magnetic constant also known as the permeability of vacuum. Equation (4.28) shows that the Cooper pair current density and the magnetic field are related.

The Meissner–Ochsenfeld effect is derived if Eq. (4.28) is combined with Maxwell's equations, namely,

$$\mathbf{j}_S(\mathbf{r}) = \frac{1}{\mu_0}\text{rot}\,\mathbf{B}(\mathbf{r}) \tag{4.30}$$

(neglecting the displacement current), and

$$div\,\mathbf{B}(\mathbf{r}) = 0 \tag{4.31}$$

Inserting Eq. (4.30) in Eq. (4.28) and using the identity for the Laplace operator $\Delta = \text{grad(div)} - \text{rot(rot)}$ and Eq. (4.31), we obtain the following equation:

$$\Delta\mathbf{B}(\mathbf{r}) - \frac{1}{\lambda^2}\mathbf{B}(\mathbf{r}) = 0 \tag{4.32}$$

To extract the physics, that is, the Meissner–Ochsenfeld effect, from Eq. (4.32), we assume that the magnetic field is oriented along the z-axis of a rectangular coordinate system and depends only on the x-coordinate. It is further assumed that the superconductor extends from $x = 0$ to $+\infty$ (and that vacuum extends from $-\infty$ to $x = 0$). Then, the magnetic field in the superconductor is given by

$$B_z(x) = B_z(x = 0)\exp\left(-\frac{x}{\lambda}\right) \tag{4.33}$$

Thus, the magnetic field decays exponentially and is negligibly small in the interior of a bulk superconductor, where it can be considered zero. This damping of the magnetic field is known as the Meissner–Ochsenfeld effect. The magnetic field is finite only in a narrow edge region whose width is approximately λ. The length λ is called the London penetration depth named after *Fritz* and *Heinz London* who described a superconductor in a magnetic field as early as 1935 [2]. The London penetration depth is typically in the range from 10 to 100 nm for type I superconductors and increases with increasing temperature and diverges as the critical temperature T_c is reached (the specific difference between type I and II superconductors will not be considered here). An equivalent formulation of the Meissner–Ochsenfeld effect is to state that a superconductor expels the magnetic field from its interior and behaves like a perfect diamagnet. The perfect diamagnetism is also the characteristic of the superconducting state, along with the disappearance of electric resistance.

The Meissner–Ochsenfeld effect is due to a screening current flowing at the surface of the superconductor as can be seen from the Maxwell equation (4.30). Taking the curl of $B_z(x)$ yields a screening current in the y-direction, that is, perpendicular to the magnetic field and parallel to the interface between the superconductor and the vacuum:

$$j_{Sy}(x) = \frac{1}{\mu_0\lambda}B_z(x = 0)\exp\left(-x/\lambda\right) \tag{4.34}$$

Thus, the magnetic field gives rise to a screening current in the edge region, which, in turn, results in a field-free interior of the superconductor.

4.2.1.2 Flux Quantization in Superconducting Rings

We consider a superconducting ring in the x–y plane and a magnetic field along the z-axis, which can be expressed by a vector potential $\mathbf{A}(\mathbf{r})$ according to Eq. (4.26). To study the magnetic flux Φ_F through the area F, which is enclosed by the ring, we use Eq. (4.27). Rewriting it in terms of the flux quantum $\Phi_0 = h/(2e)$ and the London penetration depth λ gives

$$\mu_0 \lambda^2 \mathbf{j}_S(\mathbf{r}) = -\frac{\Phi_0}{2\pi} grad\, \theta(\mathbf{r}) - \mathbf{A}(\mathbf{r}) \tag{4.35}$$

Equation (4.35) can be integrated along a closed path C in the superconducting ring. When calculating the integral over $\mathbf{A}(\mathbf{r})$, we can take advantage of Stokes' theorem and write

$$\oint_C \mathbf{A}(\mathbf{r}) \cdot \mathrm{d}\mathbf{s} = \int_{F(C)} \mathrm{rot}\mathbf{A}(\mathbf{r}) \cdot d\mathbf{f} = \int_{F(C)} \mathbf{B}(\mathbf{r}) \cdot d\mathbf{f} = \Phi_F \tag{4.36}$$

Thus, the term with the vector potential yields the magnetic flux Φ_F through the ring area F. When working out the term that contains the phase $\theta(\mathbf{r})$, one must keep in mind that the macroscopic wave function $\Psi(\mathbf{r})$ must be defined without any ambiguity. This requires that the relation

$$\oint_C grad\theta(\mathbf{r}) \cdot \mathrm{d}\mathbf{s} = -2\pi n \tag{4.37}$$

holds with n being an integer. Then the phases $\theta(\mathbf{r})$ before and after traversing the closed path C differ only by $2\pi n$, which is meaningless due to the 2π periodicity of the phase. Collecting the results of Eqs. (4.36) and (4.37), we obtain

$$\oint_C \mu_0 \lambda^2 \mathbf{j}_S(\mathbf{r}) \cdot \mathrm{d}\mathbf{s} + \Phi_F = n\Phi_0 \tag{4.38}$$

Let us assume that the ring is a bulk superconductor, that is, its width and thickness are much larger than the London penetration depth λ. The integration path C can then be chosen to be several λ away from the surface of the ring. In this case, the screening current density $\mathbf{j}_S(\mathbf{r})$ is negligible along the integration path, and Eq. (4.38) simplifies to

$$\Phi_F = n\Phi_0 \tag{4.39}$$

Equation (4.39) states that the magnetic flux through the area enclosed by a superconducting ring is quantized in units of the flux quantum (if the ring has a sufficiently large width and thickness). It is worth emphasizing that this result was derived for an uninterrupted superconducting ring without a Josephson junction. If a Josephson junction is embedded in the ring, Eq. (4.39) does not apply anymore. This case is studied in Section 4.2.2.

For an uninterrupted superconducting ring, the question arises how Φ_F can be quantized even though the external magnetic field $\mathbf{B}(\mathbf{r})$ and the external flux Φ_{ext} can vary continuously. The flux quantization is the result of the screening current that circulates close to the surface of the ring and gives rise to its field-free interior. The screening current generates a flux Φ_S whose magnitude is such that

an integer multiple of flux quanta is obtained if Φ_S is added to the external flux. Thus, the relation

$$\Phi_F = \Phi_{ext} + \Phi_S = n\Phi_0 \tag{4.40}$$

holds. The circulating Cooper pair current and the magnetic flux that it generates will be reconsidered when treating SQUIDs in Section 4.2.2.

4.2.1.3 Josephson Junctions in External Magnetic Fields and Quantum Interference

In this section, we consider a single Josephson junction in an external magnetic field to set the stage for the description of SQUIDs. To this end, it will be discussed how an external magnetic field modifies the phase difference φ across a Josephson junction and how this field dependence gives rise to quantum interference.

The quantity of interest is the supercurrent I_S across the Josephson junction according to Eq. (4.5). However, in contrast to Section 4.1, we consider spatially dependent phases θ_1 and θ_2 of the wave functions of the two superconductors that form the Josephson junction. The spatially dependent phases $\theta_1(\mathbf{r})$ and $\theta_2(\mathbf{r})$ can be obtained from Eq. (4.35) if the vector potential $\mathbf{A}(\mathbf{r})$ and the current density $\mathbf{j}_S(\mathbf{r})$ are known. Let us consider a Josephson junction where the tunnel barrier is located around $x = 0$ as shown in Figure 4.13. Superconductor 1 extends from $x = -\infty$ to the tunnel barrier and superconductor 2 from the tunnel barrier to $x = +\infty$. The superconductors shall be made of the same material and extend from $-a/2$ to $+a/2$ in the y-direction. The magnetic flux density points along the z-axis and shall be constant in the tunnel barrier.

In the superconductors, the magnetic flux density decays exponentially due to the Meissner–Ochsenfeld effect as described by Eq. (4.33). Separately for each superconductor, the vector potential and the current density can be calculated from the magnetic flux density using Eqs. (4.26) and (4.30), respectively. Both quantities have only a y component and the vector Eq. (4.35) simplifies to

$$\frac{\mathrm{d}\theta(y)}{\mathrm{d}y} = -\frac{2\pi}{\Phi_0}(\mu_0\lambda^2 j_{sy}(x) + A_y(x)) \tag{4.41}$$

As x approaches $\pm\infty$, the vector potential becomes constant (corresponding to the vanishing magnetic flux density), and the current density is found to decay to zero (see Eq. (4.34)). Since Eq. (4.41) is valid at any point x, it can be readily integrated at $x = \pm\infty$ where the current density is zero. Doing so for superconductors 1 and 2, one obtains for the phase difference across the Josephson junction

$$\varphi(y) = \theta_1(y) - \theta_2(y) = \varphi_0 + \frac{2\pi}{\Phi_0}[A_y(+\infty) - A_y(-\infty)] \cdot y \tag{4.42}$$

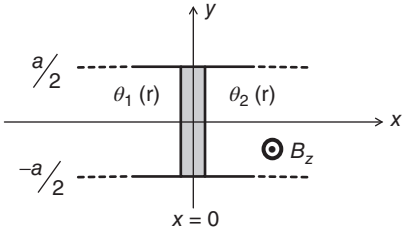

Figure 4.13 Josephson junction in a magnetic field that points along the z-direction. The tunnel barrier around $x = 0$ is shown in gray. The phase of the wave function to the left and right of the barrier is $\theta_1(\mathbf{r})$ and $\theta_2(\mathbf{r})$, respectively. Source: Göbel and Siegner [10]. Reproduced with permission of John Wiley & Sons.

with φ_0 being the phase difference at $y = 0$. The term with the vector potential can be rewritten, and we obtain

$$\varphi(y) = \varphi_0 + \frac{2\pi}{\Phi_0}\oint_C \mathbf{A}(\mathbf{r})\mathrm{d}\mathbf{s} = \varphi_0 + \frac{2\pi}{\Phi_0}\Phi(y) \tag{4.43}$$

The integral is taken along a closed loop in the x–y plane (normal to the magnetic field). The loop has a width y and a length in the x-direction that mathematically extends from $-\infty$ to $+\infty$ yet can be restricted to several times the London penetration depth λ from a physical point of view. The magnetic flux $\Phi(y)$ through this area depends on the y coordinate. As $\Phi(y)$ changes by a flux quantum Φ_0, the phase difference φ changes by 2π. Consequently, the supercurrent density

$$j_\mathrm{S}(y) = j_\mathrm{Smax}\sin(\varphi(y)) \tag{4.44}$$

is a periodic function with period Φ_0 and changes its direction depending on the position y within the Josephson junction.

The supercurrent I_S across the Josephson junction is obtained by integration of the supercurrent density $j_\mathrm{S}(y)$ over the area of the tunnel barrier using Eqs. (4.42) and (4.44). The integrations yields

$$I_\mathrm{S} = I_\mathrm{Smax}\sin\varphi_0\frac{\sin\left(\pi\frac{\Phi_A}{\Phi_0}\right)}{\pi\frac{\Phi_A}{\Phi_0}} \tag{4.45}$$

with the magnetic flux $\Phi_A = \Phi(y = a)$. Thus, Φ_A is the magnetic flux through the Josephson junction. Applying a bias current, the φ_0 term can be adjusted, but $|\sin\varphi_0| \leq 1$ always holds. Therefore, the maximum current or critical current in a magnetic field is given by

$$I_\mathrm{Smax}(\Phi_A) = I_\mathrm{Smax}\left|\frac{\sin\left(\pi\frac{\Phi_A}{\Phi_0}\right)}{\pi\frac{\Phi_A}{\Phi_0}}\right| \tag{4.46}$$

The critical current under the magnetic field is shown in Figure 4.14. The modulation induced by the magnetic flux resembles the optical diffraction pattern observed behind a slit illuminated by coherent light. This observation corroborates that interference between differently phased current contributions is at the heart of the modulation of the critical current.

The results of Section 4.2.1.3 are summarized as follows:

- Magnetic flux changes the phase difference across a Josephson junction.
- The natural unit of the magnetic flux is the flux quantum Φ_0 since a flux change of Φ_0 gives rise to a phase change of 2π.
- Quantum interference takes place when current contributions with different phases are superimposed.

4.2.2 Basics of SQUIDs

In principle, measurements of magnetic fields could be realized using the magnetic flux dependence of the critical current of a single Josephson junction as

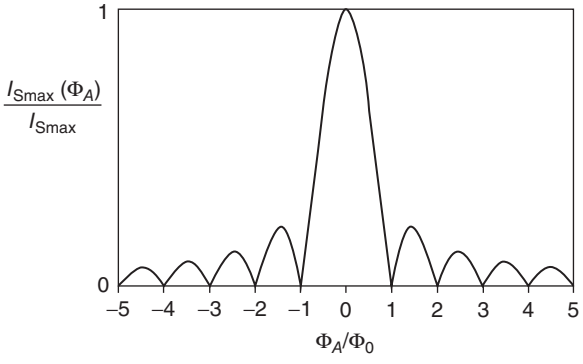

Figure 4.14 Critical current of a Josephson junction in a magnetic field (normalized to the zero-field critical current) versus magnetic flux in units of the flux quantum. Source: Göbel and Siegner [10]. Reproduced with permission of John Wiley & Sons.

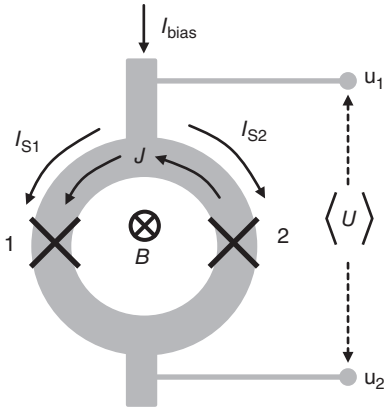

Figure 4.15 Schematic drawing of a DC SQUID with two Josephson junctions 1 and 2. The SQUID loop is penetrated by a magnetic field normal to the superconducting loop. Voltages are measured between contacts u_1 and u_2. Source: Göbel and Siegner [10]. Reproduced with permission of John Wiley & Sons.

shown in Figure 4.14. Yet, in this approach, the area over which the field is integrated is small, which limits the field resolution for a given flux resolution. A SQUID consists of a superconducting loop and thus has an increased area for field integration. The loop is interrupted by one or two Josephson junctions. To introduce the basics of SQUID physics in the context of quantum metrology, we restrict the discussion to the so-called DC SQUIDs. In DC SQUIDs, the loop is interrupted by two junctions, as shown in Figure 4.15.

Let us consider a symmetric DC SQUID with two identical ideal Josephson junctions. We assume that the area of each junction is much smaller than the area F of the superconducting loop, so that the magnetic flux through each junction is negligible. The DC SQUID is penetrated by an external magnetic field $\mathbf{B}$ normal to the plane of the SQUID loop giving rise to an external magnetic flux Φ_{ext} through the loop. The SQUID is biased with a DC current I_{bias}, which splits into two currents I_{S1} and I_{S2} through the Josephson junctions 1 and 2, respectively. For these currents, the Josephson equation (4.5) holds:

$$I_{S1,2} = I_{Smax} \sin(\varphi_{1,2}) \tag{4.47}$$

The phase differences across the junctions 1 and 2 are denoted by φ_1 and φ_2, respectively. Following the line of thought of Section 4.2.1.2, we must also account

for a circulating current, termed J in Figure 4.15. The circulating current contributes to the currents I_{S1} and I_{S2} according to the following relations:

$$I_{S1} = \frac{I_{bias}}{2} + J, \quad I_{S2} = \frac{I_{bias}}{2} - J \tag{4.48}$$

The SQUID behavior is determined by the relation between the phase differences φ_1 and φ_2 and the magnetic flux through the SQUID loop. This relation can be derived from the integration of Eq. (4.35) using the condition that the wave function is defined without any ambiguity as expressed by Eq. (4.37). Analogous to the treatment of the superconducting ring in Section 4.2.1.2, it can then be shown that

$$\frac{2\pi}{\Phi_0}\left[\oint_C \mu_0\lambda^2 \mathbf{j}_S(\mathbf{r})\cdot d\mathbf{s} + \Phi_F\right] = 2\pi n + (\varphi_1 - \varphi_2) \tag{4.49}$$

In this equation, the presence of the Josephson junctions manifests itself by the term $(\varphi_1 - \varphi_2)$. Apart from this term, the equation is identical to Eq. (4.38) of an uninterrupted superconducting ring. If the SQUID loop can be considered a bulk superconductor, the integral term can be neglected based on the argument developed in Section 4.2.1.2. The total flux is then given by Φ_F. The flux Φ_F is the sum of the external flux Φ_{ext} and the flux generated by the circulating current J flowing at the surface of the SQUID loop:

$$\Phi_F = \Phi_{ext} + LJ \tag{4.50}$$

where L is the inductance of the SQUID loop. As for a single Josephson junction in a magnetic field, Eq. (4.49) shows that the magnetic flux changes the phase term and should be quantified in terms of the natural unit Φ_0.

Next, we discuss how quantum interference in the SQUID loop provides the basis for extremely sensitive measurements of magnetic quantities. According to Kirchhoff's law, the bias current must be equal to the sum of I_{S1} and I_{S2}. Together with Eq. (4.49), in which the integral term is neglected, Kirchhoff's law yields

$$\begin{aligned} I_{bias} &= I_{Smax}[\sin(\varphi_1) + \sin(\varphi_2)] = 2I_{Smax}\cos\left(\frac{\varphi_1 - \varphi_2}{2}\right)\sin\left(\varphi_2 + \frac{\varphi_1 - \varphi_2}{2}\right) \\ &= 2I_{Smax}\cos\left(\frac{\pi\Phi_F}{\Phi_0}\right)\sin\left(\varphi_2 + \frac{\pi\Phi_F}{\Phi_0}\right) \end{aligned} \tag{4.51}$$

In general, the analysis of Eq. (4.51) is complicated since the flux Φ_F depends on the external flux and the circulating current, which also affects the phase difference across the Josephson junctions. Yet, regarding highly sensitive SQUID measurements, we can treat the simple case of very small SQUID inductance L. To make a more quantitative argument, the screening parameter

$$\beta_L = \frac{I_{Smax}L}{\Phi_0/2} \tag{4.52}$$

is defined as the maximum flux that a supercurrent in the SQUID loop can generate normalized by half a flux quantum. The case of small inductance L is then given by the condition $\beta_L \ll 1$. For $\beta_L \ll 1$, we obtain $\Phi_F = \Phi_{ext}$, and the current I_{bias} of Eq. (4.51) is modulated by the external flux Φ_{ext} only. This behavior provides the basis of measurements of the external flux or the external magnetic

field. We also note that the flux through the SQUID loop is not quantized in this case. The maximum current is obtained if the sine term of Eq. (4.51) is adjusted to the value ±1 by an appropriate choice of φ_2. Then the maximum current, that is, the critical current, is found to be

$$I_{\mathrm{Smax}}(\Phi_{\mathrm{ext}}) = 2I_{\mathrm{Smax}}\left|\cos\left(\frac{\pi\Phi_{\mathrm{ext}}}{\Phi_0}\right)\right| \tag{4.53}$$

As shown in Figure 4.16, the critical current is a periodic function of the external magnetic flux with the periodicity given by the flux quantum Φ_0. Maxima occur whenever $\Phi_{\mathrm{ext}} = n\Phi_0$, while the critical current is zero for $\Phi_{\mathrm{ext}} = (n+1/2)\Phi_0$. The modulation depth ΔI_{Smax} is given by $2I_{\mathrm{Smax}}$. The pattern of Figure 4.16 resembles the optical interference pattern observed behind a double slit, which is illuminated by coherent light. In the SQUID case, quantum interference occurs between the left-hand and the right-hand paths in the SQUID loop. The outcome of the quantum interference, that is, whether it is constructive or destructive, depends on the phases φ_1 and φ_2 across the Josephson junctions 1 and 2, respectively. Phase differences result from the magnetic flux as shown by Eq. (4.49). To take the analogy to optics one step further, we note that when plotting versus magnetic field, the pattern of Figure 4.16 has an envelope given by the pattern of a single junction. Similarly, in optics, the double-slit pattern has an envelope given by the single-slit diffraction profile. When discussing DC SQUIDs, we have neglected this single-junction effect since the area of a single junction is much smaller than that of the SQUID loop. Consequently, the magnetic field period of the single-junction pattern is much larger than that of the SQUID pattern.

For completeness, we also briefly discuss the case of large SQUID inductance L, corresponding to $\beta_{\mathrm{L}} \gg 1$. In this case, even a small circulating current J adds a nonnegligible flux to the external flux. Let us assume that the external flux is increased from zero. This flux change induces a circulating screening current J such that the associated flux LJ compensates for the increase in the external flux and the total flux remains zero. As the external flux exceeds $\Phi_0/2$, it is energetically more favorable to change the direction of the screening current J such that its magnetic flux adds up to the external one to adjust the total flux to one flux quantum Φ_0. With further increase in the external flux, this behavior repeats. More flux quanta are added so that the total magnetic flux is always given by an integer multiple of Φ_0. Obviously, this case is not favorable for measurements of

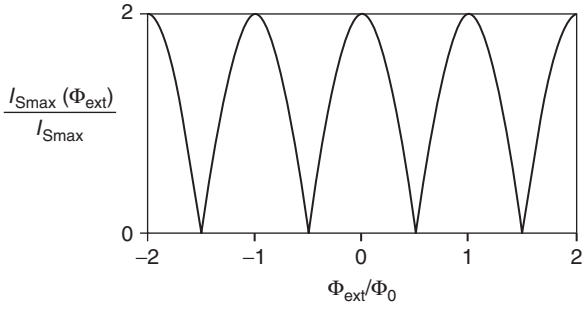

Figure 4.16 Critical current of a DC SQUID (normalized to the zero-field critical current of a single Josephson junction) versus external magnetic flux in units of the flux quantum for negligible SQUID inductance. Source: Göbel and Siegner [10]. Reproduced with permission of John Wiley & Sons.

the external magnetic flux. In fact, for large β_L, the modulation depth ΔI_{Smax} can be approximated by $\Delta I_{Smax} = \Phi_0/L = 2I_{Smax}/\beta_L$, which is much smaller than the modulation depth $\Delta I_{Smax} = 2I_{Smax}$ obtained for $\beta_L \ll 1$. The limit $\beta_L \gg 1$ is also characterized by the inequality

$$LJ \leq \Phi_0/2 \ll LI_{Smax} \tag{4.54}$$

Thus, $J \ll I_{Smax}$ holds so that the circulating screening current has only a negligible effect on the phases φ_1 and φ_2, which are almost equal in this case. Therefore, the term $(\varphi_1 - \varphi_2)$ is small in Eq. (4.49), and aspects of the physics of a superconducting ring without Josephson junctions are recovered. In particular, the total flux is found to be given by an integer number of flux quanta.

4.2.3 Applications of SQUIDs in Measurement

The most sensitive magnetic measuring instruments available today are DC SQUIDs made of low-temperature superconductors, such as niobium. Commercial instruments have a noise floor of $(1–10)\mu\Phi_0/\sqrt{\text{Hz}}$ and (1–10) $\text{fT}/\sqrt{\text{Hz}}$ for measurements of the magnetic flux and the flux density, respectively. These numbers correspond to an energy resolution of $(10^{-31}–10^{-32})$ J/Hz. The energy resolution is not far off the fundamental Heisenberg limit and corresponds to the energy required to lift an electron by 1 mm to 1 cm in the gravitational field of the earth. In this section, we briefly discuss real DC SQUIDs and the scheme for their readout, which will picture the SQUID as a highly sensitive flux-to-voltage converter. Then we discuss how DC SQUIDs are implemented in magnetometers and how their high resolution is harnessed for the precise scaling of currents and resistances and for biomagnetic measurements.

4.2.3.1 Real DC SQUIDs

In a real DC SQUID, the Josephson junctions of Figure 4.15 are real junctions as introduced in Section 4.1.3. The SQUID can then be described by the RCSJ model. Nonhysteretic overdamped junctions with McCumber parameter $\beta_C \leq 1$ are used in real DC SQUIDs. The critical current of real SQUIDs is maximum for external magnetic fluxes $\Phi_{ext} = n\Phi_0$ and minimum for $\Phi_{ext} = (n + 1/2)\Phi_0$. Thus, their flux dependence is similar to that derived for ideal SQUIDs in Section 4.2.2. The SQUIDs are biased with a DC current I_{bias}, and the time-averaged voltage drop over the SQUID $\langle U \rangle$ is measured between the contacts u_1 and u_2 as shown in Figure 4.15.

In principle, flux measurements with DC SQUIDs can be realized by increasing the bias current from zero till a finite voltage $\langle U \rangle$ is observed. The voltage drop indicates that the bias current equals and starts to exceed the critical current at the applied flux. If this measurement is repeated for different fluxes, the flux dependence of the critical current is obtained, which is a sensitive gauge of the flux. However, this is a cumbersome procedure. Therefore, in practice, the SQUID is biased with a current slightly above the maximum critical current (i.e., the critical current for $\Phi_{ext} = n\Phi_0$). Then, the voltage drop $\langle U \rangle$ is measured as the external magnetic flux is varied. Figure 4.17 schematically shows the voltage drop $\langle U \rangle$ versus the bias current I_{bias} for the two limiting flux conditions $\Phi_{ext} = n\Phi_0$

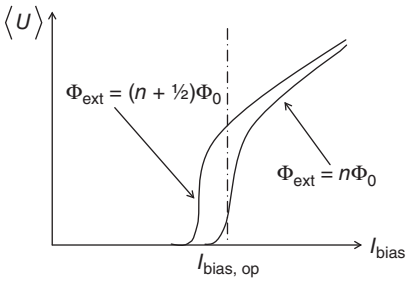

Figure 4.17 Schematic graph of time-averaged voltage versus bias current of a real DC SQUID for the two limiting magnetic flux conditions $\Phi_{ext} = n\Phi_0$ and $\Phi_{ext} = (n + 1/2)\Phi_0$. The operating bias current $I_{bias,\ op}$ is indicated by the vertical line. Source: Göbel and Siegner [10]. Reproduced with permission of John Wiley & Sons.

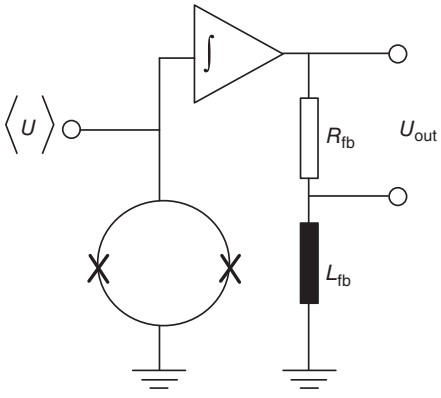

Figure 4.18 Simplified circuit diagram of a DC SQUID operated in a flux-locked loop. The output voltage U_{out} is proportional to the change of the external flux through the SQUID loop. Source: Göbel and Siegner [10]. Reproduced with permission of John Wiley & Sons.

and $\Phi_{ext} = (n + 1/2)\Phi_0$. The operating bias current is $I_{bias,\ op}$. As illustrated in Figure 4.17, the voltage drop $\langle U \rangle$ changes as Φ_{ext} is varied for a constant operating current $I_{bias,\ op}$. The voltage drop $\langle U \rangle$ is a periodic function of Φ_{ext} with periodicity Φ_0 as is the critical current. However, maxima of $\langle U \rangle$ correspond to minima of the critical current, and vice versa. Thus, voltage maxima occur for $\Phi_{ext} = (n + 1/2)\Phi_0$, while voltage minima are observed for $\Phi_{ext} = n\Phi_0$.

A SQUID operated in this mode can be considered a flux-to-voltage converter with a resolution of a fraction of the magnetic flux quantum Φ_0. Yet, the voltage $\langle U \rangle$ does not provide an unequivocal measure of the flux due to the intrinsic periodicity of the SQUID signal. This problem can be solved by operating the SQUID in a so-called flux-locked loop. A flux-locked loop feeds additional flux in the SQUID loop to keep the flux in the SQUID at a constant value while the external flux varies.

This negative feedback scheme is schematically shown in Figure 4.18. The voltage $\langle U \rangle$ is amplified and integrated. The resulting signal generates an opposing flux in the SQUID loop with the help of an inductance L_{fb} and produces the output voltage U_{out} over the resistor R_{fb}. This scheme linearizes the SQUID response since U_{out} is proportional to the change of the external flux even if this change is much larger than a flux quantum. To increase the sensitivity, flux modulation schemes and lock-in detection are applied (not shown in Figure 4.18). With these improvements, DC SQUIDs reach the outstanding magnetic flux resolution mentioned at the beginning of Section 4.2.3.

4.2.3.2 SQUID Magnetometers and Magnetic Property Measurement Systems

Magnetometers measure the magnetic flux density or the magnetic field. When a SQUID is used for these measurements, its effective area must be considered. For a given flux resolution, the field resolution can be improved if the area is increased. An increase of the area results in an increased SQUID inductance L, which reduces the modulation depth as discussed in Section 4.2.2. To maintain a sufficiently large modulation depth at a high field resolution, the concept of flux transformation is used. A flux transformer consists of a closed superconducting loop with primary inductance L_p and secondary inductance L_s as shown in Figure 4.19.

As the external flux changes by $\Delta\Phi_{ext}$, a current I is induced in the flux transformer. Flux quantization requires that the flux generated by this current compensates $\Delta\Phi_{ext}$ so that the flux through the transformer loop is $n\Phi_0$ before and after the change of the external flux. Thus, $\Delta\Phi_{ext}$ determines the current according to

$$\Delta\Phi_{ext} + (L_p + L_s)I = 0 \tag{4.55}$$

In turn, the current gives rise to a flux change $\Delta\Phi_{SQUID}$ in the SQUID via the mutual inductance M:

$$\Delta\Phi_{SQUID} = -MI = \frac{M}{L_p + L_s}\Delta\Phi_{ext} \tag{4.56}$$

The flux change $\Delta\Phi_{ext}$ increases linearly with the area of the flux transformer for a given magnetic field. As seen from Eq. (4.56), this results in an increase of the flux change $\Delta\Phi_{SQUID}$ in the SQUID (we note without proof that the inductance term decreases sublinearly with the area). Thus, the magnetic field sensitivity of a SQUID magnetometer can be increased by choosing a larger flux transformer area. The SQUID inductance is not increased, thereby avoiding detrimental effects on the SQUID modulation depth. Using flux transformation, magnetometers with a noise floor in the $\mathrm{fT}/\sqrt{\mathrm{Hz}}$ range can be realized as mentioned earlier.

SQUID magnetometers allow measurements of the magnetic flux density with outstanding resolution. However, they are not quantum standards since the effective SQUID area is not quantized. In Section 4.3, a quantum-based realization of the SI unit of the magnetic flux density, tesla, is discussed. This realization uses NMR techniques, which allow a primary standard of the tesla to be realized. SQUID magnetometers can be calibrated against such primary standards to obtain traceability to the SI.

We conclude this section on the use of SQUIDs for magnetic measurements by a brief discussion of SQUID gradiometers and SQUID-based instruments that measure the magnetic moment of materials. A first-order SQUID gradiometer

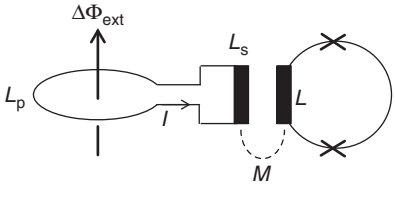

Figure 4.19 Superconducting flux transformer with primary inductance L_p and secondary inductance L_s. The magnetic flux through the transformer is coupled to the SQUID via the mutual inductance M. Source: Göbel and Siegner [10]. Reproduced with permission of John Wiley & Sons.

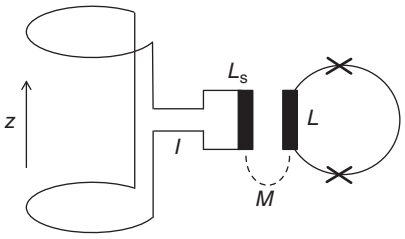

Figure 4.20 First-order SQUID gradiometer. Source: Göbel and Siegner [10]. Reproduced with permission of John Wiley & Sons.

is a special flux transformer, in which the single superconducting sensor loop or coil, shown in Figure 4.19, is replaced by two sensor coils. The arrangement of the coils is shown in Figure 4.20. The coils have opposite winding directions so that the signals from the two coils cancel each other if the magnetic field has the same value in both coils. Therefore, first-order gradiometers are only sensitive to the gradient of the magnetic field along the z-direction. This is of particular importance for highly sensitive measurements, for which the effects of background fields must be suppressed. The concept works well if the background fields are constant over the separation of the coils. This is often the case, for example, for the magnetic field of the earth. If four coils are used in a so-called second-order gradiometer, the signal from the field gradients is also suppressed. The instrument is then only sensitive to the second derivative of the magnetic field in the z-direction.

Second-order SQUID gradiometers are employed for the measurement of small magnetic moments. The magnetic sample under study is moved through the coil arrangement at a constant velocity. Due to the excellent background field suppression in the second-order gradiometer, the SQUID signal solely results from the magnetic field of the sample. The SQUID signal is recorded versus the sample position. To determine the magnetic moment, the measured curve is compared to a calibration curve obtained with a reference sample with known magnetic moment. Magnetic moments as low as 10^{-11} A m^2 can be detected with SQUID-based magnetic property measurement systems.

4.2.3.3 Cryogenic Current Comparators: Current and Resistance Ratios

The outstanding magnetic flux sensitivity of SQUIDs is also used in the so-called cryogenic current comparators (CCCs) [87]. These comparators allow current and resistance ratios to be determined with relative uncertainties of 10^{-9} and better. Precise current ratios are a cornerstone of current metrology. For example, CCCs are used to determine current ratios in a special ampere meter designed for the measurement of small currents, which is known as ultrastable low-noise current amplifier (ULCA) [88]. The ULCA allows the SI ampere to be realized linked to the defining constant e and has substantially advanced current metrology (for more details on ULCAs see Section 6.3.1).

The realization of well-known resistance ratios is of utmost importance in electrical metrology since it allows the electric resistance scale to be established. The anchor point of this scale is the realization of the SI ohm with the quantum Hall effect. As discussed in Chapter 5, the quantum Hall effect can be used to link electric resistance to the defining constants e and h with very low uncertainty.

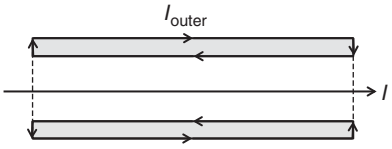

Figure 4.21 Cross section of a superconducting tube (gray). A current *I* is passed through a wire inside the tube. The current I_{outer} at the outer tube surface equals the current *I*. Source: Göbel and Siegner [10]. Reproduced with permission of John Wiley & Sons.

However, it provides only a limited set of nondecade resistance values. For practical applications in electrical engineering, decade resistance values are required from the milliohm to the teraohm range. Highly precise decade resistance values are derived from the quantum Hall resistance using CCCs at national metrology institutes.

In a CCC, current ratio measurements are based on Ampere's law combined with the Meissner–Ochsenfeld effect. The principle can be seen considering a superconducting tube with a wall thickness that is much larger than the London penetration depth λ. Inside the tube, a wire along the tube axis carries a current I, as shown in Figure 4.21. The current generates a magnetic flux density $\mathbf{B}$. To prevent the magnetic flux density from penetrating the superconductor, a screening current I_{inner} is induced at the inner surface of the tube. Applying Ampere's law to a closed integration contour inside the superconducting tube, where the magnetic flux density is zero, we obtain

$$\oint \mathbf{B} \cdot \mathrm{d}\mathbf{s} = \mu_0(I + I_{inner}) = 0 \tag{4.57}$$

The screening current flows back at the outer surface of the superconducting tube, $I_{outer} = -I_{inner} = I$.

Next, we consider a superconducting tube with two wires carrying currents I_1 and I_2. Obviously, the outer-surface current $I_{outer} = I_1 + I_2$ will be zero if (and only if) $I_1 = -I_2$, that is, if currents of equal magnitude flow in the opposite direction. This condition can be tested with a SQUID device set up to detect the magnetic field generated by I_{outer} outside the superconducting tube. Thus, the SQUID serves as a very sensitive null detector. It is important to note that the outer-surface current does not depend on the specific position of the wires inside the tube if the tube is long compared to its diameter. This is the basis of the CCC concept and ensures its high precision.

The tube arrangement realizes the current ratio $I_2/I_1 = 1$. In a CCC, the tube is replaced by a superconducting torus, whose ends overlap but are electrically isolated from each other. Inside the torus, two coils with opposite winding directions carry currents I_1 and I_2. If the winding numbers are n_1 and n_2, any rational current ratio

$$\frac{I_2}{I_1} = \frac{n_1}{n_2} \tag{4.58}$$

can be realized. The SQUID null detector is placed in the center of the torus. It monitors the magnetic flux and generates a feedback signal, which adjusts one of

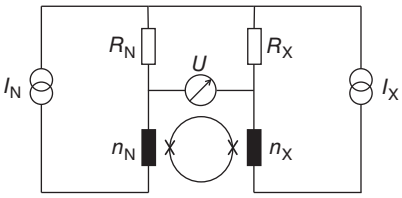

Figure 4.22 Schematic circuit diagram of a resistance bridge based on a cryogenic current comparator. Source: Göbel and Siegner [10]. Reproduced with permission of John Wiley & Sons.

the currents till Eq. (4.58) is fulfilled, that is, till the ampere turns of both coils are equal.

As mentioned earlier, CCCs are widely used for precise resistance comparisons. A schematic circuit diagram of a CCC-based resistance bridge is shown in Figure 4.22. An unknown resistor R_X is compared to a resistance standard R_N. The two coils with winding numbers n_X and n_N have opposite winding directions. The balance of ampere turns is monitored by a SQUID device, and the difference between the voltage drops over the resistors is measured by a voltmeter. When the bridge is completely balanced, the equations $I_X n_X = I_N n_N$ and $I_X R_X = I_N R_N$ are fulfilled. Thus, the resistance ratio is given by

$$\frac{R_X}{R_N} = \frac{n_X}{n_N} \tag{4.59}$$

In practice, an auxiliary circuit (not shown in Figure 4.22) is needed to completely balance the bridge. A detailed discussion of auxiliary circuits can be found, for example, in Refs. [89, 90]. The CCC-based resistance bridge is operated by periodically reversing the current polarity at low frequencies (typically below 1 Hz) to compensate for unwanted thermal electromotive forces. Relative uncertainties of 10^{-9} and better are achieved.

4.2.3.4 Biomagnetic Measurements

SQUIDs not only contribute to the scaling of electrical units but have also found "real-world" applications. Examples include geophysical surveying for oil and gas as well as nondestructive material testing, where SQUIDs can be used, for example, to detect subsurface flaws in aircraft parts. The most challenging real-world application in terms of the required magnetic field resolution is the measurement of biomagnetic signals. We briefly discuss biomagnetic measurements in this section to illustrate how the unprecedented sensitivity of a quantum-based SQUID device pushes the limits of measurements.

The most intensively investigated biomagnetic signals are those generated by the human heart (magnetocardiography, MCG) [91] and human brain (magnetoencephalography, MEG) [92]. Their investigation is of particular interest since MCG and MEG are noninvasive diagnostic tools.

MCG is the magnetic counterpart of electrocardiography (ECG), in which electric signals are measured that originate from the heartbeat. Their temporal shape provides information on the functioning of the heart. In MCG, the corresponding magnetic field is measured. ECG signals are obtained with electrodes attached to the thorax and, thus, originate from current contributions at the surface of the body. In contrast, MCG signals are measured in a contactless mode and result

from the total current distribution generated by the heart. Therefore, MCG contains additional information not accessible with ECG.

In MEG, the magnetic field distribution is measured that is generated by the electric activity of the brain. From the field distribution, information is obtained on the location of the source (often modeled as current dipole) of the magnetic field and, in turn, on the brain function. MEG combines high temporal resolution on the order of a millisecond with localization accuracy in the centimeter range and is noninvasive, as mentioned previously. This combination makes it an attractive diagnostic tool. For comparison, its electric counterpart, that is, noninvasive electroencephalography, provides much less accuracy.

The challenge that MCG and MEG presents to measurement lies in the weakness of the magnetic signals. Peak amplitudes of MCG signals are several tens of picotesla, and MEG signals are even smaller with signal levels below 1 pT. The measurements must cover a bandwidth of several 100 Hz to obtain the desired information on the temporal shapes of the signals. Therefore, magnetic field detectors with a noise level in the $\mathrm{fT}/\sqrt{\mathrm{Hz}}$ range must be used to obtain a sufficiently large signal-to-noise ratio. Consequently, SQUIDs are the magnetic field sensors of choice for MCG and MEG.

Besides the sensitivity of the detectors, screening of external static as well as alternating magnetic stray fields is required. These fields can be on the order of microtesla and would otherwise completely mask the biomagnetic signals. Therefore, the measurements are performed in magnetically shielded rooms. To date, the magnetically shielded room with the highest shielding factor has been built at the Berlin institute of the PTB. It comprises seven magnetic layers of mu-metal with varying thickness and one highly conductive eddy current layer consisting of 10 mm aluminum. In the inner measuring chamber, a noise level well below $1\,\mathrm{fT}/\sqrt{\mathrm{Hz}}$ is achieved with a white characteristic up to 1 MHz (apart from a 1/f contribution at low frequencies).

The detection system for biomagnetic measurements consists of SQUID arrays rather than a single SQUID detector. Up to several hundreds of SQUID sensors are employed to measure the magnetic field distribution caused by the bioelectric currents related to the activity of the heart or brain. The current distribution is then reconstructed from the measured magnetic field distribution. This is a so-called inverse problem, which is much more challenging than the so-called forward calculations, in which the field is determined from a known source distribution. Figure 4.23 shows a photograph of a multichannel SQUID system operated in a magnetically shielded chamber in the Benjamin Franklin hospital of the Charité university clinic in Berlin.

4.3 Traceable Magnetic Flux Density Measurements

The magnetic flux density can be resolved with outstanding resolution using SQUID magnetometers as described in Section 4.2.3. However, these instruments do not provide traceability to the SI. A conceptually straightforward way to obtain traceability is to use a calculable magnetic field coil and to pass a

Figure 4.23 Eighty-three-channel SQUID system aligned above a patient for MCG measurements. Source: Courtesy of PTB.

current through it, whose SI value is known. In practice, this concept faces severe limitations since it is difficult to establish the geometry of a coil with the required high precision. Therefore, NMR techniques are used at many national metrology institutes to realize, maintain, and disseminate the SI unit of the magnetic flux density, tesla. NMR techniques provide the basis of traceable magnetic measurements in the present SI, and they already did so in the previous SI.

NMR measurements link the magnetic flux density to the magnetic moment of a nucleon, that is, to a constant of nature. The nucleon is chosen such that the SI value of its magnetic moment is precisely known. In the context of quantum metrology, NMR involves the manipulation of nuclear spins to realize highly precise measurements. To catch the essence of NMR measurements, consider a proton with its spin components $s_z = \pm 1/2\hbar$ along the quantization axis z. If a DC magnetic field B_z is applied along z, the two spin states are shifted upward and downward in energy by

$$E_{\pm} = \pm \left(g \frac{e}{2m_{\mathrm{p}}} s_z \right) B_z \tag{4.60}$$

The expression in parenthesis is the z component of the magnetic moment, g the g-factor, and m_{p} the proton mass. According to Eq. (4.60), the energy splitting between the spin states can be expressed as

$$\Delta E = \hbar\omega = \hbar\gamma'_{\mathrm{p}} B_z \tag{4.61}$$

where ω is the (angular) spin-flip frequency. It is also named (angular) precession frequency since in a classical picture the proton spin precesses around the magnetic field with the angular frequency ω. The constant γ'_p is the gyromagnetic ratio of the proton given by twice the magnetic moment divided by $\hbar$. More strictly speaking, the prime put as superscript is supposed to indicate that a proton in a spherical sample of pure water is considered (at 25 °C). Thus, γ'_p is the shielded proton gyromagnetic ratio. Its approximate SI value is $2.675 \times 10^8\ \mathrm{s^{-1}\ T^{-1}}$ with a relative uncertainty of 1.3×10^{-8} according to the adjustment of the fundamental constants of 2014 [93]. The relative change of γ'_p is negligible from one adjustment of the fundamental constants to the next. For example, it was less than four parts in 10^8 from the adjustment of 2010 to that of 2014 [93, 94]. Therefore, Eq. (4.61) allows the SI tesla to be realized based on the SI value of γ'_p and a frequency measurement, which can be performed with a low uncertainty.

Two different approaches are used to determine the frequency in NMR measurements. For magnetic flux densities of a few millitesla and below, the water sample is polarized by a magnetic field pulse, that is, the upper spin state is populated. After the polarization pulse has been turned off, the free-precession decay is observed in the time domain measuring the voltage, which is induced by the precessing magnetic moment. The oscillating free-precession signal reveals the precession frequency. The signal decays due to the intrinsic spin–spin relaxation time and the inhomogeneity of the magnetic flux density across the water sample. Thus, the latter must be small for the technique to be applicable. Figure 4.24 shows a free-precession signal obtained at a magnetic field B_z of approximately 1.2 mT. The plotted curve is the result of a downmixing process with a reference frequency $f_{\mathrm{ref}} = 51\,090\ \mathrm{Hz}$. The downmixing generates a difference frequency f_{diff}, which can be determined from the experimental data. The precession frequency $\omega/(2\pi)$ is then obtained from $\omega/(2\pi) = f_{\mathrm{ref}} + f_{\mathrm{diff}}$.

To illustrate the application range of the free-precession technique for the realization of the tesla at national metrology institutes, we take data from the PTB as

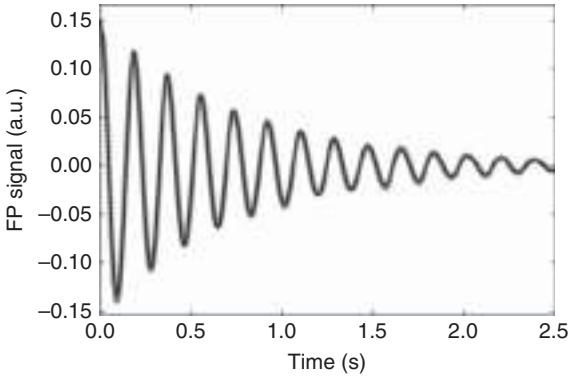

Figure 4.24 Free-precession (FP) signal of protons in a water sample at a magnetic field of approximately 1.2 mT. The precession frequency $\omega/(2\pi)$ has been downmixed with a reference frequency of 51 090 Hz to yield the observed oscillating signal. The gray dots are experimental data and the black line is a fit to determine the difference frequency and, in turn, the precession frequency. Source: Courtesy of C. Hahn, PTB.

an example. At the PTB, the technique is used to realize the unit of the magnetic flux density in the range from 10 μT to 2 mT. The lower boundary is determined by the requirement to precisely compensate the magnetic field of the earth. The relative uncertainty varies from 10^{-4} (at 10 μT) to 10^{-6} (at 2 mT) [95].

NMR absorption techniques can be used for magnetic flux densities in the millitesla range and higher [95]. The absorption of a radiofrequency (RF) magnetic field is monitored with the help of a resonator circuit to determine the precession frequency ω and, hence, the unknown DC magnetic flux density B_z [96]. Since the absorbed power scales with B_z^2 [96], the technique cannot be extended to the low field range. At the PTB, the absorption technique is used to realize the magnetic flux density from 1–2 to 150 mT with a relative uncertainty on the order of 10^{-5} [95].

References

1 Josephson, B.D. (1962). Possible new effects in superconductive tunneling. *Phys. Lett.* 1: 251–253.

2 London, F. and London, H. (1935). The electromagnetic equations of the supra-conductor. *Proc. R. Soc. London, Ser. A* 149: 71–88.

3 (a) Ginzburg, V.L. and Landau, L.D. (1950). On the theory of superconductivity. *Zh. Eksp. Teor. Fiz.* 20: 1064–1082. (b) English translation in Landau, L.D. (1965). *Collected Papers*, 546. Oxford: Pergamon Press.

4 Bardeen, J., Cooper, L.N., and Schrieffer, J.R. (1957). Microscopic theory of superconductivity. *Phys. Rev.* 106: 162–164.

5 Bardeen, J., Cooper, L.N., and Schrieffer, J.R. (1957). Theory of Superconductivity. *Phys. Rev.* 108: 1175–1204.

6 Bednorz, J.G. and Müller, K.A. (1986). Possible high Tc superconductivity in the Ba–La–Cu–O system. *Z. Phys. B: Condens. Matter* 64: 189–193.

7 Wu, M.K., Ashburn, J.R., Torng, C.J. et al. (1987). Superconductivity at 93 K in a new mixed-phase Y–Ba–Cu–O compound system at ambient pressure. *Phys. Rev. Lett.* 58: 908–910.

8 Schilling, A., Cantoni, M., Guo, J.D., and Ott, H.R. (1993). Superconductivity above 130 K in the Hg–Ba–Ca–Cu–O system. *Nature* 363: 56–58.

9 Ren, Z.-A., Che, G.-C., Dong, X.-L. et al. (2008). Superconductivity and phase diagram in iron-based arsenic-oxides ReFeAsO1-δ (Re = rare-earth metal) without fluorine doping. *Eur. Phys. Lett.* 83: 17002 (4 pp).

10 Göbel, E.O. and Siegner, U. (2015). *Quantum Metrology: Foundations of Units and Measurements*. Weinheim: Wiley-VCH.

11 Shapiro, S. (1963). Josephson currents in superconducting tunneling: the effect of microwaves and other observations. *Phys. Rev. Lett.* 11: 80–82.

12 Stewart, W.C. (1968). Current–voltage characteristics of Josephson junctions. *Appl. Phys. Lett.* 12: 277–280.

13 McCumber, D.E. (1968). Effect of AC impedance on DC voltage–current characteristics of superconductor weak-link junctions. *J. Appl. Phys.* 39: 3113–3118.

14 Kautz, R.L. and Monaco, R. (1985). Survey of chaos in the rf-biased Josephson junction. *J. Appl. Phys.* 57: 875–889.

15 Barone, A. and Paterno, G. (eds.) (1982). *Physics and Applications of the Josephson Effect*. New York: Wiley.

16 Likharev, K.K. (1986). *Dynamics of Josephson Junctions and Circuits*. New York: Gordon and Breach Science.

17 Kautz, R.L. (1996). Noise, chaos, and the Josephson voltage standard. *Rep. Prog. Phys.* 59: 935–992.

18 Kadin, A.M. (1999). *Introduction to Superconducting Circuits*. New York: Wiley.

19 Clarke, J. (1968). Experimental comparison of the Josephson voltage-frequency relation in different superconductors. *Phys. Rev. Lett.* 21: 1566–1569.

20 Tsai, J.-S., Jain, A.K., and Lukens, J.E. (1983). High-precision test of the universality of the Josephson voltage-frequency relation. *Phys. Rev. Lett.* 51: 316–319.

21 Jain, A.K., Lukens, J.E., and Tsai, J.-S. (1987). Test for relativistic gravitational effects on charged particles. *Phys. Rev. Lett.* 58: 1165–1168.

22 Behr, R., Kieler, O., Kohlmann, J. et al. (2012). Development and metrological applications of Josephson arrays at PTB. *Meas. Sci. Technol.* 23: 124002 (19 pp).

23 Harris, R.E. and Niemeyer, J. (2011). *100 Years of Superconductivity* (ed. H. Rogalla and P.H. Kes), 515–557. Boca Raton, FL: Taylor & Francis.

24 Jeanneret, B. and Benz, S.P. (2009). Applications of the Josephson effect in electrical metrology. *Eur. Phys. J. Spec. Top.* 172: 181–206.

25 Niemeyer, J., Hinken, J.H., and Kautz, R.L. (1984). Microwave-induced constant voltage steps at one volt from a series array of Josephson junctions. *Appl. Phys. Lett.* 45: 478–480.

26 Gurvitch, M., Washington, M.A., and Huggins, H.A. (1983). High quality refractory Josephson tunnel junctions utilizing thin aluminum layers. *Appl. Phys. Lett.* 42: 472–474.

27 Benz, S.P., Hamilton, C.A., Burroughs, C.J. et al. (1997). Stable 1 volt programmable voltage standard. *Appl. Phys. Lett.* 71: 1866–1868.

28 Mueller, F., Behr, R., Weimann, T. et al. (2009). 1 V and 10 V SNS programmable voltage standards for 70 GHz. *IEEE Trans. Appl. Supercond.* 19: 981–986.

29 Yamamori, H., Ishizaki, M., Shoji, A. et al. (2006). 10 V programmable Josephson voltage standard circuits using NbN/TiNx/NbN/TiNx/NbN double-junction stacks. *Appl. Phys. Lett.* 88: 042503 (3 pp).

30 Levinsen, M.T., Chiao, R.Y., Feldman, M.J., and Tucker, B.A. (1977). An inverse AC Josephson effect voltage standard. *Appl. Phys. Lett.* 31: 776–778.

31 Dresselhaus, P.D., Elsbury, M., Olaya, D. et al. (2011). 10 V programmable Josephson voltage standard circuits using NbSi-barrier junctions. *IEEE Trans. Appl. Supercond.* 21: 693–696.

32 Müller, F., Behr, R., Palafox, L. et al. (2007). Improved 10 V SINIS series arrays for applications in AC voltage metrology. *IEEE Trans. Appl. Supercond.* 17: 649–652.

33 Yamamori, H., Yamada, T., Sasaki, H., and Shoji, A. (2008). 10 V programmable Josephson voltage standard circuit with a maximum output voltage of 20 V. *Supercond. Sci. Technol.* 21: 105007 (6 pp).

34 Müller, F., Scheller, T., Wendisch, R. et al. (2013). NbSi barrier junctions tuned for metrological applications up to 70 GHz: 20 V arrays for programmable Josephson voltage standards. *IEEE Trans. Appl. Supercond.* 23: 1101005 (5 pp).

35 Kautz, R.L. (1995). Shapiro steps in large-area metallic-barrier Josephson junctions. *J. Appl. Phys.* 78: 5811–5819.

36 Benz, S.P. and Hamilton, C.A. (1996). A pulse-driven programmable Josephson voltage standard. *Appl. Phys. Lett.* 68: 3171–3173.

37 Monaco, R. (1990). Enhanced AC Josephson effect. *J. Appl. Phys.* 68: 679–687.

38 Williams, J.M., Janssen, T.J.B.M., Palafox, L. et al. (2004). The simulation and measurement of the response of Josephson junctions to opto-electronically generated short pulses. *Supercond. Sci. Technol.* 17: 815–818.

39 Benz, S.P., Dresselhaus, P.D., Rüfenacht, A. et al. (2009). Progress toward a 1 V pulse-driven AC Josephson voltage standard. *IEEE Trans. Instrum. Meas.* 58: 838–843.

40 Benz, S.P., Dresselhaus, P.D., Burroughs, C.J., and Bergren, N.F. (2007). Precision measurements using a 300 mV Josephson arbitrary waveform synthesizer. *IEEE Trans. Appl. Supercond.* 17: 864–869.

41 Kieler, O.F., Behr, R., Schleussner, D. et al. (2013). Precision comparison of sine waveforms with pulse-driven Josephson arrays. *IEEE Trans. Appl. Supercond.* 23: 1301404 (4 pp).

42 Kieler, O.F., Behr, R., Wendisch, R. et al. (2015). Towards a 1 V Josephson arbitrary waveform synthesizer. *IEEE Trans. Appl. Supercond.* 25: 1400305 (5 pp).

43 Benz, S.P., Waltman, S.B., Fox, A.E. et al. (2015). One-volt Josephson arbitrary waveform synthesizer. *IEEE Trans. Appl. Supercond.* 25. 1300108 (8 pp).

44 Benz, S.P., Waltman, S.B., Fox, A.E. et al. (2015). Performance improvements for the NIST 1 V Josephson arbitrary waveform synthesizer. *IEEE Trans. Appl. Supercond.* 25: 1400105 (5 pp).

45 Flowers-Jacobs, N.E., Fox, A.E., Dresselhaus, P.D. et al. (2016). Two-volt Josephson arbitrary waveform synthesizer using Wilkinson dividers. *IEEE Trans. Appl. Supercond.* 26: 1400207 (7 pp).

46 Flowers-Jacobs, N.E., Waltman, S.B., Fox, A.E. et al. (2016). Josephson arbitrary waveform synthesizer with two layers of Wilkinson dividers and an FIR filter. *IEEE Trans. Appl. Supercond.* 26: 1400307 (7 pp).

47 Jeanneret, B., Rüfenacht, A., Overney, F. et al. (2011). High precision comparison between a programmable and a pulse-driven Josephson voltage standard. *Metrologia* 48: 311–316.

48 Behr, R., Kieler, O., Lee, J. et al. (2015). Direct comparison of a 1 V Josephson arbitrary waveform synthesizer and an AC quantum voltmeter. *Metrologia* 52: 528–537.

49 Wood, B.M. and Solve, S. (2009). A review of Josephson comparison results. *Metrologia* 46: R13–R20.

50 BIPM (2017). *Mise en pratique* for the definition of the ampere and other electric units in the SI. https://www.bipm.org/utils/en/pdf/si-mep/MeP-a-2018.pdf (accessed 27 June 2018).

51 Funck, T. and Sienknecht, V. (1991). Determination of the volt with the improved PTB voltage balance. *IEEE Trans. Instrum. Meas.* IM-40: 158–161.

52 Thompson, A.M. and Lampard, D.G. (1956). A new theorem in electrostatics and its application to calculable standards of capacitance. *Nature* 177: 888.

53 Flowers, J. (2004). The route to atomic and quantum standards. *Science* 306: 1324–1330.

54 Giacomo, P. (1988). News from the BIPM. *Metrologia* 25: 115–119 (see also Resolution 6 of the 18th Meeting of the CGPM (1987), BIPM http://www.bipm.org/en/CGPM/db/18/6/ (accessed 23 August 2018).

55 Quinn, T.J. (1989). News from the BIPM. *Metrologia* 26: 69–74.

56 CCEM and BIPM (2017). Guidelines for Implementation of the 'Revised SI'. https://www.bipm.org/utils/common/pdf/CC/CCEM/ccem_guidelines_revisedSI.pdf (accessed 27 June 2018).

57 Behr, R., Palafox, L., Ramm, G. et al. (2007). Direct comparison of Josephson waveforms using an AC quantum voltmeter. *IEEE Trans. Instrum. Meas.* 56: 235–238.

58 Rüfenacht, A., Burroughs, C.J., and Benz, S.P. (2008). Precision sampling measurements using AC programmable Josephson voltage standards. *Rev. Sci. Instrum.* 79: 044704 (9 pp).

59 Lee, J., Behr, R., Palafox, L. et al. (2013). An Ac quantum voltmeter based on a 10V programmable Josephson array. *Metrologia* 50: 612–622.

60 Rüfenacht, A., Burroughs, C.J., Dresselhaus, P.D., and Benz, S.P. (2013). Differential sampling measurement of a 7 V RMS sine wave with a programmable Josephson voltage standard. *IEEE Trans. Instrum. Meas.* 62: 1587–1593.

61 Schubert, M., Starkloff, M., Lee, J. et al. (2015). An AC Josephson voltage standard up to the kilohertz range tested in a calibration laboratory. *IEEE Trans. Instrum. Meas.* 64: 1620–1626.

62 Schubert, M., Starkloff, M., Peiselt, K. et al. (2016). A dry-cooled AC quantum voltmeter. *Supercond. Sci. Technol.* 29: 105014 (8pp).

63 Rüfenacht, A., Howe, L.A., Fox, A.E. et al. (2015). Cryocooled 10 V programmable Josephson voltage standard. *IEEE Trans. Instrum. Meas.* 64: 1477–1482.

64 Lee, J., Behr, R., Schumacher, B. et al. (2016). From AC quantum voltmeter to quantum calibrator. *Conference on Precision Electromagnetic Measurements Digest 2016*, Electronic ISBN: 978-1-4673-9134-4, https://doi.org/10.1109/CPEM.2016.7540470.

65 Waltrip, B.C., Gong, B., Nelson, T.L. et al. (2009). AC power standard using a programmable Josephson voltage standard. *IEEE Trans. Instrum. Meas.* 58: 1041–1048.

66 Ihlenfeld, W.G.K., Mohns, E., Behr, R. et al. (2005). Characterization of a high resolution analog-to-digital converter with a Josephson AC voltage source. *IEEE Trans. Instrum. Meas.* 54: 649–652.

67 Palafox, L., Ramm, G., Behr, R. et al. (2007). Primary AC power standard based on programmable Josephson junction arrays. *IEEE Trans. Instrum. Meas.* 56: 534–537.

68 Behr, R., Williams, J.M., Patel, P. et al. (2005). Synthesis of precision waveforms using a SINIS Josephson junction array. *IEEE Trans. Instrum. Meas.* 54: 612–615.

69 Lee, J., Schurr, J., Nissilä, J. et al. (2010). The Josephson two-terminal-pair impedance bridge. *Metrologia* 47: 453–459.

70 Hellistö, P., Nissilä, J., Ojasalo, K. et al. (2003). AC voltage standard based on a programmable SIS array. *IEEE Trans. Instrum. Meas.* 52: 533–537.

71 Hagen, T., Palafox, L., and Behr, R. (2017). A Josephson impedance bridge based on programmable Josephson voltage standards. *IEEE Trans. Instrum. Meas.* 66: 1539–1545.

72 Overney, F., Flowers-Jacobs, N.E., Jeanneret, B. et al. (2016). Josephson-based full digital bridge for high-accuracy impedance comparisons. *Metrologia* 53: 1045–1053.

73 Bauer, S., Behr, R., Hagen, T. et al. (2017). A novel two-terminal-pair pulse-driven Josephson impedance bridge linking a 10 nF capacitance standard to the quantized Hall resistance. *Metrologia* 54: 152–160.

74 Lipe, T.E., Kinard, J.R., Tang, Y.-H. et al. (2008). Thermal voltage converter calibrations using a quantum AC standard. *Metrologia* 45: 275–280.

75 Behr, R., Kieler, O., and Schumacher, B. (2017). A precision microvolt-synthesizer based on a pulse-driven Josephson voltage standard. *IEEE Trans. Instrum. Meas.* 66: 1358–1390.

76 Toonen, R.C. and Benz, S.P. (2009). Nonlinear behavior of electronic components characterized with precision multitones from a Josephson arbitrary waveform synthesizer. *IEEE Trans. Appl. Supercond.* 19: 715–718.

77 Kieler, O.F.O., Scheller, T., and Kohlmann, J. (2013). Cryocooler operation of a pulse-driven AC Josephson voltage standard at PTB. *World J. Condens. Matter Phys.* 3: 189–193.

78 Benz, S.P., Pollarolo, A., Qu, J. et al. (2011). An electronic measurement of the Boltzmann constant. *Metrologia* 48: 142–153.

79 Qu, J., Benz, S.P., Pollarolo, A. et al. (2015). Improved electronic measurement of the Boltzmann constant by Johnson noise thermometry. *Metrologia* 52: S242–S256.

80 Qu, J., Benz, S.P., Coakley, K.A. et al. (2017). An improved electronic determination of the Boltzmann constant by Johnson noise thermometry. *Metrologia* 54: 549–558.

81 Flowers-Jacobs, N.E., Pollarolo, A., Coakley, K.J. et al. (2017). A Boltzmann constant determination based on Johnson noise thermometry. *Metrologia* 54: 730–737.

82 Jaklevic, R.C., Lambe, J., Silver, A.H., and Mercereau, J.E. (1964). Quantum interference effects in Josephson tunneling. *Phys. Rev. Lett.* 12: 159–160.

83 Gallop, J.C. (1991). *SQUIDs, The Josephson Effects and Superconducting Electronics*. Bristol: Adam Hilger.

84 Koelle, D., Kleiner, R., Ludwig, F. et al. (1999). High-transition-temperature superconducting quantum interference devices. *Rev. Mod. Phys.* 71: 631–686.

85 Clarke, J. and Braginski, A.I. (eds.) (2006). *The SQUID Handbook*, vol. 1 and 2. Berlin: Wiley-VCH.

86 Meissner, W. and Ochsenfeld, R. (1933). Ein neuer Effekt bei Eintritt der Supraleitfähigkeit. *Naturwissenschaften* 21: 787–788 (in German).

87 Harvey, K. (1972). A precise low temperature DC ratio transformer. *Rev. Sci. Instrum.* 43: 1626–1629.

88 Drung, D., Krause, C., Becker, U. et al. (2015). Ultrastable low-noise current amplifier: a novel device for measuring small electric currents with high accuracy. *Rev. Sci. Instrum.* 86: 024703 (10 pp).

89 Piquemal, F. (2010). *Handbook of Metrology*, vol. 1 (ed. M. Gläser and M. Kochsiek), 267–314. Weinheim: Wiley-VCH.

90 Drung, D., Götz, M., Pesel, E. et al. (2013). Aspects of application and calibration of a binary compensation unit for cryogenic current comparator setups. *IEEE Trans. Instrum. Meas.* 62: 2820–2827.

91 Koch, H. (2004). Recent advances in magnetocardiography. *J. Electrocardiol.* 37: 117–122.

92 Cohen, D. and Halgren, E. (2004). Magnetoencephalography. In: *Encyclopedia of Neuroscience*, 3rd edn (ed. G. Adelman and B.H. Smith), 1–7. New York: Elsevier.

93 Mohr, P.J., Newell, D.B., and Taylor, B.N. (2016). CODATA recommended values of the fundamental physical constants: 2014. *Rev. Mod. Phys.* 88: 035009 (73 pp).

94 Mohr, P.J., Taylor, B.N., and Newell, D.B. (2012). CODATA recommended values of the fundamental physical constants: 2010. *Rev. Mod. Phys.* 84: 1527–1605.

95 Weyand, K. (2001). Maintenance and dissemination of the magnetic field unit at PTB. *IEEE Trans. Instrum. Meas.* 50: 470–473.

96 Weyand, K. (1989). An NMR marginal oscillator for measuring magnetic fields below 50 mT. *IEEE Trans. Instrum. Meas.* 38: 410–414.

5

Quantum Hall Effect, the SI Ohm, and the SI Farad

The quantum Hall effect (QHE) occurs in two-dimensional electron systems subjected to a strong magnetic field. The QHE was first observed by K. von Klitzing et al. in 1980 when studying the magnetotransport properties of silicon metal-oxide-semiconductor field-effect transistors (MOSFETs) at low temperatures [1]. In 1985, K. von Klitzing was awarded a Noble Prize in physics for his discovery. It was early on realized that the QHE could have a tremendous impact on metrology since it provides quantized values of electric resistance. These values only depend on an integer, the elementary charge e, and the Planck constant h, which are defining constants of the present SI. Already in the previous SI, the QHE provided the foundation of resistance and impedance metrology, and it does so even more in the present SI. Its main application is the DC quantum Hall resistance standard used by national metrology institutes to realize and disseminate the SI ohm. In recent years, the QHE has also been harnessed for AC resistance measurements, that is, for impedance metrology, and the SI unit of capacitance, the farad, can be directly based on the QHE [2, 3].

From a physics point of view, the QHE relates to the fact that in a two-dimensional electron gas in high magnetic fields, noninteracting electrons lose all degrees of freedom of their motion. Their energy spectrum is then discrete, similar to the energy spectrum of atoms. In this chapter, we focus the discussion of the QHE on this aspect since it provides an understanding of the basic physics, even though it does not provide a complete description of the QHE. For a more detailed discussion, the reader is referred to, for example, Refs. [4–6].

Metrological applications of the QHE have mostly been realized using two-dimensional electron gases in GaAs/AlGaAs semiconductor structures. Therefore, we mainly consider these semiconductor structures in Sections 5.1–5.4. First, we repeat some basics of semiconductor physics, which are necessary to understand the basics of the QHE. We then introduce the GaAs/AlGaAs semiconductor structures, in which the QHE is observed, in more detail. Next, we discuss the QHE itself and elaborate on its impact on metrology, again focusing on GaAs/AlGaAs semiconductor structures. In Section 5.5, a new material, namely graphene, is introduced, and the QHE in graphene and its potential for metrology are discussed.

The New International System of Units (SI): Quantum Metrology and Quantum Standards,
First Edition. Ernst O. Göbel and Uwe Siegner.
© 2019 Wiley-VCH Verlag GmbH & Co. KGaA. Published 2019 by Wiley-VCH Verlag GmbH & Co. KGaA.

5.1 Basic Physics of Three- and Two-Dimensional Semiconductors

We consider crystalline three-dimensional bulk semiconductors of macroscopic sizes on the scale of the de Broglie wavelength or crystalline two-dimensional layered semiconductor structures. For the latter, it is assumed that the in-plane dimensions of the layers are macroscopic on the scale of the de Broglie wavelength. Thus, we assume that size quantization only occurs in the direction normal to the layers. Except for this direction, the allowed values of the wave vector $\mathbf{k}$ are determined by the semiconductor crystal's size and, hence, are quasi continuous due to the macroscopic crystal size. The eigenenergies of the electrons (and holes) and their dispersion are represented by the band structure $E(\mathbf{k})$. The electrons and holes determine the transport and optical properties of the semiconductor crystal. More precisely, these properties are governed by the uppermost occupied band and the lowest unoccupied band, labeled valence band and conduction band, respectively. These bands are separated by the band gap with energy E_g. The dispersion of these bands close to their extrema can often be approximated by the free-electron relation but with the free-electron mass replaced by the effective mass m^*. The renormalization of the mass accounts for the influence of the crystal lattice in this approximation. In the following, we only consider "quasi free" electrons, which can be described by the effective mass approximation. Moreover, we assume that the band structure is isotropic. We start with three-dimensional semiconductors and then move on to two-dimensional ones. The effect of a magnetic field is discussed for both cases.

5.1.1 Three-Dimensional Semiconductors

The energy dispersion of quasi free electrons in a three-dimensional isotropic semiconductor is given by

$$E(\mathbf{k}) = \frac{\hbar^2|\mathbf{k}|^2}{2m^*} = \frac{\hbar^2}{2m^*}(k_x^2 + k_y^2 + k_z^2) \tag{5.1}$$

Equation (5.1) is simply the kinetic energy of a free particle with mass m^*. If in Hall measurements a magnetic field is applied along the z direction, $B = B_z$, the electrons will move along cyclotron orbits in the x–y plane provided that scattering is not too strong. This condition can be expressed by the inequality $\omega_C\tau \gg 1$, in which τ is the scattering time and

$$\omega_C = \frac{eB}{m^*} \tag{5.2}$$

the (angular) cyclotron frequency. The magnetic field changes the energy dispersion. In a quantum mechanical treatment, one obtains for a magnetic field aligned along the z direction

$$E(k_z) = \frac{\hbar^2 k_z^2}{2m^*} + \left(l_C + \frac{1}{2}\right)\hbar\omega_C \pm \frac{1}{2}g\mu_B B \tag{5.3}$$

In this equation, l_C is an integer ($l_C = 0, 1, 2, 3, \ldots$), g the g-factor of the electron, and $\mu_B = e\hbar/(2m_e)$ the Bohr magneton with m_e being the free-electron mass. The

interpretation of Eq. (5.3) is straightforward. The first term represents the kinetic energy of the "free" motion in the z direction. The second term is the energy corresponding to the cyclotron motion in the x–y plane. Quantum mechanically, this motion corresponds to a harmonic oscillator, where l_C is the respective quantum number. The different bands with quantum numbers $l_C = 0, 1, 2, 3, \ldots$ are called Landau levels after the Russian physicist Lev Landau. The third term is the Zeeman energy of the electron, which has spin components $s_z = \pm 1/2\hbar$ oriented parallel or antiparallel to the magnetic field $B = B_z$. Since the Zeeman energy, $g\mu_B B/2$, is much smaller than the separation of the Landau levels, $\hbar\omega_C$, we shall neglect it for the rest of this discussion.

An important quantity for understanding the QHE is the density of states $D(E)$. It specifies the number of states available to electrons within an energy interval from E to $E + \mathrm{d}E$ (per volume in real space). Here, $\mathrm{d}E$ is an infinitesimal increase in energy. For the occupation of these states, the Pauli principle must be considered. From Eq. (5.1), one obtains for quasi free electrons in a three-dimensional semiconductor at zero magnetic field

$$D^{3D}(E) = \frac{1}{2\pi^2}\left(\frac{2m^*}{\hbar^2}\right)^{3/2} E^{1/2} \tag{5.4}$$

The square-root energy dependence of $D^{3D}(E)$ is illustrated in Figure 5.1.

In a magnetic field, the density of states is given by [8]

$$D^{1D}(E) = \frac{\hbar\omega_C}{(2\pi)^2}\left(\frac{2m^*}{\hbar^2}\right)^{3/2} \sum_{l_C} \left(E - \left(l_C + \frac{1}{2}\right)\hbar\omega_C\right)^{-1/2} \tag{5.5}$$

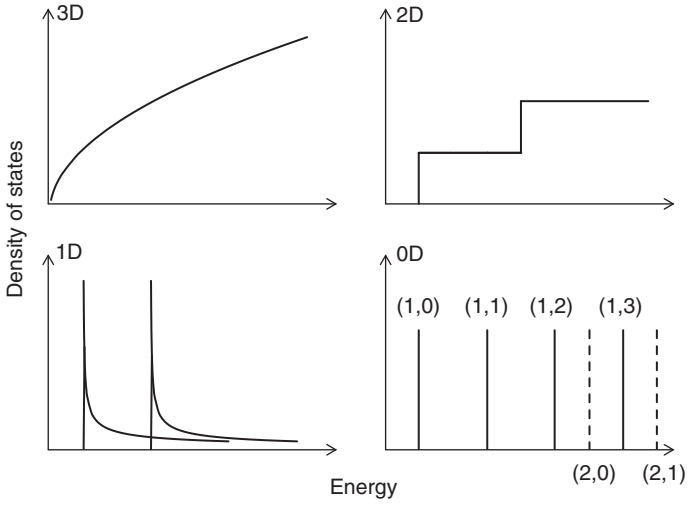

Figure 5.1 Schematic illustration of the density of states of three-, two-, one-, and zero-dimensional semiconductors. The one- and zero-dimensional systems are obtained by applying a magnetic field to three- and two-dimensional semiconductors, respectively, and show Landau levels. Only the two lowest subbands are sketched for the two- and one-dimensional case. The discrete Landau levels of the zero-dimensional semiconductor are labeled by the quantum numbers (l_z, l_C). Source: Göbel and Siegner 2015 [7]. Reproduced with permission of John Wiley and Sons.

As noted by the superscript, this is the density of states of a one-dimensional semiconductor with its characteristic one-over-square-root energy dependence. $D^{1D}(E)$ is also shown in Figure 5.1 together with $D^{3D}(E)$ and the densities of states of zero- and two-dimensional semiconductors, which are discussed in Section 5.1.2. According to Eq. (5.5), $D^{1D}(E)$ has a singularity at the bottom of each Landau level. However, in real systems, this singularity is removed, for example, due to level broadening that results from scattering. Notwithstanding that this feature is not included in Eq. (5.5), the equation shows that $D^{1D}(E)$ increases with increasing magnetic field due to the factor $\hbar\omega_C$.

Concluding this section, we emphasize that a magnetic field transforms a three-dimensional semiconductor into a one-dimensional one. If the magnetic field is applied in the z direction, the motion of quasi free electrons is quantized with regard to the wave vector components k_x and k_y and free only with regard to k_z. The energy dispersion splits up into Landau levels. The number of electrons, which can occupy a Landau level, increases with the increasing magnetic field strength.

5.1.2 Two-Dimensional Semiconductors

Confinement of the motion of quasi free electrons in one or more dimensions modifies their wave function, dispersion, and density of states. As discussed in Section 5.1.1, confinement can be caused by a magnetic field. Confinement can also be achieved geometrically by the generation of appropriate small structures. The length scale for the occurrence of so-called size quantization (see below) is given by the de Broglie wavelength of the electron. Confinement in one dimension creates a two-dimensional semiconductor. Let us assume that the confinement is due to a rectangular potential well in the z direction with an infinite barrier height. In this simple case, the energy dispersion of the electrons is given by

$$E(k_x, k_y) = E_{QW}(l_z) + \frac{\hbar^2}{2m^*}(k_x^2 + k_y^2) \tag{5.6}$$

with the quantization energy

$$E_{QW}(l_z) = \frac{\hbar^2}{2m^*}\frac{\pi^2 l_z^2}{L_z^2} \tag{5.7}$$

where L_z is the width of this so-called quantum well and l_z the quantum number ($l_z = 1, 2, \ldots, \infty$). Thus, quantized energy levels are obtained resulting from the confinement in the z direction. The quantization energy increases with the square of the quantum number l_z and with the decreasing quantum well width according to $1/L_z^2$.

The confinement changes the density of states from a square-root to a staircase function:

$$D^{2D}(E) = \frac{m^*}{\pi\hbar^2}\sum_{l_z}\Theta(E - E_{QW}(l_z)), \tag{5.8}$$

where $\Theta(E)$ is the Heaviside function ($\Theta(E < 0) = 0$ and $\Theta(E \geq 0) = 1$). The density of states for the two-dimensional case is also shown in Figure 5.1. The figure illustrates that $D^{2D}(E)$ is finite at the band edge where $D^{3D}(E)$ is zero. This difference

has important consequences for many device applications, in particular, for optoelectronic devices [9]. Confinement of electrons by real potential wells with a finite barrier height does not affect the principal features of size quantization described earlier. Yet, it modifies some important aspects. For a finite barrier height, the quantization energy for a given quantum state with quantum number l_z is lower and the number of bound quantum states is finite.

To move on to a semiconductor system that can show the QHE, we combine the confinement by a potential well with the effect of a magnetic field, which is discussed in Section 5.1.1. Again, it is assumed that the potential well confines the electron motion in the z direction and that the field is applied along the z axis, $B = B_z$. Thus, the field is applied normal to the semiconductor layers used to form a quantum well as will be discussed in more detail in Section 5.2. Combining the previous results, it becomes immediately obvious that this arrangement creates a zero-dimensional semiconductor system, in which the electron motion is confined in all three dimensions. The energy of the electrons is then given by the sum of the quantization energy $E_{\mathrm{QW}}(l_z)$ and the energy corresponding to the cyclotron motion in the x–y plane. From Eqs (5.3) and (5.7), we obtain (again neglecting the Zeeman term)

$$E(l_z, l_\mathrm{C}) = \frac{\hbar^2}{2m^*}\frac{\pi^2 l_z^2}{L_z^2} + \left(l_\mathrm{C} + \frac{1}{2}\right)\hbar\omega_\mathrm{C}. \tag{5.9}$$

The energy does not depend on the wave vector anymore; that is, there is no dispersion, since the electrons cannot move freely. The energy spectrum consists of a series of discrete energies characterized by the quantum numbers (l_z, l_C) similar to the spectrum of an atom. Consequently, the density of states, $D^{0\mathrm{D}}(E)$, shows energy gaps between adjacent Landau levels as illustrated in Figure 5.1. The quantization energy, $E_{\mathrm{QW}}(l_z)$, is usually larger than the cyclotron energy, which is accounted for in Figure 5.1. Therefore, it is often sufficient to consider only the Landau levels of the lowest quantum well state with $l_z = 1$. Henceforth, we will use this description. The number of states per Landau level (and per area), which can be occupied by electrons, is given by

$$D^{0\mathrm{D}} = \frac{e}{h}B \tag{5.10}$$

Thus, the density of states increases linearly with increasing magnetic field. Consequently, the higher Landau levels are gradually depleted as the magnetic field is increased at a constant electron density. At sufficiently high fields, all electrons will occupy the lowest Landau level with $l_\mathrm{C} = 0$. The possibility to control the occupation of the Landau levels with the magnetic field is essential for the description of the QHE as will be discussed in Section 5.3.2.

5.2 Two-Dimensional Electron Systems in Real Semiconductors

The QHE is observed in two-dimensional electron gases (2DEGs). Therefore, in this section, we discuss how a 2DEG can be realized in real semiconductors. The

section starts with an introduction to the properties of real semiconductors, such as GaAs and AlGaAs, and their heterojunctions and heterostructures. Epitaxial growth techniques are also treated briefly. The GaAs/AlGaAs semiconductor system is chosen as example because the majority of quantum Hall devices used as resistance standards in quantum metrology has been realized with this material system. The discussion shows how the concept of a two-dimensional semiconductor can be made a physical reality.

The QHE is an electron transport effect. Therefore, free conduction electrons with suitable transport properties must be inserted in a semiconductor heterostructure by an appropriate doping technique to observe the QHE. A special doping technique known as modulation doping produces electron gases with high mobility of the charge carriers as required for the QHE. Modulation doping is discussed at the end of the section.

5.2.1 Basic Properties of Semiconductor Heterostructures

Two-dimensional electron systems can be realized by the so-called semiconductor heterojunctions. These structures were first suggested by Kroemer [10]. *H. Kroemer* together with *Z.I. Alferov* received a part of the Noble Prize in physics in 2000 for the development of this technology. A heterojunction is the interface formed between two semiconductors with different band gap energy or between a semiconductor and a metal or insulator. A prominent example of a semiconductor/insulator heterojunction is the Si/SiO_2 interface in MOSFETs. A heterostructure is composed of one or more heterojunctions.

The most prominent example of a semiconductor/semiconductor heterojunction is the GaAs/AlGaAs interface. GaAs is a compound III–V semiconductor made of an element of the third (Ga) and fifth (As) group of the periodic table of elements. Other prominent III–V semiconductors are, for example, InP, InAs, AlAs, and GaSb. GaAs is a direct-gap semiconductor. The maximum of its uppermost valence band and the minimum of its lowest conduction band are located at the center of the Brillouin zone (Γ point). The band gap energy amounts to $E_g = 1.42$ eV at room temperature. In contrast, AlAs has an indirect band gap; that is, the maximum of the uppermost valence band and the minimum of the lowest conduction band are located at different points of the Brillouin zone. The valence band maximum is located at the Γ point, as in GaAs. The minimum of the conduction band is found close to the boundary of the Brillouin zone in (1,0,0) direction, that is, close to the X point. At room temperature, the energy of the indirect gap is $E_g = 2.16$ eV. Detailed information on the band structure and material parameters of GaAs and AlAs can be found, for example, in Ref. [11].

Besides the binary compounds GaAs and AlAs, a ternary mixed crystal AlGaAs can be grown. In the mixed crystal, the Ga and Al atoms are randomly distributed over the lattice sites of the group III elements. The fraction of the Ga and Al atoms of this ternary III–V compound semiconductor can be continuously varied. This property is reflected by the nomenclature $Al_xGa_{1-x}As$ with the aluminum mole fraction x varying between 0 and 1. As the aluminum mole fraction x is increased, the band gap energy varies between 1.42 eV (GaAs, $x = 0$) and 2.16 eV (AlAs, $x = 1$). For $x < 0.4$, $Al_xGa_{1-x}As$ has a direct band gap as in GaAs. For larger x, an

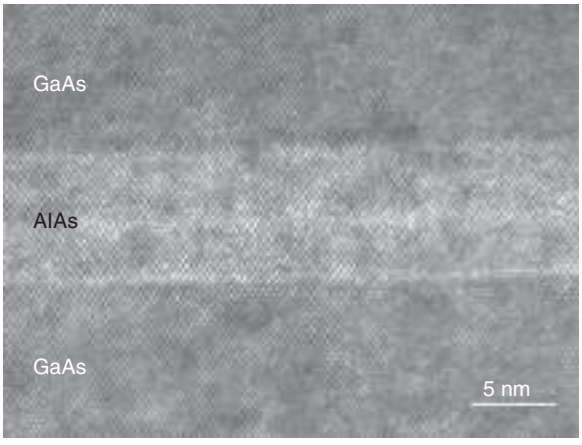

Figure 5.2 TEM image of a GaAs/AlAs/GaAs heterostructure. The individual dots represent single molecular units of GaAs (top, bottom) and AlAs (center). Source: Courtesy of PTB.

indirect band gap is obtained as in AlAs. The effective mass approximation with an isotropic effective mass m^*, as discussed in Section 5.1, is sufficient to describe electrons close the Γ point in GaAs and direct-gap $Al_xGa_{1-x}As$. Since the QHE is observed at low temperatures of a few kelvin and below, it is worth mentioning that the bandgap energies increase as the temperature is lowered, for example, to 1.52 eV in GaAs at 4 K. The principal features of the band structure do not change with temperature.

With respect to the growth of heterojunctions, semiconductor technology and, in turn, quantum metrology benefit from the fortunate circumstance that GaAs and $Al_xGa_{1-x}As$ exhibit almost the same lattice constant for all values of x. This feature allows the fabrication of GaAs/$Al_xGa_{1-x}As$ heterostructures with almost perfect single crystalline interfaces using epitaxial crystal growth techniques. The high quality of such interfaces is illustrated in Figure 5.2, which shows a transmission electron microscope (TEM) image of a GaAs/AlAs/GaAs heterostructure. The single crystalline structure is continued over the interfaces at which no crystal defects are observed.

5.2.2 Epitaxial Growth of Semiconductor Heterostructures

High-quality epitaxial crystal growth of GaAs/$Al_xGa_{1-x}As$ heterostructures is achieved using molecular beam epitaxy (MBE) [12] or metalorganic vapor-phase epitaxy (MOVPE), also known as metalorganic chemical vapor deposition (MOCVD) [13]. MBE is performed in an ultrahigh vacuum chamber with a base pressure below 10^{-10} Pa. This low pressure reflects the ultralow impurity concentration in the growth chamber. A sketch of an MBE growth chamber is shown in Figure 5.3. Attached to the chamber are effusion cells, which contain high-purity Ga, Al, and As in the solid state. The effusion cells are heated to temperatures on the order of 1000 °C so that the source materials evaporate. The gaseous source materials are released to the vacuum chamber if shutters in front of the effusion cells are opened. In the chamber, the source materials condense on the substrate, where they react with each other. The substrate is often rotated to achieve spatially uniform crystal growth over a large area. The

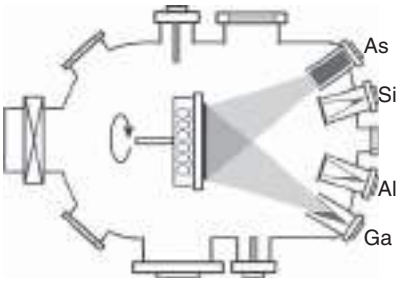

Figure 5.3 Schematic representation of an MBE chamber for the epitaxial growth of GaAs/$Al_xGa_{1-x}As$ heterostructures. The vacuum pumps needed to achieve a base pressure below 10^{-10} Pa are not shown. Source: Courtesy of K. Pierz, PTB.

reaction between Ga, Al, and As is controlled by the substrate's temperature and the flow rate of the source materials, which can be adjusted by the temperature of the effusion cells. For example, a substrate temperature above 600 °C is required for the growth of a GaAs crystal with perfect stoichiometry. The growth rate is low, typically 1 μm/h, which corresponds to the growth of one monolayer of GaAs (thickness 0.28 nm) per second. Thanks to the low growth rate, the thickness of the epitaxial layers can be precisely controlled with a resolution of a single atomic layer. The growth of the layers can be monitored *in situ* using reflection high-energy electron diffraction (RHEED). The Si effusion cell shown in Figure 5.3 can be used to add dopants to the GaAs or $Al_xGa_{1-x}As$ layers in a controlled way. The ultrahigh vacuum of the growth chamber and the high purity of the source materials ensure that the concentration of unwanted impurities is very low in MBE-grown GaAs/$Al_xGa_{1-x}As$ heterostructures.

In MOVPE, the metallic source materials, Ga and Al, are provided in the form of metalorganic compounds, such as trimethylgallium. The group-V elements are supplied as hydrides, such as arsine (AsH_3). As an alternative, less toxic group-V precursors were also developed and applied, for example, tertiarybutylarsine for the growth of As compounds [14]. Using a carrier gas (e.g. hydrogen), the metalorganic compounds are transported to the MOVPE reaction chamber. In the chamber, they chemically react with the group-V precursor at the surface of the substrate, on which the GaAs/$Al_xGa_{1-x}As$ heterostructure grows epitaxially. In contrast to MBE, MOVPE does not require ultrahigh vacuum, but is carried out at pressures on the order of 10^4 Pa.

5.2.3 Semiconductor Quantum Wells

Using MBE or MOVPE, a thin layer of GaAs can be sandwiched between two layers of $Al_x\ Ga_{1-x}$ As. Figure 5.4a depicts the band gap energy of this quantum well heterostructure versus the growth direction z, that is, the direction normal to the layers. The aluminum mole fraction is assumed to be $x = 0.3$, which results in $E_g = 1.8$ eV for $Al_xGa_{1-x}As$ at room temperature. As mentioned earlier, the band gap energy of GaAs is $E_g = 1.42$ eV at room temperature.

Most important for the electronic properties of the heterostructure is the band alignment, which is shown in Figure 5.4b at the Γ point of the Brillouin zone. The conduction band of GaAs is located below the $Al_xGa_{1-x}As$ conduction band, while the opposite order is found for the valence bands. This is referred to as

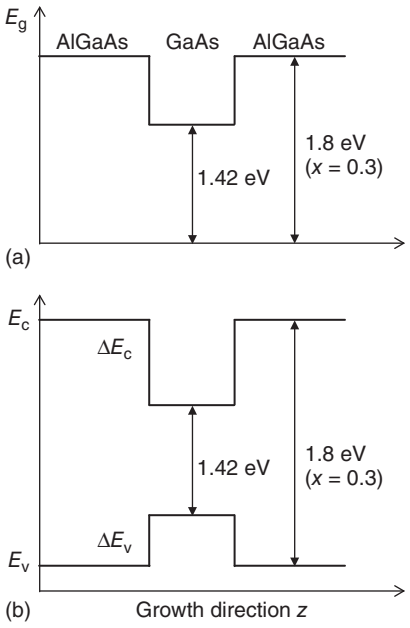

Figure 5.4 Spatial variation of the band gap energy E_g of an $Al_xGa_{1-x}As/GaAs/Al_xGa_{1-x}As$ ($x = 0.3$) quantum well heterostructure (a) and spatial variation of the conduction band and valence band (b) versus the growth direction z. The values of E_g refer to room temperature. An exchange of charge carriers between the layers, which would result in space charge regions and band bending, is not considered in the figure. Source: Göbel and Siegner 2015 [7]. Reproduced with permission of John Wiley and Sons.

type I or straddling type band alignment and results in the formation of potential wells in the conduction and valence band. The potential wells ideally have a rectangular shape corresponding to atomically smooth interfaces between GaAs and $Al_xGa_{1-x}As$, as seen in the TEM image of Figure 5.2. The depth of the wells is given by the band edge discontinuities of the conduction band, ΔE_C, and valence band, ΔE_V. At the Γ point, their sum must equal the difference between the band gap energies of GaAs and $Al_xGa_{1-x}As$, that is, $\Delta E_g = \Delta E_C + \Delta E_V$ must hold. How the band gap difference is split between the conduction and valence band depends on the detailed electronic structure of the interface. For the GaAs/AlGaAs system, we roughly have $\Delta E_C/\Delta E_V = 3/2$.

Summarizing this discussion, we note that for sufficiently thin GaAs layers (typically $L_z < 100$ nm), a rectangular quantum well with a finite barrier height is formed in both the conduction and valence band, that is, for electrons and holes. Thus, a two-dimensional semiconductor is realized, in which a two-dimensional electron gas can be introduced.

5.2.4 Modulation Doping

The tremendous technological success of semiconductors rests, to a large extent, on the fact that the concentration of mobile carriers can be varied by orders of magnitude by doping. Doping refers to the replacement of atoms of the host lattice by atoms with more (donors) or less electrons (acceptors). Doping is required to perform electron transport studies in wide-gap semiconductors at low temperatures T since for $kT \ll E_g$, the density of intrinsic conduction electrons is negligibly small. Under this condition, donors provide the required extra mobile electrons, for example, when studying the QHE. Yet, after the electrons

have been transferred from the donors to the conduction band, the positively charged donors act as scattering centers. At low temperatures, scattering at ionized donors is the limiting factor of the electron mobility $\mu = e\tau/m^*$ (τ scattering time), which is one of the key parameters for technological applications of semiconductors and also for the QHE. Scattering can be strongly reduced by modulation doping [15]. In modulation-doped structures, the donors are spatially separated from the mobile electrons, and, thus, scattering at ionized donors is greatly reduced. Electron mobilities exceeding $10^7\,\mathrm{cm^2\ V^{-1}\ s^{-1}}$ have been achieved at low temperatures [16]. This value is extremely high compared to, for example, the room temperature electron mobility of $8000\,\mathrm{cm^2\ V^{-1}\ s^{-1}}$ in GaAs.

The concept of modulation doping can be applied to a quantum well heterostructure by introducing Si donors in a thin layer in one of the AlGaAs barriers. The doped layer must be separated from the GaAs well by an undoped AlGaAs spacer layer. At elevated temperatures, the donors are thermally excited and their extra electrons are captured in the GaAs well. Thus, a 2DEG with high electron mobility forms in the quantum well. At low temperatures, the mobile electrons remain in the quantum well and provide a suitable arena for studies on the QHE. This consideration shows another advantage of modulation doping, besides the largely increased electron mobility. In modulation-doped heterostructures, the mobile electrons do not freeze out at low temperatures, in contrast to homogeneously doped semiconductors. Modulation doping has found wide applications in high-frequency field-effect transistors called MOSFETs or high-electron-mobility transistors (HEMTs).

A 2DEG can also form at a single heterojunction if band bending is considered. We examine the modulation-doped structure of Figure 5.5. From bottom

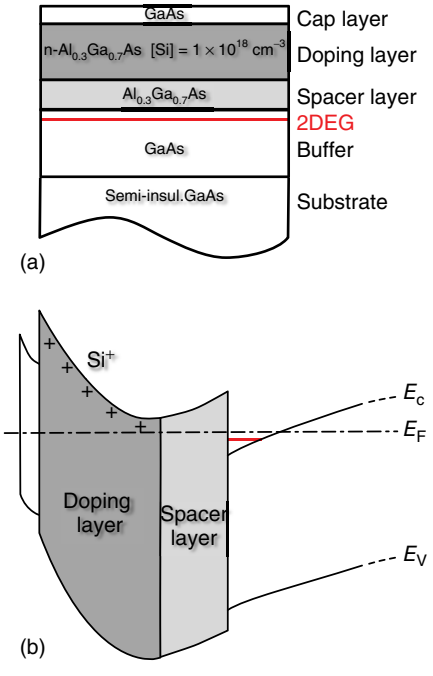

Figure 5.5 Modulation-doped $Al_{0.3}Ga_{0.7}As/GaAs$ heterostructure. (a) Layer sequence showing the GaAs substrate and buffer layer, the undoped $Al_{0.3}Ga_{0.7}As$ spacer (thickness on the order of 10 nm), the $Al_{0.3}Ga_{0.7}As$[Si] doping layer (typical thickness 50 nm, doped with Si donors at a typical concentration of $10^{18}\,\mathrm{cm^{-3}}$), and the typically 10-nm-thick GaAs cap layer. (b) Schematic band profile. In the conduction band, a triangular potential well is formed at the interface of the GaAs and the $Al_{0.3}Ga_{0.7}As$ spacer layer. E_F is the Fermi level. Shown in red in the band profile is the lowest quantized energy state of the triangular potential well. It holds a 2DEG as shown (in red) in the layer sequence. Source: Courtesy of K. Pierz, PTB.

to top, the structure consists of a GaAs substrate and buffer layer, the undoped $Al_{0.3}Ga_{0.7}As$ spacer layer, and the $Al_{0.3}Ga_{0.7}As$[Si] doping layer. A thin GaAs cap layer is required to prevent oxidation of the AlGaAs in real structures. The lower part of the figure schematically shows the conduction and valence band profile together with the Fermi level, E_F, which separates unoccupied from occupied electronic states. The Fermi level is constant in thermodynamic equilibrium as shown in the figure. The donors are ionized, and the extra electrons of the donors have been transferred across the spacer layer to the GaAs, where they are attracted to the interface by the electric field of the ionized donors. The charge transfer is accompanied by band bending so that a triangular potential well is formed at the interface of the GaAs and the $Al_{0.3}Ga_{0.7}As$ spacer layer. The lowest quantized energy level of the potential well is located below the Fermi level. Therefore, the quantized energy level is populated with electrons. As a result, a 2DEG is formed at the interface of the GaAs and the $Al_{0.3}Ga_{0.7}As$ spacer layer. Heterostructures of the type shown in Figure 5.5 can be grown more easily than rectangular quantum wells by MBE or MOVPE. Therefore, they are used in most of today's quantum Hall resistors.

5.3 The Hall Effect

The understanding of the QHE requires a basic knowledge of the classical Hall effect. Therefore, we give a brief description of the latter before we consider the QHE.

5.3.1 The Classical Hall Effect

5.3.1.1 The Classical Hall Effect in Three Dimensions

The classical Hall effect was discovered by Edwin Herbert Hall in 1879. It refers to the generation of a voltage in a current-carrying wire placed in an external magnetic field. As shown in Figure 5.6, the voltage drop occurs perpendicularly to the directions of the electric current and the magnetic field.

The Hall effect is the consequence of the Lorentz force acting on moving charge carriers in a magnetic field. If only electrons contribute to the current, the Hall effect results in the accumulation of electrons at the top surface of the conductor of Figure 5.6. The charge accumulation gives rise to an electric field E_y in the y direction. Since the current is zero in the y direction, the Lorentz force must be

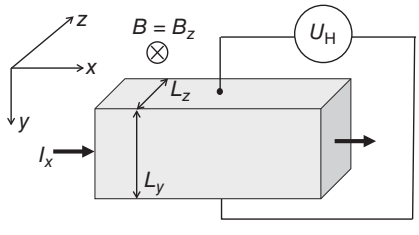

Figure 5.6 Experimental arrangement for the observation of the Hall effect in a three-dimensional conductor. Source: Göbel and Siegner 2015 [7]. Reproduced with permission of John Wiley and Sons.

balanced by the effect of the electric field E_y in the steady state. We obtain for the total force F_y in the y direction

$$F_y = (-e)E_y - (-e)\mathrm{v}_x B_z = 0 \tag{5.11}$$

where $(-e)$ is the charge of the electron and v_x the electron drift velocity. Thus, the Hall field is given by $E_y = \mathrm{v}_x B_z$ and the Hall voltage by $U_\mathrm{H} = E_y L_y = \mathrm{v}_x B_z L_y$. If the current is expressed as

$$I_x = j_x L_y L_z = (-e) n_\mathrm{3D} \mathrm{v}_x L_y L_z \tag{5.12}$$

where j_x is the current density and n_3D the electron density in a three-dimensional conductor, the Hall voltage can be written as

$$U_\mathrm{H} = -\frac{1}{e n_\mathrm{3D}} \frac{1}{L_z} I_x B_z = R_\mathrm{H} \frac{1}{L_z} I_x B_z \tag{5.13}$$

The Hall coefficient, defined as $R_\mathrm{H} = -1/(e n_\mathrm{3D})$, is a measure of the carrier density. In fact, the Hall effect is routinely used to determine the carrier density in metals and semiconductors. For the latter, a more general description can be worked out, which considers electron and hole currents. For the present discussion, the most important quantity is the Hall resistance R_{xy} defined as

$$R_{xy} = \frac{U_\mathrm{H}}{I_x} \tag{5.14}$$

The Hall resistance is to be distinguished from the longitudinal resistance $R_{xx} = U_x/I_x$, where U_x is the voltage drop in the direction of the current.

5.3.1.2 The Classical Hall Effect in Two Dimensions

The description of the Hall effect in three dimensions, as given in Section 5.3.1.1, can be extended to a two-dimensional electron gas in a straightforward way. We consider a 2DEG in the x–y plane normal to the magnetic field $B = B_z$. The dimension L_z is then meaningless and the three-dimensional electron density n_3D is to be replaced by a two-dimensional density n_2D (number of electrons per area). In two dimensions, the Hall voltage becomes

$$U_\mathrm{H} = -\frac{1}{e n_\mathrm{2D}} I_x B_z \tag{5.15}$$

The Hall resistance can be expressed as in Eq. (5.14), where U_H is taken from Eq. (5.15). The longitudinal resistance $R_{xx} = U_x/I_x$ is defined as in the three-dimensional case.

In the literature, often the resistivity ρ is considered rather than the resistance R since the resistivity characterizes the physical properties of a material or electronic system independent of its size. We note that in two-dimensional space, $R_{xx} = \rho_{xx} L_x/L_y$. Therefore, the longitudinal resistivity and resistance have the same physical dimension. Moreover, the Hall resistance and the Hall resistivity are equal and independent of the size of the two-dimensional conductor:

$$R_{xy} = \rho_{xy} = -\frac{1}{e n_\mathrm{2D}} B \tag{5.16}$$

The occurrence of components ρ_{xx} and ρ_{xy} shows that the resistivity $\boldsymbol{\rho}$ is a tensor, which is defined by the relation

$$\begin{pmatrix} E_x \\ E_y \end{pmatrix} = \begin{pmatrix} \rho_{xx} & \rho_{xy} \\ -\rho_{xy} & \rho_{xx} \end{pmatrix} \begin{pmatrix} j_x \\ j_y \end{pmatrix}. \tag{5.17}$$

The inverse of the resistivity tensor $\boldsymbol{\rho}$ is the conductivity tensor $\boldsymbol{\sigma}$, defined by

$$\begin{pmatrix} j_x \\ j_y \end{pmatrix} = \begin{pmatrix} \sigma_{xx} & \sigma_{xy} \\ -\sigma_{xy} & \sigma_{xx} \end{pmatrix} \begin{pmatrix} E_x \\ E_y \end{pmatrix}. \tag{5.18}$$

The components of $\boldsymbol{\rho}$ and $\boldsymbol{\sigma}$ are related. We explicitly state some of the relations here since they have implications in the QHE regime:

$$\rho_{xx} = \frac{\sigma_{xx}}{\sigma_{xx}^2 + \sigma_{xy}^2} \tag{5.19}$$

$$\sigma_{xx} = \frac{\rho_{xx}}{\rho_{xx}^2 + \rho_{xy}^2} \tag{5.20}$$

5.3.2 Physics of the Quantum Hall Effect

For the description of the QHE, we build on the results of Section 5.1, that is, we consider a semiconductor with parabolic bands as a model for the GaAs/AlGaAs heterostructures that are widely used in QHE metrology. The discussion will be restricted to the Landau levels of the lowest quantum well state and the Zeeman splitting will be neglected. In Section 5.1.2, we have seen that the number of electron states per Landau level (and per area) depends linearly on the magnetic field in two-dimensional semiconductors. Let us now consider a 2DEG with a given electron density n_{2D} at zero temperature. Thus, thermal excitations between different Landaus levels are suppressed. Changing the magnetic field, the density of states $D^{0D} = eB/h$ can be adjusted such that the Landau levels with $l_C = 0$, 1, …, $(i-1)$ are completely filled with electrons, while all other Landau levels (with $l_C > i-1$) are empty. The filling factor f defined as $f = n_{2D}/D^{0D}$ is then given by $f = i$, that is, by an integer. An equivalent statement is to say that the Fermi level is located in the energy gap between the Landau levels with $l_C = i-1$ and $l_C = i$. Moreover, the electron density is given by $n_{2D} = ieB/h$. If this expression is inserted in Eq. (5.16), we obtain for the absolute value of the Hall resistance

$$R_{xy}(i) = \frac{h}{e^2}\frac{1}{i} \tag{5.21}$$

For an integer filling factor, the Hall resistance only depends on fundamental constants and an integer.

Moreover, the longitudinal resistance R_{xx} vanishes, $R_{xx} = 0$, since in a completely filled Landau level scattering of electrons is suppressed due to the lack of empty final states. Consequently, the longitudinal resistivity is zero, $\rho_{xx} = 0$. Equations (5.19) and (5.20) imply that the longitudinal conductivity is also zero, $\sigma_{xx} = 0$. Thus, if the Fermi level is located in the energy gap between Landau levels, the current is driven by the Hall voltage.

The simple argument presented so far predicts the particular resistance values $R_{xx} = 0$ and $R_{xy}(i) = h/(ie^2)$ for singular values of the magnetic field, that is, if (and

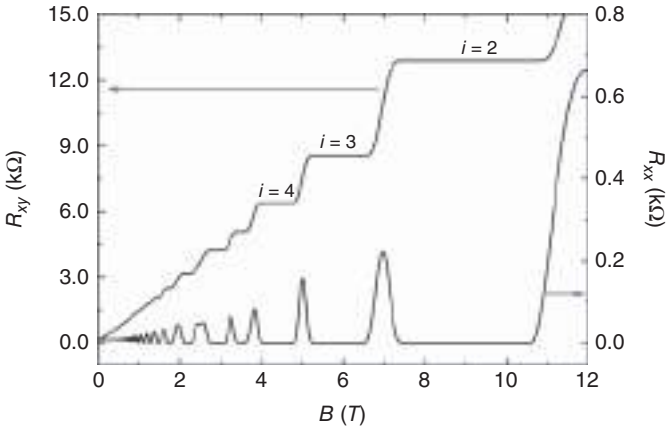

Figure 5.7 Experimentally determined Hall resistance R_{xy} (left scale) and longitudinal resistance R_{xx} (right scale) as a function of the magnetic flux density of a GaAs/AlGaAs heterostructure at a temperature $T = 0.1$ K (measurement current 1 μA). Some integer filling factors are indicated. Source: Courtesy of F. Ahlers, PTB.

only if) the field corresponds exactly to an integer filling factor. Surprisingly, however, one observes resistance values $R_{xx} = 0$ and $R_{xy}(i) = h/(ie^2)$ over extended field ranges around integer filling factors. This finding is illustrated by the experimental data of Figure 5.7, obtained from a GaAs/AlGaAs heterostructure at 0.1 K. The Hall resistance shows pronounced plateaus $R_{xy}(i) = h/(ie^2)$, and R_{xx} disappears over the corresponding field ranges. This experimental result is referred to as the QHE, discovered by K. v. Klitzing when studying 2DEGs in Si MOSFETs in 1980 [1]. The ratio h/e^2 is named the von Klitzing constant, $R_K = h/e^2$. Consequently, the quantized Hall resistance can be expressed as

$$R_{xy}(i) = \frac{R_K}{i} \tag{5.22}$$

To emphasize the close relation between the QHE and the paradigm of quantum metrology, that is, the counting of discrete quanta, the filling factor can be rewritten. We assume that A is the area of the sample and $\Phi = AB$ the magnetic flux through it and introduce the flux quantum $\Phi_0 = h/e$ (charge e since single electrons are considered rather than Cooper pairs with charge $2e$ as in Chapter 4). We can then write

$$f = \frac{n_{2D}}{D^{0D}} = \frac{An_{2D}}{AB\frac{e}{h}} = \frac{N_e}{\frac{\Phi}{\Phi_0}} = \frac{N_e}{N_\Phi} \tag{5.23}$$

with N_e and N_Φ being the number of electrons and flux quanta in the sample, respectively. Equation (5.23) shows that the filling factor can be interpreted as the ratio between the number of electrons and the number of flux quanta.

Considerable theoretical work has been spurred by the experimental result that the Hall resistance is quantized over an extended range of the magnetic field or the filling factor. Theory has been guided by the experimental observation that the width of the Hall resistance plateaus depends on the specific properties of the

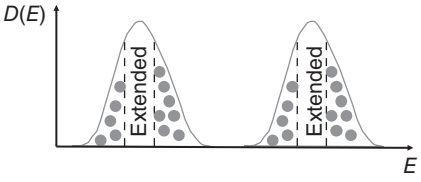

Figure 5.8 Schematic representation of the density of states of inhomogeneously broadened Landau bands. Dotted: localized states close to the lower and upper boundary of the bands. Source: Göbel and Siegner 2015 [7]. Reproduced with permission of John Wiley and Sons.

individual sample. More precisely, the width of the plateaus is found to shrink for 2DEGs with very high electron mobility (10^6 cm^2 V^{-1} s^{-1} and above). At low temperatures, when phonon scattering is strongly reduced, the electron mobility is a measure of disorder-induced scattering. Therefore, the experimental results indicate that disorder should be included in the description of the QHE.

Disorder arises from nonideal heterojunctions and from residual impurities and is an intrinsic property of ternary mixed crystals such as $Al_xGa_{1-x}As$. Thus, disorder is present in any real semiconductor mixed crystal heterostructure, where it gives rise to a spatially varying potential. Consequently, the Landau levels are inhomogeneously broadened and they are better described as Landau bands [17]. The electronic states are localized close to the upper and lower energy boundary of the inhomogeneously broadened Landau bands, as schematically shown in Figure 5.8. Electrons in these localized states are immobile and do not contribute to electronic transport. Only in the center of the Landau bands, extended states are found. Electrons in extended states can carry current in the usual way. As the magnetic field (or more generally the filling factor) is changed, the Fermi level moves through the Landau bands. Yet, as long as the Fermi level moves through localized states, the density of mobile electrons does not change. Since only the mobile electrons contribute to the current, the Hall resistance does not change either and a plateau is observed. Thus, a model involving disorder can qualitatively explain the basic feature of the QHE.

Despite the progress achieved including disorder in the theoretical description of the QHE, this approach cannot describe all aspects of the QHE. In fact, even today, there exists no complete theoretical description of the QHE in real samples. Such a theory should include the effects of finite sample size, finite temperature, and the contacts to the 2DEG.

The finite size of a real semiconductor 2DEG is considered in the edge channel model of the QHE developed by Büttiker [18], which we will briefly outline in the following text. A more detailed summary can be found, for example, in Ref. [19].

The edge channel model considers that the electron density of a 2DEG drops to zero and the Landau levels bend upward at the boundaries of a sample of finite size. Consequently, Landau levels, which are completely filled in the interior of the 2DEG, pierce the Fermi level at points close to the sample edges. At these points, these Landau levels are partially occupied. Therefore, one-dimensional conducting channels are generated close to the sample edges, one for each populated Landau level. The classical analog of these edge channels is the skipping orbits of electrons moving in a magnetic field along a boundary. Electronic

transport in edge channels can be described by the Landauer–Büttiker formalism for transport in one-dimensional conductors [20–22]. In this approach, the current is considered as the driving force and the resulting electric field distribution is calculated. The current is described by transmission and reflection coefficients and the chemical potential difference over one-dimensional conductors. If this approach is applied to a perfect one-dimensional conductor at zero magnetic field, in which no scattering occurs (i.e., ballistic transport), the inverse of the resistance (i.e. the conductance) is found to be quantized in units of e^2/h [23]. For the QHE, edge channels with opposite direction of the current must be considered, which are located at opposite edges of the 2DEG. The edge channel model of the QHE then shows that the Hall resistance is quantized, $R_{xy}(i) = h/(ie^2)$, if backscattering of electrons between edge channels of opposite direction is negligible.

The shortcoming of the edge channel model is that it assumes the current to flow only close to the boundaries of a QHE sample. This assumption contradicts experimental observations [6]. Therefore, more sophisticated models of the QHE have been developed [6, 24, 25], which, in particular, correctly describe the current distribution in the QHE regime. The details are, however, beyond the scope of this introductory text.

Still more theoretical work is needed to develop a complete description of all details of the QHE. Nonetheless, it is undisputed in theory that the QHE is a universal effect, which yields accurately quantized Hall resistance values in a variety of different materials. The universality of the QHE is strongly supported by topological arguments [26]. It has been shown that the quantized Hall conductance, and hence the quantized Hall resistance, is a topological invariant [26]. A topological phase transition and a change of the quantized Hall resistance can only occur if the number of occupied Landau levels is altered, giving rise to a robust and highly reproducible quantum effect. In 2016, David J. Thouless, F. Duncan M. Haldane, and J. Michael Kosterlitz received the Nobel Prize in physics for the theoretical discovery of topological phases of matter. With respect to the universality of the QHE, we also note that theory does not predict the QHE to depend on the gravitational field [27]. Corrections from quantum electrodynamics are predicted at the level of 1 part in 10^{20} only [28]. Experimental tests of the reproducibility and universality of the QHE are treated in Section 5.4, which addresses the impact of the QHE on metrology.

At the end of this section, we emphasize that we have discussed the integer QHE, which must be distinguished from the fractional quantum Hall effect (FQHE). The FQHE occurs in 2DEGs with electron mobilities well above $10^6\,\mathrm{cm^2\ V^{-1}\ s^{-1}}$ at very high magnetic fields above 10 T and temperatures in the mK range. Under these conditions, plateaus of the Hall resistance $R_{xy}(f) = h/(fe^2)$ are observed at fractional values of the filling factor f (such as 1/3, 2/3, 2/5, 3/7) [29]. The FQHE is the signature of a new quantum state generated by many-body interaction as first pointed out by Laughlin [30]. In 1998, D. C. Tsui, H. L. Störmer, and R. B. Laughlin received the Noble Prize in physics for the discovery of the FQHE.

5.4 Metrology Using the Quantum Hall Effect

The QHE has made a tremendous impact on resistance and impedance metrology notwithstanding that a complete theoretical description of the QHE in real semiconductor samples has not yet been presented. We review the impact of the QHE on measurements of DC resistance in Section 5.4.1. In the present SI, quantum Hall resistance standards are routinely used by national metrology institutes to realize and disseminate the SI ohm linked to the defining constants e and h. The QHE was used to set up a conventional ohm scale already in the previous SI. In Section 5.4.2, the now abrogated conventional ohm is treated, and the changes are highlighted that the present SI caused to resistance metrology upon its implementation in 2019. These changes are similar to those in voltage metrology, which are discussed in Section 4.1.5.2. The technology of the widely used GaAs-based DC quantum Hall resistors is reviewed in Section 5.4.3, which also addresses some aspects of resistance scaling.

In recent years, AC measurements have also benefitted from the QHE. It has been shown that reproducible quantized resistance values can be obtained if Hall voltages are measured on specially designed QHE resistors to which an AC current is applied [3]. The AC resistance can be directly compared to capacitance so that the QHE links capacitance to the defining constants e and h [2], thereby realizing the SI farad. Quantum Hall measurements in the AC regime and the SI farad are discussed in Section 5.4.4. Section 5.4 is concluded by a brief discussion of the relation between electrical metrology and the fine-structure constant.

5.4.1 DC Quantum Hall Resistance Standards, the SI Ohm

The QHE allows quantized DC resistance values to be realized, which depend only on the defining constants e and h and an integer. Its importance for metrology rests also on the fact that the QHE is highly reproducible and universal, that is, independent of the type of 2DEG or the particular sample properties. This property of the QHE provided an important argument to select the Planck constant h as a defining constant, as discussed in Section 7.1.

Quantized Hall resistances have been found to agree with each other within an uncertainty of a few parts in 10^{10} and better if the guidelines for QHE metrology are followed [31]. Observation of the guidelines ensures that the sample properties and experimental conditions are sufficiently close to the idealized case of the QHE treated in Section 5.3.2. The assumptions made for the idealized case include zero temperature, negligible influence of the contacts to the 2DEG, and negligible effects due to the finite measuring current. Following the guidelines [31], QHE measurements of GaAs/AlGaAs heterostructures were in agreement with measurements of Si MOSFETs within an uncertainty of 3.5 parts in 10^{10} [32]. More recently, QHE measurements of GaAs/AlGaAs heterostructures and graphene were found to agree within an uncertainty below 9 parts in 10^{11} [33–35]. This result is noteworthy since graphene is not a conventional semiconductor. Graphene consists of a monolayer of carbon atoms arranged on a hexagonal lattice, and its electronic properties and QHE are quite different

from those of GaAs/AlGaAs heterostructures or Si MOSFETs [36–40]. A more detailed description of graphene can be found in Section 5.5. The universality of the QHE was also corroborated comparing quantized Hall resistances at filling factors 2 (integer QHE) and 1/3 (fractional QHE) [41]. The expected resistance ratio of 6 was experimentally verified within an uncertainty of 6 parts in 10^8 [41]. The universality is further supported by experimental studies of the quantum anomalous Hall effect in ferromagnetically doped topological insulators at zero magnetic field [42]. These studies showed the quantized anomalous Hall resistance to agree with R_K within an uncertainty of 2.5 parts in 10^7 [42].

The excellent reproducibility of the QHE and the direct link to e and h make quantum Hall resistance standards [43] the prime choice for the realization of the SI ohm. The relative uncertainty of this SI ohm realization can be inferred from the reproducibility tests and, thus, can be better than 10^{-10}. To fully harmonize resistance metrology worldwide, the Consultative Committee for Electricity and Magnetism (CCEM) of the Meter Convention recommends the use of the following value of the von Klitzing constant, which has been calculated to 15 significant digits from the defining constants e and h introduced in Section 2.2 [44]:

$$R_K = 25\,812.807\,459\,3045\,\Omega \tag{5.24}$$

The choice of 15 significant digits allows one to quote accurate resistance values even if the uncertainty of resistance comparisons can be further reduced by some orders of magnitude below the present state of the art of parts in 10^{11}.

To highlight the impact of the QHE, we discuss an alternative method for the realization of the SI ohm, which is illustrated in Figure 5.9. This traceability route abstains from the use of the QHE. It is a valid method both in the previous SI and the present one [44]. The starting point is a calculable capacitor [45]. Such a capacitor allows an SI value of the capacitance C to be realized traceable to the meter and the SI value of the electric constant (permittivity of vacuum) ε_0 (the SI value of ε_0 is discussed in Section 5.4.5). From the SI farad, SI values of the capacitive reactance, $(\omega C)^{-1}$, can be derived. The AC resistance of artifact resistance standards is then linked to the capacitive reactance with a so-called quadrature bridge at kilohertz frequencies. The artifact resistance standards must have a calculable AC/DC difference [46, 47] so that their DC resistance can be derived to finally obtain a realization of the SI ohm. With this approach, the SI ohm can be realized with a relative uncertainty of a few parts in 10^8 [48, 49]. This uncertainty is more than two orders of magnitude greater than the uncertainty of the QHE-based realization. The maintenance and dissemination of the SI ohm are even more problematic if artifact standards are used instead of quantum Hall resistors. Artifact standards are sensitive to the environmental conditions, such as temperature and pressure. As a result, it is difficult to maintain a resistance scale with a temporal drift of less than 10^{-7} per year with artifact standards only [50].

5.4.2 The Conventional Ohm in the Previous SI

Decades before the present SI was implemented in 2019, it had already been realized that resistance metrology could be significantly harmonized using the highly

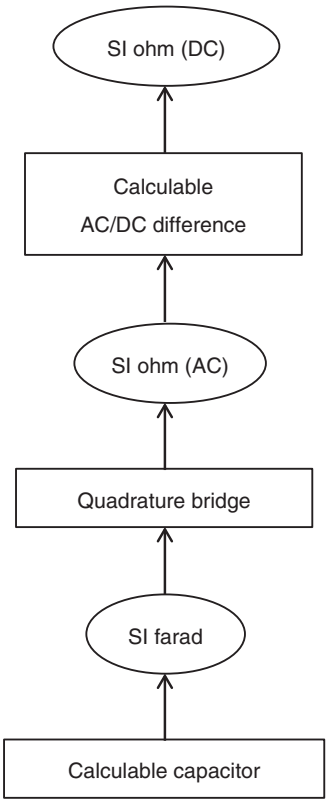

Figure 5.9 Realization of the SI ohm starting with a calculable capacitor without the QHE. Not shown in this schematic representation are the various measuring bridges required to upscale or downscale capacitances and resistances.

reproducible QHE. At the end of the 1980s, steps were taken to base resistance measurements on the use of the QHE and a fixed, agreed-upon value of the von Klitzing constant R_K. In 1987, the General Conference of the Meter Convention (CGPM) instructed the International Committee for Weights and Measures (CIPM) to recommend a value of the von Klitzing constant [51]. In 1988, the CIPM recommended a value that was determined using the best experimental data available at that time and should be used from 1 January 1990 [52]. This conventional value or agreed-upon value of R_K was denoted by $R_{K\text{-}90}$. $R_{K\text{-}90}$ was introduced together with the conventional value of the Josephson constant $K_{J\text{-}90}$ (see Section 4.1.5.2) and was given by

$$R_{K\text{-}90} = 25\,812.807\,\Omega \tag{5.25}$$

To ensure the compatibility of $R_{K\text{-}90}$ and the then valid SI value of R_K, $R_{K\text{-}90}$ was assigned a conventional relative uncertainty. The uncertainty was 2 parts in 10^7 at the time $R_{K\text{-}90}$ was introduced and reduced to 1 part in 10^7 later.

In close analogy to the Josephson case of Section 4.1.5.2, the relation

$$R_{90} = \frac{R_{K\text{-}90}}{i} \tag{5.26}$$

established a highly reproducible resistance scale R_{90}. In Eq. (5.26), $R_{K\text{-}90}$ could be treated as a constant with zero uncertainty since no comparison to SI quantities

was made. Equation (5.26) provided a representation of the unit ohm, namely, the conventional ohm or ohm_{90}, yet not a realization of the ohm according to the definition of the SI. The non-SI unit ohm_{90} was disseminated and used in electrical metrology from 1990 to the implementation of the present SI on 20 May 2019. This concept took advantage of the superior reproducibility of the QHE. Consequently, on-site resistance comparisons between the Bureau International des Poids et Mesures (BIPM) and national metrology institutes showed primary quantum Hall resistance standards to agree within an uncertainty of a few parts in 10^9 [53].

The conventional value of the von Klitzing constant $R_{\text{K-90}}$ has been abrogated in the present SI (as well as the conventional value of the Josephson constant $K_{\text{J-90}}$, see Section 4.1.5.2) [54]. The disseminated electrical units are now fully coherent with the SI. Since R_{K} of Eq. (5.24) and $R_{\text{K-90}}$ of Eq. (5.25) are slightly different, resistance-related quantities underwent a small discontinuous change when the present SI was implemented. The relative change was approximately 1.779×10^{-8} [54]. Reference [54] instructed users of electrical metrology how to deal with this change and ensured a seamless transition from the previous SI to the present one.

5.4.3 Technology of DC Quantum Hall Resistance Standards and Resistance Scaling

Nowadays, GaAs/AlGaAs heterostructures of the type shown in Figure 5.5 are mostly used as quantum Hall resistance standards. The heterostructures are patterned into Hall bars with typical widths of several hundred micrometers. Figure 5.10 shows a schematic representation of a Hall bar and Figure 5.11 a photograph of a quantum Hall resistance standard. The 2DEG of such a quantum Hall standard has a typical electron mobility $\mu = 5 \times 10^5\ \text{cm}^2\ \text{V}^{-1}\ \text{s}^{-1}$ and carrier density $n_{\text{2D}} = 5 \times 10^{11}\ \text{cm}^{-2}$ [53]. The latter corresponds to a magnetic field of 10 T for the observation of the plateaus with $i = 2$. Measurements are performed at temperatures around 1 K in liquid helium cryostats. The measuring current needs to be chosen smaller than the so-called critical current, at which the QHE breaks down. A detailed review of the breakdown of the QHE can be found, for example, in Ref. [55]. In GaAs quantum Hall resistors, the critical current density is typically 1 A/m [43], yielding a critical current of approximately 400 μA for a typical sample width of 400 μm. A measuring current of 40 μA is then a reasonable choice since it is ten times smaller than the critical current, but large enough to allow high-precision experiments to be performed.

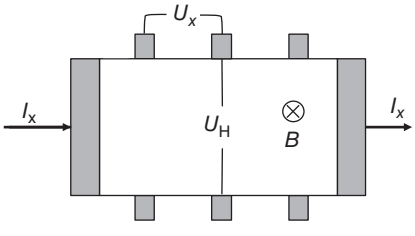

Figure 5.10 Schematic representation of a typical Hall bar with two current contacts and six voltage contacts (three on either side). Source: Göbel and Siegner 2015 [7]. Reproduced with permission of John Wiley and Sons.

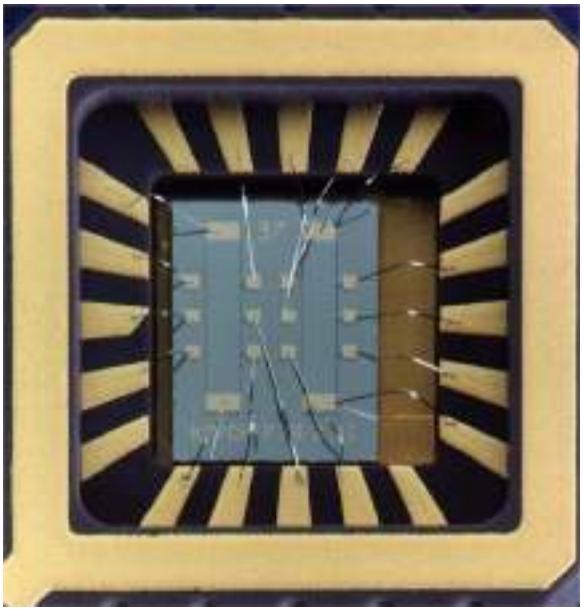

Figure 5.11 Photograph of a GaAs/AlGaAs quantum Hall resistance standard showing two Hall bars mounted in a chip carrier. Source: Courtesy of PTB.

For metrological purposes, the plateaus with $i = 2$ and 4 are mostly used. The use of odd filling factors is disadvantageous since, in real structures, the uppermost filled Landau level is then separated from the lowest empty Landau level only by the small Zeeman energy splitting. The $i = 2$ and 4 plateaus produce resistance values $R_K/2$ and $R_K/4$ of approximately 12.906 and 6.453 kΩ, respectively. Starting from these values, potentiometric methods and current comparator bridges are used to build up the resistance scale [43]. This scale extends from milliohms to teraohms and consists of decade resistance values. Among the different comparators, the cryogenic current comparator (CCC) [56] is the most accurate instrument. It allows resistance scaling to be performed with relative uncertainties of 10^{-9} and better (see Section 4.2.3.3). CCCs are used to compare quantum Hall resistance standards at liquid helium temperatures to secondary resistance standards with decade values, such as 100 Ω, at room temperature. This measurement is the first step in building up a practical decade resistance scale at room temperature.

The need for resistance values that cover a broad range raises the question whether QHE bars, such as the one shown in Figure 5.10, can be connected in series or in parallel. In principle, a series circuit of m QHE bars should realize accurate quantized resistance values mR_K/i. Similarly, a parallel circuit should realize small resistances $R_K/(mi)$.

Regarding this approach, one needs to recall that the quantized Hall resistance $R_{xy}(i) = R_K/i$ is the result of a four-terminal measurement (as is the longitudinal resistance $R_{xx} = 0$). As shown in Figure 5.10, two separate pairs of contacts are used for current and voltage measurements. Therefore, the resistances of contacts to the 2DEG do not contribute to the measurement result. In contrast, the contact resistances and the resistances of connecting wires affect the measurement

if QHE bars are connected in series or parallel circuits. To alleviate this problem, the so-called multiple connection technique was proposed. It reduces the contribution of contact resistances R_c to approximately $(R_c/R_{xy})^n$, where $n-1$ is the number of additional connections [57]. Since contact resistances have typical values below 1 Ω, their effect can be reduced to a negligible level using multiple connections.

In the earlier experimental work, series and parallel arrays of quantum Hall resistors were fabricated as integrated circuits with nominal resistance values from $R_K/200$ to 50 R_K [58, 59]. Agreement between nominal and measured values was demonstrated within an uncertainty of a few parts in 10^9 for some arrays [58]. Later, mathematical tools have been developed to design quantum Hall resistor arrays that well approximate decade resistance values using only a small number of Hall bars [60]. Reference [61] reports the experimental realization of a quantum Hall resistor array of 29 Hall bars with a nominal resistance value that deviates only by 34 μΩ from 1 kΩ. The measured value agrees with the nominal value within an uncertainty of 2 parts in 10^7 [61]. With only 16 Hall bars, a quantum Hall resistor array has been realized, whose nominal value deviates only by 340 μΩ from 10 kΩ [62]. Agreement between nominal and measured values has been demonstrated within an uncertainty of one part in 10^8 [62]. The experimental realization of a 1 MΩ quantum Hall resistor array of 88 Hall bars is reported in Ref. [63]. In Ref. [64], the relative deviation between the nominal value and the measured value of a 1 MΩ array is 2 parts in 10^8. To what extent quantum Hall resistor arrays will impact resistance metrology will be researched in the future.

5.4.4 AC Quantum Hall Resistance Standards, the SI Farad

The SI farad can be realized with a calculable capacitor [45], as discussed at the end of Section 5.4.1 and illustrated in the lower part of Figure 5.9. The uncertainty of this realization, however, is limited to a few parts in 10^8 [65]. To improve the realization of the SI farad, one may choose to directly link the farad to the defining constants e and h using the QHE, as shown in Figure 5.12. A possible traceability route starts from a DC quantum Hall resistance standard to realize the SI ohm; see the lower part of the figure. Subsequently, a DC calibration of an artifact resistance standard with calculable AC/DC difference [46, 47] is performed. The AC resistance of the artifact standard is derived from the known AC/DC difference. Finally, the SI farad can be derived from the known AC resistance using a quadrature bridge. Thus, AC resistance and capacitance measurements and, in turn, also inductance measurements can be linked to the defining constants e and h using the QHE. Thereby, the QHE is harnessed for impedance metrology in general.

So far, we have always assumed that a DC current is applied to a quantum Hall device. Alternatively, a quantum Hall device can be driven by an AC current. The corresponding physics is referred to as the AC QHE. The realization of the SI farad is substantially simplified if an AC quantum Hall resistance standard is available, as shown in Figure 5.12. The AC resistance of the QHE resistor is directly compared to a capacitance with a quadrature bridge, and the traceability routes no longer involve artifact resistance standards if the AC QHE is used.

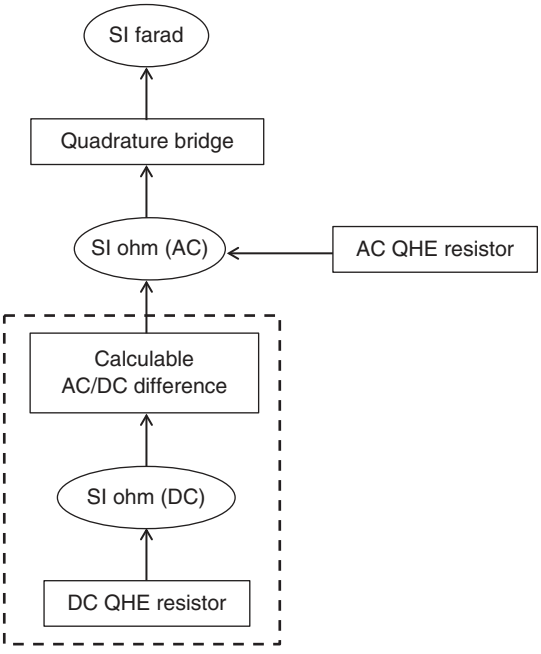

Figure 5.12 Realization of the SI farad starting from a DC quantum Hall resistance standard (dashed box) or from an AC quantum Hall resistance standard. Not shown in this schematic representation are the various measuring bridges required to upscale or downscale capacitances and resistances.

QHE measurements in the AC regime are to be performed at kilohertz frequencies to be compatible with impedance-measuring techniques. These AC QHE measurements have caused difficulties for many years. In general, the QHE plateaus were not as flat as in DC measurements and, in addition, exhibited an unwanted frequency and current dependence [66]. These findings were attributed to capacitive losses in the Hall bar and between the Hall bar and its surroundings [66, 67].

A special double-shielding technique was proposed to solve the problem of the capacitive loss currents [67]. The basic idea of this technique is to ensure that the current that reaches the current-low terminal of the QHE resistor is exactly equal to the current that generates the Hall voltage. If this condition is met, the Hall resistance is determined properly.

A doubly shielded QHE resistor is illustrated in Figure 5.13. The Hall bar is surrounded by two metallic shields separated by a narrow gap. The gap is aligned along the line of the Hall voltage measurement. The right-hand shield is connected to the current-low terminal. This connection ensures that the capacitive

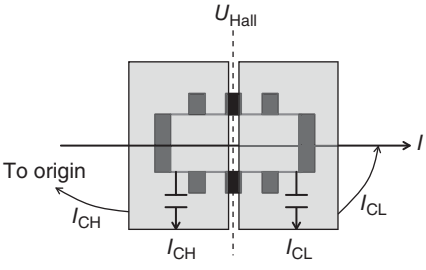

Figure 5.13 Schematic top view of a doubly shielded AC quantum Hall resistance standard. The shields (light gray) are shown as being transparent. The subscripts CL and CH stand for current-low terminal and current-high terminal, respectively. Source: Göbel and Siegner 2015 [7]. Reproduced with permission of John Wiley and Sons.

current I_{CL}, which has generated Hall voltage, reaches the current-low terminal. Next, we consider the capacitive current I_{CH}, which does not generate Hall voltage since it does not cross the Hall voltage line. This current is fed back to its origin by the left-hand shield and does not reach the current-low terminal, as required.

The double-shielding technique has made a breakthrough in AC QHE measurements. It ensures correct measurements of the Hall resistance, undistorted by AC losses. Flat QHE plateaus are observed using doubly shielded QHE resistors. The residual frequency dependence of the quantized AC Hall resistance is only 1.3 parts in $10^9\,\mathrm{kHz}^{-1}$ in the kilohertz frequency range [3]. Thus, the AC quantum Hall resistance standard is as reproducible and reliable as its DC counterpart. Ref. [2] has shown that the SI farad can be realized with an uncertainty of 6 parts in 10^9 using the AC QHE. The realization based on the AC QHE is at least as good as that based on calculable capacitors [65]. Thus, the AC QHE can substantially impact impedance metrology, very much as the DC QHE has impacted resistance metrology.

5.4.5 Relation Between Electrical Metrology and the Fine-Structure Constant

The von Klitzing constant $R_K = h/e^2$ can be expressed by the fine-structure constant α, which is the dimensionless scaling factor of the strength of the electromagnetic interaction:

$$R_K = \frac{h}{e^2} = \frac{\mu_0 c}{2\alpha}. \tag{5.27}$$

In this equation, μ_0 is the magnetic constant (permeability of vacuum) and c the speed of light in vacuum. The electric constant ε_0 (permittivity of vacuum) is related to μ_0 by the relation

$$\varepsilon_0 = 1/(\mu_0 c^2) \tag{5.28}$$

In the present SI, e, h, and c are defining constants with zero uncertainty. Therefore, a measurement of the fine-structure constant α determines the SI value of the magnetic constant μ_0 and, according to Eq. (5.28), also the SI value of the electric constant ε_0 with the same relative uncertainty as α. The fine-structure constant can be derived very precisely from atomic physics measurements, such as the measurement of the anomalous magnetic moment of the electron (see also Section 9.1.5). Thanks to atomic physics data, α is known with a relative uncertainty of only 2.3 parts in 10^{10} according to the adjustment of the fundamental constants in 2014 [68]. This uncertainty value was confirmed by the special fundamental constants adjustments performed in 2017 to determine the values of the defining constants h, e, k, and N_A [69].

The SI value of ε_0 can be used to realize the SI farad with a calculable capacitor [45], as mentioned in Sections 5.4.1 and 5.4.4. The reverse route is also possible. If the SI farad is derived from the defining constants e and h with the QHE according to Figure 5.12, a calculable capacitor can be used to determine ε_0, and, in turn,

μ_0 and α. This measurement, however, might not reach the very low uncertainty obtained from the atomic physics data.

We conclude this section with a historical note. In the previous SI, the definition of the ampere fixed the value of μ_0 to exactly $4\pi \times 10^{-7}\,\mathrm{H\,m^{-1}}$ according to Faraday's law (see Section 2.2). An experimental determination of the fine-structure constant then determined the von Klitzing constant and vice versa [1]. Since the speed of light in vacuum, c, already was an exact constant in the previous SI, the electric constant ε_0 also had an exact value with zero uncertainty. This SI value could be used to realize the farad with a calculable capacitor in the previous SI. At the day of the redefinition of the SI in 2019, μ_0 and ε_0 kept their values but acquired a relative uncertainty given by the relative uncertainty of the fine-structure constant α [69]. In the present SI, the values and the relative uncertainty of μ_0, ε_0, and α may slightly change in forthcoming adjustments of the fundamental constants. At any time, however, very precise SI values of μ_0, ε_0, and α can be obtained from the most up-to-date adjustment of the fundamental constants.

5.5 Graphene for Resistance Metrology

Quantum Hall resistance standards made from GaAs/AlGaAs heterostructures have a tremendous impact on electrical metrology in the present SI since they can be used to realize the SI ohm and the SI farad. However, their application is restricted to highly specialized users mostly working at national metrology institutes. The wider usage of these quantum Hall standards is impeded by the requirement to operate them at low temperatures and high magnetic fields. Typical values are approximately 1 K and 10 T, determined by the material properties of GaAs structures. This choice of values ensures that the energy splitting between adjacent Landau levels is sufficiently larger than the thermal energy kT (k Boltzmann constant), which is a prerequisite for precise resistance quantization.

In 2004, a new material became available to experimental physicists and engineers: graphene is a two-dimensional carbon crystal with exceptional properties [36–39]. In 2010, Andre K. Geim and Konstantin S. Novoselov were awarded the Nobel Prize in physics for the fabrication and their groundbreaking studies of graphene. The material properties of graphene offer the potential to use the QHE for metrology at elevated temperatures and lower magnetic fields and to facilitate the use of quantum Hall resistance standards. Moreover, important tests of the reproducibility and universality of the QHE can be performed with graphene, as briefly mentioned in Section 5.4.1. In this section, we give a short overview of the properties of graphene, its fabrication, and the QHE in graphene.

5.5.1 Basic Properties of Graphene

Graphene is the two-dimensional allotrope of carbon. It consists of one or a few layers of carbon atoms and can be considered as the building block of

three-dimensional graphite. Monolayer graphene is the most important type of graphene for metrology and we will restrict the discussion to monolayer graphene henceforth.

In a graphene layer, the carbon atoms occupy the sites of a hexagonal honeycomb lattice due to their sp^2 hybridization with strong in-plane σ bonds. The *p* orbitals, which are unaffected by hybridization, are oriented perpendicularly to the layer. Binding among these *p* orbitals results in the formation of a half-filled π band [70].

A tight-binding description of monolayer graphene yields the details of its band structure. The valence band and the conduction band intersect at six points in the Brillouin zone, the so-called Dirac points, which fall into two groups (*K* and *K'*) of three equivalent points [70, 71]. Thus, graphene is a semimetal with zero band gap energy. Close to the Dirac points, the dispersion $E(\mathbf{k})$ is linear in the wavevector *k* [70, 71] rather than parabolic as in conventional semiconductors, giving rise to a vanishing effective mass of the electrons. The linear dispersion is similar to the dispersion of relativistic particles with zero rest mass, and the electrons are described by the Dirac equation around the Dirac points. In undoped graphene, the Fermi energy is located at the energy where the valence and conduction bands intersect. Appropriate doping or applying an electric field generates a two-dimensional electron gas of almost massless electrons.

For parabolic bands, small effective electron masses result in a large Landau level splitting, as seen from Eqs. (5.2) and (5.3). Even though graphene has a different band structure, this simple consideration already suggests that graphene has favorable properties for the application of the QHE. The Dirac equation yields the following relation for the energy of the electron Landau levels if a magnetic field *B* is applied normal to the graphene layer [71]:

$$E_{\mathrm{LL}} = \mathrm{v_F}\sqrt{2\hbar e B l_{\mathrm{C}}} \tag{5.29}$$

In this equation, $\mathrm{v_F}$ is the Fermi velocity, which is approximately 10^6 m/s in graphene [38], and l_{C} an integer ($l_{\mathrm{C}} = 0, 1, 2, \ldots$). In contrast to semiconductors with parabolic bands, the Landau levels are not equally spaced in energy and their energies scale with the square root of the magnetic field, rather than with the field itself.

The square root dependence favors a larger Landau level splitting at lower fields. Figure 5.14 shows the energy splitting between the two lowest Landau levels, ΔE_{LL}, normalized to the thermal energy, kT, versus the magnetic field for graphene and GaAs at different temperatures. The plotted quantity indicates whether a highly reproducible QHE can be expected. Routine operation conditions of GaAs quantum Hall resistors of 10 T and 1.4 K result in $\Delta E_{\mathrm{LL}}/kT = 150$. The same ratio can be obtained, for example, at 2 T and 4.2 K using graphene. Even higher temperatures should be feasible though at the expense of higher fields, as indicated by the graphene curve for 10 K.

In Section 5.5.3, we discuss the operating conditions, under which highly accurate quantized resistance values can be observed experimentally. A comprehensive description of the electronic properties of graphene can be found, for example, in Refs. [70–72].

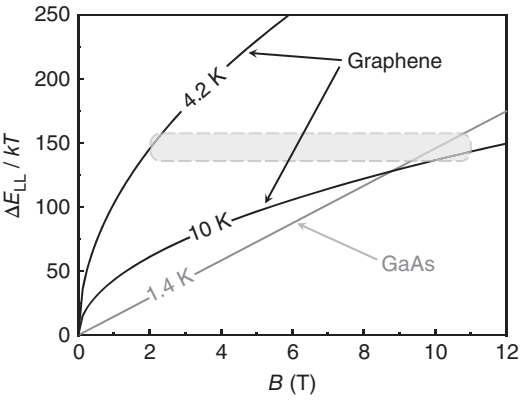

Figure 5.14 Energy splitting between the two lowest Landau levels normalized to the thermal energy versus magnetic field for graphene (black lines) and GaAs (gray line) at different temperatures. The dashed box marks an energy ratio of 150 as obtained under routine operation conditions of GaAs quantum Hall resistors of 10 T and 1.4 K. Source: Courtesy of F. Ahlers, PTB.

5.5.2 Fabrication of Graphene Monolayers for Resistance Metrology

Monolayer graphene can be produced by mechanical exfoliation from graphite. This method was used in the groundbreaking early scientific work on graphene [36–39]. Exfoliation, however, is not suited for routine fabrication and produces layers, which are rarely larger than several 10 μm. The small layer width results in a small breakdown current of the QHE [73], which limits the measuring current and, in turn, the uncertainty of a QHE measurement. Therefore, considerably larger graphene layers and more reproducible fabrication methods are required for quantum Hall metrology.

Larger graphene layers can be grown by chemical vapor deposition (CVD) on metallic surfaces [74], which act as catalyst for the decomposition of carbon hydrides. For magneto-transport experiments, the graphene layer needs to be lifted off the metallic substrate and transferred to a nonconducting substrate. This transfer is a delicate procedure, which can degrade the quality of the graphene layer. Therefore, most of the more recent QHE work in metrology used graphene monolayers grown by high-temperature sublimation of silicon carbide (SiC). These layers grow directly on a nonconductive substrate. Moreover, CVD growth on SiC has yielded graphene monolayers, which proved to be well suited for metrology [35, 75].

Epitaxial growth of graphene by the silicon carbide sublimation method mostly employs hexagonal polytypes of SiC, namely, 4H-SiC or 6H-SiC, which provide a well-suited template for the hexagonal graphene layer. Upon heating to temperatures above 1000 °C, the silicon sublimes and a thin carbon layer is formed [76]. The detailed properties of this layer, e.g. the number of atomic layers and their quality, depend on a variety of parameters and conditions. For the growth of monolayer graphene, the silicon-terminated surface of SiC is used [71]. The graphene monolayer grows on top of a carbon buffer layer, which is covalently bonded to the SiC substrate [77]. Growth in an argon atmosphere of approximately 1 bar slows down the sublimation of silicon, allowing the use of higher growth temperatures up to 2000 °C [78, 79]. The increased temperature increases the mobility of the carbon atoms on the surface, resulting in larger uniform graphene layers [78, 79]. The sublimation rate can also be controlled by arranging two SiC substrates face to face [80].

The graphene layers grown by the sublimation of SiC are not perfectly flat. During annealing, restructuring of the SiC surface results in monolayer graphene terraces at different heights separated by step edges [79, 81]. The step edges can be as high as 10 nm [81]. Along high step edges, bilayer graphene nucleates [79, 81], which can give rise to anisotropic magnetotransport and deviations from the perfect quantization of the Hall resistance [81–83].

Therefore, measures to prevent the formation of high step edges need to be taken. Ref. [84] has shown that reducing the misorientation of the SiC substrate reduces the step height. Moreover, the supply of additional carbon from a polymer adsorbate improves the high-temperature sublimation growth of monolayer graphene [85]. The additional carbon supports the growth of the buffer layer, which stabilizes the SiC surface. As a result, bilayer-free graphene monolayers are obtained with maximum step heights of only 0.75 nm, corresponding to three layers of SiC [85]. The uniform graphene monolayers can extend over millimeter distances and are very well suited for quantum Hall metrology [85]. Figure 5.15 shows an atomic force microscope image of such a bilayer-free graphene monolayer together with a Raman image. Raman spectra can be used to distinguish monolayer graphene from bilayer graphene and the carbon buffer layer [86].

In metrology, it is often intended to perform QHE measurements close to the smallest possible integer filling factor and at low magnetic fields up to 5 T. To this end, the electron density in the graphene layers needs to be adjusted to match the density of states for such a field range and filling factor (see the discussion in Section 5.3.2 and Eq. (5.10)). The suitable electron density is on the order of 10^{11} cm^{-2}. The electron density of monolayer graphene grown by the sublimation of SiC is usually much higher, namely, on the order of 10^{12}–10^{13} cm^{-2} [71]. The strong intrinsic doping is attributed to donor states in the carbon buffer layer [71]. To reduce the electron density, an electric field can be applied to a gate structure fabricated on top of the graphene monolayer. However, this approach requires additional fabrication steps, which may damage the graphene layer, and suffers from an intrinsic disadvantage that the gate voltage needs to be applied permanently to keep the electron density stable. Therefore, photochemical gating is often used to control the electron density [87]. A polymer spacer layer and a photosensitive resist layer are deposited on the graphene. Upon activation by

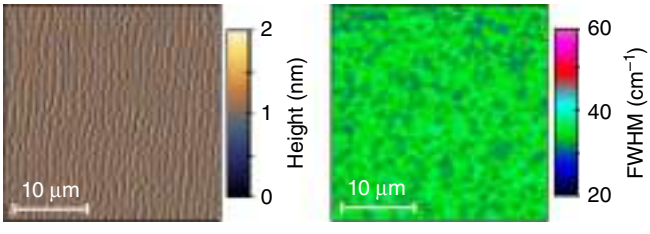

Figure 5.15 Atomic force microscope (left) and Raman (right) images of monolayer graphene grown by polymer-assisted sublimation of SiC. The analysis of the height data of the $30 \times 30\ \mu m^2$ atomic force microscope image shows that the maximum step height is 0.75 nm. The $30 \times 30\ \mu m^2$ Raman image depicts the full width at half maximum (FWHM) of the 2D peak, which is a fingerprint of graphene. The FWHM has a mean of 33 cm^{-1} and varies only slightly over the image, proving the absence of bilayer patches [86]. Source: Courtesy of K. Pierz, PTB.

ultraviolet (UV) radiation, acceptor states form in the photosensitive resist. These acceptors effectively reduce the electron density, which is reported to remain constant for several months [71]. The effect of the UV radiation can be undone by thermal annealing, and the high electron density can be recovered. The electron mobility remains in the range of 10^3–10^4 cm^2 V^{-1} s^{-1}, well suited for QHE measurements of graphene [71]. Other gating methods use polymer coatings subjected to corona discharge [88] or a treatment of the graphene layer with aqua regia [89].

5.5.3 Quantum Hall Effect in Monolayer Graphene

The QHE in graphene monolayers impacts science and metrology in various ways. From a scientific perspective, the QHE serves as an experimental fingerprint that the layer under study is indeed a graphene monolayer with massless Dirac electrons [38, 39]. In metrology, the QHE in monolayer graphene testifies to the high reproducibility and universality of the QHE [33–35, 90]. Furthermore, graphene offers the potential for more practical quantum Hall standards, which can be operated under relaxed conditions.

Monolayer graphene exhibits a so-called half-integer QHE [38, 39, 71]:

$$R_{xy}(i) = \frac{h}{4e^2}\frac{1}{(i+1/2)} \tag{5.30}$$

As in Section 5.3, i is the integer number of Landau levels that are completely filled with electrons. The dependence on $(i + 1/2)^{-1}$, rather than on i^{-1} as in conventional semiconductors, is the consequence of the Landau level $E_{\mathrm{LL}}(l_{\mathrm{C}} = 0)$ at zero energy where the valence and the conduction bands intersect [71]. This Landau level is equally shared by electrons and holes and contains half as many electrons as the higher electron Landau levels. The fourfold degeneracy results from the two states of the electron spin (up and down) and the two groups of Dirac points (K and K'). Equation (5.30) predicts plateaus of the Hall resistance with values $R_{\mathrm{K}}/2$, $R_{\mathrm{K}}/6$, $R_{\mathrm{K}}/10$, and so on. The experimental data in Figure 5.16 confirms this prediction. The measurement was performed on a $100 \times 400\,\mu\mathrm{m}^2$ wide monolayer graphene Hall bar at $T = 1.3$ K. Besides the Hall resistance R_{xy}, the longitudinal resistance R_{xx} is shown, which is seen to vanish over the field ranges of the QHE plateaus, as expected.

Since the band structure of monolayer graphene differs considerably from that of conventional semiconductors, graphene provides a perfect arena to test the reproducibility and universality of the QHE experimentally. Quantum Hall resistance values in exfoliated graphene were found to agree with those of GaAs/AlGaAs heterostructures within an uncertainty of 6 parts in 10^9 [90]. Quantum Hall measurements of GaAs/AlGaAs heterostructures and graphene grown by the sublimation of SiC were found to agree within an uncertainty slightly below 9 parts in 10^{11} [33, 34]. Agreement within an uncertainty of 8.2 parts in 10^{11} was reported for graphene produced by CVD growth on SiC [35]. These results convincingly corroborate the high reproducibility and universality of the QHE.

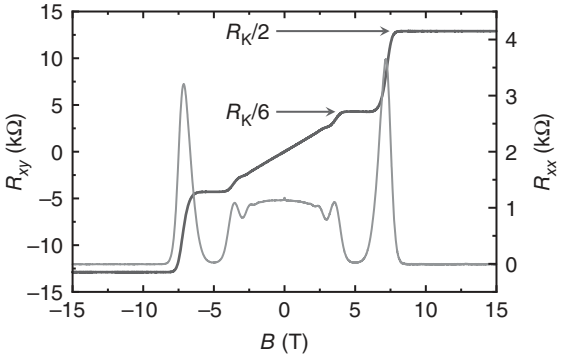

Figure 5.16 Experimentally determined Hall resistance R_{xy} (black, left scale) and longitudinal resistance R_{xx} (gray, right scale) as a function of the magnetic flux density of a $100 \times 400\ \mu m^2$ monolayer graphene Hall bar at a temperature $T = 1.3$ K (measuring current 1 μA). The graphene was grown by the silicon carbide sublimation method and the electron density was adjusted to $6.94 \times 10^{11}\ cm^{-2}$. Some plateaus of the Hall resistance are indicated. Source: Courtesy of F. Ahlers, PTB.

The reproducibility tests were performed over long measuring times and at temperatures and magnetic fields similar to those used to operate GaAs quantum Hall resistance standards. However, the QHE in graphene can also provide quantized resistance values with sufficiently low uncertainty under relaxed conditions, that is, if the magnetic field is lowered and/or the operating temperature is raised. To this end, the magnetic field, operating temperature, and measuring current need to be chosen carefully to balance counteracting effects.

As the operating temperature is raised, the magnetic field needs to be increased, as already suggested by Figure 5.14. For example, a field of 29 T was applied to observe the QHE at room temperature [40]. A measuring current in the 10-μA range is required to ensure a sufficiently large signal-to-noise ratio of the QHE measurement and, in turn, sufficiently low uncertainty. The critical current, at which the breakdown of the QHE occurs, needs to be larger than this measuring current. Breakdown is of minor concern in graphene layers with electron densities optimized for QHE measurements at large magnetic fields. For example, the critical current density in graphene is several A/m at a field of 7 T [73] and even increases to several tens of A/m for fields well above 10 T [73]. These critical current densities are larger than those of GaAs quantum Hall resistors, which are typically 1 A/m [43]. Yet, the critical current density decreases below that of GaAs in graphene layers optimized for QHE measurements at fields of 5 T and below [91]. Thus, a careful choice of magnetic field, measuring current, and layer width is required. Moreover, as the temperature is raised, the critical current decreases for all magnetic fields [73].

Despite these constraints, quantum Hall resistance measurements with an uncertainty of 10^{-9} are reported at 5 T and 5 K in Ref. [35]. A measuring current of 50 μA was applied using graphene grown by CVD on SiC [35]. With graphene grown by the sublimation of SiC, quantum Hall resistance measurements with metrological accuracy (parts per billion range) have been performed

at a temperature of around 3.8 K and magnetic fields below 5 T in a small cryogen-free system [92]. These results are important steps toward a more practical quantum Hall resistance standard.

Monolayer graphene also holds promise for quantum Hall impedance standards. Precision measurements of the quantized Hall resistance at kilohertz frequencies showed that the AC QHE plateaus were flatter than those in unshielded GaAs quantum Hall devices [93]. Furthermore, the graphene AC QHE data showed a smaller deviation from the quantized value [93, 94]. Considering that capacitive losses are unavoidable in the AC QHE regime [66, 67], these findings are attributed to the presence of positive and negative capacitive contributions with different dependence on the sample size [93]. The positive and negative contributions can partially cancel in graphene devices with sizes that are smaller than those of GaAs quantum Hall devices [93]. Of course, the double-shielding technique [67], which is described in Section 5.4.4, can also be used with graphene devices to further improve their performance as quantum Hall impedance standards.

References

1 von Klitzing, K., Dorda, G., and Pepper, M. (1980). New method for high-accuracy determination of the fine-structure constant based on quantized Hall resistance. *Phys. Rev. Lett.* 45: 494–497.

2 Schurr, J., Bürkel, V., and Kibble, B.P. (2009). Realizing the farad from two ac quantum Hall resistances. *Metrologia* 46: 619–628.

3 Schurr, J., Kucera, J., Pierz, K., and Kibble, B.P. (2011). The quantum Hall impedance standard. *Metrologia* 48: 47–57.

4 Prange, R.E. and Girvin, S.M. (eds.) (1990). *The Quantum Hall Effect*. New York: Springer.

5 Janssen, M., Viehweger, O., Fastenrath, U., and Hajdu, J. (eds.) (1994). *Introduction to the Theory of the Integer Quantum Hall Effect*. Wiley-VCH: Weinheim.

6 Weis, J. and von Klitzing, K. (2011). Metrology and microscopic picture of the integer quantum Hall effect. *Philos. Trans. R. Soc. London, Ser. A* 369: 3954–3974.

7 Göbel, E.O. and Siegner, U. (2015). *Quantum Metrology: Foundations of Units and Measurements*. Weinheim: Wiley-VCH.

8 Madelung, O. (1981). *Introduction to Solid State Theory*. Heidelberg, Berlin, New York: Springer-Verlag.

9 Weisbuch, C. and Vinter, B. (eds.) (1991). *Quantum Semiconductor Structures: Fundamentals and Applications*. San Diego, CA: Academic Press.

10 Kroemer, H. (1963). A proposed class of hetero-junction injection lasers. *Proc. IEEE* 51: 1782–1783.

11 Madelung, O. (ed.) (1987). *Landolt-Börnstein Numerical Data and Functional Relationships in Science and Technology, Group III*, vol. 22. Berlin: Springer-Verlag.

12 Cho, A.Y. and Arthur, J.R. Jr. (1975). Molecular beam epitaxy. *Prog. Solid State Chem.* 10: 157–191.

13 Stringfellow, G.B. (1999). *Organometallic Vapor-Phase Epitaxy: Theory and Practice*, 2nd edn. San Diego, CA, London: Academic Press.

14 Stolz, W. (2000). Alternative N-, P- and As-precursors for III/V-epitaxy. *J. Cryst. Growth* 209: 272–278.

15 Dingle, R., Störmer, H.L., Gossard, A.C., and Wiegmann, W. (1978). Electron mobilities in modulation-doped semiconductor heterojunction superlattices. *Appl. Phys. Lett.* 33: 665–667.

16 Umansky, V., De-Picciotto, R., and Heiblum, M. (1997). Extremely high-mobility two dimensional electron gas: evaluation of scattering mechanisms. *Appl. Phys. Lett.* 71: 683–685.

17 Prange, R.E. (1981). Quantized Hall resistance and the measurement of the fine-structure constant. *Phys. Rev. B* 23: 4802–4805.

18 Büttiker, M. (1988). Absence of backscattering in the quantum Hall effect in multiprobe conductors. *Phys. Rev. B* 38: 9375–9389.

19 Haug, R.J. (1993). Edge-state transport and its experimental consequences in high magnetic fields. *Semicond. Sci. Technol.* 8: 131–153.

20 Landauer, R. (1957). Spatial variation of currents and fields due to localized scatterers in metallic conduction. *IBM J. Res. Dev.* 1: 223–231.

21 Landauer, R. (1970). Electrical resistance of disordered one-dimensional lattices. *Philos. Mag.* 21: 863–867.

22 Büttiker, M. (1986). Four-terminal phase-coherent conductance. *Phys. Rev. Lett.* 57: 1761–1764.

23 van Wees, B.J., van Houten, H., Beenakker, C.W.J. et al. (1988). Quantized conductance of point contacts in a two-dimensional electron gas. *Phys. Rev. Lett.* 60: 848–850.

24 Wei, Y.Y., Weis, J., von Klitzing, K., and Eberl, K. (1998). Edge strips in the quantum Hall regime imaged by a single-electron transistor. *Phys. Rev. Lett.* 81: 1674–1677.

25 Siddiki, A. and Gerhardts, R.P. (2004). Incompressible strips in dissipative Hall bars as origin of quantized Hall plateaus. *Phys. Rev. B* 70: 195335 (12 pp).

26 Thouless, D.J., Kohmoto, M., Nightingale, M.P., and Den Nijs, M. (1982). Quantized Hall conductance in a two-dimensional periodic potential. *Phys. Rev. Lett.* 49: 405–408.

27 Hehl, F., Obukhov, Y.N., and Rosenow, B. (2005). Is the quantum Hall effect influenced by the gravitational field? *Phys. Rev. Lett.* 93: 096804 (4 pp).

28 Penin, A.A. (2009). Quantum Hall effect in quantum electrodynamics. *Phys. Rev. B* 79: 113303 (4 pp).

29 Tsui, D.C., Störmer, H.L., and Gossard, A.C. (1982). Two-dimensional magnetotransport in the extreme quantum limit. *Phys. Rev. Lett.* 48: 1559–1562.

30 Laughlin, R.B. (1983). Anomalous quantum Hall effect: an incompressible quantum fluid with fractionally charged excitations. *Phys. Rev. Lett.* 50: 1395–1398.

31 Delahaye, F. and Jeckelmann, B. (2003). Revised technical guidelines for reliable dc measurements of the quantized Hall resistance. *Metrologia* 40: 217–233.

32 Hartland, A., Jones, K., Williams, J.M. et al. (1991). Direct comparison of the quantized Hall resistance in gallium arsenide and silicon. *Phys. Rev. Lett.* 66: 969–973.

33 Janssen, T.J.B.M., Fletcher, N.E., Goebel, R. et al. (2011). Graphene, universality of the quantum Hall effect and redefinition of the SI system. *New J. Phys.* 13: 093026 (6 pp).

34 Janssen, T.J.B.M., Williams, J.M., Fletcher, N.E. et al. (2012). Precision comparison of the quantum Hall effect in graphene and gallium arsenide. *Metrologia* 49: 294–306.

35 Ribeiro-Palau, R., Lafont, F., Brun-Picard, J. et al. (2015). Quantum Hall resistance standard in graphene devices under relaxed experimental conditions. *Nat. Nanotechnol.* 10: 965–971.

36 Novoselov, K.S., Geim, A.K., Morozov, S.V. et al. (2004). Electric field effect in atomically thin carbon films. *Science* 306: 666–669.

37 Novoselov, K.S., Jiang, D., Schedin, F. et al. (2005). Two-dimensional atomic crystals. *Proc. Natl. Acad. Sci. U.S.A.* 102: 10451–10453.

38 Novoselov, K.S., Geim, A.K., Mozorov, S.V. et al. (2005). Two-dimensional gas of massless Dirac fermions in graphene. *Nature* 438: 197–200.

39 Zhang, Y., Tan, Y.-W., Stormer, H.L., and Kim, P. (2005). Experimental observation of the quantum Hall effect and Berry's phase in graphene. *Nature* 438: 201–204.

40 Novoselov, K.S., Jiang, Z., Zhang, Y. et al. (2007). Room-temperature quantum Hall effect in graphene. *Science* 315: 1379.

41 Ahlers, F.J., Götz, M., and Pierz, K. (2017). Direct comparison of of fractional and integer quantized Hall resistance. *Metrologia* 54: 516–523.

42 Götz, M., Fijalkowski, K.M., Pesel, E. et al. (2018). Precision measurement of the quantized anomalous Hall resistance at zero magnetic field. *Appl. Phys. Lett.* 112: 072102 (5 pp).

43 Jeckelmann, B. and Jeanneret, B. (2001). The quantum Hall effect as an electrical resistance standard. *Rep. Prog. Phys.* 64: 1603–1655.

44 BIPM (2017). *Mise en pratique* for the definition of the ampere and other electric units in the SI. https://www.bipm.org/utils/en/pdf/si-mep/MeP-a-2018.pdf (accessed 27 June 2018).

45 Thompson, A.M. and Lampard, D.G. (1956). A new theorem in electrostatics and its application to calculable standards of capacitance. *Nature* 177: 888.

46 Gibbings, D.L.H. (1963). A design for resistors of calculable AC/DC resistance ratio. *Proc. IEE* 110: 335–347.

47 Kucera, J., Vollmer, E., Schurr, J., and Bohacek, J. (2009). Calculable resistors of coaxial design. *Meas. Sci. Technol.* 20: 095104 (6 pp).

48 Small, G.W., Rickets, B.W., Coogan, P.C. et al. (1997). A new determination of the quantized Hall resistance in terms of the NML calculable cross capacitor. *Metrologia* 34: 241–243.

49 Jeffery, A.M., Elmquist, R.E., Lee, L.H. et al. (1997). NIST comparison of the quantized Hall resistance and the realization of the SI ohm through the calculable capacitor. *IEEE Trans. Instrum. Meas.* 46: 264–268.

50 Witt, T.J. (1998). Electrical resistance standards and the quantum Hall effect. *Rev. Sci. Instrum.* 69: 2823–2843.

51 Giacomo, P. (1988). News from the BIPM. *Metrologia* 25: 115–119 (see also Resolution 6 of the 18th Meeting of the CGPM (1987), BIPM http://www.bipm.org/en/CGPM/db/18/6/ (accessed 23 August 2018).

52 Quinn, T.J. (1989). News from the BIPM. *Metrologia* 26: 69–74.

53 Piquemal, F. (2010). *Handbook of Metrology*, vol. 1 (ed. M. Gläser and M. Kochsiek), 267–314. Weinheim: Wiley-VCH.

54 BIPM and CCEM (2017). Guidelines for Implementation of the 'Revised SI'. https://www.bipm.org/utils/common/pdf/CC/CCEM/ccem_guidelines_revisedSI.pdf (accessed 27 June 2018).

55 Nachtwei, G. (1999). Breakdown of the quantum Hall effect. *Physica E* 4: 79–101.

56 Harvey, K. (1972). A precise low temperature dc ratio transformer. *Rev. Sci. Instrum.* 43: 1626–1629.

57 Delahaye, F. (1993). Series and parallel connection of multiple quantum Hall-effect devices. *J. Appl. Phys.* 73: 7914–7920.

58 Poirier, W., Bounouh, A., Piquemal, F., and Andre, J.P. (2004). A new generation of QHARS: discussion about the technical criteria for quantization. *Metrologia* 41: 285–294.

59 Hein, G., Schumacher, B., and Ahlers, F.J. (2004). Preparation of quantum Hall effect device arrays. *Conference on Precision Electromagnetic Measurements Digest 2004*, 273–274, ISBN: 0-7803-8493-8.

60 Ortolano, M., Abrate, M., and Callegaro, L. (2015). On the synthesis of quantum Hall array resistance standards. *Metrologia* 52: 31–39.

61 Qing, Z., Xue-Shen, W., Jin-Jin, W. et al. (2016). A 1 kΩ standard resistor device based on quantum Hall array. *Acta Phys. Sin.* 65: 227301 (6 pp).

62 Oe, T., Matsuhiro, K., Itatani, T. et al. (2013). New design of quantized Hall resistance array device. *IEEE Trans. Instrum. Meas.* 62: 1755–1759.

63 Oe, T., Gorwadkar, S., Itatani, T., and Kaneko, N. (2017). Development of 1 MΩ quantum Hall array resistance standards. *IEEE Trans. Instrum. Meas.* 66: 1475–1481.

64 Chae, D.-H., Kim, W.-S., Oe, T., and Kaneko, N.-H. (2018). Direct comparison of 1 MΩ quantized Hall array resistance and quantum Hall resistance standard. *Metrologia* 55: 645–653.

65 Flowers, J. (2004). The route to atomic and quantum standards. *Science* 306: 1324–1330.

66 Ahlers, F.J., Jeanneret, B., Overney, F. et al. (2009). Compendium for precise AC measurements of the quantum Hall resistance. *Metrologia* 46: R1–R11.

67 Kibble, B.P. and Schurr, J. (2008). A novel double-shielding technique for ac quantum Hall measurement. *Metrologia* 45: L25–L27.

68 Mohr, P.J., Newell, D.B., and Taylor, B.N. (2016). CODATA recommended values of the fundamental physical constants: 2014. *Rev. Mod. Phys.* 88: 035009 (73 pp).

69 Mohr, P.J., Newell, D.B., Taylor, B.N., and Tiesinga, E. (2018). Data and analysis for the CODATA 2017 special fundamental constants adjustment. *Metrologia* 55: 125–146.

70 Castro Neto, A.H., Guinea, F., Peres, N.M.R. et al. (2009). The electronic properties of graphene. *Rev. Mod. Phys.* 81: 109–163.

71 Janssen, T.J.B.M., Tzalenchuk, A., Lara-Avila, S. et al. (2013). Quantum resistance metrology using graphene. *Rep. Prog. Phys.* 76: 104501 (24 pp).

72 Katsnelson, M.I. (2012). *Graphene: Carbon in Two Dimensions*. Cambridge: Cambridge University Press.

73 Alexander-Webber, J.A., Baker, A.M.R., Janssen, T.J.B.M. et al. (2013). Phase space for the breakdown of the quantum Hall effect in epitaxial graphene. *Phys. Rev. Lett.* 111: 096601 (5 pp).

74 Kim, K.S., Zhao, Y., Jang, H. et al. (2009). Large-scale pattern growth of graphene films for stretchable transparent electrodes. *Nature (London)* 457: 706–710.

75 Lafont, F., Ribeiro-Palau, R., Kazazis, D. et al. (2015). Quantum Hall resistance standards from graphene grown by chemical vapour deposition on silicon carbide. *Nature Commun.* 6: 6806 (9 pp).

76 Berger, C., Song, Z., Li, T. et al. (2004). Ultrathin epitaxial graphite: 2D electron gas properties and a route toward graphene-based nanoelectronics. *J. Phys. Chem. B* 108: 19912–19916.

77 Emtsev, K.V., Speck, F., Seyller, T. et al. (2008). Interaction, growth, and ordering of epitaxial graphene on SiC{0001} surfaces: a comparative photoelectron spectroscopy study. *Phys. Rev. B* 77: 155303 (10 pp).

78 Virojanadara, C., Syväjarvi, M., Yakimova, R. et al. (2008). Homogeneous large-area graphene layer growth on 6H-SiC(0001). *Phys. Rev. B* 78: 245403 (6 pp).

79 Emtsev, K.V., Bostwick, A., Horn, K. et al. (2009). Towards wafer-size graphene layers by atmospheric pressure graphitization of silicon carbide. *Nat. Mater.* 8: 203–207.

80 Real, M.A., Lass, E.A., Liu, F.-H. et al. (2013). Graphene epitaxial growth on SiC(0001) for resistance standards. *IEEE Trans. Instrum. Meas.* 62: 1454–1460.

81 Kruskopf, M., Pierz, K., Wundrack, S. et al. (2015). Epitaxial graphene on SiC: modification of structural and electron transport properties by substrate pretreatment. *J. Phys. Condens. Matter* 27: 185303 (7 pp).

82 Schumann, T., Friedland, K.-J., Oliveira, M.H. Jr., et al. (2012). Anisotropic quantum Hall effect in epitaxial graphene on stepped SiC surfaces. *Phys. Rev. B* 85: 235402 (5 pp).

83 Yager, T., Lartsev, A., Mahashabde, S. et al. (2013). Express optical analysis of epitaxial graphene on SiC: impact of morphology on quantum transport. *Nano Lett.* 13: 4217–4223.

84 Virojanadara, C., Yakimova, R., Osiecki, J.R. et al. (2009). Substrate orientation: a way towards higher quality monolayer graphene growth on 6H-SiC (0 0 0 1). *Surf. Sci.* 603: L87–L90.

85 Kruskopf, M., Momeni Pakdehi, D., Pierz, K. et al. (2016). Comeback of epitaxial graphene for electronics: large-area growth of bilayer-free graphene on SiC. *2D Materials* 3: 041002 (9 pp).

86 Lee, D.S., Riedl, C., Krauss, B. et al. (2008). Raman spectra of epitaxial graphene on SiC and of epitaxial graphene transferred to SiO_2. *Nano Lett.* 8: 4320–4325.

87 Lara-Avila, S., Moth-Poulsen, K., Yakimova, R. et al. (2011). Non-volatile photochemical gating of an epitaxial graphene/polymer heterostructure. *Adv. Mater.* 23: 878–882.

88 Lartsev, A., Yager, T., Bergsten, T. et al. (2014). Tuning carrier density across Dirac point in epitaxial graphene on SiC by corona discharge. *Appl. Phys. Lett.* 105: 063106 (4 pp).

89 Yang, Y., Huang, L.-I., Fukuyama, Y. et al. (2015). Low carrier density epitaxial graphene devices on SiC. *Small* 11: 90–95.

90 Woszczyna, M., Friedemann, M., Götz, M. et al. (2012). Precision quantization of Hall resistance in transferred graphene. *Appl. Phys. Lett.* 100: 164106 (3 pp).

91 Alexander-Webber, J.A., Huang, J., Maude, D.K. et al. (2016). Giant quantum Hall plateaus generated by charge transfer in epitaxial graphene. *Sci. Rep.* 6: 30296 (12 pp). https://doi.org/10.1038/srep30296.

92 Janssen, T.J.B.M., Rozhko, S., Antonov, I. et al. (2015). Operation of graphene quantum Hall resistance standard in a cryogen-free table-top system. *2D Materials* 2: 035015 (9 pp).

93 Kalmbach, C.-C., Schurr, J., Ahlers, F.J. et al. (2014). Towards a graphene-based quantum impedance standard. *Appl. Phys. Lett.* 105: 073511 (4 pp).

94 Lüönd, F., Kalmbach, C.-C., Overney, F. et al. (2017). AC quantum Hall effect in epitaxial graphene. *IEEE Trans. Instrum. Meas.* 66: 1459–1466.

6

Single-Charge Transfer Devices and the SI Ampere

The paradigm of quantum metrology is the manipulation and counting of single quanta to determine the value of macroscopic physical quantities based on fundamental constants. This concept becomes particularly obvious considering the ampere, base unit of electric current, in the present SI. The ampere is linked to the elementary charge e, which is one of the seven defining constants of the SI (see Section 2.2). A straightforward approach to realize the SI ampere is to transfer single charges through a conductor in a controlled way. Single-charge transfer entails the controlled manipulation of single electrons and single Cooper pairs in normal conductors and superconductors, respectively.

The SI ampere is realized if single charges are transferred in a clocked manner at a frequency f. This approach yields a quantized current

$$I = nef = \frac{ne}{T} \tag{6.1}$$

where n is the number of elementary charges transferred per cycle. Equation (6.1) can be viewed as the textbook definition of the current being the charge transferred through a conductor cross section per time interval $T = 1/f$. In this sense, quantized current sources provide the most direct realization of the SI ampere.

For Eq. (6.1) to be applicable, single charges must be isolated and transferred one by one through a conductor. The basic physics of single-charge transport will be discussed in Section 6.1. Section 6.2 gives an overview of quantized current sources made of normal metals, superconductors, and semiconductors. The basics of superconductors and semiconductors are summarized in Chapters 4 and 5, respectively. Detailed reviews of single-charge transfer can be found, for example, in Refs. [1–4].

The realization of the SI ampere is treated in Section 6.3. Besides realizations using single-charge transfer, we discuss realizations based on the SI volt, SI ohm, and the application of Ohm's law. In these indirect ampere realizations, the Josephson effect (see Chapter 4) and the quantum Hall effect (QHE) (see Chapter 5) are used to link the SI volt and SI ohm to e and the Planck constant h.

An important application of quantum current standards is a fundamental consistency test of electrical quantum metrology, which is known as the quantum metrology triangle (QMT), first suggested in [5]. The QMT is described in Section 6.4. The consistency test aims at verifying the relation of the Josephson effect, the QHE, and single-charge transport to the defining constants e and h.

The New International System of Units (SI): Quantum Metrology and Quantum Standards,
First Edition. Ernst O. Göbel and Uwe Siegner.
© 2019 Wiley-VCH Verlag GmbH & Co. KGaA. Published 2019 by Wiley-VCH Verlag GmbH & Co. KGaA.

6.1 Basic Physics of Single-Electron Transport

This section discusses the basics of single-charge transfer in normal metal circuits. Single-electron transport (SET) rests on two basic physical phenomena, namely, the tunneling of electrons through potential barriers and the so-called Coulomb blockade. Coulomb blockade occurs in small structures with a large capacitive charging energy. These phenomena are also the basis of single-charge transfer in semiconductors and superconductors.

6.1.1 Single-Electron Tunneling

Electrons in metals are delocalized. Therefore, the charge on a capacitor C connected to a voltage source U by metallic wires can take any value $Q = CU$ even though the electron charge ($-e$) is quantized. This fact, illustrated in Figure 6.1a, raises the question of how single electrons can be manipulated in metals. A first clue is obtained noting that a capacitor plate will carry a fixed number of electrons and, thus, quantized charge if one of the wires is broken. This situation can be realized by an open switch as shown in Figure 6.1b. Opening of the switch results in localization of the electrons on the capacitor. Of course, breaking the wire prohibits any further adjustment of the number of electrons on the capacitor and is not a practical approach. Yet, localization can also be obtained replacing the switch by a tunnel element with sufficiently large resistance. In its simplest form, a tunnel element consists of two metallic contacts separated by a sufficiently thin insulating layer, very similar to the Josephson tunnel junction described in Chapter 4. The tunnel element (with resistance R_T and capacitance C_T) and the capacitor plate form a so-called single-electron quantum box, as shown in Figure 6.1c.

A single-electron quantum box allows single-electron charges to be manipulated and can serve as a building block of SET devices if two fundamental conditions are fulfilled. First, the charging energy required to put an extra electron on the capacitor, E_C^{1e}, must be considerably larger than the thermal energy, kT

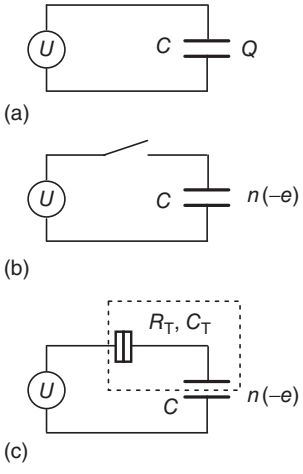

Figure 6.1 Comparison of a closed metallic circuit without charge quantization (a), an open metallic circuit with a fixed number of quantized charges n on the capacitor (b), and a single-electron quantum box (dashed box in part c) allowing the manipulation of single electrons. Source: Göbel and Siegner 2015 [6]. Reproduced with permission of John Wiley & Sons.

(k Boltzmann constant, T temperature), to prevent random thermal transfer of electrons:

$$E_C^{1e} = \frac{e^2}{2C_\Sigma} \gg kT \tag{6.2}$$

where C_Σ is the total capacitance ($C_\Sigma = C + C_T$). Relation (6.2) shows that reliable SET operation requires very small capacitances (0.1–1 fF), corresponding to structures with nanometer dimensions. Moreover, particularly for metrological applications, the temperature must be low (often in the millikelvin range).

The second condition relates to quantum fluctuations whose energy, E_{QF}, must be much smaller than E_C^{1e}. According to the Heisenberg uncertainty relation, $E_{QF} = \hbar/\tau$, where τ is the RC time constant, $\tau = R_T C_\Sigma$. Thus, we obtain as second condition

$$R_T \gg \frac{1}{\pi}\frac{h}{e^2} \approx \frac{R_K}{4}, \tag{6.3}$$

where R_K is the von Klitzing constant. Relation (6.3) expresses that the tunnel resistance must be large enough to localize electrons sufficiently well in the single-electron quantum box.

6.1.2 Coulomb Blockade in SET Transistors

Single-electron manipulation can be achieved using a so-called SET transistor if conditions (6.2) and (6.3) are fulfilled. As shown in Figure 6.2, an SET transistor is a three-terminal device and consists of two single-electron quantum boxes connected such that a small charge island is formed between the tunnel elements. The island is capacitively coupled to a gate voltage U_G via the gate capacitance C_G. Additionally, a source–drain voltage U_{SD} can be applied across the SET transistor (shown as being split symmetrically in Figure 6.2). With SET transistors, clear signatures of SET phenomena were observed as early as 1987 [7, 8].

To understand the operation of an SET transistor, its different energy terms and, in turn, its chemical potential must be considered. The total electrostatic energy of the charge island is given by

$$E_{elst} = \frac{(-en_{exc} + Q_0)^2}{2C_\Sigma} \tag{6.4}$$

where $n_{exc} = N - N_0$ is the number of excess electrons on the island and N the total number of electrons. N_0 is the number of electrons in equilibrium, that is, for $U_{SD} = 0$ and $U_G = 0$, which compensate for the positive background charge of the island. The gate electrode induces a continuously variable charge $Q_0 = C_G U_G$. For

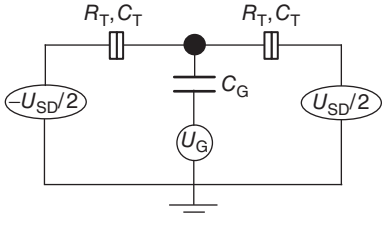

Figure 6.2 Equivalent circuit of an SET transistor. The charge island is shown as black dot. Source: Göbel and Siegner 2015 [6]. Reproduced with permission of John Wiley & Sons.

noninteracting electrons at zero temperature, the total electronic energy of the charge island, $E(N)$, is obtained if the single-particle energies ε_i of all N electrons are added to the electrostatic energy:

$$E(N) = \sum_{i=1}^{N} \varepsilon_i + \frac{(-en_{\mathrm{exc}} + C_{\mathrm{G}} U_{\mathrm{G}})^2}{2C_{\Sigma}} \tag{6.5}$$

The important quantity for the study of transport phenomena is the chemical potential μ, which is, by definition, the energy required to put an extra electron in a system. The chemical potential reflects the mere change of the particle number (to also be considered for uncharged particles) as well as changes in the electrostatic energy caused thereof (to be considered only for charged particles). If the chemical potential is constant, no net transfer of particles occurs, and the current is zero.

The chemical potential of the charge island, μ_{C}, is calculated subtracting the total electronic energy of an island with $N-1$ electrons from the corresponding term for N electrons:

$$\mu_{\mathrm{C}}(N) \equiv E(N) - E(N-1) = \varepsilon_N + \frac{\left(n_{\mathrm{exc}} - 1/2\right) e^2}{C_{\Sigma}} - e\frac{C_{\mathrm{G}}}{C_{\Sigma}} U_{\mathrm{G}} \tag{6.6}$$

The sum of the last two terms on the right-hand side is the electrostatic potential, $-e\phi_N$, while the first term is the electrochemical potential, $\mu_{\mathrm{elch}}(N)$. The electrostatic potential, $-e\phi_N$, can be adjusted by the gate voltage U_{G}. Note that $\mu_{\mathrm{C}}(N)$, $\mu_{\mathrm{elch}}(N)$, and $-e\phi_N$ have the dimension of an energy even though they are conventionally referred to as potentials.

If the number of electrons on the charge island changes by one at a constant gate voltage, the chemical potential changes by $\Delta\mu_{\mathrm{C}}$. We obtain from Eq. (6.6)

$$\Delta\mu_{\mathrm{C}} = \varepsilon_{N+1} - \varepsilon_N + \frac{e^2}{C_{\Sigma}} \tag{6.7}$$

For a small metallic island with small capacitance, we have $\varepsilon_{N+1} - \varepsilon_N \ll e^2/C_{\Sigma}$. Thus, the chemical potential levels of the island are separated by the Coulomb energy e^2/C_{Σ}.

The chemical potential across a metallic SET transistor is plotted in Figure 6.3. The chemical potential of the island is shown for occupation with $N-1$, N, or $N+1$ electrons. Furthermore, μ_{L} and μ_{R} are the chemical potential of the electron source (left) and electron drain (right), respectively, which are related to the source–drain voltage according to

$$\mu_{\mathrm{L}} - \mu_{\mathrm{R}} = eU_{\mathrm{SD}} \tag{6.8}$$

In Figure 6.3, $\mu_{\mathrm{L}} - \mu_{\mathrm{R}}$ is assumed to be smaller than the Coulomb energy e^2/C_{Σ}. Without loss of generality, we can further assume that the charge island is occupied by N electrons. Figure 6.3 then illustrates the so-called Coulomb blockade, that is, the suppression of electron transfer due to the Coulomb energy. The figure shows that electrons cannot move from the source lead to the island since μ_{L} is located below $\mu_{\mathrm{C}}(N+1)$. Similarly, electron flow from the island to the drain lead is inhibited since $\mu_{\mathrm{C}}(N)$ is located below μ_{R}. Thus, the number of electrons on the

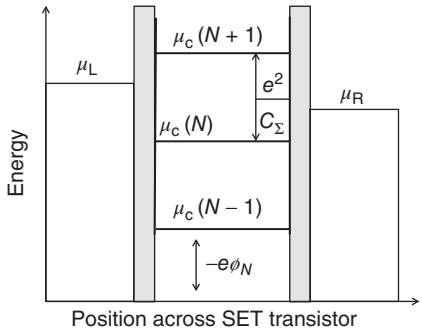

Figure 6.3 Chemical potential across a metallic SET transistor for a fixed gate voltage U_G and a small source–drain voltage U_{SD}. The tunnel barriers (gray) separate the metallic wires on the left (electron source) and right (electron drain) from the charge island. The chemical potential of the source and drain leads is μ_L and μ_R, respectively. The chemical potential of the island is shown for occupation with $N-1$, N, or $N+1$ electrons. Source: Göbel and Siegner 2015 [6]. Reproduced with permission of John Wiley & Sons.

island remains constant at N and no current flows. Of course, for this argument to be valid, we assume that kT is much smaller than the Coulomb energy.

The Coulomb blockade can be lifted if the gate voltage U_G (and thus $-e\phi_N$) is adjusted such that

$$\mu_L > \mu_C(N+1) > \mu_R \tag{6.9}$$

Under this condition, electrons can tunnel from the source lead to the island and further to the drain lead. The electrons are transferred one by one, that is, single-electron transport occurs. The simultaneous transfer of two or more electrons is not possible since $\mu_C(N+2)$, $\mu_C(N+3)$, and so on are still located well above μ_L. Consequently, the number of electrons on the charge island oscillates between N and $N+1$.

The preceding discussion has yielded the following insight, which is the basis of clocked single-charge transfer and quantized current sources:

- In an SET transistor, electron transfer occurs either one by one or is inhibited by the Coulomb blockade (for $|eU_{SD}| = |\mu_L - \mu_R| < e^2/C_\Sigma$).
- Switching between these two states can be achieved by the adjustment of the gate voltage.

6.1.3 Coulomb Blockade Oscillations and Single-Electron Detection

Let us again assume that the source–drain voltage across the SET transistor is small so that the relation $|eU_{SD}| = |\mu_L - \mu_R| < e^2/C_\Sigma$ holds. Under this condition, the so-called Coulomb blockade oscillations occur if the gate voltage is continuously tuned. The tuning causes the state of the SET transistor to periodically change between the Coulomb blockade and single-electron transport. The discussion of the physics presented in Section 6.1.2 applies to each period of the Coulomb blockade oscillation. Only the electron numbers change from period to period. If one period involves the electron numbers N and $N+1$, the next period involves $N+1$, $N+2$, and so on. This feature is illustrated in the lower part of Figure 6.4, where the number of excess electrons on the charge island, n_{exc}, is plotted versus the gate voltage U_G. The U_G axis is scaled in units of e/C_G, which is the period length of the Coulomb blockade oscillation. The period length is determined by Eq. (6.6), which shows that a gate voltage change of e/C_G shifts the chemical potential of the charge island by e^2/C_Σ. The upper part of the figure is

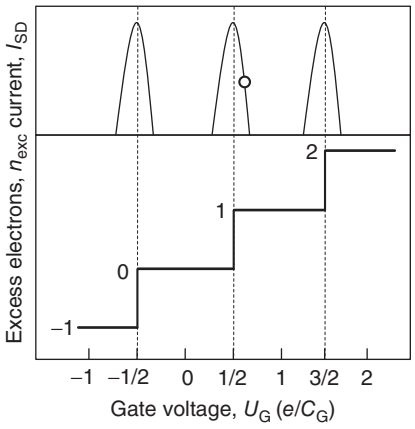

Figure 6.4 Schematic representation of the source–drain current I_{SD} (top) and the number of excess electrons n_{exc} on the charge island (bottom) versus gate voltage U_G. The dot marks the operating point of an SET electrometer. Source: Göbel and Siegner 2015 [6]. Reproduced with permission of John Wiley & Sons.

a schematic representation of the source–drain current, I_{SD}, versus gate voltage. The current shows peaks with steep slopes (whenever the number of electrons on the island oscillates corresponding to the transport of single electrons). This feature is used in applications of SET transistors as electrometers. For charge detection, a sensor electrode is coupled to the charge island of an SET transistor and the operating point is chosen on the flank of a current peak. SET electrometers reach an unprecedented charge resolution on the order of $10^{-5}e/\sqrt{\text{Hz}}$.

Coulomb blockade does not occur for larger source–drain voltages, that is, for $|eU_{SD}| = |\mu_L - \mu_R| \geq e^2/C_\Sigma$. Referring to Figure 6.3, the reason is obvious. For larger source–drain voltages, μ_L is located above $\mu_C(N+1)$ or μ_R lies below $\mu_C(N)$. Either condition precludes the Coulomb blockade. The complete dynamics of the SET transistor can be concisely summarized by the stability diagram of Figure 6.5, in which the number of excess electrons on the charge island is plotted in the plane of the gate voltage and the source–drain voltage.

We finally note that the stability diagram also illustrates the behavior of an SET transistor if U_{SD} is tuned at a constant gate voltage $U_G \neq (i+1/2)e/C_G$ (i integer). For $U_{SD} \ll 0$, negative current flow is observed, followed by the Coulomb blockade around $U_{SD} = 0$ and positive current for $U_{SD} \gg 0$. This behavior is also shown by the experimental data of Figure 6.9. It is the basis of Coulomb blockade thermometry discussed in Section 8.1.6

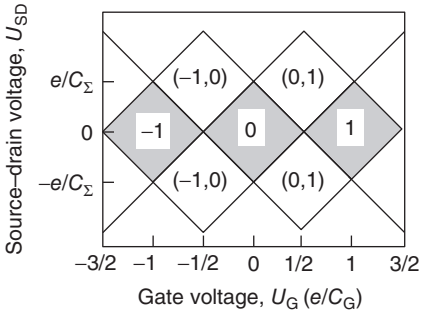

Figure 6.5 Stability diagram of an SET transistor: number of excess electrons n_{exc} on the charge island versus gate voltage U_G and source–drain voltage U_{SD}. In the gray regions, Coulomb blockade occurs and n_{exc} has a constant value as indicated. In the white regions, n_{exc} oscillates between the indicated values corresponding to nonzero current flow. Source: Göbel and Siegner 2015 [6]. Reproduced with permission of John Wiley & Sons.

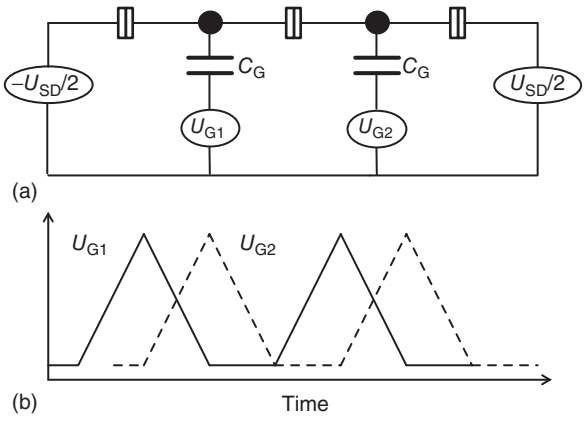

Figure 6.6 SET pump consisting of two charge islands and three tunnel junctions (a). The chemical potentials of the islands are controlled by periodic gate voltages (b). Source: Göbel and Siegner 2015 [6]. Reproduced with permission of John Wiley & Sons.

6.1.4 Clocked Single-Electron Transfer

Clocked single-electron transfer according to Eq. (6.1) can be realized with single-electron quantum boxes. However, a single normal-metal SET transistor is not sufficient for this purpose. This conclusion can be understood recalling that in the on-state, when the Coulomb blockade is lifted, the source–drain current relies on electron tunneling, which is a stochastic process. Consequently, one cannot control the exact number of electrons that tunnel from source to drain in a given time interval, even though the electrons tunnel one by one.

Controlled clocked transfer of single electrons is feasible if two (or more) SET transistors are connected in series. Figure 6.6 shows a so-called SET pump with two charge islands. The chemical potential of the islands can be individually adjusted by periodic gate voltages U_{G1} and U_{G2}. The charge islands are separated from each other and from the source and drain leads by three tunnel junctions. The lower part of the figures shows the periodic gate voltages, which are phase-shifted with respect to each other. The phase shift enables the following cycle, in which a single electron is transferred from source to drain. First, the chemical potential of island 1 is lowered by an increase in U_{G1} so that an electron can tunnel onto the island from the source. Subsequently, the chemical potential of island 1 is raised again (by lowering U_{G1}), while the chemical potential of island 2 is lowered by the increase in U_{G2}. In this phase, the electron tunnels from island 1 to island 2. In the last part of the cycle, the decrease in U_{G2} raises the chemical potential of island 2 so that the electron is emitted to the drain lead. This clocked single-electron transfer does not require the application of a source–drain bias voltage (in fact, it is even feasible against a small opposing bias). Therefore, the device is referred to as the SET pump as opposed to SET turnstile devices whose operation relies on a source–drain bias.

The dynamics of SET pumps can be analyzed with a stability diagram, which shows the number of excess electrons on charge island 1 and 2, (n_1, n_2), in the plane of the gate voltages U_{G1} and U_{G2}. Figure 6.7 is a schematic representation of the stability diagram of the SET pump of Figure 6.6. Single-electron pumping is achieved if the gate voltages are varied such that a triple point is encircled. As shown in the figure, counterclockwise rotation gives rise to clocked

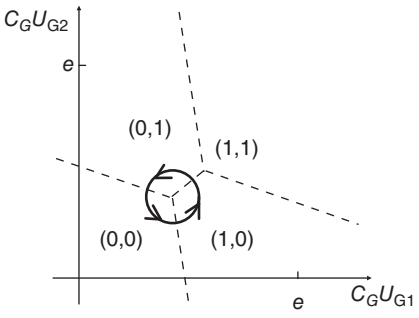

Figure 6.7 Schematic representation of the stability diagram of an SET pump that is driven by two gate voltages U_{G1} and U_{G2}. Shown is the number of excess electrons (n_1, n_2) on the charge islands 1 and 2. The closed trajectory corresponds to single-electron pumping from source to drain. Source: Göbel and Siegner 2015 [6]. Reproduced with permission of John Wiley & Sons.

single-electron transfer from the source to island 1, island 2, and further to the drain. The stability diagram illustrates in an intuitive way that the direction of the single-electron current is reversed for clockwise rotation. Thus, single-electron pumping is a reversible process whose direction is determined by the relative phase between the gate voltages.

The first metallic SET pump was demonstrated in 1991 [9], and, since then, metallic SET pumps have considerably impacted metrology. Therefore, the properties of metallic SET pumps are discussed in Section 6.2.1.

Single-electron transport through a metallic SET turnstile device was demonstrated in 1990 [10]. The device consisted of four tunnel junctions separated by three charge islands. A single alternating gate voltage was applied to the central island. To realize single-electron transport, a source–drain voltage had to be applied. This property classifies the device as turnstile, as mentioned earlier. So far, SET turnstiles made of normal metals have not reached the accuracy of SET pumps. Therefore, with our focus being on metrology, we will not discuss them in more detail. The subject of turnstiles, however, will resurface in the context of semiconducting and superconducting quantized current sources in Sections 6.2.2 and 6.2.3, respectively.

6.2 Quantized Current Sources

In this section, we discuss different implementations of clocked single-electron transport and focus on the performance of quantized current sources with respect to their benchmark parameters for the realization of the SI ampere: (i) the clock frequency, which determines the magnitude of the quantized current according to Eq. (6.1) and (ii) the accuracy with which the quantized current can be generated. The latter is not determined by the uncertainty of the frequency, which can be 10^{-15} and better if derived from atomic clocks (see Chapter 3). The accuracy of the quantized current is determined by the transfer error. This quantity describes the difference between the number of elementary charges that are actually transferred and the intended number n in Eq. (6.1). Equation (6.1) describes a perfect source. The transfer error of a real source can be expressed as $|n - \langle n_S \rangle|/n$. Here, $\langle n_S \rangle$ denotes the time-averaged number of elementary charges transferred per cycle of the clock frequency f. If, for example, two electrons are transferred instead of one in some cycles, $\langle n_S \rangle$

will be larger than $n = 1$ and the transfer error will be nonzero. The transfer error and the clock frequency are often interrelated so that a careful optimization of the overall performance is required. A comprehensive overview of SET devices is given in Ref. [4].

6.2.1 Metallic Single-Electron Pumps

Most metallic SET devices are made of aluminum since it has a stable native oxide with good dielectric properties, which can form insulating tunnel barriers. A scanning electron microscopy (SEM) image of an Al/Al oxide SET transistor is shown in Figure 6.8. For SET operation according to the concept outlined in Section 6.1, a weak magnetic field is applied to suppress superconductivity in aluminum. The application of the field yields a normal-metal/insulator system. Pronounced Coulomb blockade can be achieved in Al/Al oxide SET transistors, as illustrated in Figure 6.9.

The clock frequency of metallic SET pumps is determined by the time constant $\tau = R_T C_\Sigma$ of the tunneling process. This time constant cannot easily be reduced since the relation $R_T \gg R_K$ must hold and the reduction of C_Σ requires the fabrication of extremely fine nanostructures. The clock frequency must fulfill the condition $f \ll (R_T C_\Sigma)^{-1}$. Otherwise, tunneling events are missed due to the stochastic nature of tunneling. Lowering the frequency increases the probability that tunneling occurs in each cycle of the drive voltage. For high-accuracy single-electron pumping, the clock frequency must be limited to the 10 MHz range, corresponding to picoampere currents.

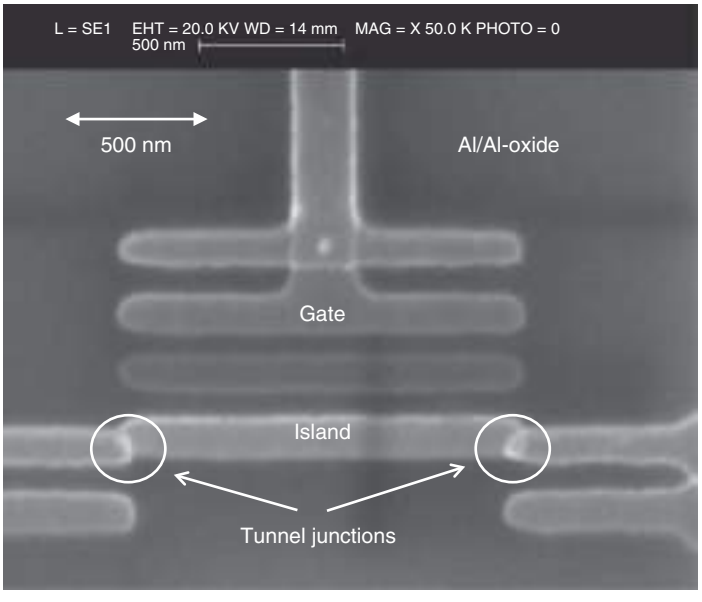

Figure 6.8 SEM image of an Al/AlO_x/Al/AlO_x/Al SET transistor. Each structure is seen twice due to the specific fabrication procedure (double-angle shadow evaporation [11, 12]). Source: Courtesy of PTB.

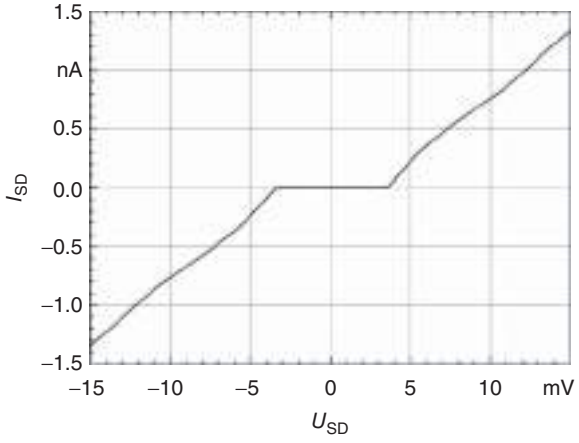

Figure 6.9 Source–drain current versus source–drain voltage of an $Al/AlO_x/Al/AlO_x/Al$ SET transistor measured at a temperature of 25 mK and a magnetic field of 1 T. The gate voltage was chosen to maximize the Coulomb blockade and a "Coulomb gap" of 7 meV is observed. Source: Courtesy of H. Scherer, PTB.

Other types of transfer errors can occur even at sufficiently low clock frequencies. A major source of error is higher-order tunneling, also named cotunneling [13, 14]. Cotunneling refers to the joint tunneling of two or more electrons through an SET transistor or SET pump in either direction. As an example, consider an SET transistor with one charge island and two tunnel barriers in the Coulomb blockade state when single-electron tunneling is energetically forbidden. One type of cotunneling process consists of the simultaneous transfer of one electron from the source lead to the island and another one from the island to the drain. This process leaves the charge on the island unchanged and does not violate energy conservation, but effectively transfers an electron to the drain. The transfer process can be viewed as quantum tunneling through a potential barrier resulting from the Coulomb energy. Obviously, this cotunneling process gives rise to a transfer error. The probability of cotunneling decreases with the increasing number of tunnel junctions in SET pumps [15].

Besides cotunneling, photon-assisted tunneling needs to be considered when analyzing the accuracy of metallic SET pumps [16, 17]. In this process, absorption of photons provides the energy required to lift an electron over the Coulomb barrier. The photon-assisted tunneling rate strongly depends on the shielding of the SET device against electromagnetic radiation [18].

Since the accuracy can be enhanced by a larger number of tunnel junctions, the National Institute of Standards and Technology (NIST) fabricated a seven-junction SET pump and experimentally demonstrated a transfer error of 1.5 parts in 10^8 at a clock frequency of 5.05 MHz [19]. The transfer error was determined pumping single electrons on and off an additional charge island, whose charge state was monitored by an SET electrometer (shuttle pumping). The excellent result of Ref. [19] was achieved by complex technology, which involves the synchronous tuning of six gate voltages. Despite the merits of metallic SET pumps, these results also illustrate their main drawbacks. Their clock frequency and current are limited, and a complex multiple-gate setup is required to achieve low uncertainties. The latter issue is aggravated by long-term stability problems due to uncontrolled background charges, which change the

properties of metallic SET pumps during operation. The nature and dynamics of the background charges are not yet completely understood.

An alternative way to suppress cotunneling using less tunnel junctions is to embed the SET device in a high-impedance environment [20]. The first so-called R-pump with three tunnel junctions and 60 kΩ on-chip resistors in series with the pump was demonstrated by the Physikalisch-Technische Bundesanstalt (PTB) in 2001 [21]. Three-junction R-pumps have not reached metrological accuracy. Therefore, five-junction R-pumps were developed, which achieved transfer errors of a few parts in 10^8 as determined by shuttle pumping [22]. Seven-junction SET pumps as well as five-junction R-pumps were used in fundamental consistency tests of electrical quantum metrology, which are discussed in Section 6.4 [23, 24].

6.2.2 Semiconducting Quantized Current Sources

Clocked single-electron transport in semiconductor structures is governed by the general principles that are outlined in Section 6.1 for metallic SET devices. Similar to their metallic counterparts, semiconducting quantized current sources are built from charge islands and tunnel barriers, sandwiched between a source and drain reservoir. Different driving schemes can be realized, such as turnstile or pumping operation.

Yet, there are two important aspects that distinguish semiconductor SET devices from metallic ones. In semiconductors, the density of free electrons is substantially smaller than in metals. The smaller density gives rise to a larger de Broglie wavelength, which is of the same order as the size of the charge island. Therefore, size quantization must be considered (see Section 5.1). The quantization energy must then be added to the Coulomb energy e^2/C_Σ. The result is a more complicated potential level structure compared to the equally spaced levels of a metallic charge island. The charge island in semiconductor SET devices should rather be viewed as a quantum dot, that is, a zero-dimensional structure with an atom-like energy spectrum.

The other important difference concerns the tunnel barriers. In metallic SET devices, the height and width of the tunnel barriers are fixed, being determined by the material properties and the thickness of the insulating layer. In contrast, the height and width of the tunnel barriers in semiconductors can be tuned by external gate voltages. We discuss in this section that the tunability of the tunnel barriers is the key to the operation of semiconductor SET devices at higher frequencies. A comprehensive review of quantized current sources with tunable barriers can be found in Ref. [25].

6.2.2.1 GaAs-Based SET Devices

Most semiconductor quantized current sources have been fabricated either from GaAs/AlGaAs or Si/SiO_2. We first discuss GaAs/AlGaAs SET devices. The fabrication of such devices starts with a high-mobility two-dimensional electron gas (2DEG) in a GaAs/$Al_xGa_{1-x}As$ heterostructure. Further details about the growth and the properties of GaAs/$Al_xGa_{1-x}As$ heterostructures can be found in Section 5.2. To fabricate a quantum dot, metal gate electrodes can be deposited on top of the heterostructure. The application of a negative voltage depletes the

Figure 6.10 Schematic layout of a GaAs/AlGaAs SET pump. Typical parameters: width of the one-dimensional channel, 700 nm; gate width, 100 nm; gate separation, 250 nm. An AC and a DC voltage are applied to the left gate, while only a DC voltage is applied to the right gate. Source: Courtesy of A. Müller, PTB.

2DEG underneath the gate electrodes and creates potential barriers. A quantum dot connected by tunnel barriers to a source and drain reservoir can be generated using appropriately shaped electrodes. The first experimental demonstration of clocked single-electron transfer in semiconductor structures was achieved with a turnstile device fabricated with this method [26].

Alternatively, first a one-dimensional conducting channel is defined by etching, which removes the 2DEG on either side of the channel. The channel is crossed by metallic gate electrodes to define tunnel barriers and, in turn, a quantum dot between the barriers. A schematic representation of such an SET device is shown in Figure 6.10. Both an AC and a DC voltage are applied to the left gate electrode (entrance gate). The potential of the exit gate on the right is adjusted by a DC voltage only.

The SET device of Figure 6.10 is a nonadiabatic GaAs/AlGaAs SET pump [27]. Its operation principle is illustrated in Figure 6.11, which schematically depicts the different phases of a pumping cycle. Shown is the potential along the conducting channel for fixed DC gate voltages. A single AC voltage modulates the entrance tunnel barrier. In (a), the entrance barrier is high and tunneling of electrons from the source reservoir into the dot is inhibited. As the entrance barrier is lowered and becomes more transparent, electrons tunnel into the quantum

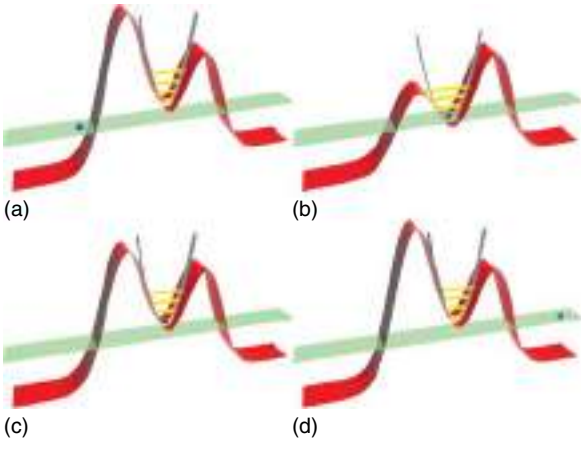

Figure 6.11 Schematic representation of the pumping cycle of a GaAs/AlGaAs SET pump. Shown is the temporally varying potential of the quantum dot (red), the energy levels of the dot (yellow), and the Fermi level (green). The transferred electron is shown as the blue dot. The different phases (a, b, c, d) of the pumping cycle are explained in the text. Source: Courtesy of A. Müller, PTB.

dot if the dot potential levels are located below the source Fermi level (b). The subsequent increase in the entrance barrier lifts the captured electrons above the Fermi level (c). As the captured electrons gain energy, they face an increasingly lower and more transparent exit barrier and, finally, tunnel out of the dot to the drain reservoir (d). For sufficiently small structures and low temperatures, the Coulomb blockade ensures that a small integer number of electrons are transferred per cycle. The integer number can be chosen by the adjustment of the DC gate voltages. A single electron is usually transferred per cycle for high-accuracy operation. Without going into details, we note that the parameters of the dynamic quantum dot do not instantaneously follow the clock frequency if it is in the megahertz to gigahertz range. This behavior classifies the pumping scheme as nonadiabatic. The nonadiabatic behavior is important since in the adiabatic limit, a directional current cannot be obtained applying a single periodic modulation signal [28].

Figure 6.12 shows the current generated with a nonadiabatic GaAs/AlGaAs SET pump as a function of the DC voltage applied to the exit gate. The entrance tunnel barrier was modulated at a clock frequency of 200 MHz and the temperature was 300 mK. The observation of a pronounced current plateaus proves that a quantized current has been generated. This current corresponds to the transfer of one electron per cycle of the clock frequency (32 pA for $f = 200$ MHz).

The uncertainty of the current measurement does not allow a meaningful value of the transfer error to be obtained from the experimental data only. However, the current–voltage characteristics can quantitatively be analyzed by a theoretical model of the transport process to estimate the transfer error [29]. The theoretical model relates the width of the current plateau to the transfer error. The model predicts a transfer error of 10^{-8} for the quantized current of Figure 6.12. This result suggests that GaAs/AlGaAs SET pumps can achieve uncertainties as low as

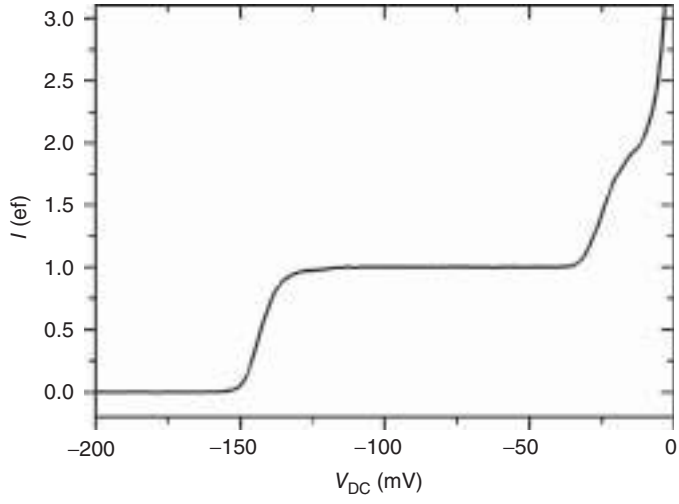

Figure 6.12 Current in units of *ef* as a function of the exit gate voltage. Clock frequency $f = 200$ MHz, temperature 300 mK, zero magnetic field. Source: Courtesy of F. Hohls, PTB.

those demonstrated with metallic SET pumps, yet at frequencies that are orders of magnitude higher.

In the following, we review the development and performance of GaAs/AlGaAs SET pumps. Their impact on metrology is discussed in Section 6.3.2. All experimental studies have in common that the GaAs/AlGaAs SET pumps are operated at low temperatures in the 1 K range and below. This temperature range ensures that the thermal energy is sufficiently small and that thermal excitations are sufficiently well suppressed.

In recent years, GaAs/AlGaAs SET pumps with a single AC gate voltage have mostly been studied [27]. This pumping scheme considerably simplifies the operation compared to schemes with two phase-shifted AC gate voltages [30]. GaAs-based SET pumps with a single AC gate voltage can generate accurately quantized currents at zero magnetic field [25, 31]. As an example, reconsider the data of Figure 6.12, which was obtained at zero magnetic field. Yet, the accuracy of GaAs-based SET pumps can often be improved by the application of a magnetic field [25, 32, 33]. This effect is not yet fully understood [25]. Nonetheless, applying a field of 14 T, the quantized current of an etch-defined GaAs SET pump was shown to agree with ef within a relative uncertainty of 1.2 parts in 10^6 at a clock frequency $f = 0.95$ GHz [34]. The quantized current was measured by comparison to a reference current, which was traceable to the Josephson effect and the QHE [34]. The quoted uncertainty is the uncertainty of the current measurement. The transfer error of the SET pump is smaller than or equal to the uncertainty of the current measurement. Thus, accurate current measuring techniques are required to exactly determine small transfer errors of SET pumps based on current measurements. A more detailed discussion of techniques for the traceable measurement of small currents can be found in Section 6.3.1.

Gate-defined GaAs SET pumps were also studied [35] using the same current measuring technique as in Ref. [34]. The quantized current was experimentally found to agree with ef within an uncertainty of 1.4 parts in 10^6 at 0.95 GHz and a field of 11 T [35]. These results indicate that well-performing nonadiabatic GaAs/AlGaAs SET pumps can be fabricated with different methods.

More information on the transfer error of nonadiabatic GaAs/AlGaAs SET pumps is obtained by an improved current measuring technique. This technique is known as ultrastable low-noise current amplifier (ULCA) [36]. It is discussed in more detail in Section 6.3.1. Using an ULCA, the quantized current of a GaAs SET pump was found to agree with ef within an uncertainty of 0.2 parts in 10^6 (at $f = 545$ MHz and a magnetic field of 16 T) [37]. The uncertainty could even be improved to 0.16 parts in 10^6 (at 600 MHz and 9.2 T) [38]. Thus, the transfer error of these GaAs SET pumps is smaller than or equal to 0.16 parts in 10^6. In Section 6.3.2, we discuss in more detail that these SET pumps realize the ampere in the present SI with an uncertainty that outperforms that of the ampere realization in the previous SI.

An important feature for the application of GaAs/AlGaAs SET pumps is their robust operation. Robust operation implies that the SET pumps can be operated over a broad range of DC gate voltages and AC voltage amplitudes. Broad operating margins of nonadiabatic single-gate GaAs/AlGaAs SET pumps were

reported as early as 2008 [39]. More recently, robust operation of a gate-defined GaAs/AlGaAs SET pump was observed at an uncertainty level of 1 part in 10^6 (at 500 MHz and 13.5 T) [40]. The robust operation of an etch-defined GaAs/AlGaAs SET pump was demonstrated at an uncertainty below 1 part in 10^6 [38].

We finally note that the single-gate pumping scheme paves the way to on-chip integration of several components due to its reduced complexity. In Ref. [41], a parallel circuit of three SET pumps was realized to increase the output current. On-chip integration of a GaAs/AlGaAs SET pump and a quantum Hall resistor was shown to yield an all-semiconductor source of quantized voltages [42]. Moreover, the integration of SET pumps and SET detectors can yield quantized current sources with improved accuracy [43, 44]. More details on this topic are given in Section 6.2.4.

6.2.2.2 Silicon-Based SET Devices

The operation principle of Si/SiO_2-based SET devices resembles that of GaAs/AlGaAs devices. The current through a narrow Si wire is controlled by metal-oxide-semiconductor field-effect transistors (MOSFETs). In their off-state, MOSFETs create opaque tunnel barriers and a quantum dot is formed between the barriers. The transparency of the barriers can be increased if the MOSFETs are switched to the on-state. SET pumping [45] and SET turnstile operation were demonstrated [46] based on the tunable barrier concept. In general, silicon technology allows very fine nanostructures to be fabricated, in which the Coulomb energy is increased. Consequently, SET operation can be observed at elevated temperatures on the order of 20 K, which are substantially higher than the operation temperatures of GaAs/AlGaAs devices.

In Ref. [45], SET pumping was demonstrated at 1 MHz and a temperature of 25 K. The transfer error was on the order of 1 part in 10^2. Soon after, turnstile operation was achieved at 20 K, producing a quantized current with a similar transfer error, yet at a considerably higher frequency of 100 MHz [46]. With a similar Si MOSFET device as in Ref. [46], single-gate SET pumping was demonstrated in Ref. [47]. In this work, the generation of a nanoampere quantized current was achieved, pumping three electrons per cycle of the clock frequency of 2.3 GHz. The transfer error was estimated to be on the order of 1 part in 10^2. A lower transfer error was reported for a quantized current generated with a device that consisted of a metallic NiSi nanowire interrupted by two tunnel barriers [48]. The barriers were defined by Si MOSFETs and the device was fabricated by industrial silicon-on-insulator (SOI) technology. A transfer error of the quantized current on the order of 1 part in 10^3 was reported for operation at a clock frequency of 650 MHz and a temperature of 0.5 K [48]. Quantized currents with a transfer error of a few parts in 10^5 could be demonstrated at a frequency of 500 MHz with an SET pump fabricated with silicon metal-oxide-semiconductor (MOS) technology [49]. The device was operated at a temperature of a few 100 mK.

More recently, a Si SET pump was studied using a current measuring system with an uncertainty slightly below 1 part in 10^6 [50]. The quantized current was found to agree with ef within an uncertainty of 0.92 parts in 10^6 at a clock frequency $f = 1$ GHz [50]. With an improved current measuring system, the quantized current of a Si SET pump could be shown to agree with ef within an

uncertainty of 0.27 parts in 10^6 at $f = 1\,\mathrm{GHz}$ [51] (more details on the current measuring systems are discussed in Section 6.3.1). The transfer error of these Si SET pumps is equal to or smaller than the quoted uncertainties. The small transfer errors were obtained at temperatures on the order of 1 K [50, 51]. A comparison with the results obtained with GaAs SET pumps (see Section 6.2.2.1) shows that semiconductor SET pumps with low transfer errors can be fabricated with different material systems, indicating the universality of the concept.

As an outlook, we like to mention that Si SET pumps were investigated, in which the pumping scheme involved trap levels or donor states [52–55]. This work is motivated by the notion that trap or donor states can have activation energies of a few 10 meV [53]. These large energies may facilitate accurate pumping of single electrons at higher frequencies and temperatures.

Looking beyond Si-based and GaAs-based semiconductor devices, it is worth noting that clocked single-electron transfer at gigahertz frequencies was also observed in a graphene structure [56] (see Section 5.5 for details about graphene).

6.2.3 Superconducting Quantized Current Sources

In this section, metallic devices are discussed, in which superconductivity plays a role. We begin with hybrid devices, which contain both normal and superconducting metals. At the end of the section, we briefly introduce devices in which all metallic elements are in the superconducting state.

Let us consider an SET transistor, like that shown in Figure 6.2, with a normal-metal charge island separated from superconducting source and drain leads by fixed insulating tunnel barriers. This SINIS structure (S superconductor, I insulator, N normal metal) was introduced in Ref. [57] together with the complementary NISIN structure. The SINIS circuit shows the better performance [4]; hence, we will restrict our discussion to it. A realistic implementation is, for example, an Al/Al oxide/Cu/Al oxide/Al structure where Al is in the superconducting state. To generate a quantized current, a periodic voltage is applied to the gate electrode of the SINIS circuit and the circuit is biased with a DC source–drain voltage. Thus, a turnstile device is realized.

In Section 6.1.4, we have discussed that clocked single-electron transfer cannot be achieved with a single all-normal-metal (NININ) SET transistor. The important difference between NININ and SINIS SET transistors is the superconducting gap, which enables clocked single-electron transfer in SINIS turnstiles. The operating principle is schematically illustrated in Figure 6.13. Frame (a) shows the tunneling of an electron from the filled states of the superconducting source lead to the normal-metal charge island. This process takes place when the filled states of the source are aligned with the lowest empty level of the charge island. After this tunneling process, the electron cannot leave the charge island since the empty states of the drain lead are located at higher energies due to the superconducting gap. Subsequently, the potential levels of the charge island are raised by an appropriate adjustment of the gate voltage as shown in frame (b). Frame (c) illustrates the final step of the cycle. The highest filled level of the island has been raised above the superconducting gap of the drain lead and the electron can tunnel to

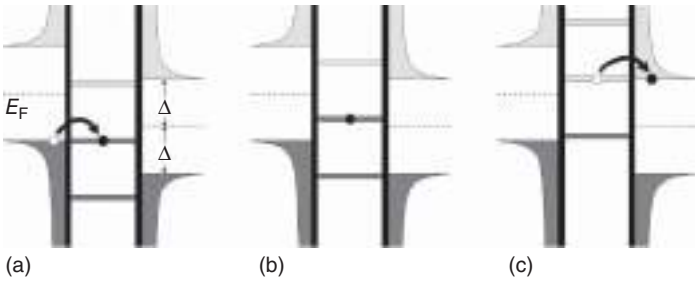

Figure 6.13 Operating principle of an SINIS turnstile. Shown is the density of states of the superconducting source (left) and drain (right) lead and the chemical potential of the normal-metal charge island (center of each frame). (a) Tunneling of a single electron onto the normal-metal charge island. (b) Increase in the chemical potential of the charge island due to the change of the gate voltage. (c) Tunneling of the electron to the superconducting drain lead. 2Δ is the superconducting gap and E_F the Fermi level. Source: Courtesy of A. Müller, PTB.

empty drain states. Note that in this phase, the superconducting gap of the source lead inhibits the uncontrolled transfer of another electron from the source to the island.

Transfer errors can occur due to higher-order tunneling processes, which are theoretically analyzed in Ref. [58]. Theory predicts that quantized currents of 30 pA can be generated with a transfer error of 10^{-8} with SINIS turnstiles [58]. For real structures, the current is expected to be limited to 10 pA at this uncertainty due to the nonuniformity of the tunnel barriers [4]. Accuracies of the quantized current on the order of 10^{-3} were experimentally demonstrated, limited by the uncertainty of the measuring instrument [59]. The experimental work has also highlighted the importance of engineering the on-chip environment of SINIS turnstiles to suppress higher-order tunneling processes [60–62].

An important advantage of SINIS turnstiles is their operation by a single periodic gate voltage only. As for semiconductor SET pumps (see Section 6.2.2), single-gate operation facilitates the fabrication of parallel circuits with increased output current. The parallel operation of 10 SINIS turnstiles was demonstrated in Ref. [63]. The parallel circuit generated a quantized current of 104 pA at a clock frequency of 65 MHz. The hybrid SINIS turnstile is a promising and versatile concept, which was also implemented with a carbon nanotube as normal conductor [64].

In the following, we discuss all-superconductor devices, which seem to have several conceptual advantages. In such devices, Cooper pairs with charge $(-2e)$ are transferred without dissipation. The dissipationless transport avoids adverse heating effects. Moreover, the doubling of the charge compared to the transport of single electrons doubles the current at a given clock frequency. One may also argue that in all-superconductor devices, the transport is coherent and, therefore, better controllable than transport based on stochastic tunneling.

Experimentally, superconducting quantized charge pumps were investigated that consisted of several superconducting charge islands separated from each other and from the superconducting source and drain leads by fixed tunnel barriers. The charge on the superconducting islands could be adjusted by gate

voltages. Thus, the device design resembles that shown in Figure 6.6. Moreover, the pumping concept resembles that described in Section 6.1.4 for normal-metal SET pumps. Three-junction and seven-junction superconducting pumps were realized with this concept [65, 66]. Yet, the transfer error of the quantized current was found to be unsatisfactory. This result is ascribed to quasiparticle tunneling, that is, the transfer of single charges e, taking place in addition to Cooper pair tunneling.

Another type of superconducting quantized charge device is the so-called superconducting sluice [67]. The device consists of a single superconducting island whose charge can be controlled by an AC gate voltage. The charge island is connected to source and drain leads using superconducting quantum interference devices (SQUIDs), which act as switches. Switching between the on- and off-state of the SQUIDs is realized by magnetic flux pulses, which modulate the critical current of the SQUIDs (see Section 4.2). The flux pulses are synchronized to the AC gate voltage so that clocked Cooper pair transfer can be realized. Quantized currents of about 1 nA were demonstrated with this concept, yet the accuracy of the current could not be improved beyond the 10^{-2} range [68].

Summarizing these results, the experimental realizations of all-superconductor quantized charge devices have not yet fulfilled the expectations discussed earlier assuming an ideal device. One reason is quasiparticle tunneling, which is not accounted for in the picture of an ideal superconducting circuit.

As an outlook, we like to mention that there are other theoretical concepts for quantized current sources based on superconductors. Examples are the phase-locking of Bloch oscillations [5] and quantum phase slip devices [69]. These concepts are intriguing since they involve current steps that are the dual of the Shapiro steps of Josephson voltage standards. In this approach, the transport of Cooper pairs does not rely on stochastic tunneling, which holds the promise of higher accuracy. However, the experimental realization of such quantized current sources is still in its infancy.

6.2.4 Self-Referenced Quantized Current Sources

In this section, we discuss a concept that has the potential to improve the accuracy of quantized current sources. With very few exceptions, quantized current sources rely on the stochastic tunneling of single electrons. Errors may occur due to the stochastic nature of single-electron tunneling. For example, there is a nonzero probability that no electron is pumped in a certain cycle of the clock frequency. Therefore, the transfer error cannot be reduced to zero. Yet, the quantized current can be determined more accurately if information on error events is available and if this information is used to determine the value of the quantized current. Consequently, it was proposed to incorporate SET detectors in a series circuit of SET current sources to monitor the error events in situ [43]. With the information on the errors, the quantized current of the series circuit can be determined with an accuracy that is higher than that of the individual SET current sources [43].

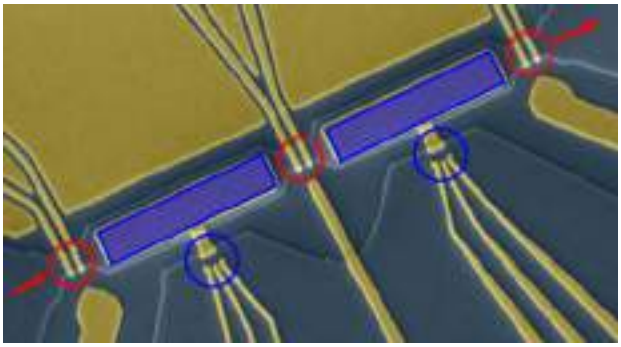

Figure 6.14 SEM image of a self-referenced quantized current source. Three GaAs/AlGaAs SET pumps (red circles) are connected in series via charge islands (blue boxes). GaAs quantum dots are used as SET detectors (blue circles) to monitor the charge on the islands. The red arrows indicate the quantized current in the electron source (left) and drain lead (right). Source: Courtesy of F. Hohls, PTB.

Figure 6.14 illustrates the concept, which is known as a self-referenced quantized current source [44]. The figure shows three GaAs/AlGaAs SET pumps connected in series and sandwiched between a source and a drain lead. Charge islands have been fabricated between adjacent SET pumps, and the charge state of these islands is monitored by SET detectors. The integrated circuit allows the errors to be monitored in situ, that is, while a quantized current is generated and supplied to the drain lead. The error accounting scheme can be applied if the bandwidth of the SET detectors is larger than the error rate [43]. The detector bandwidth does not have to exceed the much larger clock frequency. This relaxed requirement substantially facilitates the experimental implementation of self-referenced quantized current sources.

In self-referenced quantized current sources, the errors are monitored while the source generates a quantized current. To emphasize this fact, we compare them with other experimental arrangements that involve SET current sources and SET detectors. These arrangements include setups for shuttle pumping and the determination of the probability distribution of electron transfer. Shuttle pumping was used to determine the transfer error of metallic single-electron pumps [19, 22] and Si-based SET current sources [70, 71]. In shuttle pumping experiments, single electrons are pumped on and off a charge island. No net quantized current is generated during the shuttle pumping. The determination of the probability distribution of electron transfer (counting statistics) is reported in Refs. [72–74]. An SET current source was used to transfer electrons to a charge island whose charge state was monitored. These experiments did not involve the continuous supply of electrons to a drain lead. Thus, no useable current was generated.

A proof-of-principle experiment to demonstrate a self-referenced quantized current source was realized using GaAs/AlGaAs SET pumps combined with metallic SET electrometers [44]. The integrated circuit was operated at a clock frequency of 30 Hz. The uncertainty achieved with the integrated circuit was shown to be 50 times lower than that achieved with a single SET pump [44].

6.3 Realization of the SI Ampere

The SI ampere can be realized with current sources or current meters, which link the generated current or the current measurement to the elementary charge e as defining constant of the present SI. An indirect link is established using Ohm's law and realizations of the SI volt and SI ohm based on the Josephson effect and QHE, respectively. This approach is discussed in Section 6.3.1. A direct realization of the SI ampere is obtained with quantized current sources as discussed at the beginning of this chapter. The state-of-the-art of the direct ampere realization is treated in Section 6.3.2.

The quality of any unit realization is judged by its uncertainty. To establish a baseline, we briefly recall how the ampere was realized and which uncertainty was achieved in the previous SI. The most accurate realization of the previous SI ampere was based on the previous SI volt and ohm and the use of Ohm's law. The uncertainty of the SI ampere was limited by the uncertainty of the SI volt, which was larger than the uncertainty of the SI ohm. The previous SI volt could be realized with an uncertainty of approximately three parts in 10^7 using the so-called voltage balance [75], as discussed in Section 4.1.5.1. In turn, the SI ampere could be realized with the same uncertainty in the previous SI [76].

In Section 6.3, we focus on concepts for the ampere realization in the present SI, which can achieve uncertainties of a few parts in 10^7 or better, that is, realizations with uncertainties that match or outperform those achieved in the previous SI. Therefore, we mention only briefly here that the SI ampere can also be realized applying a voltage, which linearly varies in time, to a capacitor to generate a capacitive current [77]. The concept is based on the relation $I = \mathrm{d}Q/\mathrm{d}t = C\,\mathrm{d}U/\mathrm{d}t$. The SI ampere is realized if the SI values of the time-varying voltage and the capacitance are known. The method generates currents in the subnanoampere to femtoampere range with uncertainties of several 10 parts in 10^6 and larger.

6.3.1 Ampere Realization via the SI Volt and SI Ohm

In the present SI, the volt and ohm are linked to the Josephson constant K_J=$2e/h$ and the von Klitzing constant $R_\mathrm{K} = h/e^2$ by the Josephson effect and the QHE, respectively (see Chapters 4 and 5). Since voltage values are proportional to K_J^{-1} and resistance values to R_K, applying Ohm's law $I = U/R$ yields current values that are proportional to $(K_\mathrm{J}\,R_\mathrm{K})^{-1} = e/2$. Thus, the SI ampere is realized due to the link to the defining constant e.

Any current-measuring setup or current source, which involves realizations of the SI volt and SI ohm based on the Josephson effect and the QHE, respectively, can be viewed as the realization of the SI ampere. The uncertainties of SI ampere realizations vary widely. Relative uncertainties of one part in 10^6 and higher are achieved in calibrations for industry [78, 79]. The uncertainty tends to increase for smaller currents and is larger than 10 parts in 10^6 for currents below 10 nA in these calibrations [78, 79].

References [34, 35, 40, 50, 51] report current-measuring setups optimized for the measurement of small currents on the order of 100 pA. To improve the accuracy of the current measurement, a reference current was generated applying

a voltage to a resistor. The voltage was traceable to the Josephson constant K_J. Traceability to the von Klitzing constant R_K was achieved using a calibrated artifact resistance standard of 1 GΩ. The unknown current was compared to the reference current measuring the difference between the two currents. Since the difference is small, the uncertainty of this measurement affects the overall uncertainty only slightly. After the calibration of the 1 GΩ artifact standard had been improved, a relative uncertainty of 0.27 parts in 10^6 was achieved when measuring a current of 160 pA [51]. This uncertainty is comparable to that of the most accurate realization of the ampere in the previous SI.

More accurate measurements of small currents can be realized using a concept known as the ULCA [36]. The ULCA consists of two stages if it is operated as current meter. In the input stage, the current is amplified by an operational amplifier and a resistor network, which implements a 3-GΩ/3-MΩ resistance ratio in the standard configuration of Ref. [36]. Thus, a current gain of 1000 is realized. The amplified current is then converted into a voltage in the output stage. The output stage typically has a transresistance of 1 MΩ [36], yielding an overall transresistance of 1 GΩ. The resistor network of the input stage consists of several thousand carefully selected thin-film chip resistors [36]. With this concept, low input noise levels on the order of a few $\mathrm{fA/Hz^{-1/2}}$, a small drift of the transresistance (uncertainty contribution 0.1 parts in 10^6 per week), and small temperature coefficients of the current gain and transresistance (on the order of 0.1 parts in 10^6 per kelvin) can be achieved [36]. The ULCA is operated at room temperature, making it a practical and easy-to-use instrument. It can also be used as current source if the current-to-voltage conversion is not implemented.

The input stage of the ULCA, that is, the current ratio, can accurately be determined with a cryogenic current comparator (CCC) [80] (for more details on CCCs, see Section 4.2.3.3). Reference [81] has shown that this measurement can be performed with a relative uncertainty of 0.06 parts in 10^6. The transresistance of the output stage can be linked to the von Klitzing constant R_K using a CCC and a DC quantum Hall resistance standard. If the output voltage is linked to the Josephson constant K_J, the ULCA realizes the SI ampere based on Ohm's law.

Different versions of the ULCA have been developed, which can be used to realize the SI ampere from the femtoampere to the microampere range [82]. The different ULCA versions have been optimized for different purposes in low-current metrology [82, 83], whose importance increases, for example, in radiation dosimetry or for concentration measurements of nanoparticles in aerosols [79]. Regarding fundamental metrology, we like to emphasize the importance of the ULCA for the characterization of SET pumps. The ULCA allowed small currents of SET pumps to be measured with uncertainties as low as 0.16 parts in 10^6 [38], as discussed in Section 6.2.2.1.

The uncertainty of the ampere realization based on Ohm's law can be further reduced if the use of artifact standards is avoided. Reference [78] reports a quantum current generator based on a DC quantum Hall resistance standard and a programmable binary Josephson voltage standard. The quantum standards are connected using the so-called multiple connection technique to reduce the contribution of contact resistances [84] as discussed in Section 5.4.3. They generate a current without resorting to artifact voltage and resistance standards. The

current is amplified by a CCC. The Josephson voltage standard, the quantum Hall resistance standard, and the CCC are operated in three different cryogenic setups. Amplified currents of approximately 1 mA were experimentally shown to have an uncertainty of one part in 10^8, thereby realizing the SI ampere with this uncertainty. Theoretical analysis shows that through this approach the ampere can be realized with an uncertainty of one part in 10^8 over the range from 1 μA to 10 mA [78].

6.3.2 Direct Ampere Realization with Quantized Current Sources

The SI ampere is realized in a direct way, that is, without resorting to Ohm's law and the SI volt and ohm, if a quantized current is generated according to Eq. (6.1). Here, we summarize which quantized current sources have been shown to realize the SI ampere with an uncertainty of a few parts in 10^7 or better. As mentioned earlier, this uncertainty of the ampere realization was achieved in the previous SI [76] and can be viewed as the benchmark for the ampere realizations in the present SI. The important parameter, which determines the accuracy of a quantized current source and, hence, the uncertainty of the direct ampere realization, is the transfer error, as discussed at the beginning of Section 6.2.

A transfer error of 1.5 parts in 10^8 was achieved with a seven-junction metallic SET pump at a clock frequency of 5.05 MHz [19] (see Section 6.2.1). Five-junction R-pumps achieved transfer errors of a few parts in 10^8 [22]. Both types of SET devices realize the ampere in the range of 1 pA. Such small currents are sufficient for experiments, in which not the current itself is measured, but the charge that is accumulated operating the quantized current source for a well-defined time [23, 24].

An accurate ampere realization in the 100 pA range can be achieved with semiconducting quantized current sources, as discussed in Section 6.2.2. GaAs SET pumps were experimentally shown to have a transfer error of at most 0.16 parts in 10^6 when generating a current of 96 pA [38]. The quantized current of a Si SET pump was experimentally shown to have a transfer error of at most 0.27 parts in 10^6 when generating a current of 160 pA [51]. All ampere realizations with quantized current sources mentioned in this section have an uncertainty that either matches [51] or outperforms [19, 22, 38] the uncertainty of the ampere realization in the previous SI.

6.4 Consistency Tests: Quantum Metrology Triangle

The QMT is a consistency test of the three electrical quantum effects – the Josephson effect, the QHE, and single-charge transfer. The QMT aims at verifying the relation of the quantized voltage and resistance to the Josephson constant $K_J = 2e/h$ and the von Klitzing constant $R_K = h/e^2$, respectively. Moreover, the QMT intends to verify that the quantized charge q_S, which is transferred through an SET device, is exactly equal to the elementary charge e, as assumed in Eq. (6.1). Thus, the aim of the QMT is to verify that the electrical SI units can indeed be realized as described in Chapters 4–6.

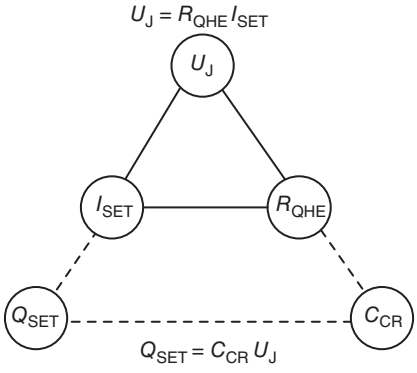

Figure 6.15 The quantum metrology triangle in the current version applying Ohm's law (upper part, solid lines). As an alternative, the charging of a capacitor is studied in the charge version of the quantum metrology triangle (lower part, dashed lines). Source: Göbel and Siegner 2015 [6]. Reproduced with permission of John Wiley & Sons.

The QMT is based on Ohm's law, which is illustrated by the upper triangle in Figure 6.15. In this section, we briefly discuss the basic idea of the QMT experiment, its experimental implementations, and their results. Comprehensive reviews can be found in Refs. [22, 85].

For convenience, we recall the respective equations of the three quantum effects:

$$U_J = \frac{n_J f_J}{K_J} \tag{6.10}$$

$$R_{QHE} = \frac{R_K}{i} \tag{6.11}$$

$$I_{SET} = \langle n_S \rangle e f_S \tag{6.12}$$

Equation (6.12) contains the average number of transferred elementary charges $\langle n_S \rangle$ to account for the occurrence of transfer errors. Using Ohm's law, we obtain from Eqs. (6.10)–(6.12)

$$\frac{n_J i}{\langle n_S \rangle} \frac{f_J}{f_S} = K_J R_K e = 2 \tag{6.13}$$

In this equation, n_J and i are known integer step numbers. The frequency ratio f_J/f_S and the average number of transferred charges $\langle n_S \rangle$ must be determined experimentally. To determine $\langle n_S \rangle$, a self-referenced quantized current source [43, 44] is needed (see Section 6.2.4 for more details on self-referenced quantized current sources). A measurement of the current is not sufficient for this purpose since it would only determine the product of q_S and $\langle n_S \rangle$. The proof that Eq. (6.13) is valid is often referred to as the closure of the QMT. Any deviation would cast doubt on the strict validity of at least one of the equations $K_J = 2e/h$, $R_K = h/e^2$, and $q_S = e$.

Different approaches have been followed to close the QMT experimentally. In a straightforward one, the quantized current generated by an SET device is supplied to a quantum Hall resistor, and the Hall voltage is measured by comparison to a Josephson voltage standard. Even if a nanoampere quantized current source is available, current amplification is required to achieve an uncertainty on the order of 10^{-7}. The use of a CCC with a high winding ratio

was suggested for this purpose [86]. Such an experiment was realized with a normal-metal three-junction R-pump as quantized current source [87]. Yet, the experimental setup did not allow $\langle n_S \rangle$ to be measured independently. Therefore, the closure of the QMT could not be investigated. At the time of writing, the closure of a QMT, which directly implements Ohm's law, was not yet reported.

In an indirect approach developed first at the NIST, a cryogenic capacitor with capacitance C_{CR} is charged by an SET device. The "charge version" of the QMT is illustrated in the lower part of Figure 6.15. A total charge $Q_{SET} = \langle n_S \rangle e f_S T_S$ is accumulated over a well-known time T_S. The voltage across the capacitor is measured by comparison to a Josephson voltage standard. As described in Section 5.4.4, the value of C_{CR} can be linked to R_{QHE} via a quadrature bridge. The QMT experiment can be combined with an electron shuttle pumping measurement, which determines the average number of transferred elementary charges $\langle n_S \rangle$. Using a seven-junction SET pump, the NIST experiment demonstrated the closure of the QMT with a relative standard uncertainty of 0.9 parts in 10^6 [23, 88]. The PTB reported the closure of the QMT with an uncertainty of 1.7 parts in 10^6 using a five-junction R-pump to charge the capacitor [24].

Regarding the implications of these results, we first recall that the Josephson effect and the QHE are highly reproducible, as discussed in Sections 4.1.4 and 5.4.1, respectively. Yet, strictly speaking, the high reproducibility only implies that the effects are universal, but does not give information on how well they are described by the defining constants e and h. More information is obtained from theory, which does not predict any appreciable deviation from $K_J = 2e/h$ and $R_K = h/e^2$ (for a more detailed discussion, see [4, 85]). However, theory alone cannot provide a rigorous proof of the validity of the relations, but experimental data should also be analyzed. Such an analysis has been made in the framework of the adjustment of the fundamental constants [89]. The adjustment of 2014 verifies the validity of the relations $R_K = h/e^2$ and $K_J = 2e/h$ at the level of 10^{-8} [89]. Thus, the present QMT results mainly support the precision of charge quantization at the level of 10^{-6}. The improvement of QMT experiments toward the 10^{-8} level is desirable even though the electrical quantum effects already rest on very solid grounds.

References

1 Grabert, H. and Devoret, M.H. (eds.) (1992). *Single Charge Tunneling*. New York: Plenum Press.

2 Likharev, K.K. (1999). Single-electron devices and their application. *Proc. IEEE* 87: 606–632.

3 Ono, Y., Fujiwara, A., Nishiguchi, K. et al. (2005). Manipulation and detection of single electrons for future information processing. *J. Appl. Phys.* 97: 031101 (19 pp).

4 Pekola, J.P., Saira, O.-P., Maisi, V.F. et al. (2013). Single-electron current sources: toward a refined definition of the ampere. *Rev. Mod. Phys.* 85: 1421–1472.

5 Likharev, K.K. and Zorin, A.B. (1985). Theory of the Bloch-wave oscillations in small Josephson junctions. *J. Low Temp. Phys.* 59: 347–382.

6 Göbel, E.O. and Siegner, U. (2015). *Quantum Metrology: Foundations of Units and Measurements*. Weinheim: Wiley-VCH.

7 Fulton, T.A. and Dolan, G.J. (1987). Observation of single-electron charging effects in small tunnel junctions. *Phys. Rev. Lett.* 59: 109–112.

8 Kuzmin, L.S. and Likharev, K.K. (1987). Direct experimental observation of discrete correlated single-electron tunneling. *JETP Lett.* 45: 495–497.

9 Pothier, H., Lafarge, P., Orfila, P.F. et al. (1991). Single electron pump fabricated with ultrasmall normal tunnel junctions. *Physica B* 169: 573–574.

10 Geerligs, L.J., Anderegg, V.F., Holweg, P.A.M. et al. (1990). Frequency-locked turnstile device for single electrons. *Phys. Rev. Lett.* 64: 2691–2694.

11 Niemeyer, J. and Kose, V. (1976). Observation of large DC supercurrents at nonzero voltages in Josephson tunnel junctions. *Appl. Phys. Lett.* 29: 380–382.

12 Dolan, G.J. (1977). Offset masks for liftoff photoprocessing. *Appl. Phys. Lett.* 31: 337–339.

13 Averin, D.V. and Odintsov, A.A. (1989). Macroscopic quantum tunneling of the electric charge in small tunnel junctions. *Phys. Lett. A* 140: 251–257.

14 Geerligs, L.J., Averin, D.V., and Mooij, J.E. (1990). Observation of macroscopic quantum tunneling through the coulomb energy barrier. *Phys. Rev. Lett.* 65: 3037–3040.

15 Jensen, H.D. and Martinis, J.M. (1992). Accuracy of the electron pump. *Phys. Rev. B* 46: 13407–13427.

16 Martinis, J.M. and Nahum, M. (1993). Effect of environmental noise on the accuracy of Coulomb-blockade devices. *Phys. Rev. B* 48: 18316–18319.

17 Kautz, R.L., Keller, M.W., and Martinis, J.M. (2000). Noise-induced leakage and counting errors in the electron pump. *Phys. Rev. B* 62: 15888–15902.

18 Kemppinen, A., Lotkhov, S.V., Saira, O.-P. et al. (2011). Long hold times in a two-junction electron trap. *Appl. Phys. Lett.* 99: 142106 (3 pp).

19 Keller, M.W., Martinis, J.M., Zimmerman, N.M., and Steinbach, A.H. (1996). Accuracy of electron counting using a 7-junction electron pump. *Appl. Phys. Lett.* 69: 1804–1806.

20 Odintsov, A.A., Bubanja, V., and Schön, G. (1992). Influence of electromagnetic fluctuations on electron cotunneling. *Phys. Rev. B* 46: 6875–6881.

21 Lotkhov, S.V., Bogoslovsky, S.A., Zorin, A.B., and Niemeyer, J. (2001). Operation of a three-junction single-electron pump with on-chip resistors. *Appl. Phys. Lett.* 78: 946–948.

22 Scherer, H. and Camarota, B. (2012). Quantum metrology triangle experiments: a status review. *Meas. Sci. Technol.* 23: 124010 (13 pp).

23 Keller, M.W., Eichenberger, A.L., Martinis, J.M., and Zimmerman, N.M. (1999). A capacitance standard based on counting electrons. *Science* 285: 1706–1709.

24 Camarota, B., Scherer, H., Keller, M.V. et al. (2012). Electron counting capacitance standard with an improved five-junction R-pump. *Metrologia* 49: 8–14.

25 Kaestner, B. and Kashcheyevs, V. (2015). Non-adiabatic quantized charge pumping with tunable-barrier quantum dots: a review of current progress. *Rep. Prog. Phys.* 78: 103901 (27 pp).

26 Kouwenhoven, L.P., Johnson, A.T., van der Vaart, N.C. et al. (1991). Quantized current in a quantum-dot turnstile using oscillating tunnel barriers. *Phys. Rev. Lett.* 67: 1626–1629.

27 Kaestner, B., Kashcheyevs, V., Amakawa, S. et al. (2008). Single-parameter nonadiabatic quantized charge pumping. *Phys. Rev. B* 77: 153301 (4 pp).

28 Moskalets, M. and Büttiker, M. (2002). Floquet scattering theory of quantum pumps. *Phys. Rev. B* 66: 205320 (10 pp).

29 Kashcheyevs, V. and Kaestner, B. (2010). Universal decay cascade model for dynamic quantum dot initialization. *Phys. Rev. Lett.* 104: 186805 (4 pp).

30 Blumenthal, M.D., Kaestner, B., Li, L. et al. (2007). Gigahertz quantized charge pumping. *Nat. Phys.* 3: 343–347.

31 Seo, M., Ahn, Y.-H., Oh, Y. et al. (2014). Improvement of electron pump accuracy by a potential-shape-tunable quantum dot pump. *Phys. Rev. B* 90: 085307 (5 pp).

32 Wright, S.J., Blumenthal, M.D., Gumbs, G. et al. (2008). Enhanced current quantization in high-frequency electron pumps in a perpendicular magnetic field. *Phys. Rev. B* 78: 233311 (4 pp).

33 Kaestner, B., Leicht, C., Kashcheyevs, V. et al. (2009). Single-parameter quantized charge pumping in high magnetic fields. *Appl. Phys. Lett.* 94: 012106 (3 pp).

34 Giblin, S.P., Kataoka, M., Fletcher, J.D. et al. (2012). Towards a quantum representation of the ampere using single electron pumps. *Nat. Commun.* 3: 930 (6 pp).

35 Bae, M.-H., Ahn, Y.-H., Seo, M. et al. (2015). Precision measurement of a potential-profile tunable single-electron pump. *Metrologia* 52: 195–200.

36 Drung, D., Krause, C., Becker, U. et al. (2015). Ultrastable low-noise current amplifier: a novel device for measuring small electric currents with high accuracy. *Rev. Sci. Instrum.* 86: 024703 (10 pp).

37 Stein, F., Drung, D., Fricke, L. et al. (2015). Validation of a quantized-current source with 0.2 ppm uncertainty. *Appl. Phys. Lett.* 107: 103501 (5 pp).

38 Stein, F., Scherer, H., Gerster, T. et al. (2017). Robustness of single-electron pumps at sub-ppm current accuracy level. *Metrologia* 54: S1–S8.

39 Kaestner, B., Kashcheyevs, V., Hein, G. et al. (2008). Robust single-parameter quantized charge pumping. *Appl. Phys. Lett.* 92: 192106 (3 pp).

40 Giblin, S.P., Bae, M.-H., Kim, N. et al. (2017). Robust operation of a GaAs tunable barrier electron pump. *Metrologia* 54: 299–306.

41 Mirovsky, P., Kaestner, B., Leicht, C. et al. (2010). Synchronized single electron emission from dynamical quantum dots. *Appl. Phys. Lett.* 97: 252104 (3 pp).

42 Hohls, F., Welker, A.C., Leicht, C. et al. (2012). Semiconductor quantized voltage source. *Phys. Rev. Lett.* 109: 056802 (5 pp).

43 Wulf, M. (2013). Error accounting algorithm for electron counting experiments. *Phys. Rev. B* 87: 035312 (5 pp).

44 Fricke, L., Wulf, M., Kaestner, B. et al. (2014). Self-referenced single-electron quantized current source. *Phys. Rev. Lett.* 112: 226803 (6 pp).

45 Ono, Y. and Takahashi, Y. (2003). Electron pump by a combined single-electron/field-effect transistor structure. *Appl. Phys. Lett.* 82: 1221–1223.

46 Fujiwara, A., Zimmerman, N.M., Ono, Y., and Takahashi, Y. (2004). Current quantization due to single-electron transfer in Si-wire charge-coupled devices. *Appl. Phys. Lett.* 84: 1323–1325.

47 Fujiwara, A., Nishiguchi, K., and Ono, Y. (2008). Nanoampere charge pump by single-electron ratchet using silicon nanowire metal-oxide-semiconductor field-effect transistor. *Appl. Phys. Lett.* 92: 042102 (3 pp).

48 Jehl, X., Voisin, B., Charron, T. et al. (2013). Hybrid metal–semiconductor electron pump for quantum metrology. *Phys. Rev. X* 3: 021012 (7 pp).

49 Rossi, A., Tanttu, T., Yen Tan, K. et al. (2014). An accurate single-electron pump based on a highly tunable silicon quantum dot. *Nano Lett.* 14: 3405–3411.

50 Yamahata, G., Giblin, S.P., Kataoka, M. et al. (2016). Gigahertz single-electron pumping in silicon with an accuracy better than 9.2 parts in 10^7. *Appl. Phys. Lett.* 109: 013101 (5 pp).

51 Zhao, R., Rossi, A., Giblin, S.P. et al. (2017). Thermal-error regime in high-accuracy gigahertz single-electron pumping. *Phys. Rev. Appl.* 8: 044021 (8 pp).

52 Tettamanzi, G.C., Wacquez, R., and Rogge, S. (2014). Charge pumping through a single donor atom. *New J. Phys.* 16: 063036 (17 pp).

53 Yamahata, G., Nishiguchi, K., and Fujiwara, A. (2014). Gigahertz single-trap electron pumps in silicon. *Nat. Commun.* 5: 5038 (7 pp).

54 Wenz, T., Hohls, F., Jehl, X. et al. (2016). Dopant-controlled single-electron pumping through a metallic island. *Appl. Phys. Lett.* 108: 213107 (4 pp).

55 Yamahata, G., Giblin, S.P., Kataoka, M. et al. (2017). High-accuracy current generation in the nanoampere regime from a silicon single-trap electron pump. *Scientific Reports* 7: 45137 (8 pp).

56 Connolly, M.R., Chiu, K.L., Giblin, S.P. et al. (2013). Gigahertz quantized charge pumping in graphene quantum dots. *Nat. Nanotechnol.* 8: 417–420.

57 Pekola, J.P., Vartiainen, J.J., Möttönen, M. et al. (2008). Hybrid single-electron transistor as a source of quantized electric current. *Nat. Phys.* 4: 120–124.

58 Averin, D.V. and Pekola, J.P. (2008). Nonadiabatic charge pumping in a hybrid single-electron transistor. *Phys. Rev. Lett.* 101: 066801 (4 pp).

59 Aref, T., Maisi, V.F., Gustafsson, M.V. et al. (2011). Andreev tunneling in charge pumping with SINIS turnstiles. *Europhys. Lett.* 96: 37008 (6 pp).

60 Lotkhov, S.V., Kemppinen, A., Kafanov, S. et al. (2009). Pumping properties of the hybrid single-electron transistor in dissipative environment. *Appl. Phys. Lett.* 95: 112507 (3 pp).

61 Pekola, J.P., Maisi, V.F., Kafanov, S. et al. (2010). Environment-assisted tunneling as an origin of the dynes density of states. *Phys. Rev. Lett.* 105: 026803 (4 pp).

62 Saira, O.-P., Möttönen, M., Maisi, V.F., and Pekola, J.P. (2010). Environmentally activated tunneling events in a hybrid single-electron box. *Phys. Rev. B* 82: 155443 (6 pp).

63 Maisi, V.F., Pashkin, Y.A., Kafanov, S. et al. (2009). Parallel pumping of electrons. *New J. Phys.* 11: 113057 (9 pp).

64 Siegle, V., Liang, C.-W., Kaestner, B. et al. (2010). A molecular quantized charge pump. *Nano Lett.* 10: 3841–3845.

65 Geerligs, L.J., Verbrugh, S.M., Hadley, P. et al. (1991). Single Cooper pair pump. *Z. Phys. B* 85: 349–355.

66 Aumentado, J., Keller, M.W., and Martinis, J.M. (2003). A seven-junction Cooper pair pump. *Physica E* 18: 37–38.

67 Niskanen, A.O., Pekola, J.P., and Seppä, H. (2003). Fast and accurate single-island charge pump: implementation of a Cooper pair pump. *Phys. Rev. Lett.* 91: 177003 (4 pp).

68 Vartiainen, J.J., Möttönen, M., Pekola, J.P., and Kemppinen, A. (2007). Nanoampere pumping of Cooper pairs. *Appl. Phys. Lett.* 90: 082102 (3 pp).

69 Mooij, J.E. and Nazarov, Y.V. (2006). Superconducting nanowires as quantum phase-slip junctions. *Nat. Phys.* 2: 169–172.

70 Yamahata, G., Nishiguchi, K., and Fujiwara, A. (2011). Accuracy evaluation of single-electron shuttle transfer in Si nanowire metal-oxide-semiconductor field-effect transistors. *Appl. Rev. Lett.* 98: 222104 (3 pp).

71 Yamahata, G., Nishiguchi, K., and Fujiwara, A. (2014). Accuracy evaluation and mechanism crossover of single-electron transfer in Si tunable-barrier turnstiles. *Phys. Rev. B* 89: 165302 (9 pp).

72 Fricke, L., Wulf, M., Kaestner, B. et al. (2013). Counting statistics for electron capture in a dynamic quantum dot. *Phys. Rev. Lett.* 110: 126803 (5 pp).

73 Tanttu, T., Rossi, A., Tan, K.Y. et al. (2015). Electron counting in a silicon single-electron pump. *New J. Phys.* 17: 103030 (6 pp).

74 Giblin, S.P., See, P., Petrie, A. et al. (2016). High-resolution error detection in the capture process of a single-electron pump. *Appl. Rev. Lett.* 108: 023502 (5 pp).

75 Funck, T. and Sienknecht, V. (1991). Determination of the volt with the improved PTB voltage balance. *IEEE Trans. Instrum. Meas.* IM-40: 158–161.

76 Flowers, J. (2004). The route to atomic and quantum standards. *Sciene* 306: 1324–1330.

77 Willenberg, G.-D., Tauscher, H.N., and Warnecke, P. (2003). A traceable precision current source for currents between 100 aA and 10 pA. *IEEE Trans. Instrum. Meas.* 52: 436–439.

78 Brun-Picard, J., Djordjevic, S., Leprat, D. et al. (2016). Practical quantum realization of the ampere from the elementary charge. *Phys. Rev. X* 6: 041051 (15 pp).

79 Kaneko, N.-H., Nakamura, S., and Okazaki, Y. (2016). A review of the quantum current standard. *Meas. Sci. Technol.* 27: 032001 (20 pp).

80 Harvey, K. (1972). A precise low temperature DC ratio transformer. *Rev. Sci. Instrum.* 43: 1626–1629.

81 Drung, D., Götz, M., Pesel, E., and Scherer, H. (2015). Improving the traceable measurement and generation of small direct currents. *IEEE Trans. Instrum. Meas.* 64: 3021–3030.

82 Drung, D. and Krause, C. (2017). Ultrastable low-noise current amplifiers with extended range and improved accuracy. *IEEE Trans. Instrum. Meas.* 66: 1425–1432.
83 Krause, C., Drung, D., and Scherer, H. (2017). Measurement of sub-picoampere direct currents with uncertainties below ten attoamperes. *Rev. Sci. Instrum.* 88: 024711 (8 pp).
84 Delahaye, F. (1993). Series and parallel connection of multiple quantum Hall-effect devices. *J. Appl. Phys.* 73: 7914–7920.
85 Keller, M.W. (2008). Current status of the quantum metrology triangle. *Metrologia* 45: 102–109.
86 Piquemal, F. and Geneves, G. (2000). Argument for a direct realization of the quantum metrological triangle. *Metrologia* 37: 207–211.
87 Devoille, L., Feltin, N., Steck, B. et al. (2012). Quantum metrological triangle experiment at LNE: measurements on a three-junction R-pump using a 20 000:1 winding ratio cryogenic current comparator. *Meas. Sci. Technol.* 23: 124011 (11 pp).
88 Zimmerman, N.M. and Eichenberger, A.L. (2007). Uncertainty budget for the NIST electron counting capacitance standard, ECCS-1. *Metrologia* 44: 505–512.
89 Mohr, P.J., Newell, D.B., and Taylor, B.N. (2016). CODATA recommended values of the fundamental physical constants: 2014. *Rev. Mod. Phys.* 88: 035009 (73 pp).

7

The SI Kilogram, the Mole, and the Planck Constant

Mass is a difficult quantity. This becomes obvious when trying to explain in a few words what mass is all about. Macroscopically, it is related to matter, though matter is not a clearly defined concept in physics. Mass (gravitational mass) is proportional to the weight of a body, which is the gravitational force imposed by the gravitational field of a second mass, for example, the earth. More strictly speaking, weight is any force that affects the free fall of a body. Mass (inertial mass) reflects the resistance of a body to change its velocity, and the force needed to change its velocity is proportional to its mass. According to Einstein's equivalence principle, inertial mass and gravitational mass are identical. This has been confirmed by experiments on the level of 10^{-12}. Furthermore, mass is equivalent to energy according to Einstein's famous formula

$$E = m_0 c^2 \tag{7.1}$$

as reflected in the so-called mass deficit corresponding to the binding energy of a composed system. In this equation, m_0 is the mass of a body at rest. According to special relativity, the inertial mass depends on its velocity, v:

$$m(\mathrm{v}) = \frac{m_0}{\sqrt{1 - \frac{\mathrm{v}^2}{c^2}}} \tag{7.2}$$

Macroscopic masses come about by the sum of the mass of the constituting elementary particles reduced by the mass deficit. However, how elementary particles receive their mass has long been a puzzle. Within the standard model of particle physics, elementary particles receive their mass through the interaction with the so-called Higgs field. It was named after *Peter Higgs* who together with *Francois Englert* received the 2013 Nobel Prize in physics after the discovery of a particle at the European Organization for Nuclear Research (CERN) Large Hadron Collider, which is the long-searched Higgs boson.

In spite of all these complications with the quantity mass, the definition of its unit, kilogram, in the previous SI was apparently straightforward and simple: it related any mass to the mass of the International Kilogram Prototype (IKP). The mass of the kilogram prototype was historically defined to be equal to the mass of a cubic decimeter of pure water at the temperature of its highest density of about 4 °C. It had been realized by the *Kilogramme des Archives* of the French Academy of Sciences (for further reading of the history of the kilogram definition

The New International System of Units (SI): Quantum Metrology and Quantum Standards,
First Edition. Ernst O. Göbel and Uwe Siegner.
© 2019 Wiley-VCH Verlag GmbH & Co. KGaA. Published 2019 by Wiley-VCH Verlag GmbH & Co. KGaA.

and prototype, see [1, 2]). The choice of the inert Pt/Ir alloy as the material of the prototype should ensure a stable standard provided the appropriate handling and cleaning procedure would be applied. At the time of the first *Conférence Générale des Poids et Mesures* (CGPM) in 1889, 30 Pt/Ir copies of the prototype had been produced and distributed among the 17 signature countries of the Metre Convention (*Convention du Mètre*) as their national mass standard and the *Bureau International des Poids et Mesures* (BIPM). Countries joining the Metre Convention at a later time (at the time of writing, there were 60 signatories of the Metre Convention) were also entitled to receive a Pt/Ir copy of the prototype. Subsequent comparisons of the national prototypes with the IKP performed in 1950 and 1990 revealed a problem with the apparently straightforward and simple definition of the mass unit kilogram: obviously, there has been a drift between the mass of the international prototype and its copies by an average of about 30 µg over 100 years with a trend toward an increase of the mass of most national prototypes (see Figure 7.1). However, the results shown in Figure 7.1 could as well indicate a mass drift of the international prototype instead.

To overcome the obvious weakness of the previous SI definition, the kilogram is now defined by the Planck constant (in conjunction with $\Delta\nu_{Cs}$ and c; see Section 2.2.3). The Planck constant, conventionally labeled h, is one of the fundamental constants of nature. It was introduced originally by Max Planck in 1900 when developing a theoretical description of the emission spectrum of a so-called blackbody radiator [4]. Its consequence that the energy of a harmonic oscillator has to be quantized in terms of $E = h\nu$ (ν being the frequency) laid the base for the quantum theory.

The question on how fundamental a constant is really is not always easy to answer (see, e.g. [5–7]). Without question, however, the speed of light in vacuum, c, and the Planck constant, h, are fundamental in the theory of relativity

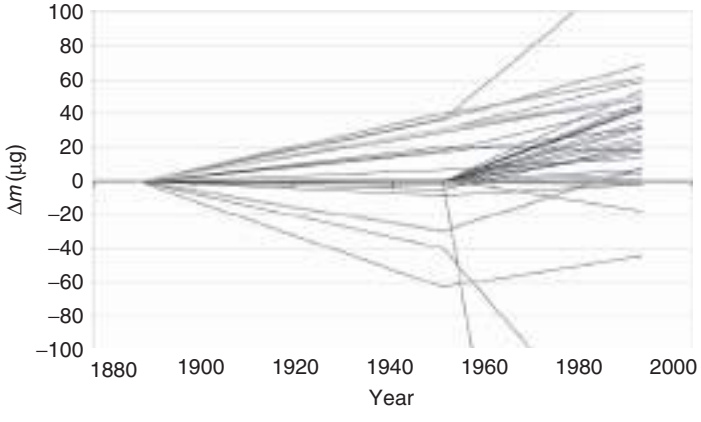

Figure 7.1 Mass difference of different National Kilogram Prototypes (black) and BIPM working standards (gray) and the International Kilogram Prototype defining the horizontal line at $\Delta m = 0$. Source: Göbel and Siegner 2015 [3]. Reproduced with permission of John Wiley & Sons.

and quantum physics, respectively. Indeed, as first pointed out by Planck, c and h together with Newton's gravitational constant, G, set up universal units for length, time, and mass (Planck units), which, however, turned out to be unpractical (see, e.g. [8]). Of course, there are further requirements for the choice of the defining constants of the SI. Most important, their values must be known with the required uncertainty, and there must exist a link between the unit and the respective defining constants. However, as already mentioned in Chapter 2, the definitions in the present SI leave room for different realizations. For the kilogram, the Consultative Committee for Mass and Related Quantities (CCM) of the International Committee for Weights and Measures (*Comitè International des Poids et Mesures*) (CIPM) had required one measurement of the Planck constant with a relative uncertainty of at least 2×10^{-8} [9]. Furthermore, the CCM required that at least three independent experiments yielded consistent values for the Planck constant with relative standard uncertainties not larger than 5×10^{-8}.

Several experimental approaches have or had been pursued to provide the link between a macroscopic mass and the Planck constant, for example, voltage balance, superconducting magnetic levitation, the Avogadro experiment, and the Kibble balance (formerly called Watt balance). The last two are described in more detail in Sections 7.2 and 7.3.

In a voltage balance [10–12], the force between the electrodes of a capacitor with a voltage applied to it is compared to the weight of a calibrated mass. Though these experiments were initially performed to realize the volt or to determine the Josephson constant (see Section 4.1.2), they could also link a mass to the Planck constant if the capacitance is traced back to the von Klitzing constant (see Section 5.4.4). However, to our knowledge, these experiments have not been pursued since the best relative uncertainty achieved was at the 10^{-7} level. A dynamic version of a voltage balance for measuring inertial mass and relating it to the Planck constant has been developed at the National Institute of Metrology (NIM), China [13] (see Section 7.3). Superconducting magnetic levitation experiments [14–17] make use of the ideal diamagnetic property of a superconductor (see Section 4.2.1.1): a superconducting material with a calibrated mass is levitated in the magnetic field created by a current driven coil. Change of the current results in the levitation of the superconducting mass at different heights. Measuring the current in terms of the Josephson and quantum Hall effects then provides the link between mass and the Planck constant. Even though fractional uncertainties of order 10^{-6} had been achieved, these experiments have not been continued.

Before describing the Avogadro and Kibble balance experiments in Sections 7.2 and 7.3, respectively, we briefly discuss in Section 7.1 the history and arguments that led to the decision to choose the Planck constant as the defining constant for the kilogram. In Section 7.4, we discuss the present definition of the mole and its realization. Finally, in Section 7.5, we summarize the Committee on Data for Science and Technology (CODATA) evaluation of the value of the defining Planck constant as well as the present realization, maintenance, and dissemination of the kilogram.

7.1 From "Monitoring the Stability of the Kilogram" to the Planck Constant

In this section, we sketch the process that finally led to the decision to base the definition of the kilogram on a fixed value of the Planck constant.

It was the concern about the stability of the IKP and/or its official copies that triggered the discussion about new definitions of the kilogram and other SI base units. Despite the pretended simple 1889 definition of the unit kilogram as the mass of the IKP it never had been that simple in praxis. One of the major concerns has been the cleaning procedure to be applied (see, e.g. [1]). However, it was not until in 1988 in preparation of the third official comparison (verification) of the IKP with the national prototypes and the BIPM official copies that a careful and well-documented study of the effect of cleaning on the mass of the respective standard had been performed [18]. This study was lead by Georges Girard, the then head of the mass section of the BIPM. The IKP lost about 57 μg and further 6 μg after, respectively, a first and second cleaning step with a jet of steam from pure water. Further, the IKP and the other standards showed a rapid increase in their mass by about 5 μg within the first 120 days after cleaning. This finding raised the question on how the 1889 definition had to be interpreted. In 1989, the CIPM decided [18] after consultation with the CCM that the 1889 definition referred to the mass of the IKP just after cleaning by the BIPM procedure [19].

The results of the third verification of the kilogram as depicted in Figure 7.1 showed a clear trend that the difference between the mass of the IKP and its copies increased to about an average of 30 μg [20]. Nevertheless, based on results of these verifications, no conclusion was possible as to which of the masses had changed though it seemed likely that the mass of the IKP had decreased. The steady increase of the mass difference between the IKP and its copies, however, was not found by a fourth verification in 2014 performed to calibrate the mass standards used for the Kibble balance and Avogadro experiment. Instead, the masses seemed to be stable between the third and fourth verification [21, 22]. All this called for methods to monitor the stability of the kilogram and finally come to an absolute mass standard. And indeed, the CIPM recommendation 4 in 1993 [23] and the 20th CGPM under resolution 5 recommended [24] "that national laboratories pursue their work on experiments, and develop new ones, with a view to monitoring the stability of the international prototype of the kilogram and in due course opening the way to a new definition of the unit of mass based upon fundamental or atomic constants."

Regarding the fundamental constant, the Planck constant, conventionally labeled h, seemed to be an obvious choice. The Planck constant has the unit of action, which is J s equal to $m^2\,kg\,s^{-1}$. Since in the previous and present SI the second and the meter are defined in terms of fundamental constants, namely the hyperfine splitting of the electronic ground state of ^{133}Cs ($\Delta\nu_{Cs}$) and the speed of light in vacuum (c), the kilogram can be defined via the Planck constant, provided its value is known with the required uncertainty of a few parts in 10^8 as required by the CCM and CIPM [9]. As said above, several experiments that could provide a direct link of the kilogram to the Planck constant were

considered and pursued, for example, the voltage balance, superconducting magnetic levitation, and the Kibble and Joule balances. The Kibble balance provides a direct link between the Planck constant and a macroscopic mass via a virtual comparison of electric and mechanic power induced by a test mass, which had been the reason for labeling this experiment "Watt balance." Later, in honor of the inventor of this experiment, *Brian Kibble*, its name has been changed to Kibble balance.

A direct link of the kilogram to an atomic constant, specifically to an atomic mass could be accomplished by the silicon single crystal (Avogadro) experiment and the ion accumulation experiment. Of course, the same requirements for the uncertainty of the experiment were valid. Since it seemed more likely that the Avogadro experiment than the ion accumulation experiment could reach the 10^{-8} uncertainty level the Physikalisch–Technische Bundesanstalt (PTB) (National Metrology Institute of Germany) decided to abolish the ion accumulation experiment and to concentrate its efforts on the Avogadro experiment, which has been pursued in an internationally coordinated project (IAC, International Avogadro Coordination). The Avogadro experiments (also called X-ray crystal density, XRCD method) directly determines the Avogadro constant, N_A, by counting the number of atoms in an isotopically enriched ^{28}Si single crystal (see Section 7.2). The link to the kilogram would have been given by the defining equation

$$1\,\mathrm{kg} \equiv 10^3 \{N_A\}\, m_u \tag{7.3}$$

which followed from the previous definition of the mole. $\{N_A\}$ is the Avogadro number, i.e. the numerical value of the Avogadro constant, and $m_u = 1/12\, m(^{12}C)$ the atomic mass constant.

So, there were two options, namely, redefining the kilogram by choosing as the defining constant the Planck constant, h, or the Avogadro constant, N_A, or similarly the atomic mass constant m_u. (Note that a direct definition of the kilogram via a fixed Avogadro constant according to Eq. (7.3) rests on the previous definition of the mole.) In either case, the determination of either constant, N_A or h with a relative uncertainty of order 10^{-8} as it had been required by the CCM [9] would also determine the respective other constant with the same uncertainty [25, 26]. This is because the molar Planck constant

$$N_A h = \frac{\alpha^2 c}{2R_\infty} A_r^e M_u \tag{7.4}$$

(with the fine-structure constant α, the Rydberg constant R_∞, the relative atomic mass of the electron A_r^e, and the molar mass unit M_u) is known with an relative uncertainty of few parts in 10^{-10} [27], which is considerably smaller than the uncertainty required for the new definition of the kilogram.

There have been pros and cons for either option. Pros for defining the kilogram by fixing the value of h are, e.g. [25], given as follows:

(i) The two major pillars of our present understanding of physics are theories of relativity and quantum physics. The respective fundamental constants in these theories are the speed of light in vacuum, c, and the Planck constant,

h, respectively. The speed of light c had already been fixed in the previous SI and is still fixed in the present SI by the definition of the meter. Defining the kilogram by a fixed value of h thus complements the meter definition in such that both fundamental constants are then part of the SI. Further, the constants that appear in the fundamental relations $E = mc^2$, $E = h\nu$, and the de Broglie equation $\lambda = h/p = h/m\text{v}$ then all have exactly known values.

(ii) Since in the present SI the value of the elementary charge e as defining constant for the ampere is fixed and thus exactly known, the Josephson constant $K_\text{J} = 2e/h$ and the von Klitzing constant $R_\text{K} = h/e^2$ (see Chapters 4 and 5) have exact values and thus $K_\text{J-90}$ and $R_\text{K-90}$, the conventional values for K_J and R_K in the previous SI are abolished. Hence, the conventional (non-SI) units volt, V_{90}, and ohm, Ω_{90}, are also eliminated. Instead, these electrical units are now realized by a primary realization tracing them directly back to defining constants of the SI.

The major con for choosing h as the defining constant for the kilogram has been the missing direct link to a mass making it difficult to easily explain it outside the metrology community. In contrast, choosing the Avogadro constant, N_A, as the defining constant for the kilogram would have been much easier to communicate since it directly relates the kilogram to a mass, e.g. m_u.

Both options were therefore discussed intensively by the respective organizations of the meter convention, the CCM, the Consultative Committee for Units (CCU), and the CIPM as reflected in their respective resolutions as well as the resolutions of the CGPM (see, e.g. [28, 29]). For the final decision of the CIPM [30] and CGPM [31], the pro (ii) was the decisive argument for choosing h as the defining constant in the present definition of the SI.

In Sections 7.2 and 7.3, we present, respectively, the Avogadro and Kibble balance experiments, which finally determined the value of the defining constant, h.

Naturally both are ideal for the realization and dissemination of the mass unit kilogram [32].

7.2 The Avogadro Experiment

The Avogadro experiment [33, 34], or XRCD experiment, is aimed at the determination of the Avogadro constant, N_A, by counting the number of atoms in a mole of a high-purity Si single crystal. However, as mentioned in Section 7.1, it also provides an independent approach for a precise determination of the Planck constant through Eq. (7.4). It had originally been pursued to provide an alternative definition of the kilogram by tracing it to an exactly defined atomic mass, such as ^{12}C or ^{28}Si, or the mass of an elementary particle [35]. Since the relative masses of atoms and elementary particles such as the electron can be determined very accurately using Penning traps, one basically would have been free in the choice of the reference mass.

It is worth mentioning here the other experiment that also would provide a direct link of a macroscopic to an atomic mass, the so-called ion accumulation

experiment [36]. Its idea has been to use a modified mass spectrometer where ions of a specific element are generated and finally collected in a Faraday cup connected to a balance. The moving ions result in a current, which can be measured by the Josephson and quantum Hall effects (see Chapters 4 and 5) and integrated over the entire accumulation time, thereby providing the number of ions impinging onto the Faraday cup. The monoisotopic elements ^{197}Au and ^{209}Bi had been used as ion sources. A proof of principle had been demonstrated by accumulating 38 mg of Bi. The atomic mass unit determined from this experiment agreed with the CODATA value within 9×10^{-4} [37]. Nevertheless, foreseeing the difficulties encountered to reduce the uncertainty by more than 4 orders of magnitude, the experiment has not been pursued further.

Coming back to the Avogadro experiment, the Avogadro constant is the number of specified entities in the amount of substance of 1 mol in a pure substance. It is a scaling factor that links atomic and macroscopic properties.

For a perfect pure silicon single crystal, the Avogadro experiment relates its mass, m, to the number of Si atoms contained in the crystal, N_{Si}, and the mass of the Si atom, m_{Si}:

$$m = N_{\mathrm{Si}} m_{\mathrm{Si}} = N_{\mathrm{Si}} \frac{M_{\mathrm{Si}}}{N_{\mathrm{A}}} \tag{7.5}$$

where M_{Si} is the molar mass of Si. For a perfect single crystal, the number of atoms contained is given by its volume, V, divided by the volume occupied by one atom, V_{Si}; thus,

$$N_{\mathrm{Si}} = \frac{V}{V_{\mathrm{Si}}} = \frac{8V}{a_0^3} \tag{7.6}$$

where a_0 is the lattice parameter (lattice constant) and thus a_0^3 is the volume of the Si crystal unit cell. The factor 8 accounts for the fact that in a perfect Si single crystal, the unit cell contains eight Si atoms. Combining Eqs. (7.6) and (7.5) yields

$$m = \frac{8V}{a_0^3} \frac{M_{\mathrm{Si}}}{N_{\mathrm{A}}} \tag{7.7}$$

As Si has three stable isotopes, ^{28}Si, ^{29}Si, and ^{30}Si, the molar mass, M_{Si}, is given by the sum of the molar mass of the isotopes weighted by their (amount of substance) abundances, f_i:

$$M_{\mathrm{Si}} = \sum_i f_i M_{\mathrm{Si}}^i = \sum_i f_i A_{\mathrm{r}}^i M_{\mathrm{u}} \tag{7.8}$$

with A_{r}^i being the relative atomic mass and M_{u} being the molar mass unit. For natural Si, the abundances are about $f_{28} = 0.922$, $f_{29} = 0.047$, and $f_{30} = 0.031$. If we now finally consider Eq. (7.4), we end up with the basic relation linking a macroscopic mass to the Planck constant [26]:

$$m = \frac{8V}{a_0^3} \frac{2R_\infty h}{c\alpha^2} \sum_i \frac{f_i A_{\mathrm{r}}^i}{A_{\mathrm{r}}^{\mathrm{e}}} \tag{7.9}$$

where R_∞ is the Rydberg constant, c the velocity of light in vacuum, α the fine-structure constant, and $A_{\mathrm{r}}^{\mathrm{e}}$ the relative atomic mass of the electron. Note

that the Avogadro constant does not enter explicitly, yet, the name "Avogadro experiment" is kept. For the determination of the Planck constant before the revision of the SI according to Eq. (7.9), the volume of the single crystal, the lattice parameter, and the isotopic composition had to be measured. Of course, the mass of the used single crystal must also be determined with the required uncertainty. The relative atomic masses of the Si isotopes are measured by comparing cyclotron frequencies in Penning traps and their abundances in the specific Si crystal by mass spectroscopy. The constants appearing additionally in Eq. (7.9) are known with sufficiently small uncertainty: the speed of light in vacuum is defined and thus exact. The Rydberg constant, fine-structure constant, and relative atomic mass of the electron are known with relative standard uncertainties of 5.9×10^{-12}, 2.3×10^{-10}, and 2.9×10^{-11} [27], respectively, and thus, their uncertainty contribution can be neglected at the required 10^{-8} level.

We now discuss the individual measurements a little more in detail, considering also additional constraints. Silicon has become the material of choice due to its use in microelectronics where large-sized high-purity and almost perfect crystals can be synthesized. However, in view of the small fractional uncertainty of the order 10^{-8} required for the realization of the new kilogram, crystal perfection and purity (i.e. defect (vacancy) and impurity concentration) have to be investigated quantitatively. The major impurities to be considered, after growth and purification by multiple float zone crystallization, are interstitial oxygen and substitutional carbon and boron. Their concentration can be determined by infrared spectroscopy [38]. An estimate of the vacancy concentration can be obtained by positron annihilation experiments [39].

In view of the most precise determination of the volume of the macroscopic Si single crystal, a sphere has been chosen (see Figure 7.2). The volume of the sphere can be determined by a series of diameter measurements scanning the entire surface. The diameters are measured by optical interferometry [40, 41]. The layout of a specially constructed spherical Fizeau interferometer is schematically shown in Figure 7.3. The central part consists of a temperature-controlled vacuum chamber containing the sphere and the Fizeau optics. The two arms of the interferometer are illuminated by plane wave light coming from tunable

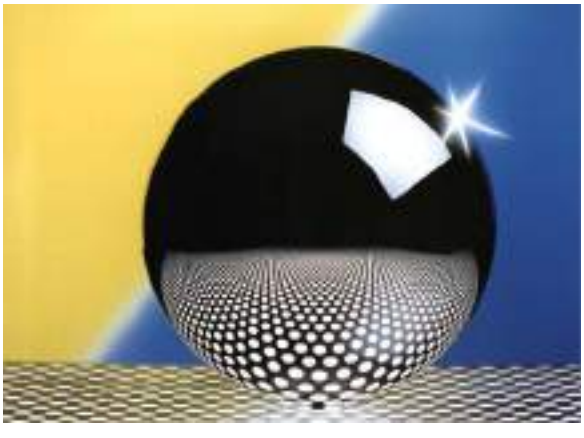

Figure 7.2 Photo of a single crystal Si sphere used in the Avogadro experiment. The diameter and mass, respectively, are about 10 cm and 1 kg. Source: Courtesy of PTB.

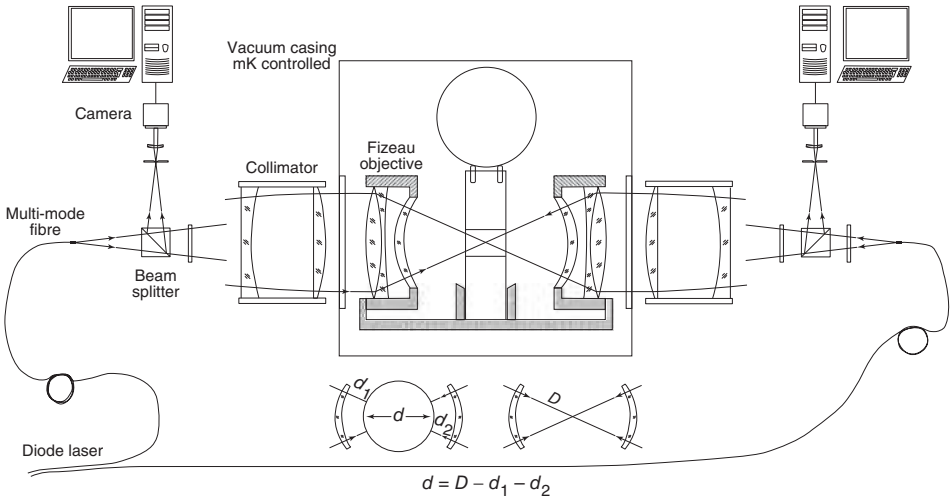

Figure 7.3 Schematic drawing of the spherical Fizeau interferometer constructed at PTB. Source: Courtesy of A. Nicolaus, PTB.

diode lasers through multimode optical fibers. The Fizeau objectives are carefully adjusted to have their focal point in the center of the sphere. First, the diameter of the empty etalon, D, and subsequently the distances between the sphere surface and the reference surfaces, d_1 and d_2, are measured. The diameter of the sphere, d, is then obtained by subtracting d_1 and d_2 from D. With this technique, some 10 000 diameters can be measured simultaneously depending on the resolution of the camera system. The sphere can be rotated around the horizontal and vertical axes to cover it completely by overlapping diameter measurements. The obtainable uncertainty depends critically on how well the shape of the sphere matches the wave front of the interferometer light. Having high-quality objectives and production of an almost perfect sphere are thus the most critical issues. Furthermore, the surface of the sphere is generally covered by different surface layers, in particular, silicon oxide, which not only have to be considered for the mass correction but also for evaluating the interferometry results, due to their different index of refraction and resulting phase shifts.

A measured diameter topography of a silicon sphere is shown in Figure 7.4. Peak-to-valley deviations from a perfect sphere are of the order of some 10 nm, resulting in uncertainty of the volume determination of presently about 10^{-8} [42–46].

As mentioned earlier, the composition and thickness of the surface layer of the Si spheres must be determined for both mass correction and volume determination. It is important to note that for the mass correction, only the relative mass of the respective elements with respect to Si enters, and thus, the traceability to a mass standard is not required. The standard methods applied for thickness and optical constants measurement are X-ray reflectometry (XRR) and optical spectral ellipsometry (SE). However, since the surface layer not only may contain different silicon oxides (SiO_x) but possibly also chemisorbed water

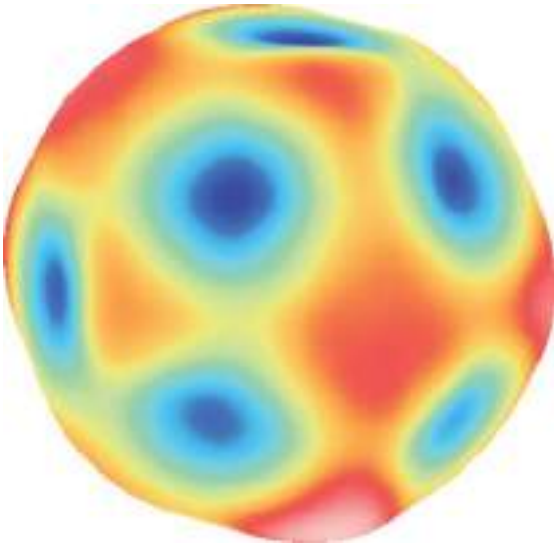

Figure 7.4 Diameter variations of a single crystal Si sphere. Source: Courtesy of A. Nicolaus, PTB.

and other contaminants, analytical methods, in particular, X-ray photoelectron spectroscopy (XPS), X-ray fluorescence (XRF), and near-edge X-ray absorption fine structure (NEXAFS), are applied (see, e.g. [47]). Combining the results of the individual experiments enabled to develop a detailed model of the surface layer [48] and to estimate its contribution to the overall fractional uncertainty of the experiment to presently below 10^{-8}.

For the measurement of the lattice parameter, a combined optical and X-ray interferometer is used [49], as schematically shown in Figure 7.5. The X-ray interferometer follows the design by Bonse and Hart [50]. It consists of three monolithically fabricated parallel single crystal Si plates, each of about 1 mm thickness and separated by the same amount. The surface of these plates is orthogonal to the lattice plates to be measured. In the case of Si, the spacing d_{220} of the {220}

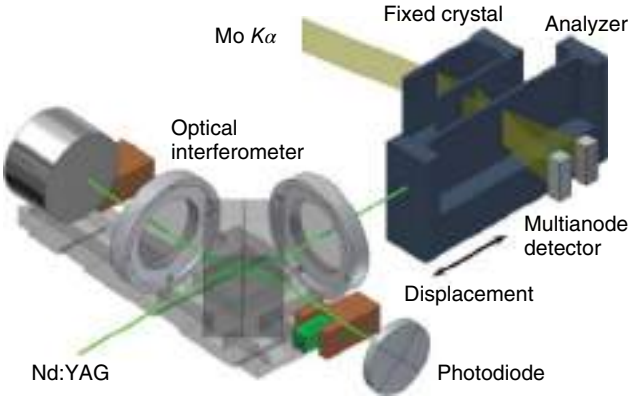

Figure 7.5 Schematic layout of the combined optical and X-ray interferometer for measuring the lattice constant of crystalline Si. Source: Courtesy of E. Massa, G. Mana, INRIM.

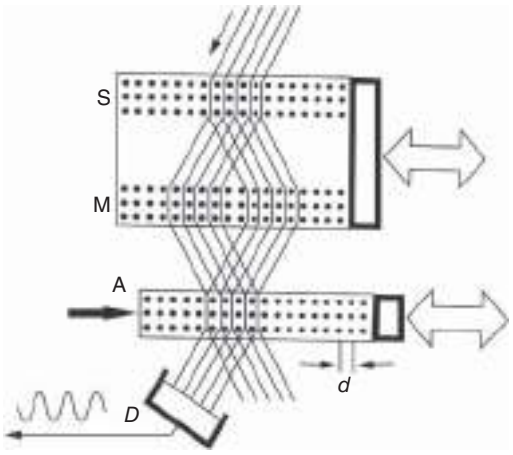

Figure 7.6 Operation principle of a Bonse–Hart X-ray interferometer. The three single crystal plates labeled S, M, and A act, respectively, as beam splitter and transmission optics for the incident X-ray. The crystal planes are indicated by the black dots representing the atom position (not to scale). The crystal plates must have equal thickness, and the spacing between them must be the same. Source: Göbel and Siegner 2015 [3]. Reproduced with permission of John Wiley & Sons.

planes is measured because of their low absorption. The lattice parameter a_0 is then obtained according to $a_0 = \sqrt{8}d_{220}$.

The operation principle of the X-ray interferometer is illustrated in Figure 7.6. The first plate (labeled S) acts as a beam splitter for the incident X-ray due to Bragg reflection at the crystal planes. The two other plates (M and A) act as transmission optics, where the two plane waves generated by plate S are recombined by plate M at the position of the analyzer (plate A). Moving the analyzer orthogonal to the direction of the lattice planes causes a periodic modulation of the transmitted and diffracted beams (Moiré effect) with a period of the lattice spacing, d, and independent of the X-ray wavelength. The central part of the X-ray interferometer of the Italian metrology institute INRIM (National Institute of Metrology of Italy), Torino, [49] is shown in Figure 7.7. Considering the effect of point defects on the lattice parameter, the average lattice constant of a macroscopic Si sphere can be determined presently with a fractional uncertainty of the order of 10^{-9}

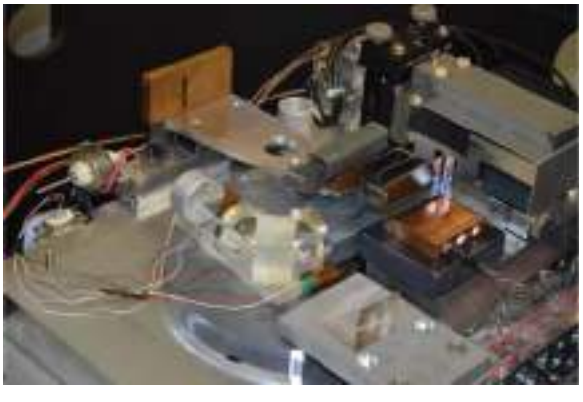

Figure 7.7 Photo of the central part of the INRIM X-ray interferometer showing the Si crystal plates right in the center. The experiment is performed in a temperature-stabilized vacuum chamber. A Mo K_α X-ray source and an iodide-stabilized single-mode He–Ne laser are used for the X-ray and optical interferometer, respectively. Source: Courtesy of E. Massa, G. Mana, INRIM.

[49] corresponding to attometer resolution. As pointed out recently at this level of precision dimensional measurements by laser interferometry as applied in the combined X-ray/optical interferometer require a careful correction because of diffraction [51, 52].

Finally, the ratio of the atomic masses of silicon with its specific isotope composition and the electron (factor $\sum_i f_i A_r^i / A_r^e$ in Eq. (7.9)) must be determined, which is basically a molar mass determination of the Si crystal (c.f. Eq. (7.8)). The standard technique for molar mass determination is by gas mass spectrometry, which, of course, requires the crystal to be dissolved and transferred to a gaseous compound by chemical reactions [53, 54]. It turned out in the frame of the determination of the Avogadro constant that the uncertainty of the molar mass determination of natural Si of about 3×10^{-7} limited the achievable total uncertainty to about 10^{-7} [55]. This was the start of an international research effort to produce a high-purity single crystal with highly enriched ^{28}Si [56] where ^{29}Si and ^{30}Si make only a small correction to the molar mass. In fact, for a crystal with $f_{28} \sim 0.9999\%$, the uncertainty of the molar mass could in principle be reduced by several orders of magnitude compared to natural Si [57].

Two different high-quality ^{28}Si single crystals have been produced so far for the Avogadro experiment. The first 5 kg ^{28}Si single crystal labeled "AVO28" was produced for the IAC project in 2004 to 2007. The production proceeded in several steps starting with the enrichment of SiF_4 gas by centrifugation at the Science and Technical Center (Centrotech) in St. Petersburg, Russia, from which, after conversion into SiH_4, a polycrystal was grown at the Institute of Chemistry of High-Purity Substances of the Russian Academy of Sciences (ICHPS RAS) in Nizhny Novgorod. Finally, the polycrystal was transformed into a 5 kg ^{28}Si single crystal by floating zone (FZ) single crystal growth at the Leibniz Institute for Crystal Growth (IKZ) in Berlin, Germany. Two precise spheres were produced from the single-crystal rod at the CSIRO, Australia [58], for the subsequent determination of the Avogadro constant [42–44]. In 2012, the PTB started a new project named kg-2 [45, 59] to produce two additional 5 kg ^{28}Si crystals. The isotopic enrichment was again performed in Russia but this time at the Stock Company "Production Association Electrochemical Plant" in Zelenogorsk near Krasnoyarsk. The subsequent production steps were the same as for "AVO28" except that the spheres were produced at PTB. The first crystals of this production with an enrichment of 99.9985% became available in 2015, and three spheres were produced for the experimental determination of the Avogadro constant at PTB and the National Metrology Institute of Japan (NMIJ), respectively [45, 46].

Despite the high enrichment, the molar mass must be measured. Measurement was done by a modified isotope dilution mass spectrometry (IDMS) in combination with a multicollector inductively coupled plasma (ICP) mass spectrometer [60]. In IDMS, a spike with an isotope of the substance to be determined is added to the sample to be analyzed. Since the chemical properties of the isotopically marked substance and the nonmarked substance are identical, their peak ratio of the mass spectrometer signal reflects the mass ratio of both. As the mass of the spike can be measured before adding it to the sample, this serves as a calibration, and the unknown mass fraction can be determined. The basic idea of the IDMS molar mass determination of the enriched ^{28}Si crystal

was to treat the sum of ^{29}Si and ^{30}Si as a virtual element in the sample. Preparing gravimetrically a blend with a ratio $R(^{30}\mathrm{Si}/^{29}\mathrm{Si}) \sim 1$ for calibration and adding a spike of a highly enriched ^{30}Si crystal to the sample enabled the determination of the mass fraction of all three isotopes by measuring the amount ratio $R(^{30}\mathrm{Si}/^{29}\mathrm{Si})$ in the original and spiked samples [61–63]. This procedure avoided to explicitly measure the very small amount ratio $R(^{29}\mathrm{Si}/^{28}\mathrm{Si})$ and $R(^{30}\mathrm{Si}/^{28}\mathrm{Si})$, which could hardly be measured with the required precision [61]. With this new approach, the molar mass of the enriched Si crystal was determined with a fractional uncertainty of 1.4×10^{-9} [45, 64].

The results for the three different spheres produced with the new ^{28}Si crystal differed only by $7 \times 10^{-9}\ N_\mathrm{A}$. The average Avogadro constant value amounts to $N_\mathrm{A} = 6.022\,140\,526\ (70) \times 10^{23}\ \mathrm{mol}^{-1}$ with a relative standard uncertainty of 1.2×10^{-8} [45], which is slightly different (by $3.9(2.1) \times 10^{-8}$, relatively) from the 2015 value for the AVO28 crystal ($N_\mathrm{A} = 6.022\,140\,76(12) \times 10^{23}\ \mathrm{mol}^{-1}$ with a relative standard uncertainty of 2×10^{-8} [43, 44]). Both results thus have fulfilled the CCM requirement of a relative uncertainty of 2×10^{-8} [9]. Their relation to the Kibble balance determination of the defining constant, h, and contribution to its final value are discussed in Section 7.5. A summary of the results achieved with enriched ^{28}Si since 2011 can be found in Ref. [65].

We finally mention that the production of high-quality enriched ^{28}Si crystals has given a boost not only to future mass metrology but also to other areas in science, such as quantum information technology, see, e.g. [66].

7.3 The Kibble Balance Experiment

The Kibble balance experiment, see, e.g. [67–72], also provides a direct link between a macroscopic mass and the Planck constant. It compares mechanic and electric power, which explains its former label "Watt balance." The basic idea for this experiment was first proposed by Kibble [73] and realized by Kibble et al. at the National Physics Laboratory, NPL, UK [74], and by Olson et al. at the National Bureau of Standards/National Institute of Technology, NBS/NIST, Gaithersburg, USA [75, 76].

The Kibble balance experiment is performed in two phases. The principle of the experiment is illustrated in Figure 7.8. Consider two coils: one (coil 1) carrying current, I_1, is fixed, and the other one (coil 2) carrying current, I_2, is movable in the vertical direction (upper left part of Figure 7.8). The vertical (z) component of the force imposed on the movable coil, F_z, is given by

$$F_z = I_2 \frac{\partial \Phi_{12}}{\partial z} \tag{7.10}$$

where $\partial\Phi_{12}/\partial z$ is the vertical gradient of the magnetic flux generated by the current through coil 1. This force can be balanced (force mode) by connecting coil 2 to a balance loaded with an appropriate mass, such that $mg = -F_z$ (g is the local gravitational acceleration). Thus,

$$mg = -I_2 \frac{\partial \Phi_{12}}{\partial z} \tag{7.11}$$

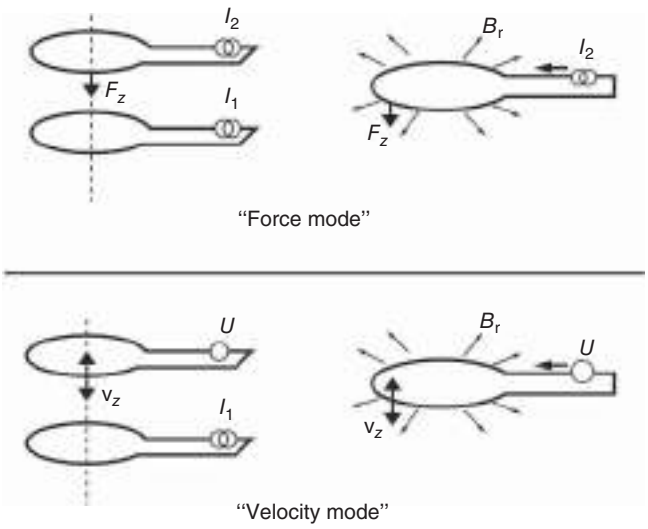

Figure 7.8 Principle of the Watt balance experiment. Source: Göbel and Siegner 2015 [3]. Reproduced with permission of John Wiley & Sons.

In the second phase (velocity mode), the second coil is an open circuit, and the induced voltage is measured when moving it vertically with a constant velocity, v_z. The induced voltage is given by

$$U_2 = -\frac{\partial \Phi_{12}}{\partial t} = -\frac{\partial \Phi_{12}}{\partial z}\frac{\partial z}{\partial t} = -\frac{\partial \Phi_{12}}{\partial z} v_z \tag{7.12}$$

Combining Eqs. (7.11) and (7.12) then yields

$$mgv_z = I_2 U_2 \tag{7.13}$$

(The subscript 2 will be abolished in the following text.) This equation equals mechanic and electric power.

The same result is obtained for a geometry as indicated in the right-hand part of Figure 7.8 where a coil with wire length L is placed in a horizontal, purely radial magnetic field B_r. $\partial \Phi_{12}/\partial z$ in Eqs. (7.10)–(7.12) is then to be replaced by $-B_r L$.

Since except for the BIPM experiment (see below) the experiment is split into these two phases, it is actually a virtual comparison of the electrical and mechanical watt. Note, however, that Eq. (7.10) is only one component of a vector equation. Neglecting the other components implies tremendous constraints on the alignment of the experiment.

If the voltage, U, is measured against a Josephson voltage standard, it can be expressed as (see Chapter 4)

$$U = C_1 U_{J,1} = C_1 i f_{J,1} K_J^{-1} = C_1 i f_{J,1} \left(\frac{h}{2e}\right) \tag{7.14}$$

where i is an integer (Shapiro step number), $f_{J,1}$ the Josephson frequency, K_J the Josephson constant, and C_1 the calibration factor. The current, I, can be measured as the voltage drop across a resistor, R. Measuring the voltage and resistance in

terms of the Josephson and von Klitzing constants, respectively, then yields

$$I = \frac{U}{R} = \frac{C_2 U_{\mathrm{J},2}}{C_3 \frac{1}{n} R_{\mathrm{K}}} = \frac{C_2 i f_{\mathrm{J},2} \left(\frac{h}{2e}\right)}{C_3 \frac{1}{n} \left(\frac{h}{e^2}\right)} = \frac{C_2}{C_3} jn \frac{e}{2} f_{\mathrm{J},2} \tag{7.15}$$

where j and n are integer numbers, j denoting the respective Shapiro step and n labeling the quantum Hall plateau (filling factor), and R_{K} is the von Klitzing constant. Combining Eqs. (7.13)–(7.15) yields

$$m = \frac{C}{4} f_{\mathrm{J},1} f_{\mathrm{J},2} \frac{h}{g \mathrm{v}_z} \tag{7.16}$$

where C is a combination of the different calibration factors multiplied with the integer numbers i, j, and n. Equation (7.16) is the fundamental Kibble balance equation relating a macroscopic mass to the Planck constant corresponding to Eq. (7.9) in the Avogadro experiment. Since none of the quantities on the right-hand side of Eq. (7.16) requires traceability to a mass standard, the Kibble balance experiment can also serve as a primary realization of the kilogram. Thus, the quantities to be measured in the Kibble balance experiment are the Josephson frequencies $f_{\mathrm{J},1}$ and $f_{\mathrm{J},2}$; the gravitational acceleration, g; and the velocity, v_z, given the numbers of the Shapiro step i and j and the filling factor n used in the calibration. For the determination of the Planck constant, the mass has to be measured as well.

The following are the essential ingredients of a Watt balance experiment (see, e.g. [68]):

- A suitable balance also allowing the required alignment (a detailed description of the alignment procedure can be found, e.g. in Refs. [72, 77, 78]).
- A magnet providing the magnetic flux, which could be a permanent magnet, an electromagnet (mostly superconducting solenoids), or a combination of both.
- A setup for the velocity measurement. For this, the movement of the coil is detected by an interferometer, usually operated in vacuum to avoid uncertainties due to the refractive index of air.
- A Josephson and quantum Hall standards for measuring the current in the force mode and the voltage induced in the coil in the velocity mode.
- A gravimeter to measure the gravitational acceleration and its spatial profile.

In addition, sensors and actors are required to monitor and control the alignment.

At the time of writing, about 10 laboratories had a Kibble balance in operation or under construction worldwide, including the NIST, the National Research Council of Canada (NRC), the Swiss Federal Institute of Metrology (METAS), the Laboratoire National de Métrologie (LNE) of France, the Measurement Standards Laboratory of New Zealand (MSL), the Korea Research Institute of Standards and Science (KRISS), the National Metrology Institute of Turkey (UME), and the BIPM. Though they are based on the same underlying principle described earlier, they differ in their specific design as described in detail in recent reviews [68, 69, 71, 72]. As an example, the schematic drawing of the NIST Kibble balance (NIST-4) is shown in Figure 7.9a [72], and a photo in Figure 7.9b.

(a)

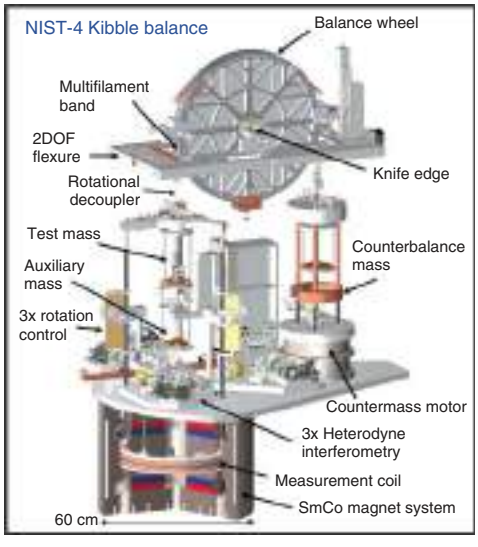

(b)

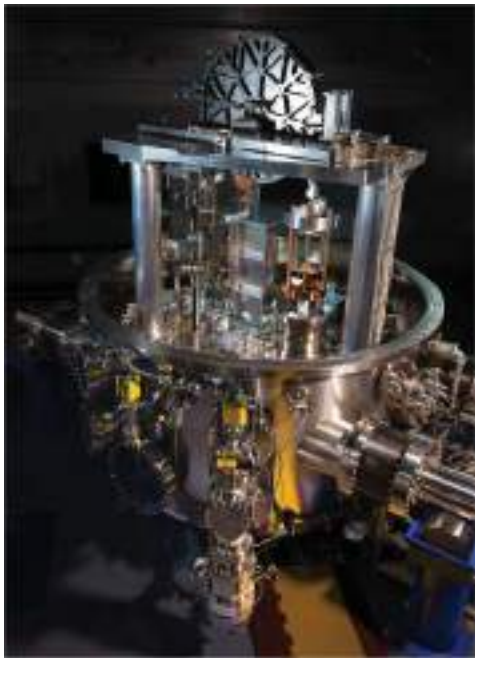

Figure 7.9 (a) Schematic drawing of the NIST-4 Kibble balance [72]. The magnetic field is generated by a two-disk permanent Sm_2Co_{17} magnet system. Source: Courtesy of NIST. (b) Photo of the NIST-4 Kibble balance with the vacuum chamber open. Source: Courtesy of NIST. Photo by Jennifer Lauran Lee/NIST.

While in the previous version "NIST 3" a superconducting magnet provided the radial magnetic field, a permanent magnet system is used in NIST-4 generating a radial field with a flux density of 0.55 T. As in the previous versions, a wheel balance with a test mass of 1 kg is used. Early results of the NIST Kibble (Watt) balance experiments were reported, e.g. in Refs. [79, 80]. The original NPL Kibble balance used a beam balance and permanent magnet [74]. Following the decision of NPL to stop their Watt balance project, the latest version of the NPL Mark II Watt balance was transferred to the NRC, and the first results were reported in 2012 [81].

The specific features of the METAS Kibble balance were to separate the force mode and velocity mode and to use a 100 g test mass instead of 1 kg. Furthermore, a parallel and homogeneous horizontal magnetic field generated by two flat poles of a SmCo permanent magnet was used [68, 82]. The first results have been reported by Eichenberger et al. [83].

The LNE Watt balance experiment [84, 85] uses atomic interferometry for gravimetry [86], a special guiding stage to ensure motion of the coil along the vertical axis, and a programmable Josephson array associated with a programmable bias source as voltage reference [87]. Determination of the Planck constant with the LNE Kibble balance was reported in 2015 and 2017 [88, 89].

The specific approach of the BIPM Kibble balance is to carry out the force mode and velocity mode simultaneously [90, 91]. A major challenge in this technique is to separate the induced voltage due to the motion of the coil from the resistive voltage drop due to the simultaneously flowing balance current. One possible way to overcome this could be to employ a superconducting moving coil [92]. The balance current driven through the coil in the force mode would then not cause a voltage drop, and the measured voltage solely would be due to the induced voltage of the velocity mode. The present activities at BIPM, however, are focused on the development of a room temperature version which enables both the simultaneous (one phase) and the conventional two-phase operations [69, 91].

At this end, METAS, NPL, NIST, and NRC have reported values of the Planck constant with the lowest uncertainty of 9×10^{-9} achieved in the NRC experiment [93]. For the sake of completeness, the Joule balance experiment at the NIM, China, must be included here, although it differs from the Kibble balance experiments discussed so far. It follows the design of an electrodynamometer and operates in the force mode only equating the magnetic energy difference and the gravitational potential energy difference between two known vertical positions of a coil [94]. The electromagnetic force to compensate the weight of the test mass is created by two coils aligned parallel to each other, which requires the determination of a mutual inductance between the two coils. A relative uncertainty for the Planck constant of 2.4×10^{-7} has been achieved so far, yet further improvement seems possible [95].

7.4 The Mole: Unit of Amount of Substance

The mole is the unit of the quantity amount of substance and one of the base units of the SI, sometimes called the "SI unit of chemists." It is used to quantify

an ensemble of entities in a thermodynamic sense (like in the ideal gas equation $pV = nRT$) and to quantify entities in stoichiometric chemical reactions [96]. In the present SI, the magnitude of the mole is set by the fixed value of the defining Avogadro constant, N_A. A mole thus is the amount of substance of a system that contains N_A specified entities. The previous definition of the mole was based on a fixed value of the molar mass of ^{12}C, $M(^{12}C)$:

$$M\left(^{12}C\right) = A_r\left(^{12}C\right) M_u = 0.012\,\mathrm{kg\,mol^{-1}} \tag{7.17}$$

with $A_r(^{12}C)$ and $M_u = 10^{-3}\,\mathrm{kg\,mol^{-1}}$ being the relative atomic mass of ^{12}C and the molar mass unit, respectively. This definition linked the mole to the kilogram. In the present SI, this dependence on the kilogram definition is abandoned. However, as a consequence, the molar mass of ^{12}C is no longer exact but has an uncertainty equal to the uncertainty of the molar mass unit M_u, which at the time of redefinition was less than 1×10^{-9} [97, 98]. This, in general, will add only a minor contribution to the molar mass ($M(X)$) uncertainty of any atom or molecule X

$$M(X) = A_r(X) M_u \tag{7.18}$$

as well as to the most widely used method to determine the amount of substance, n, through weighing according to

$$n = \frac{m}{A_r(X) M_u} \tag{7.19}$$

The primary realization of the mole with smallest uncertainty, of course, is through the Avogadro experiment. In practice, however, other primary direct methods as described, for example, in [98, 99] will generally be applied. Thus, the daily life of an analytical chemist has not been changed, yet the new definition adds to the consistency of the new SI and makes clear the distinction between the quantities of amount of substance and mass; see also [100].

7.5 The CODATA Evaluation of the Value of the Defining Planck Constant and the Maintenance and Dissemination of the Kilogram

7.5.1 The CODATA Evaluation and the Final Value of the Defining Planck Constant, *h*

The CGPM at its 24th meeting in 2011 invited the CODATA, through its Task Group on Fundamental Constants to "continue to provide adjusted values of the fundamental physical constants based on all relevant information available and to make the results known to the International Community through its Committee for Units since these values and uncertainties will be those for the revised SI" [101]. Further the CIPM decided in 2015 [102] that results to be considered by the CODATA Task Group should be accepted for publication by 1 July 2017. The CODATA Task Group subsequently carried out a special least square adjustment of the values of the physical constants during the summer 2017. The data and analysis are described in detail in Ref. [103]. The final results of this special

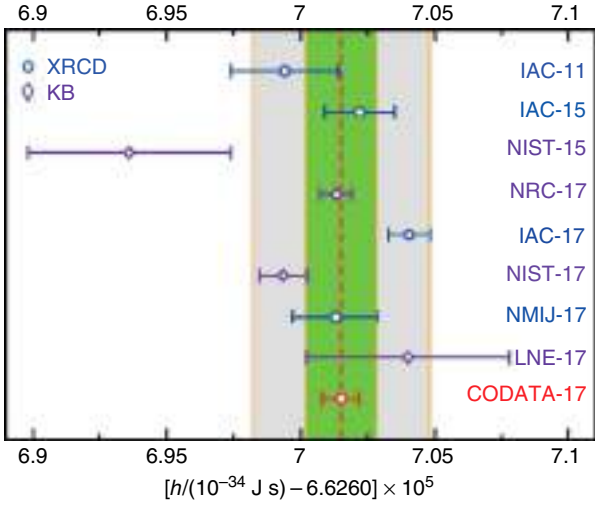

Figure 7.10 Values of the Planck constant inferred from Kibble balance (KB) and Avogadro (XRCD) experiments together with the CODATA 2017 value [104]. The labeling represents the following results: IAC-11 [44], IAC-15 [44], NIST-15 [105], NRC-17 [93], IAC-17 [45, 59], NIST-17 [106], NMIJ-17 [46], LNE-17 [89]. The inner green band is ±2 parts in 10^8 and the outer gray band is ±5 parts in 10^8. Source: © Bureau International des Poids et Mesures. Reproduced by permission of IOP Publishing. All rights reserved.

adjustment for the defining constants, h, e, k, and N_A are reported by the Task Group in [104].

The results for the Planck constant, h, are depicted in Figure 7.10. Obviously, these experimental data are not fully consistent within the uncertainties claimed. To overcome this issue, the CODATA Task Group followed the usual practice by multiplying the uncertainties by an expansion factor (1.7 in this case) to establish consistency. With this procedure, the obtained final value for the Plank constant is [103]

$$h = 6.626\,070\,150(69) \times 10^{-34}\ \mathrm{J\,s}$$

resulting in a value for the defining constant, h, in the present SI of [104]:

$$h = 6.626\,070\,15 \times 10^{-34}\ \mathrm{J\,s}$$

The value of the defining constant was rounded choosing the minimum number of digits, which ensures that the present and previous SI are consistent. As explained before, the defining constant does not possess an uncertainty. Instead, the relative uncertainty of the CODATA value of 1.0×10^{-8} is transferred to the IKP. Similarly, μ_0, the magnetic constant (permeability of vacuum), which, according to the definition of the ampere, was constant with zero uncertainty in the previous SI, will now be a constant to be determined experimentally with an initial uncertainty given by the uncertainty of the fine-structure constant α [103].

7.5.2 Realization, Maintenance, and Dissemination of the Kilogram

The subject of maintenance and dissemination of the kilogram is discussed in detail in Refs. [32, 107, 108] and only can be summarized here.

In the previous SI, the IKP stored at the BIPM was the only experimental access to the kilogram definition. The present definition of the kilogram does not imply any particular experiment for its realization. Any method that derives a mass value traceable to the value of the defining Planck constant (including the definition of the meter and the second) can be a primary method; see also Ref. [32]. At the time of writing, the two experiments described in Sections 7.2 and 7.3 proved the capability to realize the kilogram within the required relative standard uncertainty of a few parts 10^8. This was also confirmed by a pilot study organized by the BIPM "Comparison of realizations of the kilogram," which had been performed before the redefinition of the kilogram in 2016 and early 2017 [108]. Within this pilot study, a key comparison of the realization of the kilogram by five participating national metrology institutes, namely, LNE (France), NIST (USA), NMIJ (Japan), NRC (Canada), and PTB (Germany) took place. The LNE, NIST, and NRC used the Kibble balance; the NMIJ and PTB used enriched ^{28}Si spheres. The results reported in Refs. [108, 109] showed good agreement. However, the results for the determination of the Planck constant shown in Figure 7.10, which were published after the completion of the pilot study, showed that the individual results are not in agreement within the uncertainties claimed; the claimed uncertainties of Figure 7.10 are smaller than those claimed in the pilot study, giving rise to the disagreement. As a result, applying smaller uncertainties, the different realizations of the kilogram would not agree, which would be unacceptable to ensure a harmonized global mass scale. To resolve this problem, the CCM suggested that the NMIs operating realization experiments should disseminate a temporary "consensus value" instead of their own local realization [110]. This consensus value shall be obtained on the base of key comparisons according to the regulations of the Mutual Recognition Arrangement of the CIPM, CIPM MRA [111].

An NMI not operating its own realization experiment may obtain traceability from an NMI operating a realization experiment through calibration of their mass standard as it is common practice in all fields of metrology. Mass dissemination still can be provided by the BIPM with their afore calibrated "ensemble of reference mass standards" (ERMS) [32, 112] and working standards. A comparison of the previous and present traceability chain for the kilogram is shown in Figure 7.11. As mentioned, the major change is the replacement of the IKP, which, per definition, had zero uncertainty, by a primary realization of the kilogram (presently the Kibble balance or Avogadro [XRCD] experiments with the option that other experiments may join), which will result in an uncertainty not exceeding 10 μg. Further, since the Kibble balance and Avogadro experiments are in vacuum, a vacuum/air transfer correction must be included. All this results in an increased uncertainty for the end user, which, however, still satisfies the needs of advanced calibration laboratories. This is obviously the price to pay for the universality of the kilogram definition.

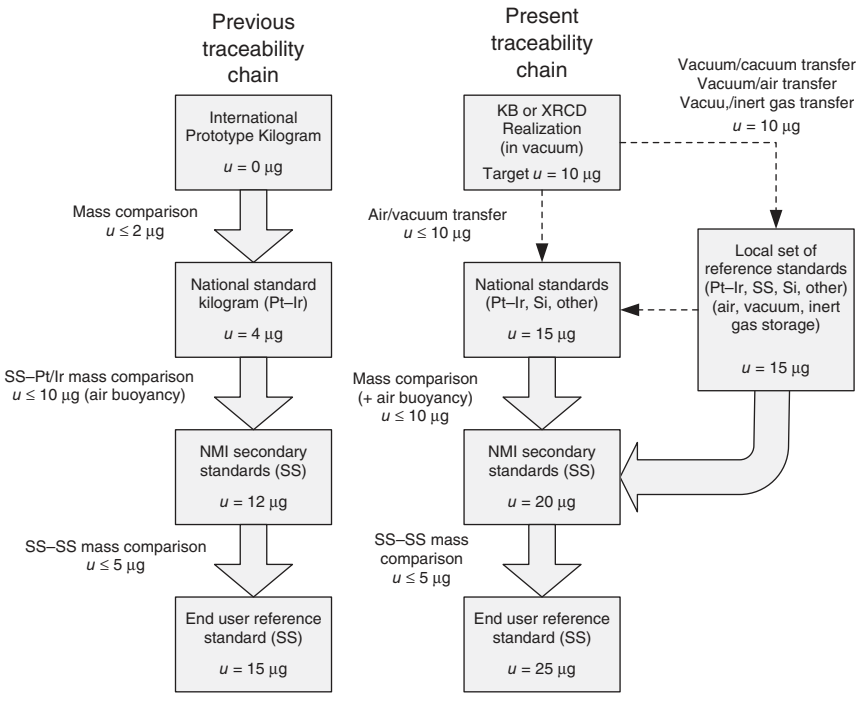

Figure 7.11 Previous and present traceability chain for the dissemination of the kilogram. Source: After Stock et al. 2017 [107].

A collection of all the relevant publications regarding the present kilogram definition can be found in The Focus Issue of *Metrologia*: Realization, Maintenance, and Dissemination of the Kilogram [113].

References

1 Quinn, T. (2012). *From Artifacts to Atoms*. Oxford, New York: Oxford University Press.
2 Davis, R. (2003). The SI unit of mass. *Metrologia* 40: 299–305.
3 Göbel, E.O. and Siegner, U. (2015). *Quantum Metrology: Foundation of Units and Measurements*, 2018. Weinheim: Wiley-VCH.
4 Planck, M. (1900). Zur Theorie des Gesetzes der Energieverteilung im Normalspektrum. *Verh. Dtsch. Phys. Ges.* 2: 237–245 (in German).
5 Flowers, J. and Petley, B. (2004). *Astrophysics, Clocks and Fundamental Constants* (ed. S.G. Karshenboim and E. Peik), 75–93. Berlin, Heidelberg: Springer-Verlag.
6 Lévy-Leblond, J.-M. (1979). *Problems in the Foundations of Physics*, Proceedings of the International School of Physics "Enrico Fermi" Course LXXII (ed. G.T. di Francia), 237–263. Amsterdam: North Holland.

7 Uzan, J.-P. (2003). The fundamental constants and their variation: observational and theoretical status. *Rev. Mod. Phys.* 75: 403.

8 Okun, L.B. (2004). *Astrophysics, Clocks and Fundamental Constants* (ed. S.G. Karshenboim and E. Peik), 57–74. Berlin, Heidelberg: Springer-Verlag.

9 BIPM (2013). Resolution CCM/13-31a resolution CCM G1. http://www.bipm.org/utils/common/pdf/CC/CCM/CCM14.pdf (accessed June 2018).

10 Clothier, W.K., Sloggett, G.J., Bairnsfather, H. et al. (1989). A determination of the volt. *Metrologia* 26: 9–46.

11 Bego, V., Butorac, J., and Illic, D. (1999). Realization of the kilogram by measuring at 100 kV with the voltage balance ETF. *IEEE Trans. Instrum. Meas.* 48: 212–215.

12 Funck, T. and Sienknecht, V. (1991). Determination of the volt with the improved PTB voltage balance. *IEEE Trans. Instrum. Meas.* 40: 158–161.

13 Li, S., Zhang, Z., He, Q. et al. (2013). A proposal for absolute determination of inertial mass by measuring oscillation periods based on the quasielastic electrostatic force. *Metrologia* 50: 9–14.

14 Frantsuz, E.T., Gorchakov, Y.D., and Khavinson, V.M. (1992). Measurements of the magnetic flux quantum, Planck constant, and elementary charge at VNIIM. *IEEE Trans. Instrum. Meas.* 41: 482–485.

15 Frantsuz, E.T., Khavinson, V.M., Genevès, G., and Piquemal, F. (1996). A proposed superconducting magnetic levitation system intended to monitor stability of the unit of mass. *Metrologia* 33: 189–196.

16 Shiota, F. and Hara, K. (1987). A study of a superconducting magnetic levitation system for an absolute determination of the magnetic flux quantum. *IEEE Trans. Instrum. Meas.* 36: 271–274.

17 Shiota, F., Miki, Y., Fujii, Y. et al. (2000). Evaluation of equilibrium trajectory of superconducting magnetic levitation system for the future kg unit of mass. *IEEE Trans. Instrum. Meas.* 49: 1117–1121.

18 CIPM (1989). Report of the 78th Meeting 1989. http://www.bipm.org/utils/common/pdf/CIPM-PV-OCR/CIPM1989.pdf (accessed November 2018).

19 Girard, G. (1990). The washing and cleaning of kilogram prototypes at the BIPM, BIPM Monographie 1990/1. http://www.bipm.org/utils/en/pdf/Monographie1990-1-EN.pdf (accessed November 2018).

20 Girard, G. (1994). The third periodic verification of national prototypes of the kilogram (1988–1992). *Metrologia* 31: 317.

21 de Mirandes, E., Barat, P., Stock, M., and Milton, M.J.T. (2016). Calibration campaign against the international prototype of the kilogram in anticipation of the redefinition of the kilogram, part II: evolution of the BIPM as-maintained mass unit from the 3rd periodic verification to 2014. *Metrologia* 53: 1204.

22 In addition, the fourth verification had shown an unexpected offset of 0,035 μg of the BIPM as maintained mass unit with respect to the IKP. See [21] and Stock, M., Barat, P., Davis, S.R. et al. (2014). Calibration campaign against the international prototype of the kilogram in anticipation of the redefinition of the kilogram part I: comparison of the international prototype with its official copies. *Metrologia* 52: 310.

23 BIPM (1993). CIPM resolution CI-4. http://www.bipm.org/en/committees/cipm/publications-cipm.html (accessed November 2018).
24 BIPM (1995). 20th CGPM resolution 5. http:/www.bipm.org/en/CGPM/db/20/5 (accessed November 2018).
25 Mills, I.M., Mohr, P.J., Quinn, T.J. et al. (2005). Redefinition of the kilogram: a decision whose time has come. *Metrologia* 42: 71.
26 Stenger, J. and Göbel, E.O. (2012). The silicon route to a primary realization of the kilogram. *Metrologia* 49: L25.
27 Mohr, P.J., Taylor, B.N., and Newell, D.B. (2016). CODATA recommended values of the fundamental physical constants: 2014. *Rev. Mod. Phys.* 88, 035009 (73 pp).
28 Milton, M.J.T., Davis, R., and Fletcher, N. (2014). Towards a new SI: a review of progress made since 2011. *Metrologia* 51: R21.
29 Richard, P., Fang, H., and Davis, R. (2016). Foundation for the redefinition of the kilogram. *Metrologia* 53: A6.
30 CIPM (2010). Draft resolution A. http://www.bipm.org/utils/en/pdf/CIPM/CIPM2010-EN.pdf (accessed November 2018).
31 BIPM (2014). 25th CGPM resolution 1, http://www.bipm.org/utils/common/pdf/CGPM-2014/25th-CGPM-Resolutions.pdf (accessed November 2018).
32 BIPM (2018). *Mise en pratique* for the definition of the kilogram, www.bipm.org/utils/en/pdf/si-mep/MeP-kg-2018.pdf (accessed November 2018).
33 Becker, P. (2001). History and progress in the accurate determination of the Avogadro constant. *Rep. Prog. Phys.* 64: 1945–2008.
34 Becker, P. and Bettin, H. (2011). The Avogadro constant: determining the number of atoms in a single-crystal ^{28}Si sphere. *Philos. Trans. R. Soc. London, Ser. A* 369: 3925–3935.
35 Becker, P. (2003). Tracing the definition of the kilogram to the Avogadro constant using a silicon single crystal. *Metrologia* 40: 366–375.
36 Gläser, M. (2003). Tracing the atomic mass unit to the kilogram by ion accumulation. *Metrologia* 40: 376–386.
37 Schlegel, C., Scholz, F., Gläser, M. et al. (2007). Accumulation of 38 mg of bismuth in a cylindrical collector from a 2.5 mA ion beam. *Metrologia* 44: 24–28.
38 Zakel, S., Wundrack, S., Niemann, H. et al. (2011). Infrared spectrometric measurement of impurities in highly enriched ^{28}Si. *Metrologia* 48: S14–S19.
39 Gebauer, J., Rudolf, F., Polity, A. et al. (1999). On the sensitivity limit of positron annihilation: detection of vacancies in as-grown silicon. *Appl. Phys. A* 68: 411–416.
40 Kuramoto, N., Fujii, K., and Yamazawa, K. (2011). Volume measurement of ^{28}Si spheres using an interferometer with a flat etalon to determine the Avogadro constant. *Metrologia* 48: S83–S95.
41 Bartl, G., Bettin, H., Krystek, M. et al. (2011). Volume determination of the Avogadro spheres of highly enriched ^{28}Si with a spherical Fizeau interferometer. *Metrologia* 48: S96–S103.
42 Andreas, B., Azuma, Y., Bartl, G. et al. (2011). Determination of the Avogadro constant by counting the atoms in a 28 Si crystal. *Phys. Rev. Lett.* 106: 030801–1–030801-4.

43 Andreas, B., Azuma, Y., Bartl, G. et al. (2011). Counting the atoms in a ^{28}Si crystal for a new kilogram definition. *Metrologia* 48: S1–S13.

44 Azuma, Y., Barat, P., Bartl, G. et al. (2015). Improved measurement results for the Avogadro constant using a ^{28}Si-enriched crystal. *Metrologia* 52: 360–375.

45 Bartl, G., Becker, P., Beckhoff, B. et al. (2017). A new ^{28}Si single crystal: counting the atoms for the new kilogram definition. *Metrologia* 54: 693–715.

46 Kuramoto, N., Mizushima, S., Zhang, L. et al. (2017). Determination of the Avogadro constant by the XRCD method using a ^{28}Si-enriched sphere. *Metrologia* 54: 716–729.

47 Müller, M., Beckhoff, B., Beyer, E. et al. (2017). Quantitative surface characterization of silicon spheres by combined XRF and XPS analysis for the determination of the Avogadro constant. *Metrologia* 54: 653–662.

48 Busch, I., Azuma, Y., Bettin, H. et al. (2011). Surface layer determination for the Si spheres of the Avogadro project. *Metrologia* 48: S62–S82.

49 Massa, E., Mana, G., Kuetgens, U., and Ferroglio, L. (2011). Measurement of the {220} lattice-plane spacing of a ^{28}Si X-ray interferometer. *Metrologia* 48: S37–S43.

50 (a) Bonse, U. and Hart, M. (1965). An X-ray interferometer. *Appl. Phys. Lett.* 6: 155–156. (b) Bonse, U. and Hart, M. (1965). Principles and design of Laue-case X-ray interferometer. *Z. Phys.* 188: 154–164.

51 Mana, G., Massa, E., Sasso, C.P. et al. (2017). A new analysis for diffraction correction in optical interferometry. *Metrologia* 54: 559–565.

52 Mana, G., Massa, E., and Sasso, C.P. (2018). Wavefront errors in a two-beam interferometer. *Metrologia* 55: 535–540.

53 De Bièvre, P., Lenaers, G., Murphy, T.J. et al. (1995). The chemical preparation and characterization of specimens for "absolute" measurements of the molar mass of an element, exemplified by silicon, for redeterminations of the Avogadro constant. *Metrologia* 32: 103–110.

54 Bulska, E., Drozdov, M.N., Mana, G. et al. (2011). The isotopic composition of enriched Si: a data analysis. *Metrologia* 48: S32–S36.

55 Becker, P., Bettin, H., Danzebrink, H.-U. et al. (2003). Determination of the Avogadro constant via the silicon route. *Metrologia* 40: 271–287.

56 Becker, P., Schiel, D., Pohl, H.-J. et al. (2006). Large-scale production of highly enriched ^{28}Si for the precise determination of the Avogadro constant. *Meas. Sci. Technol.* 17: 1854–1860.

57 Becker, P., Friedrich, H., Fujii, K. et al. (2009). The Avogadro constant determination via enriched silicon-28. *Meas. Sci. Technol.* 20: 092002-1–092002-20.

58 Leistner, A. and Zosi, G. (1987). Polishing a 1 kg silicon sphere for a density standard. *Appl. Opt.* 26: 600–601.

59 Abrosimov, N.V., Aref'ev, D.G., Becker, P. et al. (2017). A new generation of 99.999% enriched ^{28}Si single crystals for the determination of Avogadro's constant. *Metrologia* 54: 599–609.

60 Rienitz, O., Pramann, A., and Schiel, D. (2010). Novel concept for the mass spectrometric determination of absolute isotopic abundances with improved

measurement uncertainty: Part I. Theoretical derivation and feasibility study. *Int. J. Mass Spectrom.* 289: 47–53.

61 Pramann, A., Rienitz, O., Schiel, D. et al. (2011). Molar mass of silicon highly enriched in ^{28}Si determined by IDMS. *Metrologia* 48: S20–S25.

62 Mana, G. and Rienitz, O. (2010). The calibration of Si isotope-ratio measurements. *Int. J. Mass Spectrom.* 291: 55–60.

63 Mana, G., Rienitz, O., and Pramann, A. (2010). Measurement equations for the determination of the Si molar mass by isotope dilution mass spectrometry. *Metrologia* 47: 460–463.

64 Praxmann, A., Narukawa, T., and Rienitz, O. (2017). Determination of the isotopic composition and molar mass of a new 'Avogadro' crystal: homogeneity and enrichment-related uncertainty reduction. *Metrologia* 54: 738–747.

65 Fujii, K., Massa, E., Bettin, H. et al. (2018). Avogadro constant measurements using enriched ^{28}Si monocrystals. *Metrologia* 55: L1–L4.

66 Saeedi, K., Simmons, S., Salvali, J.Z. et al. (2013). Room-temperature quantum bit storage exceeding 39 minutes using ionized donors in Silicon-28. *Science* 342: 830–833.

67 Eichenberger, A., Jeckelmann, B., and Richard, P. (2003). Tracing Planck's constant to the kilogram by electromechanical methods. *Metrologia* 40: 356–365.

68 Eichenberger, A., Genevès, G., and Gournay, P. (2009). Determination of the Planck constant by means of a watt balance. *Eur. Phys. J. Spec. Top.* 172: 363–383.

69 Stock, M. (2013). Watt balance experiments for the determination of the Planck constant and the redefinition of the kilogram. *Metrologia* 50: R1–R16.

70 Steiner, R. (2013). History and progress on accurate measurements of the Planck constant. *Rep. Prog. Phys.* 76: 016101.

71 Special Issue Watt and Joule Balances, the Planck Constant and the Kilogram Robinson, I.A. (ed.) (2014). *Metrologia* 51 (2): S1–S140.

72 Haddad, D., Seifert, F., Chao, L.S. et al. (2016). Invited article: a precise instrument to determine the Planck constant, and the future kilogram. *Rev. Sci. Instrum.* 87: 06103-1-14.

73 Kibble, B.P. (1976). *Atomic Masses and Fundamental Constants*, vol. 5 (ed. J.H. Sanders and A.H. Wapstra), 545–551. New York: Plenum Press.

74 Kibble, B.P., Robinson, I.A., and Bellis, J.H. (1990). A realization of the SI watt by the NPL moving-coil balance. *Metrologia* 27: 173–192.

75 Olsen, P.T., Bower, V.E., Phillips, W.D. et al. (1985). The NBS absolute ampere experiment. *IEEE. Trans. Instrum. Meas.* 34: 175–181.

76 Olsen, P.T., Elmquist, R.E., Phillips, W.D. et al. (1989). A measurement of the NBS electrical watt in SI units. *IEEE Trans. Instrum. Meas.* 38: 238–244.

77 Robinson, I.A. and Kibble, B.P. (2007). An initial measurement of Planck's constant using the NPL Mark II watt balance. *Metrologia* 44: 427–440.

78 Robinson, I.A. (2012). Alignment of the NPL Mark II watt balance. *Meas. Sci. Technol.* 23, 124012 (17 pp).

79 Steiner, R., Newell, D., and Williams, E. (2005). Details of the 1998 watt balance experiment determining the Planck constant. *J. Res. Natl. Inst. Stand. Technol.* 110 (1): –26.

80 Steiner, R.L., Williams, E.R., Newell, D.B., and Liu, R. (2005). Towards an electronic kilogram: an improved measurement of the Planck constant and electron mass. *Metrologia* 42: 431–441.

81 Steele, A.G., Meija, J., Sanchez, C.A. et al. (2012). Reconciling Planck constant determinations via watt balance and enriched-silicon measurements at NRC Canada. *Metrologia* 49: L8–L10.

82 Baumann, H., Eichenberger, A., Cosandier, F. et al. (2013). Design of the new METAS watt balance experiment Mark II. *Metrologia* 50: 235–242.

83 Eichenberger, A., Baumann, H., Jeanneret, B. et al. (2011). Determination of the Planck constant with the METAS watt balance. *Metrologia* 48: 133–141.

84 Geneves, G., Gournay, P., Gosset, A. et al. (2005). The BNM watt balance project. *IEEE Trans. Instrum. Meas.* 54: 850–853.

85 Gournay, P., Geneves, G., Alves, F. et al. (2005). Magnetic circuit design for the BNM Watt balance experiment. *IEEE Trans. Instrum. Meas.* 54: 742–745.

86 dos Pereira, Santos, F., Le Gouet, J., Mehlstäubler, T. et al. (2008). Gravimètre à atoms froids. *Rev. Fr. Métrol.* 13: 33–40 (in French).

87 Maletras, F.-X., Gournay, P., Robinson, I.A., and Geneves, G. (2007). A bias source for dynamic voltage measurements with a programmable Josephson junction array. *IEEE Trans. Instrum. Meas.* 56: 495–499.

88 Thomas, M., Espel, P., Ziane, D. et al. (2015). First determination of the Planck constant using the LNE watt balance. *Metrologia* 52: 433–443.

89 Thomas, M., Ziane, D., Pinot, P. et al. (2017). A determination of the Planck constant using LNE Kibble balance in air. *Metrologia* 54: 468–480.

90 Picard, A., Bradley, M.P., Fang, H. et al. (2011). The BIPM watt balance: improvements and developments. *IEEE Trans. Instrum. Meas.* 60: 2378–2386.

91 Fang, H., Kiss, A., Picard, A., and Stock, M. (2014). A watt balance based on a simultaneous measurement scheme. *Metrologia* 51: S80–S87.

92 de Mirandes, E., Zeggah, A., Bradley, M.P. et al. (2014). Superconducting moving coil system to study the behaviour of superconducting coils for a BIPM cryogenic watt balance. *Metrologia* 51: S123–S131.

93 Wood, B.M., Sanchez, C.A., Green, R.G., and Liard, J.O. (2017). A summary of the Planck constant determinations using the NRC Kibble balance. *Metrologia* 54: 399–409.

94 Zhang, Z., He, Q., Li, Z. et al. (2011). Recent development on the Joule balance at NIM. *IEEE Trans. Instr. Meas.* 60: 2533–2538.

95 Li, Z., Zhang, Z., Lu, Y. et al. (2017). The first determination of the Planck constant with the Joule balance NIM-2. *Metrologia* 54: 763–774.

96 Milton, M.J.T. and Mills, I.M. (2009). Amount of substance and the proposed new definition of the mole. *Metrologia* 46: 332–338.

97 BIPM (2018). BIPM Draft SI Brochure. https://www.bipm.org/utis/en/pdf/si-revised-brochure/Draft-SI-Brochure-2018.pdf (accessed June 2018).

98 BIPM (2016). Draft *Mise en practique* of the definition of the mole. https://www.bipm.org/cc/CCQM/Allowed/22/CCQM16-04_Mole_m_en_p_draft.pdf (accessed November 2018).

99 Milton, M.J.T. and Quinn, T.J. (2001). Primary methods for the measurement of amount of substance. *Metrologia* 38: 289–296.

100 Brown, R.J.C. (2018). The evolution of chemical metrology: distinguishing between amount of substance and counting quantities, now and in future. *Metrologia* 55: L25–L33.

101 CGPM (2011). Resolution 1 of the 24th CGPM. https://www.bipm.org/utils/common/pdf/24_CGPM_Resolutions.pdf/ (accessed November 2018).

102 CIPM (2015). Decision CIPM/104–09 of the 104th CIPM, Session I. www.bipm.org/en/committees/cipm/meeting/104(I).html (accessed November 2018).

103 Mohr, P.J., Newell, D.B., Taylor, B.N., and Tiesinga, E. (2018). Data and analysis for the CODATA 2017 special fundamental constants adjustment. *Metrologia* 55: 125–146.

104 Newell, D.B., Cabiati, F., Fischer, J. et al. (2018). The CODATA 2017 values of *h, e, k*, and N_A for the revision of the SI. *Metrologia* 55: L13–L15.

105 Schlamminger, S., Steiner, R.L., Haddad, D. et al. (2015). A summary of the Planck constant measurements using a watt balance with a superconducting solenoid at NIST. *Metrologia* 52 (2): L5.

106 Haddad, S.F., Chao, L.S., Possolo, A. et al. (2017). Measurement of the Planck constant at the National Institute of Standards and Technology from 2015 to 2017. *Metrologia* 54 (5): 633–641.

107 Stock, M., Davidson, S., Fang, H. et al. (2017). Maintaining and disseminating the kilogram following its redefinition. *Metrologia* 54: S99–S107.

108 Stock, M., Barat, P., Pinot, P. et al. (2018). A comparison of future realizations of the kilogram. *Metrologia* 55: T1–T7.

109 Stock, M., Barat, P., Beaudoux, F. et al. (2017). Report on the CCM Pilot Study CCM.R-kg-P1: Comparison of Future Realizations of the Kilogram. *Final Report*. www.bipm.org/cc/CCM/Allowed/16/03-7B2_CCM-PilotStudy-FinalReport.pdf (accessed November 2018).

110 BIPM (2017). CCM Recommendation G1 2017. For a new definition of the kilogram in 2018. www.bipm.org/cc/CCM/Allowed/16/06E_Final_CCM-Recommendation_G1-2017.pdf (accessed November 2018).

111 BIPM (1999). Mutual recognition arrangement. https://www.bipm.org/en/cipm-mra/ (accessed November 2018).

112 BIPM (2018). Ensemble of mass standards. www.bipm.org/en/bipm/mass/pool_artefacts/ (accessed November 2018).

113 IOPScience (2019). Focus Issue on 'Realization, Maintenance, and Dissemination of the Kilogram. http://iopscience.iop.org/journal/0026-1394/page/Focus_on_Realization_Maintenance_and_Dissemination_of_the_Kilogram (accessed November 2018).

8

The SI Kelvin and the Boltzmann Constant

The previous definition of the unit of thermodynamic temperature, kelvin, was based on a material artifact, namely, the triple-point-of-water (TPW) temperature. The TPW is the temperature (273.16 K) and pressure (611.73 Pa) where all three phases of water, that is, liquid, solid (ice), and vapor, coexist. Though ideally the TPW can be considered a constant of nature, its precise temperature depends on many parameters, such as isotopic composition, purity, which are often difficult to quantify precisely. Nevertheless, according to the previous definition of the kelvin, the temperature of the TPW has always been exactly 273.16 K with no uncertainty. In the present SI, the TPW temperature is a quantity to be measured with an initial uncertainty equal to the uncertainty of the Boltzmann constant before defining its value. The effect of isotope composition had been considered in the previous kelvin definition by defining the sort of water to be used [1]. Keeping in mind that the determination of isotope ratios also exhibits uncertainties and that purity and its temporal variation are very difficult to specify absolutely, it is obvious that we had been at a situation which was not so different from the previous kilogram definition via the International Kilogram Prototype, IKP. The realization of the kelvin according to the previous definition through the TPW temperature was possible with an uncertainty of one part in 10^7.

In the present SI, the definition of the kelvin by a material artifact is abolished. Instead it is defined by the fixed value of the defining Boltzmann constant, k. Since, in the fundamental statistical laws of physics, temperature in any case appears as thermal energy, kT, it was natural to take the Boltzmann constant, k, as the defining constant, as decided by the 26th General Conference on Weights and Measures (CGPM) in 2018 [2]. Earlier the conditions for the determination of the Boltzmann constant as specified by the *Comité consultatif de thermométrie* (CCT) of the International Committee for Weights and Measures (*Comité International des Poids et Mesures*) (CIPM), [3] had been fulfilled as shown below. The CCT had requested that an uncertainty of the order of 1×10^{-6} must be achieved, including at least two fundamentally different methods of primary thermometry with a relative standard uncertainty not larger than three parts in 10^6.

The present definition of the kelvin links the unit of temperature to the unit of energy, the joule ($1\,\mathrm{J} = 1\,\mathrm{kg\,m^2\,s^{-2}}$). The unit of temperature is thus independent of a particular temperature in contrast to the previous definition. This is

The New International System of Units (SI): Quantum Metrology and Quantum Standards,
First Edition. Ernst O. Göbel and Uwe Siegner.
© 2019 Wiley-VCH Verlag GmbH & Co. KGaA. Published 2019 by Wiley-VCH Verlag GmbH & Co. KGaA.

of advantage when realizing and disseminating the kelvin at very high and low temperatures.

In the following section, we discuss some of the primary thermometers that have been the major pillars for the precise determination of the Boltzmann constant and hence will be the obvious choice for the realization of the kelvin [4]. For more detailed reviews, the reader is referred to Refs. [5, 6].

8.1 Primary Thermometers

For primary thermometers, the relation between the measurand and the thermodynamic temperature is explicitly known or calculable with the necessary uncertainty and does not contain any other temperature-dependent quantities and constants. The most common primary thermometers relevant for the determination of the Boltzmann constant and the realization of the kelvin in the present SI are based on thermal equations of state, such as the constant volume gas thermometer (CVGT), the refractive index gas thermometer (RIGT), and the dielectric constant gas thermometer (DCGT). Another gas thermometer based on measuring the speed of sound, the acoustic gas thermometer (AGT), had received great attention in view of a precise determination of the Boltzmann constant [7]. We shall briefly describe DCGT and AGT as well as radiation thermometers (total radiation as well as spectral radiation). In the frame of quantum metrology, noise thermometers and thermometers based on molecule absorption spectroscopy (Doppler broadening thermometry, DBT) as well as Coulomb blockade thermometers (CBTs) will be considered finally. Other primary thermometers, which had been of less relevance for the determination of the Boltzmann constant, such as magnetic thermometers, will not be discussed here, but the reader is referred to the respective literature [8, 9].

The base for many primary thermometers is given by the thermal state equation for ideal gases:

$$pV = nRT = NkT \tag{8.1}$$

where p, V, and T are the state variables for pressure, volume, and temperature, respectively; n is the amount of substance; N is the number of particles; and R is the universal gas constant, $R = kN_A$ (N_A is the Avogadro constant; see Chapter 7). Even though in particular noble gases behave approximately like ideal gases at the TPW temperature, for a precise determination of the Boltzmann constant even the smallest deviations from the ideal gas behavior had to be considered. This is usually accomplished by determining experimentally at a constant temperature the dependence of the measurand (e.g. pressure) on the density of the gas. These isotherms are then fitted according to a virial expansion

$$pV = nRT(1 + B(T)/V_m + C(T)/V_m^2 + \cdots) \tag{8.2}$$

and extrapolated to zero density. $B(T)$ and $C(T)$ in Eq. (8.2) are, respectively, the second and third density virial coefficients, and V_m is the molar volume, $V_m = V/n$. For absolute isotherm CVGT, a constant volume is subsequently

filled with different amounts of gas at constant temperature to obtain different pressures. From a plot of $(pV)/n$ versus $1/V_m$, the product RT is then directly obtained according to Eq. (8.2). However, we will not discuss CVGT any further because the achievable uncertainty seems to be limited to a few parts in 10^5 [7].

8.1.1 Dielectric Constant Gas Thermometry

DCGT is based on the Clausius–Mossotti relation relating the relative dielectric constant of a gas, ε_r, to its static electric polarizability, α_0, according to

$$\frac{\varepsilon_r - 1}{\varepsilon_r + 2} = \frac{N}{V}\frac{\alpha_0}{3\varepsilon_0} \tag{8.3}$$

where ε_0 is the electric constant. Replacing the number density (N/V) in Eq. (8.3) using the state equation of the ideal gas (Eq. (8.1)), considering that $\varepsilon_r\varepsilon_0 = \varepsilon$, and approximating $\varepsilon_r + 2 \approx 3$ as valid for ideal gases yields

$$p = \frac{kT(\varepsilon - \varepsilon_0)}{\alpha_0} \tag{8.4}$$

The dielectric constant ε is determined by capacity measurements. Accordingly, in the DCGT experiment, the pressure dependence of the capacitance of a capacitor containing the measuring gas at the TPW temperature must be measured. However, in addition, the polarizability, α_0, must be known with the required uncertainty. This is fulfilled for ^{4}He, where *ab initio* quantum electrodynamics (QED) calculations for α_0 have meanwhile achieved an uncertainty well below 10^{-6} [10], and recent experiments have confirmed this on an uncertainty level of 2 parts per million [11]. As already said earlier, for a precise determination of k, deviations from the ideal gas behavior must be considered. Combining the virial expansion (Eq. (8.2)) with the Clausius–Mossotti relation (8.3) then yields [7]

$$p \approx \frac{\chi}{\frac{3A_\varepsilon}{RT} + \kappa_{\text{eff}}}\left[1 + \frac{B(T)}{(3A_\varepsilon)}\chi + \frac{C(T)}{(3A_\varepsilon)^2}\chi^2 + \ldots\right] \tag{8.5}$$

where $\chi = (\varepsilon/\varepsilon_0 - 1)$ is the dielectric susceptibility, $A_\varepsilon = N_A\,\alpha_0/3\varepsilon_0$ is the molar polarizability, and κ_{eff} is the effective compressibility of the capacitor used to measure χ, considering changes of its dimension with pressure [12]. The relative change of the capacitance is given by

$$\frac{C(p) - C(0)}{C(0)} = \chi + \frac{\varepsilon}{\varepsilon_0}\kappa_{\text{eff}}p \tag{8.6}$$

where $C(p)$ and $C(0)$ are, respectively, the capacitance of the gas-filled and evacuated capacitor. The relative change is then measured at constant temperature. From a polynomial fit of the plot of p versus $C(p) - C(0)/C(0)$ at the TPW temperature, $3A_\varepsilon/RT_{\text{TPW}}$ and thus the Boltzmann constant k are obtained. A schematic sketch of the DCGT setup used at the Physikalisch–Technische Bundesanstalt (PTB) (National Metrology Institute of Germany) is shown in Figure 8.1.

Because of the very small susceptibility of gases (e.g. for He at the TPW temperature and 0.1 MPa $\chi \approx 7 \times 10^{-5}$), these measurements are extremely demanding

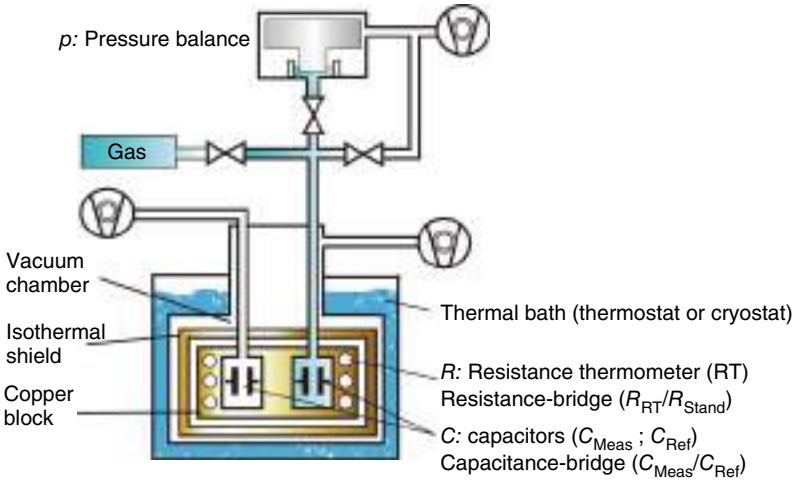

Figure 8.1 Schematic sketch of the DCGT setup used at PTB [13]. Source: © Bureau International des Poids et Mesures. Reproduced with permission of IOP Publishing. All rights reserved.

as they require audio-frequency capacitance bridges providing uncertainties of a few parts in 10^9 [14] and pressure measurement up to 7 MPa with a relative standard uncertainty of order one part in 10^6. The most recent value of the Boltzmann constant obtained with PTB's DCGT experiment at the TPW has an estimated relative standard uncertainty of 1.9×10^{-6} [15]. For a more detailed description of the DCGT experiment, see Ref. [13].

8.1.2 Acoustic Gas Thermometry

Acoustic gas thermometry (AGT) [16] applies a resonance method to measure the low-pressure speed of sound. It is based on the two relations valid for an ideal gas:

$$\frac{1}{2} m \mathrm{v}_{\mathrm{rms}}^2 = \frac{3}{2} kT \tag{8.7}$$

and

$$\mathrm{v}_{\mathrm{rms}}^2 = \frac{3}{\gamma_0} u_0^2. \tag{8.8}$$

In Eq. (8.7), m is the mass of the atom and $\mathrm{v}_{\mathrm{rms}}^2$ its root-mean-square velocity. Equation (8.7) thus relates the kinetic energy of an atom to its thermal energy kT. Equation (8.8) then relates $\mathrm{v}_{\mathrm{rms}}^2$ to the zero-frequency speed of sound of the gas, u_0, where $\gamma_0 = c_{\mathrm{p}}/c_{\mathrm{v}}$ is the zero-pressure limit of the ratio of specific heat capacitance at constant pressure (c_{p}) and constant volume (c_{v}). Combining Eqs. (8.7) and (8.8) and replacing the mass of an atom by the molar mass, M, of the gas divided by the Avogadro constant, $m = M/N_{\mathrm{A}}$, yield

$$k = \frac{M u_0^2}{\gamma_0 N_{\mathrm{A}} T} \tag{8.9}$$

For a monatomic gas, $\gamma_0 = 3/5$. The Avogadro constant, N_A, is fixed in the present SI but had an uncertainty in the previous SI of 1.2×10^{-8} according to Committee on Data for Science and Technology (CODATA) [17]. When the experiment is performed at the TPW temperature, the molar mass, M, and the speed of sound, u_0, must be measured to determine k.

Argon and helium have been used in the AGT experiments. Since Ar has three stable isotopes, ^{40}Ar, ^{36}Ar, and ^{38}Ar (in total, 23 isotopes of Ar are known), quantifying its isotopic composition and purity (chemical composition) is challenging in molar mass determination. A detailed study of the molar mass determination can be found in, for example, [18, 19]. The speed of sound is measured in an acoustic resonator. Today, spherical or almost (quasi-)spherical resonators (see, e.g. [18, 20, 21]) and cylindrical resonators [22] are used. While in the early high-precision experiments [20, 21], the resonator was filled with high-purity mercury to estimate its geometric dimensions (volume), microwave resonances of the same resonator are now frequently used to determine its dimension [23]. Quasi-spherical resonators are more advantageous compared to perfect spherical resonators because the otherwise degenerate microwave modes are then partly resolved, allowing a better determination of the dimensions and their thermal variation [24]. Together with the measured frequencies of the acoustic resonances, the speed of sound is then derived. A photo of an AGT resonator is shown in Figure 8.2.

Figure 8.2 Photo of the assembled National Physics Laboratory (NPL) 1 l copper AGT resonator. Source: Reproduced with permission of NPL Management Limited.

Although AGT had already been applied in the late 1970s to determine the universal gas constant [25], the first high-precision determination of the Boltzmann constant using AGT was reported by Moldover et al. [20, 21] using a stainless steel spherical resonator, in which the uncertainty of the value of the Boltzmann constant was reported to be 1.8×10^{-6}. More recent experiments have confirmed that uncertainties at the 10^{-6} level can readily be obtained [5, 18, 19, 26, 27]. Experiments using He instead of Ar have been reported, e.g. in Refs. [28–32]. The smallest relative uncertainty so far of 0.6×10^{-6} was achieved using ^{4}He in a quasi-spherical resonator [32]. By combining this latest result with the former data, the uncertainty could be further reduced to 0.56×10^{-6} [32]. Cylindrical, instead of spherical, resonators have been employed in the experiments of the National Institute of Metrology (NIM), China [22, 33, 34]. Combing their experimental results, a relative standard uncertainty for k of 2×10^{-6} has been achieved [34]. Overall, the AGT experiments have made considerable progress over the last decade and have been a major pillar for the determination of the value of the defining constant k for the kelvin.

8.1.3 Radiation Thermometry

For absolute radiation thermometry (RT), blackbody radiators are used. Blackbody radiators are primary sources of electromagnetic radiation linking directly the spectral and total radiance to temperature. Note that synchrotrons can also act as primary radiation sources [35] and are successfully used to realize the primary scale for the spectral radiance from the visible to X-ray spectral regime. However, synchrotron radiation cannot be employed for absolute RT or for the determination of the Boltzmann constant because of the missing link to temperature.

Absolute thermometers based on blackbody radiometers measure the spectral radiance as a function of frequency, $L_\nu(\nu, T)$, or the frequency integrated total radiance, $L(T)$. The temperature dependence of the spectral radiance of a blackbody radiator is described by the Planck law [36]:

$$L_\nu(\nu, T) = \frac{2h}{c^2}\nu^3 \left[\exp\left(\frac{h\nu}{kT}\right) - 1\right]^{-1} \tag{8.10}$$

The total radiance is given by the Stefan–Boltzmann law:

$$L(T) = \int_0^\infty L_\nu(\nu, T)\mathrm{d}\nu = \frac{\sigma}{\pi}T^4 \tag{8.11}$$

with the Stefan–Boltzmann constant:

$$\sigma = \frac{2\pi^5 k^4}{15c^2h^3} \tag{8.12}$$

An ideal blackbody absorbs all incoming radiation regardless of its frequency and angle of incidence. Its absorptivity and emissivity equal 1, and the emission spectrum as described by Eq. (8.10) is the maximum possible radiance at a given frequency and temperature. The challenge for the construction of blackbody radiators is to meet the ideal conditions as close as possible. Blackbodies usually consist of a cavity with a small hole. The inner surface of this cavity

is covered with a suitable material. The choice of the material depends on the temperature and frequency considered. The blackbody radiators developed at the Physikalisch–Technische Reichsanstalt (PTR) by Lummer and Kurlbaum [37] allowed at that time an unprecedented precise determination of their emission spectrum and paved the way for the Planck law.

Precise absolute RT became possible only through the development of cryogenic radiometers [38, 39]. Cryogenic radiometers are electrical substitution calorimeters where the heating by the incoming radiation is compared to an equal electrical heating. Operating the radiometer at cryogenic temperatures (usually using liquid He), compared to room temperature, results in a considerable increase in sensitivity and accuracy (e.g. due to the much smaller heat capacity and hence increased thermal diffusivity of the used material [e.g. Cooper]) as well as smaller radiation losses and background radiation [38]. In practice, RT does not detect the total radiation emitted into a complete hemisphere but only the radiation passing through a suitable aperture system. Consequently, additional sources of error relate to its temperature, geometry, and diffraction effects [38].

Spectral radiometry, compared to total radiometry, has the advantage that it can select and restrict the frequency to the maximum of the emission spectrum of the blackbody. For the determination of k with the smallest possible uncertainty in the previous SI, the operating temperature should have been at the TPW or close to it.

With all these restrictions, RT did not achieve the uncertainties required to contribute to the final value of the Boltzmann constant; however, with the present definition of the kelvin, spectral radiometry will play an important role in the dissemination of the high-temperature scale [4].

8.1.4 Doppler Broadening Thermometry

Doppler broadening of spectral emission or absorption lines of atomic or molecular gases has already been discussed in Chapter 3. The Doppler effect for electromagnetic waves accounts for the frequency change when source and detector move relative to each other. For an atom or molecule with a resonance frequency ν_0 moving with velocity (speed), s, toward a tunable laser source at rest, absorption will take place when the frequency of the laser, ν', is shifted to the red according to (neglecting the second-order Doppler effect)

$$\nu' = \nu_0 \left(1 - \frac{s}{c}\right) \tag{8.13}$$

Considering next a gas at low pressure in thermal equilibrium at a given temperature, the velocity distribution of the atoms or molecules then will be described by the Maxwell–Boltzmann distribution proportional to $\exp[-(s/s_0)^2]$ where $s_0^2 = 2kT/m$ with m being the mass of the atom or molecule. This transforms into a Gaussian absorption profile with half width, $\Delta\nu_D$:

$$\frac{\Delta\nu_D}{\nu_0} = \left(\frac{2kT}{mc^2}\right)^{1/2} \tag{8.14}$$

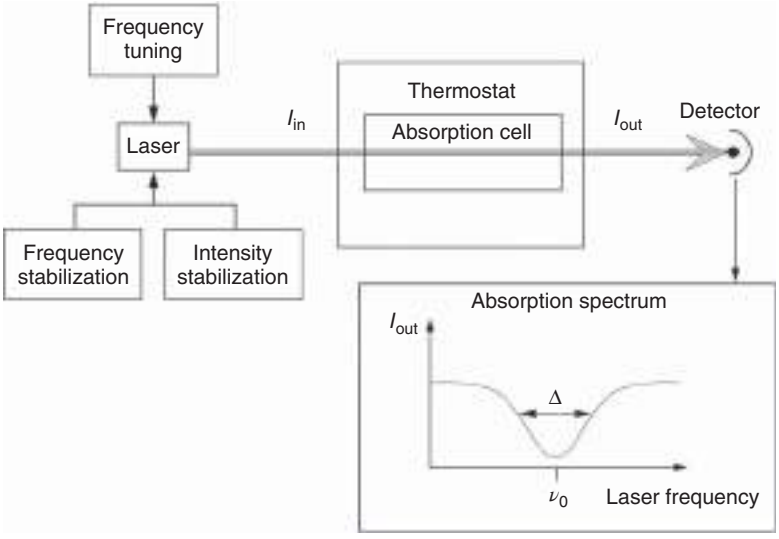

Figure 8.3 Schematic of the laser spectrometer setup for DBT. Source: Göbel and Siegner 2015 [42]. Reproduced with permission of John Wiley & Sons.

The relative mass of the respective ion can be measured with small uncertainty (of order 10^{-9} or better) using Penning traps. Conversion to absolute masses requires knowledge of the Avogadro constant (relative uncertainty in the previous SI according to CODATA $u = 1.2 \times 10^{-8}$ [17]), or, alternatively, an independent measure of the mass of the ion or molecule is needed. If the experiment is then performed at a known temperature, for example, at the TPW, the Boltzmann constant can be determined by measuring frequencies. This proposal was first made by Bordé [40], and an experimental proof of principle was demonstrated by Daussy et al. [41].

A laser spectroscopy setup as used for DBT is schematically shown in Figure 8.3. Key features of the setup are (i) the stabilized, frequency tunable laser system whose frequency is traced back to the SI unit, for example, by employing a femtosecond frequency comb (see Section 9.1.1); (ii) the temperature-stabilized absorption cell containing the molecular gas; and (iii) the detection system. The laser system of choice, of course, depends on the gas and its spectral feature used for the experiment. A rovibrational absorption line of the ammonia molecule $^{14}NH_3$ at the frequency of 28 953 694 MHz and a CO_2 laser stabilized to an absorption line of OsO_4 were used in the initial demonstration of DBT [41]. The absolute laser frequency (linewidth <10 Hz) was measured by comparison with a Cs fountain clock (see Section 3.3). Tunability of the laser source had been achieved by electro-optic sideband modulation.

A component (R12) of the $\nu_1 + 2\nu_2^0 + \nu_3$ combination band of CO_2 (ν_1 and ν_3 are the symmetric and antisymmetric stretching modes, respectively, and ν_2^0 is the bending mode) and an external-cavity diode laser emitting at 2.006 μm (linewidth ~1 MHz) were used by Casa et al. [43, 44]. Further, a rovibrational absorption line in $^{13}C_2H_2$ was investigated by Koichi et al. using a tunable diode laser locked

to a frequency comb [45], and a line at 1.39 µm in the $\nu_1 + \nu_3$ band of $H_2{}^{18}O$ was measured using a pair of offset-frequency-locked external-cavity diode lasers [46].

The DBT experiment naturally requires the best achievable control of the gas temperature. To keep the uncertainty of the temperature measurement as small as possible, the temperature of the TPW or close to it had been used for the determination of k. The French group, for example, used an ice-water-filled thermostat, keeping the temperature at 213.15 K [41, 47, 48]. A gas cell included in a temperature-controlled thermal shield, surrounded by a cooled enclosure under vacuum, was used in the experiments of the Italian group [43, 44], allowing a variation of the gas temperature between 270 and 330 K.

When fitting the measured absorption profile to determine the Doppler broadening, other line broadening (or narrowing) mechanisms must be considered such as the contribution of the Lorentzian-shaped homogeneous linewidth (see Section 3.3), the second-order Doppler effect, the Lamb–Dicke narrowing, the possible overlap with neighboring absorption lines, and collision broadening (for a detailed lineshape analysis, see, e.g. Refs. [49–53]).

The smallest uncertainty of the value of the Boltzmann constant measured by DBT has been of the order of some 10 ppm [46, 47, 50]. Major limiting factors are the line shape model, statistical fluctuations, and the spectral purity of the probe laser. Recent development of a new spectrometer based on quantum cascade lasers [54] leaves room for further improvements for the ammonia experiments. Though not yet listed in the present *Mise en pratique* for the definition of the kelvin [4] as a primary thermometer, DBT will have the potential for dissemination of the kelvin.

8.1.5 Johnson Noise Thermometry

Johnson noise thermometry (JNT) is based on the Nyquist relation [55]

$$\langle U^2 \rangle = 4kTR\Delta f \tag{8.15}$$

relating the mean square noise voltage of a resistor, $\langle U^2 \rangle$, to its resistance, R, the Boltzmann constant, and temperature. Δf is the frequency bandwidth. Equation (8.15) is a high-temperature approximation valid for frequencies $f \ll kT/h$. As the noise voltage is generated by the thermal motion of the electrons in the resistor, the statistical nature of this mechanism requires sufficiently long measuring times, t, depending on the uncertainty required. For the determination of a certain temperature, this is quantified by the relation

$$\frac{\Delta T}{T} \approx \frac{2.5}{\sqrt{t\Delta f}} \tag{8.16}$$

According to Eq. (8.16), for example, at a bandwidth of 20 kHz, a measurement time of several weeks is required to obtain an uncertainty of order 10^{-5}. Given the very small noise voltages, this long measurement time is naturally causing considerable problems such as the stability of the electronic devices and extra noise sources (e.g. amplifiers, leads). Thus, the determination of an unknown temperature is usually done by comparing the mean square noise voltage of the resistor

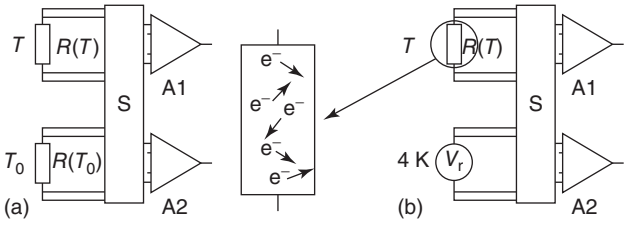

Figure 8.4 Schematic block diagram for the switched-input noise correlator: (a) shows the conventional relative method and (b) the absolute method employing a quantum voltage noise source (V_r) as the reference. Source: Fischer 2010 [8]. Reproduced with permission of John Wiley & Sons.

with that of a resistor at a known reference temperature, T_0, at equal bandwidth. At present, the switched-input digital correlator technique is frequently used for these measurements [56, 57].

In this correlator, the signals stemming from the two channels are digitized, and the required operations (averaging, multiplication) are done by software. Thus, amplifier noise, noise of the leads, and drift are eliminated. For relative temperature measurement (see Figure 8.4a), the unknown temperature, T_S, is then obtained by

$$T_S = \frac{\langle U(T_S)^2 \rangle}{\langle U(T_0)^2 \rangle} \frac{R(T_0)}{R(T_S)} T_0 \tag{8.17}$$

Absolute temperature measurements and the determination of the Boltzmann constant, however, require the reference resistor to be replaced by a voltage standard (see Figure 8.4b). This has been implemented in a cooperation led by the National Institute of Standards and Technology (NIST) by employing pulse-driven AC Josephson standards (see Section 4.1.4.4) as quantized voltage noise sources (QVNSs) [58–61]. The Josephson QVNS is a Σ–Δ digital-to-analog converter producing a sequence of pulses with the quantized pulse area

$$\int U(t)\mathrm{d}t = nK_J^{-1} \tag{8.18}$$

where K_J is the Josephson constant, $K_J = 2e/h$ (see Chapter 4). An M-bit long digital code is then used to synthesize a waveform composed of a series of harmonics of the pulse pattern repetition frequency with equal amplitude but random phase. This results in a pseudo-random noise waveform with calculable power spectral density and thus pseudo-noise voltage spectral density, U_{QVNS}:

$$U_{QVNS} = K_J^{-1} Qm(Mf_S)^{1/2} \tag{8.19}$$

with m being the number of Josephson junctions, M the number of bits that determine the length of the digital waveform, and f_S the clock frequency. Note that M is proportional to the clock frequency f_S (and to the inverse of the spacing between the harmonic tones that make up the noise waveform) [62] so that the voltage generated by the pulse-driven Josephson array is proportional to the clock

frequency, as discussed in Section 4.1.4.4. Q is a dimensionless amplitude factor [62]. Comparing the mean square noise voltage spectral density of the thermal resistor $\langle U^2(T)/\Delta f\rangle$ to the mean square pseudo-noise voltage spectral density using again a switched-input digital correlator (see Figure 8.4b) yields

$$\frac{\langle U^2(T)/\Delta f\rangle}{\langle U^2_{\mathrm{QVNS}}\rangle} = \frac{4kTR}{K_{\mathrm{J}}^{-2}Q^2m^2Mf_{\mathrm{S}}} \tag{8.20}$$

Measuring the resistance in units of the von Klitzing constant, $R = X_{\mathrm{R}}R_{\mathrm{K}}$, the absolute temperature is obtained according to

$$T = \frac{\langle U^2(T)/\Delta f\rangle}{\langle U^2_{\mathrm{QVNS}}\rangle}\frac{hQ^2m^2Mf_{\mathrm{S}}}{16kX_{\mathrm{R}}} \tag{8.21}$$

Performing the measurement at the TPW allows the determination of the Boltzmann constant, as demonstrated by Benz et al. [62], who reported the relative uncertainty to be 12 parts in 10^6. With an improved setup at NIST, a new determination of the Boltzmann constant achieved a combined standard uncertainty of 5.0×10^{-6} [63]. Further, in a cooperation between the NIST and NIM, a JNT system has been established at the NIM [64] with a first determination of the Boltzmann constant with a combined relative uncertainty of 3.9×10^{-6} in 2015 [65]. New measurements with a further improved system at the NIM resulted in an improved relative uncertainty of 3×10^{-6} [66], thus fulfilling the requirement of the CCT [3]. As analyzed in [67], one main uncertainty component is caused by the frequency–response mismatch between the two sets of leads connecting the sources with the amplifiers. A JNT quantum standard has also been developed at the Japanese NMIJ/AIST (National Metrology Institute of Japan/National Institute of Advanced Industrial Science and Technology) with first results reported in 2017 [68]. Altogether, JNT absolute quantum standards have improved considerably and contributed to the determination of the final value of the Boltzmann constant (see Section 8.2.1) and are very attractive to realize and disseminate the low-temperature scale [69].

8.1.6 Coulomb Blockade Thermometry

Although Coulomb blockade thermometry [70, 71] is not yet referred to as a primary thermometer in the *Mise en Pratique* for the definition of the kelvin [4], we briefly describe it here in the context of quantum standards. CBT is a low-temperature technique ($T < 4\,\mathrm{K}$) based on the current–voltage characteristic of metallic single-electron transport (SET) transistors fabricated, for example, based on ($\mathrm{Al/AlO}_x$) tunnel junctions (see Section 6.1). Because of the Coulomb blockade, the differential conductance, $\mathrm{d}I_{\mathrm{SD}}/\mathrm{d}U_{\mathrm{SD}}$, exhibits a dip around zero source–drain voltage (see Figure 8.5). The characteristic parameter for the occurrence of this dip is the ratio of the Coulomb energy

$$E_{\mathrm{c}} = \frac{e^2}{C_\Sigma} \tag{8.22}$$

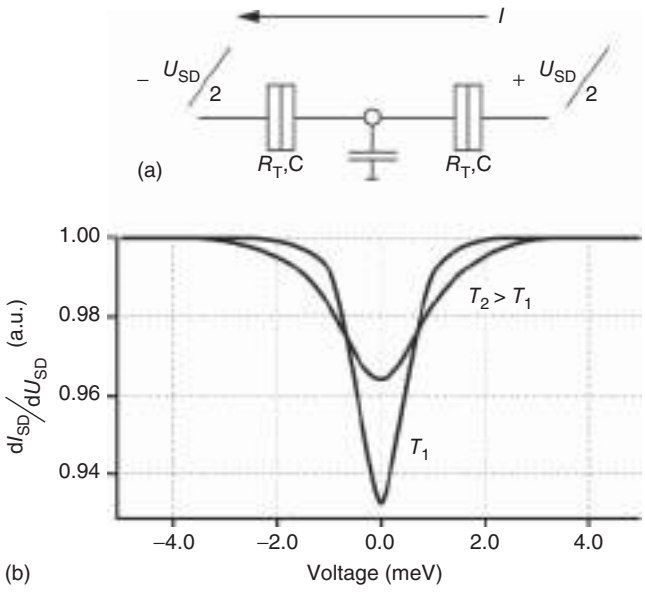

Figure 8.5 Schematic illustration of the differential conductance (b) of an SET transistor (a) in the weak Coulomb blockade regime. Source: Göbel and Siegner 2015 [42]. Reproduced with permission of John Wiley & Sons.

where C_Σ is the total capacitance of the SET transistor, to the thermal energy kT. The Coulomb blockade is very pronounced for $E_C \gg kT$, resulting in a wide and deep dip in the differential conductance. With increasing temperature, this dip broadens and its depth decreases. In the temperature regime where E_C is comparable to or even smaller than kT (respectively, intermediate and weak Coulomb blockade regimes), the half width of the conductance dip depends solely on the temperature. For an SET array with N tunnel junctions, the half width (in the first order) in the weak Coulomb blockade regime is given by [70]

$$\Delta V_{1/2} \cong 5.44N\frac{kT}{e} \tag{8.23}$$

For a one SET transistor with one metallic island and two tunnel junctions (one on either side of the island), the half width is then equal to 10.88 kT/e. One of the limiting factors for the accuracy is the inevitable spread of the junction parameters [72]. To reduce this, many sophisticated junction arrays have been realized [73–75]. The uncertainties that have been achieved so far are of the order 10^{-4} [71, 73, 74] and operation at temperatures down to 10 mK has been demonstrated [76]. CBTs based on Si Schottky barriers have also been fabricated and tested [77].

Finally, we mention another low-temperature electronic thermometer using tunnel elements and measuring the voltage generated in these elements in the shot noise regime (shot noise thermometer, SNT) [78, 79].

8.2 The CODATA Evaluation of the Value of the Defining Boltzmann Constant, Realization and Dissemination of the New Kelvin

8.2.1 The CODATA Evaluation of the Final Value of the Defining Boltzmann Constant

As requested by the CGPM at its 24th meeting [80], the CODATA through its Task Group on Fundamental Constants carried out a special least square adjustment of the values of the physical constants during the summer 2017. The data and analysis are described in detail in Ref. [81]. The results of this special adjustment for the defining constants *h, e, k,* and N_A are reported by the Task Group in Ref. [82] and are depicted in Figure 8.6 for the Boltzmann constant.

The major contributions come from AGT. JNT (NIM/NIST-17) and DCGT (PTB-17) each had one data input. The CODATA value 2017 for *k* was determined to be [82]

$$k = 1.380\,649\,03(51) \times 10^{-23}\ \mathrm{J\,K^{-1}}$$

The relative standard uncertainty amounts to 3.7×10^{-7}. From this result, the value of the defining Boltzmann constant was deduced [82]:

$$k = 1.380\,649 \times 10^{-23}\ \mathrm{J\,K^{-1}}$$

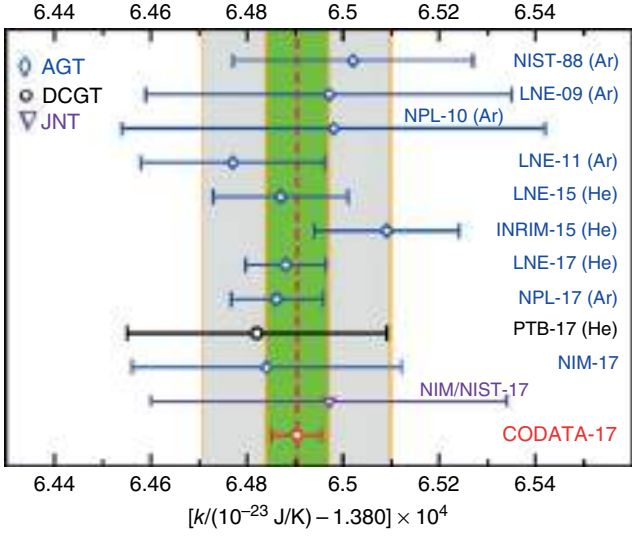

Figure 8.6 Values of the Boltzmann constant contributing to the final value of the defining constant, *k*, in chronological order together with the CODATA 2017 value [82]. The labeling refers to the following references: NIST-88(Ar): [21], LNE-09(Ar): [26], NPL-10(Ar): [83], LNE-11(Ar): [15], LNE-15(He): [31], INRIM-15(He): [29], LNE-17(He): [32], NPL-17(Ar): [19], PTB-17(He): [15], NIM-17: [34], NIM/NIST-17: [66]. The inner green band is ±5 parts in 10^7 and the outer gray band is ±15 parts in 10^7. Source: © Bureau International des Poids et Mesures. Reproduced by permission of IOP Publishing. All rights reserved.

The number of digits has been chosen such that the triple point of water temperature, T_{TPW}, remains 273.16 K, yet, now with an uncertainty of about 0.4 mK [1].

8.2.2 Realization and Dissemination of the Kelvin

Realization and dissemination of the kelvin can be accomplished by absolute primary thermometers. Presently, the following are listed in the *Mise en Pratique for the Definition of the Kelvin* [4]: AGT, radiometric thermometry, polarizing gas thermometry (dielectric-constant gas thermometry (DCGT), refractive index gas thermometry (RIGT)), and JNT. For practical realization of the kelvin, the CIPM has adopted a series of International Temperature Scales, the latest being the International Temperature Scale of 1990 (ITS-90) and the Provisional Low Temperature Scale PLTS-2000. These scales are set up by defining exact fix-point temperatures for the respective scale temperature. The ITS-90 is valid for temperatures from 0.65 K upward and the PLTS-2000 from 0.9 mK to 1 K. Both scales will remain in use in the foreseeable future for practical reasons. The present definition of the kelvin in terms of the Boltzmann constant does not affect the temperature values or realization uncertainties of the International Temperature Scales. Guides for the realization of the ITS-90 and estimates of the difference between thermodynamic temperature and the ITS-90 as well as for the realization of the PLTS-2000 can be found on the International Bureau for Weights and Measures (*Bureau International des Poids et Mesures)* (BIPM) website [84].

References

1 BIPM (2014). SI Brochure: The International System of Units (SI) [8th edition, 2006; updated in 2014]. http://www.bipm.org/en/publications/si-brochure/kelvin.html (accessed November 2018).
2 BIPM (2018). BIPM resolution 1, 26th CGPM 2018. https://www.bipm.org/utils/common/pdf/CGPM-2018/26th-CGPM-Resolutions.pdf (accessed November 2018).
3 BIPM (2014). Consultative Committee for Thermometry. http://www.bipm.org/utils/common/pdf/CC/CCT/CCT27.pdf (accessed November 2018).
4 BIPM (2019). Draft *Mise en pratique* for the definition of the kelvin in the SI. https://www.bipm.org/utils/en/pdf/si-mep/MeP-K-2018.pdf (accessed November 2018).
5 Fischer, J., Fellmuth, B., Gaiser, C. et al. (2018). Review: the Boltzmann project. *Metrologia* 55: R1–R20.
6 Metrologia (2015). Focus on the Boltzmann Constant. http://iopscience.iop.org/journal/0026-1394/page/Focus_on_the_Boltzmann_Constant (accessed 27 February 2019).
7 Fellmuth, B., Gaiser, C., and Fischer, J. (2006). Determination of the Boltzmann constant—status and prospects. *Meas. Sci. Technol.* 17: R145–R159.
8 Fischer, J. (2010). *Handbook of Metrology*, vol. 1 (ed. M. Gläser and M. Kochsiek), 349–381. Weinheim: Wiley-VCH.

9 Fischer, J. and Fellmuth, B. (2005). Temperature metrology. *Rep. Prog. Phys.* 68: 1043–1094.

10 Piszczatowski, K., Puchalski, M., Komasa, J. et al. (2015). Frequency-dependent polarizability of helium including relativistic effects with nuclear recoil terms. *Phys. Rev. Lett.* 114: 173004-1-5.

11 Gaiser, C. and Fellmuth, B. (2018). Polarizability of helium, neon, and argon: new perspectives for gas metrology. *Phys. Rev. Lett.* 120: 123203-1-5.

12 Zandt, T., Gaiser, C., Fellmuth, B. et al. (2013). *Temperature: Its Measurement and Control in Science and Industry, Volume 8, AIP Conference Proceedings, Volume 1552*, 130–135. AIP.

13 Gaiser, C., Zandt, T., and Fellmuth, B. (2015). Dielectric-constant gas thermometry. *Metrologia* 52: S217–S226.

14 Fellmuth, B., Bothe, H., Haft, N., and Melcher, J. (2011). High-precision capacitance bridge for dielectric-constant gas thermometry. *IEEE Trans. Instrum. Meas.* 60: 2522–2526.

15 Gaiser, C., Fellmuth, B., Haft, N. et al. (2017). Final determination of the Boltzmann constant by dielectric-constant gas thermometry. *Metrologia* 54: 280–289.

16 For a recent review see: Moldover, M.R., Gavioso, R.M., Mehl, J.B. et al. (2014). Acoustic gas thermometry. *Metrologia* 51: R1–R19.

17 Mohr, P.J., Newell, D.B., and Taylor, B.N. (2016). CODATA recommended fundamental physical constants: 2014. *Rev. Mod. Phys.* 88: 035009-1-73.

18 de Podesta, M., Underwood, R., Sutton, G. et al. (2013). A low-uncertainty measurement of the Boltzmann constant. *Metrologia* 50: 354–376.

19 The result reported in reference 18 has been corrected in: de Podesta, M., Mark, D.F., Dymock, R.C. et al. (2017). Re-estimation of argon isotope ratios leading to a revised estimate of the Boltzmann-constant. *Metrologia* 54: 683–692.

20 Moldover, M.R., Trusler, J.P.M., Edwards, T.J. et al. (1988). Measurement of the universal gas constant *R* using a spherical acoustic resonator. *J. Res. Natl. Bur. Stand.* 93: 85–144.

21 Moldover, M.R., Trusler, J.P.M., Edwards, T.J. et al. (1988). Measurement of the universal gas constant *R* using a spherical acoustic resonator. *Phys. Rev. Lett.* 60: 249–252.

22 Zhang, J.T., Lin, H., Feng, X.J. et al. (2011). Progress towards redetermination of the Boltzmann constant with a fixed-path-length cylindrical resonator. *Int. J. Thermophys.* 32: 1297–1329.

23 Mehl, J.B. and Moldower, M.R. (1986). Measurement of the ratio of the speed of sound to the speed of light. *Phys. Rev. A* 34: 3341–3344.

24 Mehl, J.B., Moldover, M.R., and Pitre, L. (2004). Designing quasi-spherical resonators for acoustic thermometry. *Metrologia* 41: 295–304.

25 Colclough, A.R., Quinn, T.J., and Chandler, T.R.D. (1979). An acoustic determination of the gas constant. *Proc. R. Soc. London, Ser. A* 368: 125–139.

26 Pitre, L., Guianvarc'h, C., Sparasci, F. et al. (2009). An improved acoustic method for the determination of the Boltzmann constant at LNE-INM/CNAM. *C.R. Phys.* 10: 835–848.

27 Pitre, L., Sparasci, F., Truong, D. et al. (2011). Measurement of the Boltzmann constant k using a quasispherical acoustic resonator. *Int. J. Thermophys.* 32: 1825–1886.

28 Gavioso, R.M., Benedetto, G., Madonna Ripa, D. et al. (2011). Progress in INRIM experiment for the determination of the Boltzmann constant with a quasispherical resonator. *Int. J. Thermophys.* 32: 1339–1354.

29 Gavioso, R.M., Madonna Ripa, D., Steur, P.P.M. et al. (2015). A determination of the molar gas constant R by acoustic thermometry in helium. *Metrologia* 52: S274–S304.

30 Segovia, J.J., Vega-Maza, D., Martín, M.C. et al. (2010). An apparatus based on a spherical resonator for measuring the speed of sound in gases and for determining the Boltzmann constant. *Int. J. Thermophys.* 31: 1294–1309.

31 Pitre, L., Risegari, L., Sparasci, F. et al. (2015). Determination of the Boltzmann constant *k* from the speed of sound in helium gas at the triple point of water. *Metrologia* 52: S263–S237.

32 Pitre, L., Sparasci, F., Risegari, L. et al. (2017). New measurement of the Boltzmann constant *k* by acoustic thermometry of helium-4 gas. *Metrologia* 54: 856–873.

33 Zhang, J., Lin, H., Feng, X.J. et al. (2013). Improved determination of the Boltzmann constant using a single, fixed-length cylindrical cavity. *Metrologia* 50: 417–432.

34 Feng, X.J., Zhang, J.T., Lin, H. et al. (2017). Determination of the Boltzmann constant with cylindrical acoustic gas thermometry: new and previous results combined. *Metrologia* 54: 748–762.

35 see e.g. Ulm, G. (2003). Radiometry with synchrotron radiation. *Metrologia* 40: S101–S106.

36 Planck, M. (1900). Zur Theorie der Energieverteilung im Normalspektrum. *Verh. Dtsch. Phys. Ges.* 2: 237–245.

37 Lummer, O. and Kurlbaum, F. (1898). Der elektrisch geglühte absolut schwarze Körper und seine Temperaturmessung. *Verh. Dtsch. Phys. Ges.* 17: 106–111.

38 Quinn, T.J. and Martin, J.E. (1985). A radiometric determination of the Stefan–Boltzmann constant. *Proc. R. Soc. London, Ser. A* 316: 85–189.

39 Martin, J.E., Fox, N.P., and Key, P.J. (1985). A cryogenic radiometer for absolute radiometric measurements. *Metrologia* 21: 147–155.

40 (a)Bordé, C.J. (2002). Atomic clocks and inertial sensors. *Metrologia* 39: 435–463. (b) Bordé, C. (2005). Base units of the SI, fundamental constants and modern quantum physics. *Philos. Trans. R. Soc. London, Ser. A* 363: 2177–2201.

41 Daussy, C., Guinet, M., Amy-Klein, A. et al. (2007). Direct determination of the Boltzmann constant by an optical method. *Phys. Rev. Lett.* 98: 250801-1–250801-4.

42 Göbel, E.O. and Siegner, U. (2015). *Quantum Metrology: Foundation of Units and Measurements*. Weinheim: Wiley-VCH.

43 Casa, C., Castrillo, G., Galzerano, G. et al. (2008). Primary gas thermometry by means of laser-absorption spectroscopy: determination of the Boltzmann constant. *Phys. Rev. Lett.* 100: 200801-1–200801-4.

44 Castrillo, A., Casa, G., Merlone, A. et al. (2009). On the determination of the Boltzmann constant by means of precision molecular spectroscopy in the near–infrared. *C.R. Phys.* 10: 894–906.

45 Koichi, M.T., Yamada, K.M.T., Onae, A. et al. (2009). Precise determination of the Doppler width of a rovibrational absorption line using a comb-locked diode laser. *C.R. Phys.* 10: 907–915.

46 Moretti, L., Castrillo, A., Fasci, E. et al. (2013). Determination of the Boltzmann constant by means of precision measurements of $H_2{}^{18}O$ line shapes at 1.39 μm. *Phys. Rev. Lett.* 111: 060803-1–060803-5.

47 Lemarchand, C., Djerroud, K., Darquié, B. et al. (2010). Determination of the Boltzmann constant by laser spectroscopy as a basis for future measurements of the thermodynamic temperature. *Int. J. Thermophys.* 31: 1347–1359.

48 Djerroud, K., Lemarchand, C., Gauguet, A. et al. (2009). Measurement of the Boltzmann constant by the Doppler broadening technique at a 3.8×10^{-5} level. *C.R. Phys.* 10: 883–893.

49 Bordé, C.J. (2009). On the theory of linear absorption line shapes in gases. *C.R. Phys.* 10: 866–882.

50 Lemarchand, C., Triki, M., Darquié, B. et al. (2011). Progress towards an accurate determination of the Boltzmann constant by Doppler spectroscopy. *New J. Phys.* 13: 1–22.

51 Rohart, F., Mejri, S., Sow, L., and Daussy, C. (2014). Absorption-line-shape recovery beyond the detection-bandwidth limit: application to the precision spectroscopy measurement of the Boltzmann constant. *Phys. Rev. A* 90: 042506-1-12.

52 Mejri, S., Sow, P.L.T., Kozlova, O. et al. (2015). Measuring the Boltzmann constant by mid-infrared laser spectroscopy of ammonia. *Metrologia* 52: S314–S323.

53 De Vizia, M.D., Odintsova, T., and Gianfranti, L. (2016). Hyperfine structure effects in Doppler-broadening thermometry on water vapor at 1.4 μm. *Metrologia* 53: 800–804.

54 Sow, P.L.T., Mejri, S., Tokunaga, S.K. et al. (2014). A widely tunable 10 μm quantum cascade laser phase-locked to a state-of-the-art mid-infrared reference for precision molecular spectroscopy. *Appl. Phys. Lett.* 104: 264101-1-4.

55 Nyquist, H. (1928). Thermal agitation of electronic charge in conductors. *Phys. Rev.* 32: 110–113.

56 Brixi, H., Hecker, R., Oehmen, J. et al. (1992). *Temperature and its Measurement and Control in Science and Industry*, vol. 6 (ed. J.F. Schooley), 993–996. New York: American Institute of Physics.

57 White, D.R., Galleano, R., Actis, A. et al. (1996). The status of Johnson noise thermometry. *Metrologia* 33: 325–335.

58 Benz, S.P., Martinis, J.M., Nam, S.W. et al. (2002). *Proceedings TEMPMEKO 2001 International Symposium on Temperature and Thermal Measurements in Industry and Science*, vol. 8 (ed. B. Fellmuth, J. Seidel and G. Scholz), 37–44. Berlin: VDE.

59 Tew, W.L., Benz, S.P., Dresselhaus, P.D. et al. (2010). Progress in noise thermometry at 505 K and 693 K using quantized voltage noise ratio spectra. *Int. J. Thermophys.* 31: 1719–1738.

60 Benz, S., White, D.R., Qu, J.F. et al. (2009). Electronic measurement of the Boltzmann constant with a quantum-voltage-calibrated Johnson noise thermometer. *C.R. Phys.* 10: 849–858.

61 White, D.R., Benz, S.P., Labenski, J.R. et al. (2008). Measurement time and statistics for a noise thermometer with a synthetic-noise reference. *Metrologia* 45: 395–405.

62 Benz, S.P., Pollarolo, A., Qu, J. et al. (2011). An electronic measurement of the Boltzmann constant. *Metrologia* 48: 142–153.

63 Flowers-Jacobs, N.E., Pollarolo, A., Coakley, K.J. et al. (2017). A Boltzmann constant determination based on Johnson noise thermometry. *Metrologia* 54: 730–737.

64 Qu, J.F., Zhang, J.T., Fu, Y. et al. (2013). Development of a quantum-voltage-calibrated noise thermometer at NIM. In: *Temperature: Its Measurement and Control in Science and Industry*, vol. 8 (ed. C.W. Meyer), 29–33. New York: American Institute of Physics.

65 Qu, J.F., Benz, S.P., Pollarolo, A. et al. (2015). Improved electronic measurement of the Boltzmann constant by Johnson noise thermometry. *Metrologia* 52: S242–S256.

66 Qu, J.F., Benz, S.P., Coakley, K.J. et al. (2017). An improved electronic determination of the Boltzmann constant by Johnson noise thermometry. *Metrologia* 54: 549–558.

67 White, D.R. and Qu, J.F. (2018). Frequency-response mismatch effects in Johnson noise thermometry. *Metrologia* 55: 38–45.

68 Urano, C., Yamazawa, K., and Kaneko, N.-H. (2017). Measurement of the Boltzmann constant by Johnson noise thermometry using superconducting integrated circuit. *Metrologia* 54: 847–855.

69 see also Engert, J., Beyer, J., Drung, D. et al. (2009). Practical noise thermometers for low temperatures. *J. Phys. Conf. Ser.* 150: 012012.

70 Pekola, J.P., Hirvi, K.P., Kauppinen, J., and Paalanen, M.A. (1994). Thermometry by arrays of tunnel junctions. *Phys. Rev. Lett.* 73: 2903–2906.

71 Hahtela, O., Mykkänen, E., Kemppinen, A. et al. (2017). Traceable Coulomb blockade thermometry. *Metrologia* 54: 69–76.

72 Hirvi, K.P., Kauppinen, J.P., Korotkov, A.N. et al. (1995). Arrays of normal metal tunnel junctions in weak Coulomb blockade regime. *Appl. Phys. Lett.* 67: 2096–2098.

73 Begsten, T., Claeson, T., and Delsing, P. (1999). Coulomb blockade thermometry using a two-dimensional array of tunnel junctions. *J. Appl. Phys.* 86: 3844–3847.

74 Pekola, J.P., Holmqvist, T., and Meschke, M. (2008). Primary tunnel junction thermometry. *Phys. Rev. Lett.* 101: 206801-1–206801-4.

75 Feschchenko, A.V., Meschke, M., Gunnarson, D. et al. (2013). Primary thermometry in the intermediate Coulomb blockade regime. *J. Low Temp. Phys.* 173: 36–44.

76 Casparis, L., Meschke, M., Maradan, D. et al. (2012). Metallic Coulomb blockade thermometry down to 10 mK and below. *Rev. Sci. Instrum.* 83: 083903-1-3.

77 Tuboltsev, V., Savin, A., Rogozin, V.D., and Räisänen, J. (2014). Silicon based Coulomb blockade thermometer with Schottky barriers. *Appl. Phys. Lett.* 104: 163507-1-4.
78 Spitz, L., Lehnert, K.W., Siddigi, I., and Schoelkopf, R.J. (2003). Primary electronic thermometry using the shot noise of a tunnel junction. *Science* 300: 1929–1932.
79 Spitz, L., Schoelkopf, R.J., and Pari, P. (2006). Shot noise thermometry down to 10 mK. *Appl. Phys. Lett.* 89: 183123-1-3.
80 CGPM (2011). Resolution 1 of the 24th CGPM. www.bipm.org/en/CGPM/db/24/1/ (accessed 15 June 2018).
81 Mohr, P.J., Newell, D.B., Taylor, B.N., and Tiesinga, E. (2018). Data and analysis for the CODATA 2017 special fundamental constants adjustment. *Metrologia* 55: 125–146.
82 Newell, D.B., Cabiati, F., Fischer, J. et al. (2018). The CODATA 2017 values for *h, e, k,* and N_A for the revision of the SI. *Metrologia* 55: L13–L16.
83 Sutton, G., Underwood, R., Pitre, L. et al. (2010). Acoustic resonator experiments at the triple point of water: first results for the Boltzmann constant and remaining challenges. *Int. J. Thermophys.* 31: 1310–1346.
84 BIPM (1989). The international temperature scale of 1990 (ITS-90). www.bipm.org/en/committees/cc/cct/publications-cc.html (accessed February 2019).

9

Beyond the Present SI: Optical Clocks and Quantum Radiometry

In this section, we present some recent progress in metrology research, which in due time may result in a change of the defining constant of the base unit second and an alternative realization of the radiometric quantities and hence a change of the defining constant for the photometric base unit of luminous intensity, the candela. Regarding the second, optical clocks meanwhile have reached stability and accuracy superior to the microwave Cs clock. Therefore, a new definition of the second in terms of an optical transition frequency is feasible. We sketch some recent developments on optical clocks in Section 9.1 including femtosecond frequency combs for optical frequency measurements. Further, we briefly summarize results on optical clock applications to study possible variations of the fine-structure constant, α, in Section 9.1.5. Another exciting development in metrology research is the now availability of single-photon sources paving the way to base radiometric quantities, such as spectral radiative power, luminous flux, and luminous intensity, the candela, on counting of single photons with given energy (frequency). Single-photon emitters as the key elements of future quantum radiometry are discussed in Section 9.2.

9.1 Optical Clocks and a New Second

Since the short-term stability of a frequency standard scales with the quality factor, Q, of the respective transition (see Eq. (3.8)), it would be favorable to move the "clock transition" to higher frequencies than presently used in the Cs clocks. Moving to the visible range of the electromagnetic spectrum at several hundred THz would, in principle, result in an improvement of as much as 10^5 compared to the 9.2 GHz frequency of the microwave clock transition in Cs provided the linewidth remains the same. This, in fact, has driven the development of optical frequency standards. The remarkable and still ongoing progress in recent years now justifies calling some of these standards "optical clocks," i.e. they exhibit sufficiently long operation times to establish or a least contribute to a timescale [1–4]. However, these exciting developments can again only be touched here. For further reading see, for example, [5–8]. It has been particularly the development of advanced laser cooling and trapping techniques for both neutral atoms and ions, which promoted the development of optical clocks. One of the essential

The New International System of Units (SI): Quantum Metrology and Quantum Standards,
First Edition. Ernst O. Göbel and Uwe Siegner.
© 2019 Wiley-VCH Verlag GmbH & Co. KGaA. Published 2019 by Wiley-VCH Verlag GmbH & Co. KGaA.

requirements for suitable atoms or ions is the presence of a strong dipole-allowed optical transition (e.g. S → P) for laser cooling together with a transition with narrow homogeneous (sometimes also called "natural") linewidth since the more narrower the linewidth the more precise a determination of the line center frequency is possible. The half width of the homogeneous, i.e. Lorentzian shaped, optical transition, $\Delta\nu$, is determined by the phase relaxation time, T, of the coherent polarization created by the driving laser field

$$\Delta\nu = \frac{1}{2\pi T} \tag{9.1}$$

with T given according to

$$\frac{1}{T} = \frac{1}{2T_1} + \frac{1}{T_2} \tag{9.2}$$

where T_1 is the population lifetime and T_2 accounts for all other phase relaxation processes such as collisions. For pure recombination damping, we have $T = 2T_1$.

Consequently, narrow linewidth requires long excited-state lifetime as it is the case, for example, for dipole-forbidden optical transitions (e.g. S → D [quadrupole transition], S → F [octupole transition]), or appropriate intercombination transitions. Intercombination transitions involve a change of the spin state ($\Delta S \neq 0$; e.g. singlet → triplet). They are forbidden since the electric field cannot induce a spin flip. This is strictly true for light atoms, but for heavier atoms, the transitions become weakly allowed due to spin–orbit coupling.

For the choice of the atom or ion species, several, sometimes contradicting, issues must be considered, such as energy of the respective transitions and accessibility by available stable laser systems, robustness against external perturbations like magnetic and electric fields, and so on.

The principle of operation (Figure 9.1) of an optical clock is very similar to that of a microwave clock (see Chapter 3). A sufficiently stable local oscillator realized by a narrowband laser source (see, e.g. [10, 11]) is needed to perform

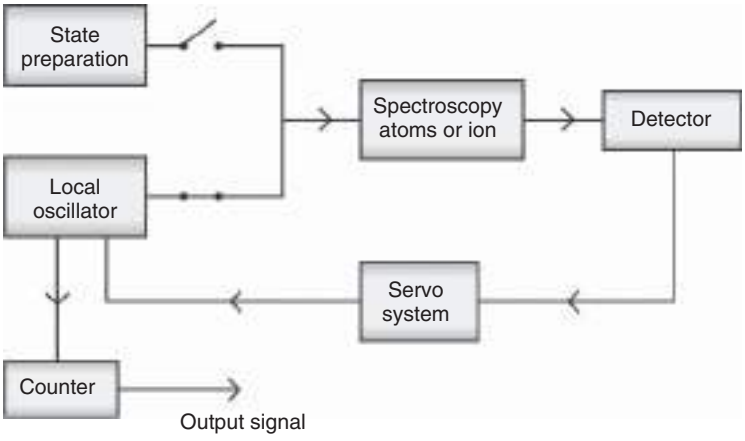

Figure 9.1 Principle of operation of an optical clock. Source: Göbel and Siegner 2015 [9]. Reproduced with permission of John Wiley & Sons.

spectroscopy of the atoms or ions that have been prepared, for example, by laser cooling and trapping. During the spectroscopy phase, the state preparation system is generally switched off to avoid perturbations. Fluorescence is used for detection in most cases providing the internal state information and thus the feedback signal for the local oscillator. In most cases, fluorescence is excited and detected on an auxiliary transition that is connected selectively to the ground or excited state of the clock reference transition. By providing many photons per atom and interrogation cycle, this method provides a large gain in detection sensitivity. Femtosecond frequency combs are finally used as frequency dividers providing the microwave output signal.

For the spectroscopy, high-resolution techniques such as free-space saturated absorption [12–14] and free-space Bordé–Ramsey atom interferometry are used. For trapped atoms within the Lamb–Dicke regime (see Section 9.1.2), pulsed laser excitation with a single pulse (Rabi) or multiple pulses (Ramsey) is used.

In Rabi excitation, in each interrogation cycle a single π-pulse is used to resonantly drive the respective clock transition. In Ramsey excitation, two subsequent $\pi/2$-pulses separated by a dark interval are used (c.f. Section 3.1). While Ramsey excitation provides narrower Fourier-limited linewidth than Rabi excitation, it usually requires higher laser intensity.

For saturated absorption spectroscopy, two counterpropagating laser beams with the same frequency are directed into the atom cloud. Due to the Doppler effect, atoms with different velocities with respect to the beam directions are probed if the laser is tuned slightly off resonance. If, for example, the laser is detuned toward lower frequencies with respect to the resonance frequency, absorption can occur only if atoms with suitable velocity move opposite to the direction of the laser beam; thus, while one of the laser beams will be absorbed by the atoms with a velocity component $+v$ in the direction of the laser beams, the other beam will be absorbed by the atoms with $-v$. Only when the laser frequency is exactly at resonance, the same subgroup of atoms with zero velocity component in the beam directions will be addressed. Since both beams must share the atoms for absorption, total absorption will be reduced and a dip in the absorption profile occurs. Under ideal conditions, the spectral width of this so-called Lamb dip can approach the natural linewidth of the transition.

The Bordé–Ramsey atom interferometry [15, 16] is the extension of the Ramsey separated field technique (see Section 3.1) to the optical regime. The basics of this technique can be explained as follows: consider a two-level atom. Absorption of a resonant photon transfers not only the atom from the ground state $|g\rangle$ to the excited state $|e\rangle$ but also the recoil momentum $\mathbf{K}$ with $|\mathbf{K}| = {}^{2\pi}/_{\lambda}$ to the atom. Consequently, the trajectory of the excited-state atoms is slightly changed with respect to those remaining in the ground state. In the matter wave picture, where the atoms with mass M and velocity v are represented by their de Broglie wavelength $\lambda_{\mathrm{dB}} = h/(M\mathrm{v})$, this process can be viewed as a beam splitter. For a properly (pulse duration and amplitude) chosen excitation pulse ($\pi/2$ pulse), amplitudes of the two partial matter waves are equal. By setting up four interaction zones with temporal delay between these zones, the atom beam can be split and recombined by the lasers if the interaction is still coherent and a time-domain Mach–Zehnder interferometer can be set up as illustrated in Figure 9.2. This interferometer

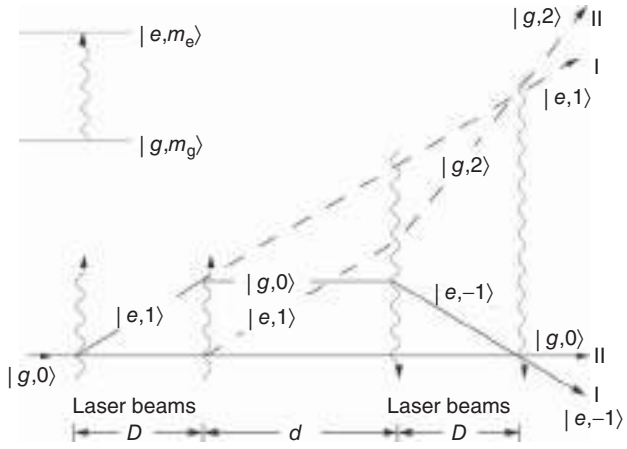

Figure 9.2 Scheme of a Bordé–Ramsey atom interferometer. The laser beams are shown as oscillatory lines with the arrow indicating the direction. The labeling $|i, m\rangle$ refers to the state of the atom where $i = g$ and e refers to the ground and excited states, respectively, and $m = 0$, 1, and -1 stands for the number of photon momenta transferred to the atom. The transition from $|e, 1\rangle$ to $|g, 0\rangle$ at the second interaction zone reflects stimulated emission. Two equivalent interferometers are set up by the interaction as shown in the figure. The two output ports of each interferometer labeled I and II correspond to atoms leaving the interferometer in the excited and ground states, respectively. Source: Göbel and Siegner 2015 [9]. Reproduced with permission of John Wiley & Sons.

has two output ports where the atoms leave, respectively, in the ground and excited states. The probability of finding the atom in either port depends on the phase difference of the partial waves, and thus, the output signal detected, for example, by fluorescence will exhibit interference fringes as a function of detuning with the fringe width, $\Delta\nu$, inversely proportional to the flight time, T_f ($\Delta\nu = 1/(4T_f)$). Also, the phase shift can be affected externally, for example, by gravitation or by rotation of the interferometer (Sagnac effect), which makes atom interferometers a very sensitive measurement instrument [17].

Finally, to complete an optical clock, a technique for counting the high-frequency optical cycles had to be developed. Today, this is accomplished by femtosecond frequency combs, which are briefly described in the following section.

9.1.1 Femtosecond Frequency Combs

For an absolute measurement of an optical frequency, for example, at 500 THz, this frequency must be traced back to the frequency of the defining constant of the second of the present SI, $\Delta\nu_{Cs}$, at 9.2 GHz. Thus, approximately 5 orders of magnitude must be bridged [18].

For this purpose, coherent frequency dividing or multiplying techniques had been used originally. Technically very demanding frequency chains had been developed at several national metrology institutes. In the case of the frequency chain of the Physikalisch–Technische Bundesanstalt (PTB), the National

Metrology Institute of Germany, a delicate setup filling three laser laboratories consisting of seven intermediate oscillators and seven nonlinear mixing steps had been established. This setup provided a direct link between a Ca optical frequency standard at 455.9 THz, that is, a dye laser stabilized to the $^3P_1 \rightarrow {}^1S_0$ intercombination transition in ^{40}Ca, and the Cs frequency [19].

A breakthrough in absolute optical frequency measurements has been the development of optical frequency combs based on mode-locked femtosecond lasers [20–23] for which *T. Hänsch* and *J. Hall* received the Nobel Prize in physics in 2005.

Mode locking refers to the phase-coherent superposition of the longitudinal modes of a laser resonator supported by the respective gain medium. For a textbook description, see, for example, [24]. For active mode locking, intracavity electro-optic or acousto-optic modulators are applied to modulate the loss of the laser cavity periodically with a frequency corresponding to the round-trip time of light in the laser resonator ($T = 2L/v_g$, v_g is the group velocity) or higher harmonics of the inverse of the round-trip time. Alternatively, the gain can be periodically modulated (synchronous pumping). For passive mode locking, a nonlinear device is placed inside the laser resonator, which by itself causes the periodic modulation, for example, a saturable absorber. A saturable absorber exhibits a nonlinear transmission becoming fully transparent at high irradiance. It thereby forces the longitudinal modes of the laser resonator to add up constructively to achieve highest irradiance. The total electric field can be written as

$$E(t) = \sum_q A_q e^{i(\omega_0 + q\Delta\omega)t} + cc \tag{9.3}$$

where q is the mode number and the mode spacing is given by $\Delta\omega = 2\pi/T = 2\pi f_{rep}$ with the repetition rate f_{rep}. The output in the time domain thus corresponds to a pulse train with pulses separated by the round-trip time, T, and a width of $\sim(N\Delta\omega)^{-1}$, where N is the number of longitudinal modes. $(N\Delta\omega)$ corresponds to the effective gain bandwidth. Ideally, the individual pulses would just be time-shifted copies, that is, $E(t) = E(t - T)$. In reality, however, in particular for lasers with a large gain bandwidth generating extremely short pulses in the femtosecond or even subfemtosecond regime, intracavity dispersion must be considered resulting in different group and phase velocities (in lowest order). Consequently, the carrier wave exhibits a constant phase shift, $\Delta\Phi_{gpo}$, for each subsequent pulse, as seen in the upper part of Figure 9.3. In the frequency domain, this results in an offset with respect to zero frequency $\omega_{ceo} = \Delta\Phi_{gpo}/T$ when extrapolating the frequency comb spanned by the longitudinal modes to zero frequency. The frequency of an individual laser mode, m, is then given by

$$\omega_m = \omega_{ceo} + m\Delta\omega \tag{9.4}$$

Any frequency falling in between two adjacent laser modes can be measured by detecting in the radio-frequency regime the beat note between the unknown frequency and the adjacent laser mode, provided the mode spacing, $\Delta\omega$, the mode number, m, and the carrier envelope offset frequency, ω_{ceo}, are known. Since the mode spacing, which corresponds to the repetition rate, typically is of the order

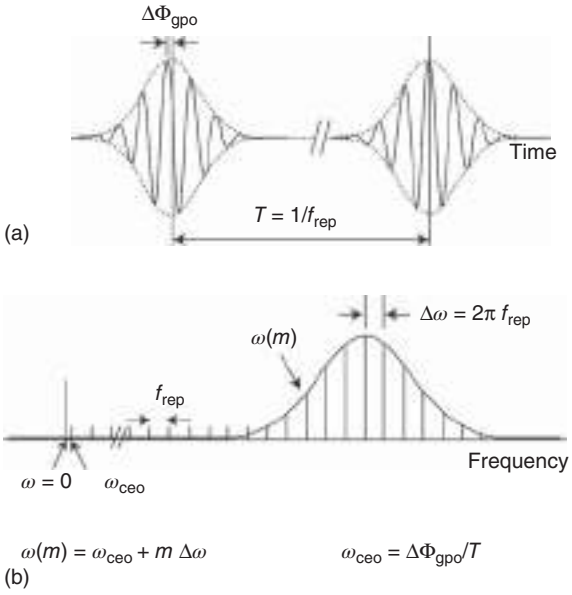

Figure 9.3 Time trace of a mode-locked laser pulse train (a) and the corresponding frequency spectrum (b), as shown schematically. Source: Göbel and Siegner 2015 [9]. Reproduced with permission of John Wiley & Sons.

of 100 MHz, it can easily be measured with a photodiode calibrated by a convenient frequency standard in the microwave regime. The mode number, m, can be obtained by a crude estimate of the unknown frequency with a wavemeter providing a resolution of the order of the mode spacing. The carrier envelope offset frequency can be measured by beating the second harmonic of an individual mode with mode number m, $2\omega_m$, with the mode with mode number $2m$, ω_{2m} (self-referencing). The second harmonic is given by $2\omega_m = 2\omega_{ceo} + 2m\Delta\omega$, while the frequency of mode $2m$ is $\omega_{2m} = \omega_{ceo} + 2m\Delta\omega$. The beat note $2\omega_m - \omega_{2m} = \omega_{ceo}$ thus yields directly the carrier envelope offset frequency. This procedure requires, however, that the frequency comb spans at least one octave. As ω_{ceo} and $\Delta\omega$ are in the radio-frequency regime, they can be locked to a stable microwave oscillator traced back to the Cs clock. Frequency combs can be applied for absolute optical frequency measurement by measuring the beat note between the unknown optical frequency and its adjacent comb line [23, 25, 26], for direct comparison of optical transition lines [27], for precise measurement of frequency ratios [28], and as a clockwork in an optical clock to transfer the optical frequency into the microwave regime. It meanwhile has been established that optical frequency combs generated with femtosecond lasers can generate optical frequencies with a fractional accuracy better than 10^{-18}.

The mode-locked lasers most frequently used for frequency comb generation are titanium–sapphire lasers (Ti:Al_2O_3) and fiber lasers. The active medium in the titanium–sapphire laser is a sapphire (Al_2O_3) crystal heavily doped (about 0.1% in weight) with Ti^{3+} ions replacing Al ions. The titanium–sapphire laser exhibits a large gain bandwidth from about 670 nm to 1.1 µm due to the crystal field splitting of the electronic states involved. The setup of a mode-locked Ti:Al_2O_3 laser is shown in Figure 9.4. Excitation of the Ti:Al_2O_3 crystal is usually by a frequency-doubled Nd:YAG laser with a few watt pump power. Mode

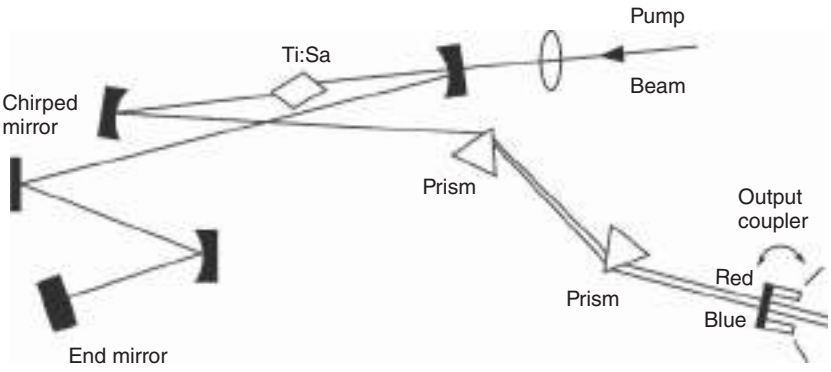

Figure 9.4 Setup of a mode-locked Ti-sapphire laser with a linear resonator. Source: Göbel and Siegner 2015 [9]. Reproduced with permission of John Wiley & Sons.

locking is achieved by the so-called Kerr lens mode locking [29] due to the optical Kerr effect, that is, a nonlinear dependence of the refractive index, n, of the sapphire crystal on optical irradiance, I, $n \cong n_0 + n_2 I$. This Kerr effect causes a spatial variation of the phase in transverse direction, resulting in self-focusing like an optical lens. This effect, of course, is stronger for pulsed light with higher intensity compared to continuous wave (cw) light. A sufficiently small aperture behind the sapphire crystal, which also can be provided by the narrow focus of the pump laser itself, thus acts in the same way as a saturable absorber, resulting in self-starting mode locking. This self-starting can be supported by a semiconductor saturable absorber. The pair of intracavity prisms together with the chirped mirror [30] compensate for group velocity dispersion and self-phase modulation imposed on the spectrum of the pulses.

Pulse trains with a pulse width of the order of some 10 fs and below at a repetition rate of about 100 MHz up to 10 GHz [31] can be readily obtained with mode-locked Ti:Al_2O_3 lasers in a wavelength regime of about 700–900 nm. The mode comb spectral width of Ti–sapphire lasers with a pulse width of some 10 fs, however, does not cover a full octave. The comb width can be broadened externally by applying the so-called holey fibers [32]. These silica fibers consist of a two-dimensional periodic array of bores close to their core providing a very small waveguide with a high refractive index contrast allowing compensation of material dispersion by tailored waveguide dispersion. With these fibers, coherent supercontinuum spectra covering the entire visible spectrum and the near-infrared and frequency combs with more than one octave spectral width can be generated [33].

Mode-locked Er-doped fiber laser systems are very attractive to realize compact optical frequency comb generators [34–36]. Figure 9.5 shows the setup of a mode-locked Er-doped fiber laser oscillator (a) with an amplifier stage (b). The unidirectional Er-fiber oscillator is pumped by diode lasers emitting at 980 nm. Mode locking is achieved by nonlinear polarization rotation. Nonlinear polarization rotation is again due to the optical Kerr effect causing self-phase and cross-phase modulation. As a result, the polarization state in an optical fiber depends on the irradiance. Combined with a linear polarizer, this causes an

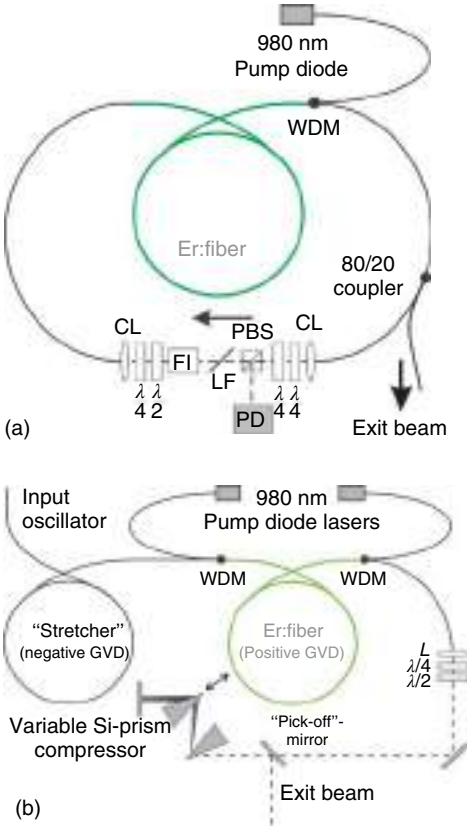

Figure 9.5 Mode-locked Er:fiber laser oscillator (a) and amplifier (b) for optical frequency comb generation (WDM = wavelength division multiplexer, PBS = polarizing beam splitter, PD = photo diode, FI = Faraday isolator, LF = Lyot filter (a special type of spectral filter), CL = collimating lens, GVD = group velocity dispersion). Source: Courtesy of F. Adler and A. Leitenstorfer, University Konstanz.

intensity-dependent loss again like a saturable absorber. By properly adjusting the two polarization controlling stages, self-starting mode locking can be initiated. The center wavelength is at about 1.55 µm, and a few mW average output power can be generated. The oscillator output is then coupled into an amplifier stage pumped by two diode laser chips. The pulses are first stretched by a fiber with negative group velocity dispersion and then amplified whereby the prechirped pulses are shortened during amplification due to the positive group velocity dispersion of the Er-doped fiber. In addition, a Si-prism pulse compressor is used to control the group velocity dispersion of the output. Pulse widths are in the order of 50–100 fs at an average power of about 200 mW. The output pulse train then can be used for supercontinuum generation and second harmonic generation for self-referencing of the comb [34].

Finally, it should be mentioned that alternative nonlinear techniques have also been applied to generate frequency combs such as microresonators [37, 38], which, however, due to their short length consequently exhibit very large mode spacing. Further, extreme ultraviolet radiation frequency combs using high-harmonic generation of femtosecond laser pulses in rare gases have been developed [39–41], extending considerably the spectral range for precision

spectroscopy and ultrafast science. Both techniques may become important for future optical clocks and their applications.

Before discussing some of the most promising optical frequency standards for optical clocks, we review the cooling and trapping techniques applied in Section 9.1.2.

9.1.2 Trapping of Ions and Neutral Atoms for Optical Clocks

9.1.2.1 Ion Traps

Electrically charged particles can be trapped spatially by the combined action of electric and magnetic fields. The so-called Penning trap uses a combination of static electric and magnetic fields [42], while the Paul trap uses an AC electric field (rf trap) [43]. In either case, the particles are trapped in vacuum, possibly by adding some buffer gas.

A Penning trap uses a static spatially homogeneous magnetic field generated by a cylindrical magnet and a static spatially inhomogeneous electric field generated by a quadrupole–ring electrode configuration. The magnetic field confines the particles in the plane perpendicular to the magnetic field direction, and the electric field hinders them to escape along the direction of the magnetic field. Penning traps are very successfully applied to measure properties of ions and particles (such as mass, *g*-factor). For spectroscopy applications, the large Zeeman splitting induced by the magnetic field and the cyclotron and magnetron motions are usually disturbing. In conjunction with laser cooling, Paul traps are advantageous.

The Paul trap, also known as quadrupole ion trap, can be realized in a linear and three-dimensional configuration. The electrode configuration of the three-dimensional Paul trap is the same as that of the Penning trap, as shown in Figure 9.6. It consists of two hyperbolic electrodes (a) and a hyperbolic ring electrode (b). The two hyperbolic electrodes are centered in the ring electrode facing each other. The rf electric field is applied between the ring electrode and the hyperbolic electrodes, generating an oscillating electric quadrupole field. A

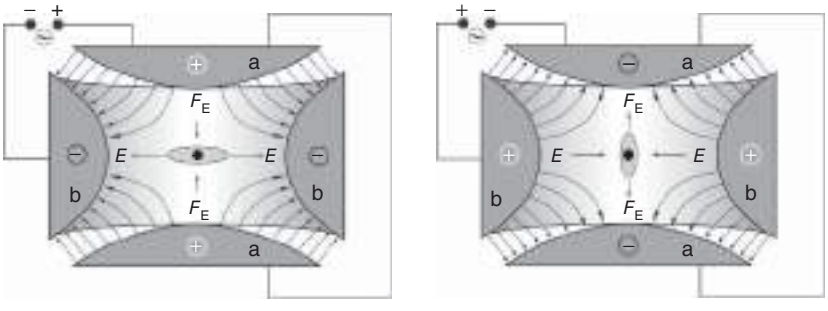

Figure 9.6 Two-dimensional sectional view of the electrode configuration and electric field distribution of a three-dimensional Paul trap. a: upper and lower hyperbolic cap electrode, b: hyperbolic ring electrode. The left and right panels show the two half cycles of the rf field. The arrows labeled E and F_E denote the instantaneous electric field and force, respectively. Source: Göbel and Siegner 2015 [9]. Reproduced with permission of John Wiley & Sons.

charged particle faces oscillating forces under such conditions; in the first half cycle of the field, the ions are focused in the axial direction and defocused in the perpendicular direction, while in the second half cycle, they are defocused in the axial and focused in the perpendicular direction. Since both effects alternate with a high frequency (typically of the order of megahertz), the ions are trapped in the space between these three electrodes. Mathematically, the motion of the charged particles in such a field is described by Mathieu's differential equations. A rigorous treatment can be found in [44]. An intuitive understanding has been presented by *Wolfgang Paul* himself: the motion of the charged particle can be seen analogously to the motion of a mechanical particle, for example, a ball, in a three-dimensional saddle point landscape; putting the ball on top of the saddle point would lead to an unstable situation, resulting in the ball rolling down the hill. However, if the saddle point landscape is rotated with sufficiently high frequency around its symmetry axis piercing through the top of the saddle point, the ball will be stabilized near the top because there is not enough time for it to roll down before the potential has changed due to its rotation.

In a linear Paul trap, the electrodes are formed by metallic rods arranged in a rectangular configuration (see Figure 9.7). Axial confinement then can be achieved by either including additional ring electrodes (Figure 9.7a) or by using segmented rods with three isolated parts (Figure 9.7b) and a DC potential applied to the outer parts.

It must be noted that generally a Doppler broadening of optical transitions of trapped ions in an rf trap occurs due to the oscillatory micromotion, which for the first-order Doppler effect can be avoided when the ion is confined to a regime smaller than the wavelength of the interacting laser field (Lamb–Dicke regime) [45].

If more than one ion is trapped in a linear trap, Coulomb repulsion between them must be considered. If the kinetic energy of the ions is lower than the repulsion energy, crystalline structures are formed, a linear chain in the simplest case (see Figure 9.8). These and more complex (2D, 3D) quasicrystalline structures can be used for quantum information processing [46] and to mimic solid-state phenomena otherwise difficult to study (see, e.g. [47]). As in real crystals, collective motion of the ions can be excited, resulting in a harmonic-oscillator-like discrete

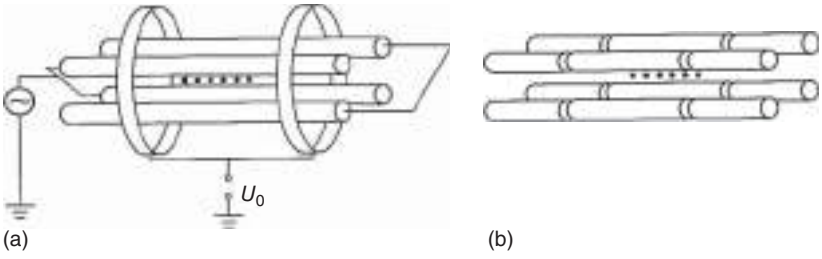

Figure 9.7 Configuration of linear Paul traps with additional ring electrodes (a) or segmented rods (b) for axial confinement. Source: Riehle 2004 [44]. Reproduced with permission of John Wiley & Sons.

Figure 9.8 Yb^+ ions (seen by their fluorescence) in a linear Paul trap. The distance between the ions is about 10–20 μm. Source: Courtesy of T. Mehlstäubler, PTB.

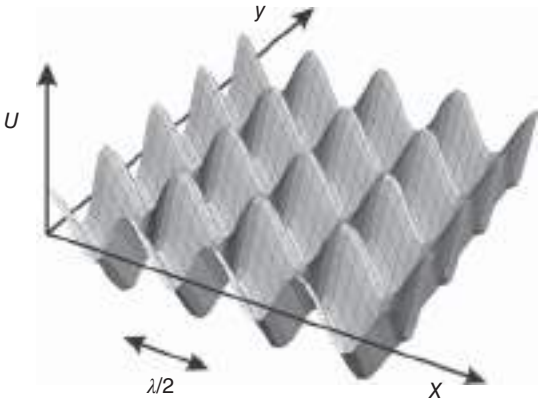

Figure 9.9 Potential landscape of a two-dimensional optical lattice. Source: Göbel and Siegner 2015 [9]. Reproduced with permission of John Wiley & Sons.

vibrational excitation spectrum. This feature can be used for cooling of ions in the trap (sideband cooling) [48, 49] and enables entanglement of ions [46, 50, 51].

9.1.2.2 Optical Lattices

Trapping and manipulation of neutral particles by laser radiation was first demonstrated by A. Ashkin [52] for which he received the Nobel Prize in physics in 2018. Particularly, neutral atoms can be trapped in a standing-wave light field generated by interference between two (or more) laser beams due to the intensity-dependent "light shift" of the energy levels (Stark shift) and the resulting dipole force [53]. The potential landscape of a two-dimensional optical lattice is shown in Figure 9.9. As can be seen, a periodic lattice of potential minima is formed. The period of the minima is $\Delta = \lambda/2$, while their depth, which depends on the laser intensity, is typically of the order of 10 μK.

Optical lattices have also been extensively used to simulate and investigate complex solid-state systems (see, e.g. [54–58]).

9.1.3 Neutral Atomic clocks

Atomic clocks based on clouds of cold neutral atoms can be operated with high signal-to-noise ratio (compared to single ions) due to the large number of atoms (up to 10^8). However, a shift of the respective clock transition may occur due to the interaction of the atoms, collision-related frequency shifts, in addition to all other processes that could cause frequency shifts, such as magnetic and electric fields, blackbody radiation.

Promising neutral atom standards to date are the $1S \rightarrow 2S$ two-photon transition in hydrogen [59]; intercombination transitions ($^1S_0 \rightarrow {}^3P_1$) in alkaline

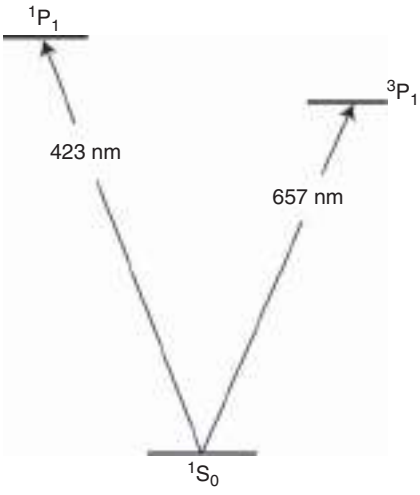

Figure 9.10 Simplified diagram of the relevant energy levels of ^{40}Ca. Source: Göbel and Siegner 2015 [9]. Reproduced with permission of John Wiley & Sons.

earth atoms such as strontium (^{88}Sr), calcium (^{40}Ca), and ytterbium (Yb); and ($^1S_0 \rightarrow {}^3P_0$) transitions between levels with vanishing total electronic angular momentum in Sr, Yb. Hg, Mg, and Cd. These originally dipole-forbidden transitions become weakly allowed due to the HFS-mixing of the $J = 0$ and $J = 1$ states, which in fermionic isotopes (e.g. ^{87}Sr, ^{171}Yb) is mediated through the nuclear spin, while in bosonic isotopes (e.g. ^{88}Sr, ^{174}Yb) through external magnetic fields. We next briefly describe the Sr and Ca frequency standards, for example.

Optical transitions in the neutral ^{40}Ca have been investigated for clock applications mainly at the National Institute of Technology of the United States (NIST) [60–62] and PTB [63, 64].

A simplified diagram of the relevant energy levels of ^{40}Ca indicating the cooling transition at 423 nm and intercombination transition at 657 nm is shown in Figure 9.10. The 657 nm clock transition has a natural linewidth of about 400 Hz. The Ca atoms are cooled in an magneto-optical trap (MOT) (see Section 3.2.1) to temperatures of a few millikelvin well below the Doppler limit of the $^1S_0 \rightarrow {}^1P_1$ transition by involving the forbidden $^1S_0 \rightarrow {}^3P_1$ transition as well [65, 66]. For the spectroscopy phase, the trapping laser and the magnetic field of the MOT are turned off, and the free-falling and expanding atoms are excited by the 657 nm laser radiation in a Bordé–Ramsey interferometer configuration. To obtain the absorption dip profile, the number of atoms in the excited $^3P_1$ state must be measured as a function of frequency. Since the weak $^3P_1 \rightarrow {}^1S_0$ fluorescence is difficult to detect, the so-called electron shelving techniques are frequently applied [60, 63, 67]. In this technique, the strong $^1P_1 \rightarrow {}^1S_0$ fluorescence is used to monitor the $^3P_1$ state population. Since both transitions share the same ground state, atoms excited to the long-lived $^3P_1$ state will reduce the $^1P_1 \rightarrow {}^1S_0$ fluorescence; atoms in the $^3P_1$ state are shelved for some time.

The precise frequency of the 657 nm probe laser stabilized to the central fringe of the interferometer has been measured with a femtosecond comb [61, 64, 68] with a fractional uncertainty well below 10^{-13}.

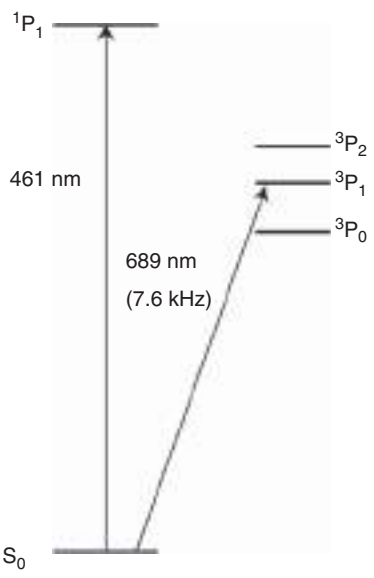

Figure 9.11 Simplified term scheme of neutral ^{88}Sr, indicating the cooling transition at 461 nm and the $^1S_0 \rightarrow {}^3P_1$ intercombination transition at 689 nm with a natural linewidth of 7.6 kHz. Source: Göbel and Siegner 2015 [9]. Reproduced with permission of John Wiley & Sons.

Finally, it should be mentioned that a transportable Ca frequency standard has also been developed at the Wuhan Institute of Physics (China) [69] and PTB [70], and the latter was used for the comparison of standards at the PTB and NIST.

The frequency of the $^1S_0 \rightarrow {}^3P_1$ intercombination transition in ^{88}Sr (Figure 9.11) has been measured by saturated absorption spectroscopy in a thermal beam by Ferrari et al. [71] and in a free-falling ultracold atom beam by Ido et al. [14]. The latter authors achieved a relative uncertainty of the order of 10^{-15} by particularly accounting for the collision-induced frequency shift.

Very promising results have been achieved with the doubly forbidden $^1S_0 \rightarrow {}^3P_0$ transition in ^{87}Sr atoms trapped and stored in optical lattices [72–79]. The simplified term diagram of ^{87}Sr is similar to that shown in Figure 9.11 for ^{88}Sr. The cooling transition is again the $^1S_0 \rightarrow {}^1P_1$ transition at 461 nm. The clock transition ($^1S_0 \rightarrow {}^3P_0$) is at 698 nm. This transition becomes weakly allowed in ^{87}Sr because of hyperfine interaction with the large nuclear spin ($\mathbf{I} = 9/2$). However, the lifetime-limited natural linewidth is still expected to be extremely narrow (~1 mHz). Trapping and storing the atoms in an optical lattice are very attractive because many atoms can be involved and kept in the Lamb–Dicke regime while still reducing collisional frequency shifts by proper design of the lattice spacing. Yet, because in one-dimensional lattices the confinement is only in one direction and in addition the wavelength is not a free parameter but determined by the magic wavelength, collision shifts may still occur. In this respect, three-dimensional optical lattices are superior [80, 81]. In general, the rather strong light field creating the optical lattice would also cause frequency shifts due to the AC Stark effect. It has been proven, however, that it is possible to find a wavelength for the trapping light where the AC Stark shift of the ground state and the excited state are the same (magic wavelength) due to the nonresonant coupling of these states to higher energy levels [82–84]. At present, the results for the $^1S_0 \rightarrow {}^3P_0$ transition in ^{87}Sr atoms agree on a level of

10^{-16}. Given its high stability [85–88] and low uncertainty [89, 90], the Sr lattice clock transition becomes a serious candidate for a new defining constant for the second. Recent experiments with three-dimensional optical lattices [80, 81] have reached a precision at the 10^{-19} level [81]. The $^1S_0 \rightarrow {}^3P_0$ transition in ^{87}Sr is also already recommended as one of the secondary representations of the second [91, 92]. Besides Sr, lattice clocks with Yb [93], Hg [94], and Mg [95] have been realized. Finally, a transportable Sr optical lattice clock with 7×10^{-17} uncertainty has been developed [96] and applied in high-precision geodesy experiments [97].

9.1.4 Atomic Ion Clocks

The major advantage of single-ion frequency standards [5, 98] compared to atom clouds is the absence of interaction effects and their amazingly long storage time, which can simply be several months. This means practically unlimited interrogation times for the probe laser. However, the price to pay is lower signal intensity and thus lower signal-to-noise ratio, which can be partly overcome by using multi-ion clocks [99–101]. Trapped single-ion frequency standards have been realized with the $^1S_0 \rightarrow {}^3P_0$ transition in $^{115}In^+$ [102] and $^{27}Al^+$, the $^2S_{1/2} \rightarrow {}^2D_{5/2}$ electric quadrupole transition in $^{199}Hg^+$ [103–105], the $^2S_{1/2} \rightarrow {}^2D_{5/2}$ electric quadrupole transition in $^{88}Sr^+$ at 674 nm [106, 107] and $^{40}Ca^+$ [108–110], as well as $^{171}Yb^+$. We briefly describe the results obtained with $^{171}Yb^+$ and $^{27}Al^+$ in the following text.

Ion frequency standards usually start with a neutral atom beam created by evaporation and subsequent ionization by either electron impact or optical radiation followed by the cooling and trapping procedure.

The *ytterbium ion* ($^{171}Yb^+$) is a particularly interesting candidate for an optical clock since besides the electric quadrupole transition ($^2S_{1/2} \rightarrow {}^2D_{3/2}$) at 436 nm, it has a second highly forbidden octupole transition ($^2S_{1/2} \rightarrow {}^2F_{7/2}$) at 467 nm with an extremely long excited-state lifetime of several years. A partial energy scheme is shown in Figure 9.12.

Measurements of the $^2S_{1/2}$ ($F = 0$) $\rightarrow {}^2D_{3/2}$ ($F = 2$) transition have been reported by Tamm et al. [111] and of the $^2S_{1/2}$ ($F = 0$) $\rightarrow {}^2D_{5/2}$ ($F = 0$) transition at 411 nm by Roberts et al. [112] using quantum jump fluorescence detection [113]. The concept of quantum jump fluorescence detection is that the fluorescence at the cooling transition at 370 nm is quenched (dark) whenever the ion is excited to the $^2D_{3/2}$ or $^2D_{5/2}$ state by the clock laser. The absolute frequency of the 436 nm transition has been determined with a femtosecond comb with a relative uncertainty of 1.1×10^{-15} [114] and by using cross-linked optical and microwave oscillators with an uncertainty of 1.1×10^{-16} [115]. A comparison of the frequencies of ions in two independent traps shows agreement on a level of 4×10^{-16} [116].

The electric octupole transition in $^{171}Yb^+$ is of special interest not only because of its long excited-state lifetime and thus narrow homogeneous linewidth in the nanohertz regime but also because the quadrupole transition and the octupole transition exhibit quite different relativistic corrections [117], thus providing an ideal probe to investigate possible time variations of the fine-structure constant, α (see Section 9.1.5). The $^2S_{1/2}$ ($F = 0$) $\rightarrow {}^2F_{7/2}$ ($F = 3$) transition

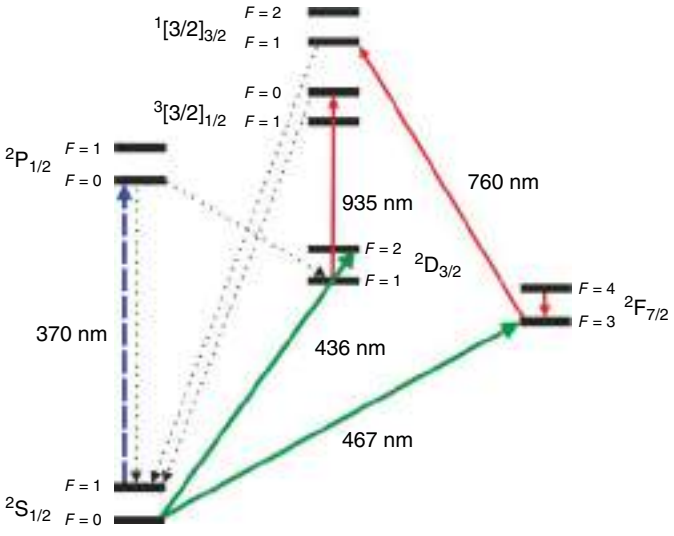

Figure 9.12 Partial energy scheme of $^{171}Yb^+$ indicating the cooling transition at 370 nm (dashed blue arrow), the electric quadrupole transition at 436 nm as well as the electric octupole transition at 467 nm (green arrows). The other transitions to higher D-states (red arrow) are used for repumping. The dotted arrows indicate spontaneous transitions. The notation at the upper left refers to a specific coupling-scheme (JK- or J_1L_2-coupling) particularly applied, for example, for rare-earth atoms.
Source : Courtesyof N.Huntemannand E.Peik, PTB.

had been first investigated at the National Physical Laboratory (NPL) [118]. A difficulty encountered with the octupole transition is high intensity of the probe laser needed to drive this very weak transition, resulting in a considerable AC Stark shift. Initially, extrapolation schemes have been used to determine the unperturbed transition frequency. Later modified Ramsey schemes have been proposed and demonstrated [119–121] that suppress the excitation-related shifts and thus open the way to even more precise measurements on the level of a few parts in 10^{18} [122].

Recent measurements of the octupole transition frequency show agreement on the 10^{-15} level [123, 124]. Figure 9.13 shows an excitation spectrum of the octupole transition using the quantum jump detection technique. The transition is excited by a laser system with excellent stability better than 2×10^{-15} at one second averaging time [125].

The aluminum ion ($^{27}Al^+$) is also a promising candidate for an optical clock because its $^1S_0 \rightarrow {}^3P_0$ intercombination transition exhibits a narrow linewidth of 8 mHz [113, 126] and it has low sensitivity to electromagnetic perturbations and blackbody radiation. However, the $^{27}Al^+$ ion does not possess an accessible strong optical transition for laser cooling and detection. However, using quantum logic spectroscopy [50], an Al^+ ion frequency standard has been constructed at the NIST for the first time [127]. In quantum logic spectroscopy, an auxiliary atom (logic atom) is used to cool the vibrational motion and probe the internal state of the atom to be investigated (spectroscopy atom). For this purpose, both

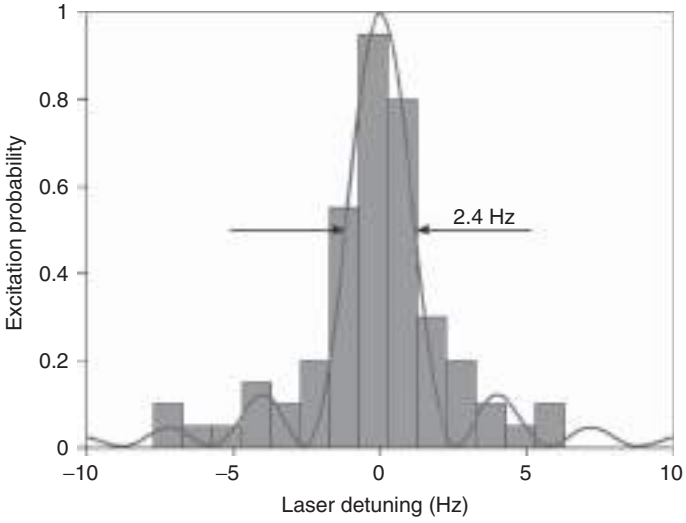

Figure 9.13 Excitation spectrum of the $^2S_{1/2}$ ($F = 0$) → $^2F_{7/2}$ ($F = 3$) transition in $^{171}Yb^+$. Source : Courtesyof N.Huntemann, PTB.

ions are trapped together in a linear Paul trap, and the ion pair forms a two-ion linear Coulomb crystal along the axis of the trap due to their repulsive Coulomb interaction. The quantum mechanical state transfer is brought about by their joint motion, giving rise to vibronic sidebands. The spectroscopy ion is cooled through the laser-cooled logic ion via their Coulomb interaction (sympathetic cooling). The spectroscopy of the ion is then performed with a suitable laser, and the internal state is transferred to the logic ion by coherent interaction with a sequence of laser pulses on both ions. The outcome of the spectroscopy is then detected on the logic ion using the quantum jump technique [113].

In the first spectroscopy experiment, the $^1S_0 \rightarrow {}^3P_0$ clock transition in $^{27}Al^+$ was probed by a $^9Be^+$ ion [127]. When driving the $^1S_0 \rightarrow {}^3P_0$ transition by a clock laser, this will also modulate the $^1S_0 \rightarrow {}^3P_1$ transition due to electron shelving, and this state is then transferred to the Be^+ ion. This experiment enabled the first precise measurement of the $^1S_0 \rightarrow {}^3P_0$ transition frequency with a fractional uncertainty of 5×10^{-15} and the determination of the $^3P_0$ state lifetime of 20.6 ± 1.4 seconds. Further, the frequency ratio of the Al^+ and Hg^+ single-ion optical clock has been measured at the NIST with an uncertainty better than 10^{-16} [105]. A second version of the Al^+ ion clock constructed at the NIST uses Mg^+ as logic ions, which better match the mass of the Al^+ ion, thus enabling more efficient sympathetic cooling [128]. A comparison of this Al^+–Mg^+ clock with the Al^+–Be^+ clock showed fractional agreement of both measured frequencies on the 10^{-17} level and a relative stability of a few times $10^{-15}\ \tau^{-1/2}$ (with τ being the averaging period; c.f. Eq. (3.8)) [129]. This demonstrates their potential not only for clock applications but maybe even more for fundamental physics studies such as the investigation of possible changes of fundamental constants, particularly the fine-structure constant (see Section 9.1.5), relativity, and geodesy applications [97, 130–132].

We finally mentioned recent developments that may lead to optical clocks with even higher accuracy and stability. These are clocks based on optical transitions in nuclei and highly charged ions.

Atomic clocks based on optical transitions in a nucleus are of interest for optical clock applications because they are less sensitive to external perturbations [133–136]. Yet, the most severe restriction for the possible choice of a suitable nucleus is the accessibility of the respective transition by high-resolution laser spectroscopy. High-precision γ-spectroscopy [137] had indicated that ^{229}Th indeed should possess an isomeric excited state above the ground state by only about 3.5 eV. Later measurements resulted in the presently accepted value of 7.8 eV [138]. These two states are linked optically by a magnetic dipole transition. Possible laser spectroscopy techniques to access this transition had been suggested by Peik and Tamm already in 2003 [133], but it was not until recently that this transition had been investigated [139, 140], however, not yet directly by high-resolution laser spectroscopy as required for atomic clock applications. Nevertheless, high-resolution spectroscopy of the hyperfine structure of electronic transitions of $^{229}Th^{2+}$ meanwhile has provided detailed information about the fundamental nuclear properties of the isomer [140]. Since the ^{229}Th nuclear clock has been proposed as a particularly sensitive system to search for temporal variations of the fine-structure constant [141], these developments not only pave the way to optical clocks that outperform existing atomic timekeepers but will also contribute to answer most fundamental questions in basic physics (see Section 9.1.5).

Optical clocks with highly charged ions should also be less sensitive to external perturbations and thus may exhibit higher accuracy and stability than conventional optical clocks based on neutral atoms or singly charged ions [142]. In addition, electronic optical transitions in selected highly charged ions should also exhibit high sensitivity to variations of the fine-structure constant [143–145].

9.1.5 Possible Variation of the Fine-Structure Constant, α

The dimensionless fine-structure constant, α, is considered a fundamental constant of nature.

$$\alpha = \frac{e^2}{4\pi\varepsilon_0\hbar c} \approx \frac{1}{137} \tag{9.5}$$

According to quantum electrodynamics (QED), α is a measure of the strength of the electromagnetic interaction. Its value, however, cannot be calculated within QED but must be determined by experiment. Presently, the most precise value comes from the determination of the Landé g-factor of the electron [146, 147], and based on these results combined with QED calculations, α has been determined with a relative standard uncertainty of 7×10^{-10} [148], while the latest CODATA (International Council for Science: Committee on Data for Science and Technology) result lists an uncertainty of 2.3×10^{-10} [149]. The fine-structure constant can also be determined by the quantum Hall effect (see Section 5.4.5).

Recently, considerable attention has been paid to search for possible temporal variations of fundamental constants, in particular, the fine-structure constant

and the proton-to-electron mass ratio [150–152]. According to the present understanding of the laws of physics including quantum theory and relativity, the fundamental constants do not vary in time. This is a consequence of Einstein's equivalence principle (EEP). In particular, the local time and position invariance states that in any local free-falling reference frame, the result of a measurement is independent of space and time. On the other hand, theories beyond the standard model of physics, which aim at unifying the theory of all forces and bringing together quantum theory and gravitation, allow for space–time variation of fundamental constants. This would mean that frequency of an optical transition might vary in time. Whether this contradicts the EEP is not obvious but depends on the detailed physics behind. Further, studies of the absorption lines of interstellar clouds in the light of distant quasars have been interpreted as evidence for a variation of the fine-structure constant α on cosmological timescales of some 10 billion years [153]. According to their interpretation, a relative increase in the fine-structure constant $\Delta\alpha/\alpha$ of the order of 10^{-6} should have occurred in the first half of the evolution of the universe. Assuming a linear variation with time that would continue up to today, this would extrapolate to a relative increase in α of some 10^{-16} per year. In contrary, other studies rule out a change of α [154].

It is only with the development of the most recent optical frequency standards that this order of magnitude is accessible by laboratory experiment in reasonable time intervals [105, 155–162]. To analyze frequency measurements in respect to possible variations of α, the electronic transition frequency can be expressed as [163]

$$\nu = \text{const} \cdot R_y \cdot F(\alpha) \tag{9.6}$$

where the Rydberg frequency $R_y = m_e e^4/8\varepsilon_0 h^3$ is the common scaling factor for the energy levels in atoms and the dimensionless factor $F(\alpha)$ accounts for relativistic corrections of the energy levels. The "constant" prefactor depends only on the quantum numbers of the atomic states involved and is independent of time. The relative temporal variation of ν is given by

$$\frac{\mathrm{d}\ln\nu}{\mathrm{d}t} = \frac{\mathrm{d}\ln R_y}{\mathrm{d}t} + A\frac{\mathrm{d}\ln\alpha}{\mathrm{d}t} \text{ with } A = \frac{\mathrm{d}\ln F}{\mathrm{d}\ln\alpha}. \tag{9.7}$$

A variation of the Rydberg frequency given by the first term would be common for all transition frequencies. In contrast, the second term is specific to the atomic transition considered. The so-called sensitivity factor A accounts for the sign and strength of the effect of a variable α on the transition frequency and has been calculated for several transitions of interest [164, 165].

A summary of recent results is depicted in Figure 9.14 where the estimated relative temporal variation of the optical transition frequencies measured with respect to the ^{133}Cs ground state hyperfine transition frequency, $\Delta\nu_{\mathrm{Cs}}$, (i.e. in SI units) is plotted versus their respective sensitivity factor A. Based on these data, a constraint for the time variation of

$$\frac{\mathrm{d}\ln\alpha}{\mathrm{d}t} = (-0.22 \pm 0.20) \times 10^{-16} \text{ per year} \tag{9.8}$$

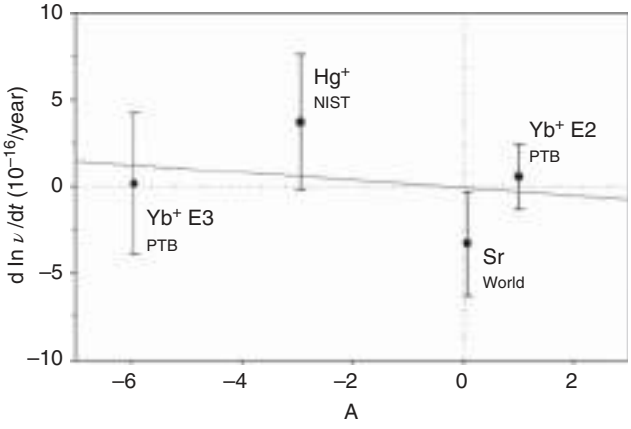

Figure 9.14 Time variation of measured transition frequencies in different atoms and ions versus their respective sensitivity parameter. Source : Courtesy of E. Peik, PTB. For the original data see (the respective transition is given in brackets): $^{199}Hg^{+}(^{2}S_{1/2} \rightarrow {}^{2}D_{5/2})$: Ref. [159]; ^{87}Sr ($^{1}S_{0} \rightarrow {}^{3}P_{0}$): Ref. [160]; $^{171}Yb^{+}$ E2 ($^{2}S_{1/2} \rightarrow {}^{2}D_{3/2}$): Ref. [115]; $^{171}Yb^{+}$ E3 ($^{2}S_{1/2} \rightarrow {}^{2}F_{7/2}$): Ref. [161].

has been obtained [161]. Further, a constraint for the relative change of the proton-to-electron mass ratio $\mu = m_p/m_e$ has been given in Ref. [161]:

$$\frac{\mathrm{d}\ln\mu}{\mathrm{d}t} = (-0.5 \pm 1.6) \times 10^{-16} \text{ per year} \tag{9.9}$$

Similar results have been obtained by Godun et al. by analyzing the quadrupole (436 nm) and octupole transitions (467 nm) in $^{117}Yb^{+}$ [162]. Recently published data on a test of general relativity based on long-term comparison of atomic transition frequencies are also in agreement with these results [166].

So, the present results of laboratory studies of possible changes of α and the proton-to-electron mass ratio using the latest state-of-the-art optical clocks do not give evidence for a change on the uncertainty level of order of 10^{-17} per year. This, however, cannot exclude possible changes on cosmic timescales. Further improvement of optical clocks including possibly clocks based on nuclear transitions and highly charged ions (see above) and clock assemblies in space [167] definitely will provide even more accurate tests of fundamental physics and thereby contribute to solving the remaining puzzles in the understanding of nature.

Let us close Section 9.1 with some general remarks: The unit second is still defined by the Cs hyperfine transition within the present SI, and one might ask about the "when and how" of a new definition [168–170]. Concerning the "when," one must state that the development of ultraprecise and stable optical clocks presently is primarily driven by basic science. Present technical and industrial requirements are generally satisfied by the best Cs clocks notwithstanding that the availability of improved technologies often results in new applications, e.g. improved relativistic geodesy and satellite navigation systems. In addition, the accepted secondary realizations of the second including the best optical clocks [91, 92] leave room for further scientific progress. A new definition of the second should only be considered when the physical grounds for the definition

and its realization are proven and generally accepted [92, 170]. This brings us to "how" the new second should be defined. If we consider optical clocks, it must be decided on which atom or ion transition frequency is chosen as the defining constant of the second with the femtosecond comb technique providing traceability of other optical clocks as secondary realizations. The essential requirement is that extensive intercomparisons of the frequencies of the optical clocks must take place to develop a robust and generally accepted base for a new definition. These optical clock frequency comparisons are under way. On-site clock comparisons today can be performed at the 10^{-19} uncertainty level using femtosecond combs by taking into account the (eventually remaining) height difference and the related gravitational redshift. The comparison of remote clocks with the required uncertainty level, however, turns out to be a much bigger problem, since the established two-way satellite microwave frequency transfer techniques are limited to some 10^{-15} uncertainty at averaging times of a day. Establishing direct optical (laser) links via satellites [171, 172] would bear the potential for optical clock comparisons; however, these techniques are much dependent on environmental conditions and not yet fully established. Alternatively, frequency transfer by optical fibers has been demonstrated over almost 2000 km with an uncertainty of 4×10^{-19} at only 100 seconds averaging time [173]. This already has made it possible to test special relativity with unprecedented statistical uncertainty by frequency comparison of remote optical clocks located in, respectively, France, the United Kingdom, and Germany [174]. Finally, transportable optical clocks [96] will enable remote clock comparison.

9.2 Single-Photon Metrology and Quantum Radiometry

Photons are the massless bosonic quanta of electromagnetic radiation carrying the energy $E = h\nu$, where ν is the light frequency. The concept of photons dates back to Planck [175] and Einstein [176] at the beginning of the twentieth century even though the name *photon* (from the Greek word *phos* meaning *light*) was created only in 1926 by Lewis [177, 178].

Max Planck, while developing his famous radiation formula, postulated that the energy exchange between electromagnetic radiation and the wall of a black body can take place only in discrete quanta of energy $h\nu$. *Albert Einstein* then used the concept of light quanta to explain the photoelectric effect, for which he was awarded the 1921 Nobel Prize in physics.

The concept of photons, however, became much more prominent with the development of quantum optics showing that there is more to quantify the nature of light than the wavelike quantities such as frequency, intensity, and polarization. These are, in particular, the coherence properties of light as described by correlation functions for the field, intensity, and photon number [179, 180].

The first-order (field-) correlation function

$$g^{(1)}(\boldsymbol{r}_1, t_1; \boldsymbol{r}_2, t_2) = \frac{\left\langle \boldsymbol{E}^*(\boldsymbol{r}_1, t_1)\boldsymbol{E}(\boldsymbol{r}_2, t_2)\right\rangle}{\left[\left\langle \left|\boldsymbol{E}(\boldsymbol{r}_1, t_1)\right|^2\right\rangle \langle |\boldsymbol{E}(\boldsymbol{r}_2, t_2)|^2\rangle\right]^{1/2}} \tag{9.10}$$

describes the spectral properties. The pointed brackets ⟨ ⟩ denote an ensemble average. The Fourier transform of $g^{(1)}(\boldsymbol{r}_1, t_1; \boldsymbol{r}_2, t_2)$ is the spectrum of the radiation source and accounts for the contrast (visibility) of interference patterns of the electromagnetic field reflecting the phase correlation of the light field. For plane waves and stationary fields where the ensemble average can be replaced by a time average and neglecting further spatial dependencies, Eq. (9.10) simplifies to

$$g^{(1)}(\tau) = \frac{\langle \boldsymbol{E}^*(t)\boldsymbol{E}(t+\tau)\rangle}{\langle |\boldsymbol{E}(t)|^2\rangle} \tag{9.11}$$

The second-order correlation function $g^{(2)}(\boldsymbol{r}_1, t_1; \boldsymbol{r}_2, t_2)$ describes the intensity correlations:

$$g^{(2)}(\boldsymbol{r}_1, t_1; \boldsymbol{r}_2, t_2) = \frac{\langle \boldsymbol{E}^*(\boldsymbol{r}_1, t_1)\boldsymbol{E}^*(\boldsymbol{r}_2, t_2)\boldsymbol{E}(\boldsymbol{r}_1, t_1)\boldsymbol{E}(\boldsymbol{r}_2, t_2)\rangle}{[\langle |\boldsymbol{E}(\boldsymbol{r}_1, t_1)|^2\rangle\langle |\boldsymbol{E}(\boldsymbol{r}_2, t_2)|^2\rangle]} \tag{9.12}$$

For plane waves and stationary classical fields, this can be written in terms of intensities, *I:*

$$g^{(2)}(\tau) = \frac{\langle I(t+\tau)I(t)\rangle}{\langle |I(t)|^2\rangle} \tag{9.13}$$

More general, in terms of photon creation and annihilation operators, respectively, $\boldsymbol{a}^\dagger(t)$ and $\boldsymbol{a}(t)$, the second-order correlation function for stationary fields neglecting again any spatial dependencies is given by

$$g^{(2)}(\tau) = \frac{\langle \boldsymbol{a}^\dagger(t)\boldsymbol{a}^\dagger(t+\tau)\boldsymbol{a}(t)\boldsymbol{a}(t+\tau)\rangle}{\langle \boldsymbol{a}^\dagger(t)\boldsymbol{a}(t)\rangle^2} \tag{9.14}$$

where $\boldsymbol{a}^\dagger\,\boldsymbol{a}$ gives the photon number, n, of the respective mode.

While the first-order correlation function can be measured , for example, by a standard Michelson interferometer, the second-order correlation function is by using a Hanbury Brown and Twiss interferometer [181] (Figure 9.15]). To further prove that photons are indistinguishable, two-photon interference (Hong–Ou–Mandel experiment [182]) must be performed. For the following, we shall consider $g^{(2)}(\tau)$ only.

For any state of light $g^{(2)}(\tau \to \infty) = 1$, because photon emission is uncorrelated for large delay times (Figure 9.16). For $\tau = 0$, the probability for simultaneous detection of two photons can be increased, unaltered, or decreased with

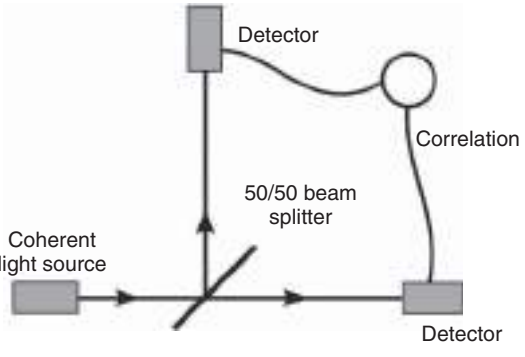

Figure 9.15 Set-up of the Hanbury Brown and Twiss interferometer. Source: Göbel and Siegner 2015 [9]. Reproduced with permission of John Wiley & Sons.

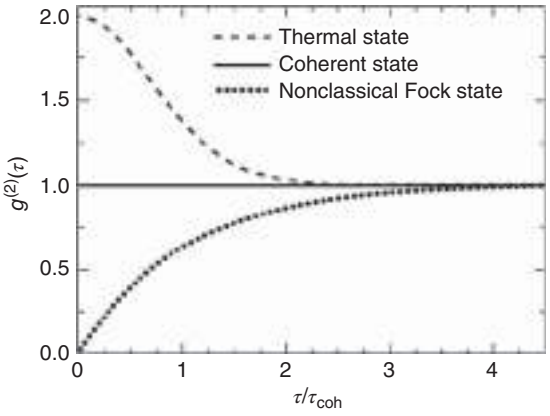

Figure 9.16 Second-order correlation function $g^2(\tau)$ versus delay time τ normalized to the coherence time τ_{coh}. Source: Göbel and Siegner 2015 [9]. Reproduced with permission of John Wiley & Sons.

respect to $g^{(2)}(\tau \to \infty)$. For thermal light, $g^{(2)}(0) = 2$; for coherent light (coherent in second order), $g^{(2)}(0) = 1$; and for nonclassical light, $g^{(2)}(0) < 1$. For a "true" single-photon emitter (single-photon Fock state), $g^{(2)}(0) = 0$. While $g^{(2)}(0) = 2$ corresponds to bunching of photons, $g^{(2)}(0) < 1$ reflects antibunching. In terms of photon-counting statistics, $g^{(2)}(0) = 2$ corresponds to Bose–Einstein statistics, while $g^{(2)}(\tau) \equiv 1$ reflects Poisson statistics [183]. $g^{(2)}(0) < 1$ is associated with sub-Poissonian statistics [184].

Bunching of thermal light is simply a manifestation of fluctuating electromagnetic fields and Bose statistics: more photons are emitted when the instantaneous light intensity is higher than the mean intensity. Consequently, the probability to detect another photon is increased. In contrast, antibunching of a single two-level emitter is because when a photon is emitted, the emitter returns into the ground state and a second photon cannot be emitted simultaneously.

Single-photon emitters are of considerable interest for quantum information applications such as quantum cryptography and quantum computing [185]. In quantum metrology, another promising application could be in the field of radiometry and photometry, where they could provide quantum standards for (spectral) radiative power and luminous flux on the base of counting photons from a single-photon emitter [186]. Knowing the photon energy $h\nu$, the (spectral) radiative power of a single-photon emitter, Φ, is given by the number of photons emitted per time interval, r, multiplied by $h\nu$:$\Phi = r \cdot h\nu$ (note the analogy to quantized currents, Eq. (6.1)). However, due to the small energy of a single photon, for example, a photon at a wavelength of 500 nm carries an energy of about 4×10^{-19} J, single-photon sources with high repetition rate are needed to bridge the many orders of magnitude in power relevant for practical applications.

9.2.1 Single-Photon Sources

Even though "quasi" single photons may be generated by strongly attenuating a coherent light source, for example, a laser, the photon statistics will be unaltered; that is, it remains Poissonian. Therefore, here, we have to consider a different

approach for sources that emit nonclassical light, showing $g^{(2)}(0) < 1$ (preferably $g^{(2)}(0) = 0$) and thus obeying a sub-Poissonian statistics.

The fundamental element of a single-photon source is an optical transition (a two-level system in the simplest case) of an individual radiation source preferably with high quantum efficiency. This could be single neutral atoms, single ions, single molecules, single color centers, or semiconductor quantum dots. A single photon can be emitted at any arbitrary time or also triggered by the user, thus being a deterministic source. The single-photon emitter often will be coupled to a resonant cavity that causes the radiation to be emitted into a well-defined spatial mode with high collection efficiency. Furthermore, the cavity can enhance the spontaneous emission rate (Purcell effect) and narrow the spectral bandwidth of the emission. For the sake of completeness, probabilistic single-photon sources should also be mentioned. These sources are based on parametric downconversion or four-wave mixing producing always pairs of photons where one photon can be used to herald the creation of the other one (the so-called "heralded single photon"). For further reading, see, for example, [187–190].

Photon antibunching was first observed in the resonance fluorescence of Na atoms continuously excited by a dye laser by Kimble et al. [191]. Dietrich and Walther observed antibunching emission of a laser-cooled single ion stored in a Paul radio-frequency trap [192]. In molecule fluorescence, antibunching was first reported by De Martini et al. [193], Kitson et al. [194], and Brunel et al. [195]. Further, a single-photon source based on Rydberg excitations in an Rb gas held in a linear optical lattice was demonstrated [196–198]. In view of potential applications, however, solid-state single-photon emitters might be more promising even though in some cases they may require cooling to low temperatures. Here, two systems have gained considerable interest, namely, color centers in diamond, in particular, nitrogen-vacancy (NV) and silicon-vacancy (SiV) centers, and semiconductor quantum dots.

9.2.1.1 (NV) Color Centers in Diamond

A (NV) color center in diamond is formed by a substitutional nitrogen atom and an adjacent vacancy in the diamond lattice. The (NV) centers are prepared in type 1 synthetic diamond that usually contains homogeneously dispersed nitrogen impurities. Vacancies are created by electron or neutron irradiation. Subsequent annealing at about 900 °C results in the formation of (NV) centers (a small number of (NV) centers are already present without extra annealing). The (NV) center exhibits two charge states, electrically neutral and negatively charged. A simplified energy level structure of the $(NV)^-$ center is shown in Figure 9.17.

Electron transitions between the ^3A ground state and the ^3E excited state (the labeling of the energy levels is according to the C_{3V} symmetry group), separated by 1.945 eV (637 nm), produce absorption and luminescence. The ^3A state and the ^3E state are split into the states with spin quantum number $m_S = \pm 1$ and $m_S = 0$ by ~5.6 μeV [199, 200] and ~2.9 μeV [201], respectively, due to the magnetic interaction of the unpaired electrons at the NV^- center. The $m_S = \pm 1$ states are further split due to hyperfine interaction – the interaction between the electron and nuclear spins. The metastable singlet state ^1A that acts as a nonradiative

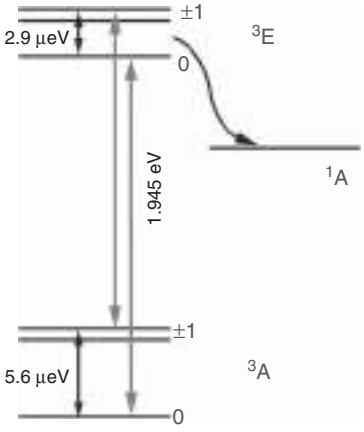

Figure 9.17 Energy-level structure (not to scale) of the $(NV)^-$ center. Source: Göbel and Siegner 2015 [9]. Reproduced with permission of John Wiley & Sons.

trap state for excitation is also indicated. However, its energetic position is not known exactly.

The room temperature photoluminescence of the $(NV)^-$ centers exhibits a zero-phonon emission line at 637 nm accompanied by a broad (≈120 nm) phonon-assisted recombination band [202, 203]. The $(NV)^-$ emission shows high quantum efficiency close to one and short recombination lifetime (≈11 ns) [202]. Individual (NV) centers can be addressed using microscope imaging technique. Figure 9.18a shows a confocal microscopy raster scan of a part of a diamond sample with (NV) color centers. The bright regions show the emission from $(NV)^-$ centers in nanodiamonds [204]. The second-order correlation function of the emission of an individual center is shown in Figure 9.18b. The pronounced dip at $\tau = 0$ clearly shows the quantum nature of the emission. We note that $g^{(2)}(\tau)$ is larger than one for delay times that are larger than the radiative recombination lifetime. This fact relates to the presence of the ^{1}A state to which the excited state can relax [202].

Besides the emission from the NV center with photon rates up to 1 MHz [204], other defect-related emission of diamond [205] such as the emission from SiV centers in diamond nanocrystals was investigated [206, 207]. These centers exhibit emission between approximately 730 and 750 nm, depending on the local stress in the nanodiamonds with zero-phonon linewidth on the order of 0.7–2 nm and photon rates of up to 6 MHz [206–209]. Other defect centers under investigation in diamond are the nickel-related color center (NE8) [210], the chromium-related center [211, 212], and the interstitial carbon-related color center, TR 12, emitting at 470 nm. In the last case, single color centers can be created selectively using focused ion beams [213].

As a further promising step toward practical applications, electrical excitation of the $(NV)^0$ color center in diamond at room temperature has been realized [214] by fabricating a standard LED structure, a pin diode with p- and n-doped diamond layers separated by an intrinsic diamond layer that contains the (NV) center. Besides its potential for single-photon emitters, color center defects in diamond are of interest for single-spin manipulation [215]. Further, nanoscale

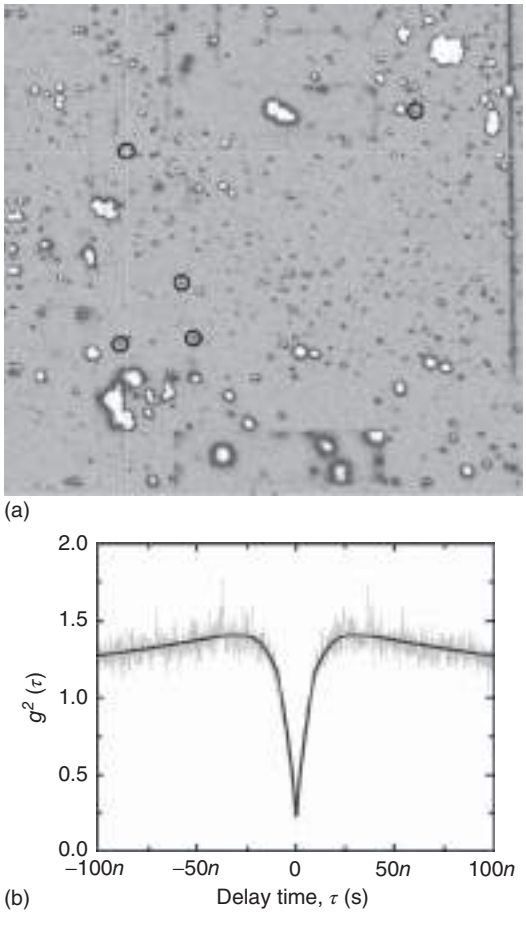

Figure 9.18 (a) Confocal microscopy raster scan of a part of a diamond sample with $(NV)^-$ color centers. The bright regions show the emission of the (NV) centers in nanodiamonds. (b) Second-order correlation function $g^{(2)}(\tau)$ of spectrally filtered emission from an individual $(NV)^-$ center (some are marked by circles in (a)). The pronounced dip at $\tau = 0$ clearly shows the quantum nature of the emission. Source: Courtesy of S. Kück, PTB.

nuclear magnetic resonance (NMR) spectra have been recorded using the (NV) center [216–219].

9.2.1.2 Semiconductor Quantum Dots

The characteristic feature of semiconductor quantum dots is their discrete electronic states due to size quantization in all three spatial dimensions (i.e. $L < 100$ nm; see Chapter 5). The electronic states thus resemble those of atoms, therefore, semiconductor quantum dots are often called artificial atoms. For further reading, see Refs. [220–222]. One way to fabricate semiconductor quantum dots is to start with a two-dimensional electron gas (2DEG) formed in semiconductor heterostructures such as GaAs/AlGaAs or InGaAs/GaAs (see Section 5.2). Quantum dots then can be formed by (electron beam) lithography and subsequent chemical etching (see, e.g. [223]). However, the optical quality of free-standing quantum dots is poor even when overgrown with a larger bandgap material. Semiconductor quantum dots have also been fabricated by laser-induced interdiffusion [224]. Most fabrication techniques, however, rely on self-assembled quantum dots formed during epitaxial growth of slightly

lattice-mismatched semiconductors (Stranski–Krastanov growth mode [225]). III–V (e.g. InP in GaAs and InGaAs in GaAs) as well as II–VI heterostructures (e.g. CdSe in ZnS) have been mostly studied so far. Single-photon emitters in the blue spectral regime have also been realized with InGaN/GaN quantum dots [226]. The photoluminescence at low temperatures and weak excitation originates from neutral and charged excitons (and biexcitons), that is, Coulomb-bound electron–hole pair recombination [227, 228]. A photoluminescence spectrum of a single InGaAs/GaAs quantum dot is shown in Figure 9.19 [229].

Antibunching of the exciton emission has been demonstrated in quantum dots embedded in resonant microcavities [230–232]. The cw photoluminescence spectrum of an InAs/GaAs quantum dot embedded in a microdisk resonator structure is shown in Figure 9.20 together with the second-order correlation function (inset). The photoluminescence clearly exhibits the exciton (1X) and biexciton (2X) emission together with some spurious background emission (M), which couples to a whispering gallery mode of the microdisk. The second-order

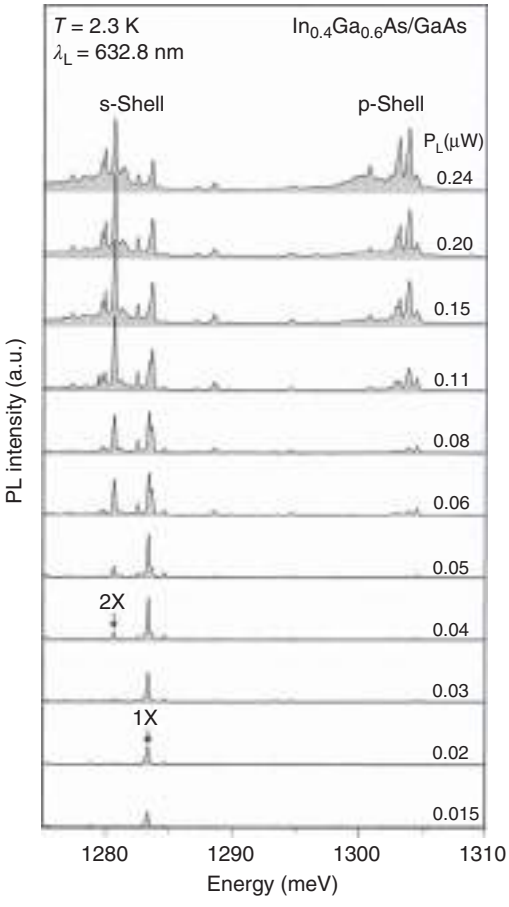

Figure 9.19 Photoluminescence spectra ($T = 2.3$K) of a single InGaAs/GaAs quantum dot for different excitation intensities, showing at low excitation a single line due to the lowest state (s-shell) exciton recombination (1X). At higher excitation also biexciton (2X) recombination and emission from the next excited state (p-shell) of the quantum dot are observed. Source: Findeis et al. 2000 [229]. Reproduced with permission of Elsevier.

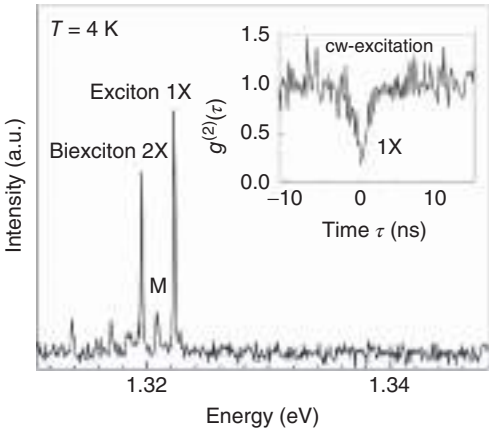

Figure 9.20 cw-Photoluminescence of an InAs/GaAs quantum dot and second-order correlation function of the exciton (1X) emission. Source: Courtesy of P. Michler, University Stuttgart.

correlation function of the spectrally filtered exciton emission clearly shows the nonclassical behavior of the emission.

Electrical excitation of single-photon quantum dot emission has also been achieved [233–236]. In either case, optical or electrical excitation, it must be assured that radiative transition is only excited once at a time to ensure single-photon emission. In the case of optical excitation, this occurs through absorption saturation together with the combined effect of an anharmonic multiexciton spectrum and slow relaxation of highly excited quantum dots [231, 232], while in the electrical excitation through Coulomb blockade (see Section 6.1.2) [234, 236].

9.2.2 Single-Photon Detectors

Single-photon detectors are required to test the fidelity of single-photon sources. Photon detectors usually convert an incoming photon into an electric signal, which is further processed (e.g. amplified) electronically. Single-photon detectors are sometimes classified into nonphoton-number-resolving and photon-number-resolving detectors even though this distinction is not always strict. For a detailed listing and comparison of single-photon detectors, see [189]. Nonphoton-number-resolving detectors can only distinguish between zero and more than zero photons, while photon-number-resolving detectors can count the number of incoming photons (within a certain uncertainty). For a detailed overview, see [189, 237].

9.2.2.1 Nonphoton-Number-Resolving Detectors

Most familiar nonphoton-number-resolving detectors are *photomultiplier tubes (PMTs)* and avalanche photodiodes (APDs). While the detection efficiency of APDs (up to 80% for InGaAs APDs; for the near-IR spectral regime, the quantum efficiency is lower) is higher than that for PMTs (typically 25%, up to 40%), the dark count rate of APDs is higher, which often requires cooling below room temperature. Further, since APDs for single-photon detection (single-photon avalanche diodes, SPADs) [238] are usually operated in the so-called Geiger

mode with a bias voltage greater than the breakdown voltage of the diode, the avalanche current does not terminate by itself after an incoming photon pulse but instead must be turned off by lowering the bias voltage. As a result, dead times of SPADs are generally larger than for PMTs, depending, of course, crucially on the detector electronics. The dead time limit of SPADs can be overcome partly by using a multiplex detector array consisting of fiber splitters and an array of detectors addressable individually by optical switches [239].

9.2.2.2 Photon-Number-Resolving Detectors

Photon-number-resolving detectors are often based on superconducting materials with sharp superconducting to normal metal transitions. Most promising devices to date are superconducting transition-edge sensors (TESs) [240] due to their high efficiency and low dark counts. TESs are basically microcalorimeters that measure the energy of the absorbed photons. The operation principle of a TES is illustrated in Figure 9.21.

The thermal sensor of the TES is made from a thin film of superconducting material deposited on an isolating substrate. TESs have been made with tungsten and aluminum [240, 241], titanium [242], and hafnium [243]. Also, bilayers of a superconductor and a normal metal (Ti/Au and Ti/Pd) [244] and trilayers of Ti/Au/Ti [245] have been used, which enables to vary the superconductor transition temperature due to the proximity effect. The superconducting film is structured by standard lithography techniques and contacted by superconducting wires, mostly Al.

A constant bias voltage of the superconducting film provides an electrothermal feedback (ETF) such that the temperature is maintained [240]. The constant bias voltage source can also be realized by a constant current source together with a bias resistor with much lower resistance than the TES resistance. The reduction of the current flowing through the sensor due to absorption of photons is read out with a DC superconducting quantum interference device (SQUID) operated in a flux-locked loop (see Section 4.2.3.1) [244] (see Figure 9.22).

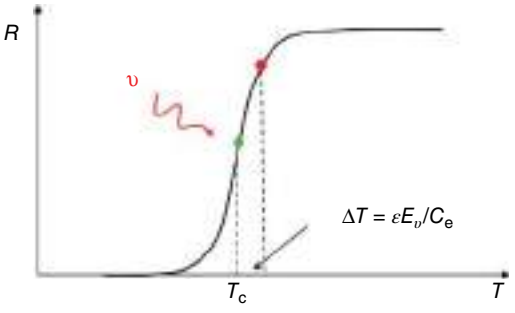

Figure 9.21 Operation principle of a TES depicting the resistance, R, versus temperature, T, close to the superconductor transition temperature T_C. ΔT is the increase in the temperature due to the absorption of a photon (ε is the detection efficiency, $E_\nu = h\nu$ is the energy of the photon, and C_e the electronic heat capacity). Source: Göbel and Siegner 2015 [9]. Reproduced with permission of John Wiley & Sons.

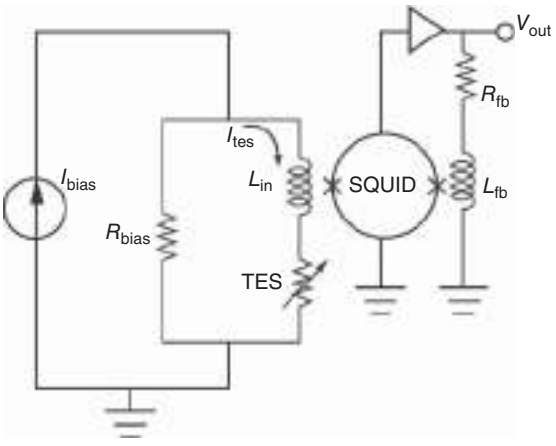

Figure 9.22 ETF-TES bias circuit with a dc SQUID read-out. Source: Göbel and Siegner 2015 [9]. Reproduced with permission of John Wiley & Sons.

Figure of merit of TES single-photon detectors are detection efficiency, ε (ratio of the detected energy to the incident energy) and rise and fall time of the sensor. While detection efficiency in fiber-coupled devices can be quite high (up to 98% [242]), fall times are usually moderate (some hundred nanoseconds to several microseconds).

9.2.3 Metrological Challenge

The major challenge for the use of single-photon emitters as quantum standards for radiative power or luminous flux is to provide the link between optical power measurements in the milliwatts regime to the level of single-photon emitters. This would require either single-photon sources operating at extremely high repetition rate or linear detectors traced to a primary standard (e.g. a cryoradiometer).

To calibrate SPADs operating in the few photon regime, that is, below about 10^6 photons per second, many orders in intensity must be bridged to transfer the SI scale down to these very small intensities, considering the limited linearity of SPADs. Thus, careful attenuation of a calibrated light source, for example, a laser, is required, using two or more neutral density filters with high attenuation subsequently measured *in situ* (see Figure 9.23a [246, 248]). Alternatively, a synchrotron radiation source, where the emitted radiation power is proportional to the number of stored electrons, has been used. Since the number of stored electrons can be widely varied from one up to more than 10^{11}, a SPAD can be calibrated in the single-photon regime without using attenuators [247, 249]. Figure 9.23b depicts the principle of this experiment.

Finally, we note that heralded single photons as generated by parametric down-conversion can also be used for absolute calibrations of APDs in the few photon regime [190, 250, 251].

Calibration of a single-photon source based on single NV at room temperature with respect to its photon flux and spectral photon rate density has recently been achieved by Rodiek et al. [252].

Presently, a new definition of radiometric or photometric quantities based on single-photon sources is not considered because quantum radiometry (or

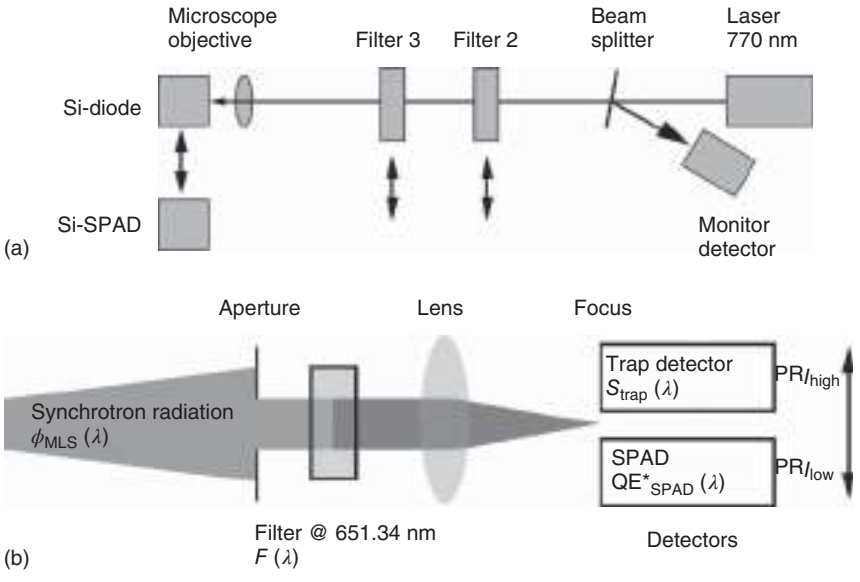

Figure 9.23 Schematic of two setups used to calibrate single-photon avalanche diodes (SPADs). (a) Using in situ calibration of neutral density filters and the known radiative power of a stabilized laser. The Si diode is calibrated, for example, using a cryoradiometer. The subsequent calibration of the individual filters is required because of their very high attenuation factor. For the calibration of the SPAD, both filters are applied together. Source: Kück et al. 2014 [246]. Reproduced with permission of John Wiley & Sons (b) Calibration using synchrotron radiation. The photon rate (PR I_{high}) in the high ring current range is measured in the focus of the spectrally filtered synchrotron radiation by a calibrated trap detector using its known responsivity, $S_{trap}(\lambda)$. In a second step, the count rate of the SPAD is measured in the low ring current range. The quantum efficiency of the SPAD, $QE^*_{SPAD,}$ then can be calculated using the synchrotron current ratio in the high and low current mode. Source: Müller et al. 2012 [247] and Göbel and Siegner 2015 [9]. Reproduced with permission of John Wiley & Sons.

photometry) is not yet mature for practical applications. However, keeping in mind the progress that has been made in scaling up the current generated by single-electron devices (see Chapter 6) and the improvement in the collection efficiency of single-photon emitters [253], it might be feasible soon.

References

1 Yao, J., Parker, T., Ashby, N., and Levine, J. (2017). Incorporating an optical clock into a time scale. *IEEE Trans. Ultrason. Ferroelectr. Freq. Control* 65 (1): 127–134.
2 Le Targat, R., Lorini, L., Le Coq, Y. et al. (2013). Experimental realization of an optical second with strontium lattice clocks. *Nat. Commun.* 4: 2109.
3 Grebing, C., Al-Masoudi, A., Dörscher, S. et al. (2016). Realization of a timescale with an accurate optical lattice clock. *Optica* 3: 563–569.

4 Ido, T., Hachisu, H., Nakagawa, F., and Hanado, Y. (2016). Rapid evaluation of time scale using an optical clock. *J. Phys. Conf. Ser.* 723: 012041.
5 Ludlow, A.D., Boyd, M.M., Ye, J. et al. (2015). Optical atomic clocks. *Rev. Mod. Phys.* 87: 637.
6 Hollberg, L., Oates, C.W., Curtis, E.A. et al. (2001). Optical frequency standards and measurements. *IEEE J. Quantum Electron.* 37: 1502–1513.
7 Gill, P., Barwood, G.P., Klein, H.A. et al. (2003). Trapped ion frequency standards. *Meas. Sci. Technol.* 14: 1174–1186.
8 Gill, P. (2005). Optical frequency standards. *Metrologia* 42: S125–S137.
9 Göbel, E.O. and Siegner, U. (2015). *Quantum Metrology: Foundation of Units and Measurements*. Weinheim: Wiley-VCH, 2018.
10 Kessler, T., Hagemann, C., Grebing, C. et al. (2012). A sub-40-mHz-linewidth laser based on a silicon single-crystal optical cavity. *Nat. Photon.* 6: 687–692.
11 Matei, D.G., Legero, T., Häfner, S. et al. (2017). 1.5 μm lasers with sub-10 mHz linewidth. *Phys. Rev. Lett.* 118: 263202-1-6.
12 Letokhov, V.S. (1976). *High Resolution Laser Spectroscopy*, Topics in Applied Physics, vol. 13 (ed. K. Shimoda), 95–171. Berlin, Heidelberg, New York: Springer-Verlag.
13 Oates, C.W., Wilpers, G., and Hollberg, L. (2005). Observation of large atomic-recoil-induced asymmetries in cold atom spectroscopy. *Phys. Rev. A* 71: 023404-1–023404-6.
14 Ido, T., Loftus, T.H., Boyd, M.M. et al. (2005). Precision spectroscopy and density-dependent frequency shifts in ultracold Sr. *Phys. Rev. Lett.* 94: 153001-1–153001-4.
15 Bordé, C. (1989). Atomic interferometry with internal state labeling. *Phys. Lett. A* 140: 10–12.
16 Helmcke, J., Zevgolis, D., and Yen, B.Ü. (1982). Observation of high contrast, ultra-narrow optical Ramsey fringes in saturated absorption utilizing four interaction zones of travelling waves. *Appl. Phys. B* 28: 83–84.
17 Riehle, F., Kisters, T., Witte, A. et al. (1991). Optical Ramsey spectroscopy in a rotating frame: Sagnac effect in a matter-wave interferometer. *Phys. Rev. Lett.* 67: 177–180.
18 Holberg, L., Diddams, S., Bartels, A. et al. (2005). The measurement of optical frequencies. *Metrologia* 42: S105–S124.
19 Schnatz, H., Lipphardt, B., Helmcke, J. et al. (1996). First phase-coherent frequency measurement of visible radiation. *Phys. Rev. Lett.* 76: 18–21.
20 Hall, J.L. (2006). Defining and measuring optical frequencies. *Rev. Mod. Phys.* 78: 1279–1295.
21 Hänsch, T.W. (2006). Passion for precision. *Rev. Mod. Phys.* 78: 1297–1309.
22 Ye, J. and Cundiff, S.T. (2005). *Femtosecond Optical Frequency Comb Technology: Principle, Operation, and Applications*. New York: Springer Science + Business Media, Inc. ISBN: 0-387-23790-9.
23 Diddams, S.A., Jones, D.J., Ye, J. et al. (2000). Direct link between microwave and optical frequencies with a 300 THZ femtosecond laser comb. *Phys. Rev. Lett.* 84: 5102–5105.

24 Diels, J.-C. and Rudolph, W. (1996). *Ultrashort Laser Pulse Phenomena: Fundamentals, Techniques, and Applications on a Femtosecond Timescale*. San Diego, CA: Academic Press.

25 Udem, T., Reicher, J., Holzwarth, R., and Hänsch, T.W. (1999). Absolute optical frequency measurement of the cesium D_1 line with a mode-locked laser. *Phys. Rev. Lett.* 82: 3568–3571.

26 Reichert, J., Nierig, M., Holzwarth, R. et al. (2000). Phase coherent vacuum-ultraviolet to radio frequency comparison with a mode-locked laser. *Phys. Rev. Lett.* 84: 3232–3235.

27 Udem, T., Reichert, J., Holzwarth, R., and Hänsch, T.W. (1999). Accurate measurement of large optical frequency differences with a mode-locked laser. *Opt. Lett.* 24: 881–883.

28 Stenger, J., Schnatz, H., Tamm, C., and Telle, H.R. (2002). Ultra-precise measurement of optical frequency ratios. *Phys. Rev. Lett.* 88: 073601-1–073601-4.

29 Siegner, U. and Keller, U. (2001). *Handbook of Optics* (ed. M. Bass, J.M. Enoch, E.W. Van Stryland and W.L. Wolfe), 18.1–18.30. New York: McGraw-Hill.

30 Szipöcs, R., Spielmann, C., Krausz, F., and Ferencz, K. (1994). Chirped multi-layer coatings for broadband dispersion control in femtosecond lasers. *Opt. Lett.* 19: 201–203.

31 Bartels, A., Heinecke, D., and Diddams, S.A. (2008). Passively mode-locked 10GHz femtosecond Ti: sapphire laser. *Opt. Lett.* 33: 1905–1907.

32 Russell, P. (2003). Photonic crystal fibers. *Science* 299: 358–362.

33 Husakou, A., Kalosha, V.P., and Hermann, J. (2003). *Optical Solitons. Theoretical and Experimental Challenges*, Lecture Notes in Physics (ed. K. Porsezian and V.C. Kuirakose), 299–326. Heidelberg, New York: Springer-Verlag.

34 Tauser, F., Leitenstorfer, A., and Zinth, W. (2003). Amplified femtosecond pulses from an Er: fiber system: nonlinear pulse shortening and self-referencing detection of the carrier-envelope phase evolution. *Opt. Express* 11: 594–600.

35 Liehl, A., Fehrenbacher, D., Sulzer, P. et al. (2015). Free running performance and full control of a passively phase-stable Er: fibre frequency comb. *Optica* 2 (10): 917–923.

36 Brida, D., Krauss, G., Sell, A., and Leitenstorfer, A. (2014). Ultrabroad Er: fiber lasers. *Laser Photon. Rev.* 8 (3): 409–428.

37 Del Haye, P., Schliesser, A., Arcizet, O. et al. (2007). Optical frequency comb generation from a monolithic microresonator. *Nature* 450: 1214–1217.

38 Spencer, D.T., Drake, T., Briles, T.C. et al. (2018). An optical-frequency synthesizer using integrated photonics. *Nature* 557: 81–85.

39 Gohle, C., Udem, T., Herrmann, M. et al. (2005). A frequency comb in the extreme ultraviolet. *Nature* 436: 234–237.

40 Kandula, D.Z., Gohle, C., Pinken, T.J. et al. (2011). XUV frequency-comb metrology on the ground state of helium. *Phys. Rev. A* 84: 062512-1–062512-16.

41 Benko, C., Allison, T.K., Cingöz, A. et al. (2014). Extreme ultraviolet radiation with coherence time greater than 1 s. *Nat. Photon.* 8: 530–536.

42 Demelt, H.G. (1967). *Advances in Atomic and Molecular Physics*, vol. 3 (ed. D.R. Blates and I. Esterman), 53–72. New York, London: Academic Press.
43 Paul, W. and Steinwedel, H. (1953). Ein neues Massenspektrometer ohne Magnetfeld. *Z. Naturforsch. A* 8 (7): 448–450 (in German).
44 Riehle, F. (2004). *Frequency Standards*. Weinheim: Wiley-VCH.
45 Dicke, R.H. (1953). The effect of collisions upon the Doppler width of spectral lines. *Phys. Rev.* 89: 472–473.
46 Cirac, J.I. and Zoller, P. (1955). Quantum computations with cold trapped ions. *Phys. Rev. Lett.* 74: 4091–4094.
47 Pyka, K., Keller, J., Partner, H.L. et al. (2013). Topological defect formation and spontaneous symmetry breaking in ion Coulomb crystals. *Nat. Commun.* 4: 2291.
48 Wineland, D. and Dehmelt, H. (1975). Proposed 1014 $\delta\nu < \nu$ laser fluorescence spectroscopy on Ti+ mono-ion oscillator. *Bull. Am. Phys. Soc.* 20: 637.
49 Dietrich, F., Berquist, J.C., Bollinger, J.J. et al. (1989). Laser cooling to the zero-point energy of motion. *Phys. Rev. Lett.* 62: 403–406.
50 Schmidt, P.O., Rosenband, T., Langer, C. et al. (2005). Spectroscopy using quantum logic. *Science* 309: 749–752.
51 Wolf, F., Wan, Y., Heip, J.C. et al. (2016). Non-destructive state detection for quantum logic spectroscopy of molecular ions. *Nature* 530: 457–460.
52 Ashkin, A. (1970). Acceleration and trapping of particles by radiation pressure. *Phys. Rev. Lett.* 24 (4): 156–159.
53 Letokhov, V.S. (1968). Narrowing of the Doppler width in a standing light wave. *JETP Lett.* 7: 272–275.
54 Bloch, I., Dalibard, J., and Zwerger, W. (2008). Many body physics with ultracold atoms. *Rev. Mod. Phys.* 80: 885–964.
55 Kolkowitz, S., Bromley, S.L., Bothwell, T. et al. (2016). Spin-orbit-coupling fermions in an optical lattice. *Nature* 542: 66–70.
56 Aidelsburger, M., Atala, M., Lohse, M. et al. (2013). Realization of the Hofstadter Hamiltonian with ultracold atoms in optical lattices. *Phys. Rev. Lett.* 111: 185301-1–185301-5.
57 Hirokazu, M., Siviloglou, G.A., Kennedy, C.J. et al. (2013). Realizing the Harper Hamiltonian with laser-assisted tunneling in optical Lattices. *Phys. Rev. Lett.* 111: 185302-1–185302-5.
58 Lohse, M., Schweitzer, C., Price, H.M. et al. (2018). Exploring 4D quantum Hall physics with a 2D topological charge pump. *Nature* 553: 55–58.
59 Niering, M., Holzwarth, R., Reichert, J. et al. (2000). Measurement of the hydrogen 1*S*- 2*S* transition frequency by phase coherent comparison with a microwave cesium fountain clock. *Phys. Rev. Lett.* 84: 5496–5499.
60 Oates, C.W., Bondu, F., Fox, R.W., and Hollberg, L. (1999). A diode-laser optical frequency standard based on laser-cooled Ca atoms: sub-kilohertz spectroscopy by optical shelving detection. *Eur. Phys. J. D* 7: 449–460.
61 Udem, T., Diddams, S.A., Vogel, K.R. et al. (2001). Absolute frequency measurements of the Hg^+ and Ca optical clock transitions with a femtosecond laser. *Phys. Rev. Lett.* 86: 4996–4999.

62 Olson, J., Fox, R., Fortier, T. et al. (2018). Optical frequency stabilization at the 10^{-16} fractional level utilizing Ramsey-Bordé atom interferometry. IEEE CPEM 2018, Paris, Conference Digest.

63 Riehle, F., Schnatz, H., Lipphardt, B. et al. (1999). The optical calcium frequency standard. *IEEE Trans. Instrum. Meas.* 48: 613–617.

64 Schnatz, H., Lipphardt, B., Degenhardt, C. et al. (2005). Optical frequency measurements using fs-comb generators. *IEEE Trans. Instrum. Meas.* 54: 750–753.

65 Curtis, E.A., Oates, C.W., and Hollberg, L. (2001). Quenched narrow-line laser cooling of ^{40}Ca to near the photon recoil limit. *Phys. Rev. A* 64: 031403-1–031403-4.

66 Binnewiss, T., Wilpers, G., Sterr, U. et al. (2001). Doppler cooling and trapping on forbidden transitions. *Phys. Rev. Lett.* 87: 123002-1–123002-4.

67 Wilpers, G., Binnewies, T., Degenhardt, C. et al. (2002). Optical clock with ultracold neutral atoms. *Phys. Rev. Lett.* 89: 230801-1–230801-5.

68 Stenger, J., Binnewies, T., Wilpers, G. et al. (2001). Phase-coherent frequency measurement of the Ca intercombination line at 657 nm with a Kerr-lens mode-locked laser. *Phys. Rev. A* 63: 021802-1-4.

69 Cao, J., Zhang, P., Shang, J. et al. (2017). A compact, transportable single ion optical clock with 7.8×10^{-17} systematic uncertainty. *Appl. Phys. B* 123 (112): 1–9.

70 Kersten, P., Mensin, F., Sterr, U., and Riehle, F. (1999). A transportable optical calcium frequency standard. *Appl. Phys. B* 68: 27–38.

71 Ferrari, G., Cancio, P., Drullinger, R. et al. (2003). Precision frequency measurement of visible intercombination lines of strontium. *Phys. Rev. Lett.* 91: 243002–243005.

72 Oates, C.W. and Ludlow, A.D. (2015). Optical lattice clocks. *Opt. Photon. News* 26 (1): 36–43.

73 Boyd, M.M., Ludlow, A.D., Blatt, S. et al. (2007). ^{87}Sr Lattice clock with inaccuracy below 10^{-15}. *Phys. Rev. Lett.* 98: 083002-1-4.

74 Baillard, X., Fouché, M., Le Targat, R. et al. (2008). An optical lattice clock with spin-polarized ^{87}Sr atoms. *Eur. Phys. J.* 48: 11–17.

75 Campbell, G.K., Ludlow, A.D., Blatt, S. et al. (2008). The absolute frequency of the ^{87}Sr optical clock transition. *Metrologia* 45: 539–548.

76 Takamoto, M., Hong, F.-L., Higashi, R., and Katori, H. (2005). An optical lattice clock. *Nature* 435: 321–324.

77 Katori, H. (2011). Optical lattice clocks and quantum metrology. *Nat. Photon.* 5: 203–210.

78 Middelmann, T., Falke, S., Lisdat, C., and Sterr, U. (2012). High accuracy correction of blackbody radiation shift in an optical lattice. *Phys. Rev. Lett.* 109: 263004-1-5.

79 Lemonde, P. (2009). Optical lattice clocks. *Eur. Phys. J. Spec. Top.* 172: 81–96.

80 Campbell, S.L., Hutson, R.B., Marti, G.E. et al. (2017). A Fermi-degenerate three-dimensional optical lattice clock. *Science* 358: 90–94.

81 Marti, G.E., Ross, B., Goban, A. et al. (2018). Imaging optical frequencies with 100 μHz precision and 1.1 μm resolution. *Phys. Rev. Lett.* 120: 103201-1-6.

82 Ido, T. and Katori, H. (2003). Recoil-free spectroscopy of neutral Sr atoms in the Lamb-Dicke regime. *Phys. Rev. Lett.* 91: 053001-1–053001-4.

83 Takamoto, M. and Katori, H. (2003). Spectroscopy of the $^1S_0$- $^3P_0$clock transition in ^{87}Sr in an optical lattice. *Phys. Rev. Lett.* 91: 223001-1–223001-4.

84 Ye, J., Kimble, H.J., and Katori, H. (2008). Quantum state engineering and precision metrology using state-insensitive light traps. *Science* 320: 1734–1738.

85 Hagemann, C., Grebing, C., Kessler, T. et al. (2013). Providing 1E-16 short-term stability of a 1.5 μm laser to optical clocks. *IEEE Trans. Instrum. Meas.* 62: 1556–1562.

86 Jiang, Y.Y., Ludlow, A.D., Lemke, N.D. et al. (2011). Making optical atomic clocks more stable with 10−16 level laser stabilization. *Nat. Photon.* 5: 158–161.

87 Takamoto, M., Takano, T., and Katori, H. (2011). Frequency comparison of optical lattice clocks beyond the Dicke limit. *Nat. Photon.* 5: 288–292.

88 Al-Masodi, A., Dörscher, S., Hafner, S. et al. (2015). Noise and instability of an optical lattice clock. *Phys. Rev. A* 92: 063814-1–063814-7.

89 Bloom, B.J., Nicholson, T.L., Williams, J.R. et al. (2014). An optical lattice clock with accuracy and stability at the 10^{-18} level. *Nature* 506: 71–75.

90 Ludlow, A.D., Zelevinsky, T., Campbell, G.K. et al. (2008). Sr Lattice clock at 1×10^{-16} fractional uncertainty by remote optical evaluation with a Ca clock. *Science* 319: 1805–1808.

91 BIPM (2019). Practical realizations of the definitions of some important units. http://www.bipm.org/en/publications/mises-en-pratique/standard-frequencies.html (accessed February 2019).

92 Riehle, F., Gill, P., Arias, F., and Robertsson, L. (2018). The CIPM list of recommended frequency standard values: guidelines and procedures. *Metrologia* 55: 188–200.

93 Hinkley, N., Sherman, J.A., Phillips, N.B. et al. (2013). An atomic clock with 10^{-18} instability. *Science* 341 (6151): 1215–1218.

94 McFerran, J.J., Yi, L., Majri, S. et al. (2014). Statistical uncertainty of 2.5×10^{-16} for the ^{199}Hg $^1S_0$–$^3P_0$ clock transition against a primary frequency standard. *Phys. Rev. A* 89: 043432-1-8.

95 Kulosa, A.P., Fim, D., Zipfel, K.H. et al. (2015). Towards a Mg lattice clock: observation of the $^1S_0$–$^3P_0$ transition and determination of the magic wavelength. *Phys. Rev. Lett.* 115: 240801-1-5.

96 Koller, S.B., Grotti, J., Voght, S. et al. (2017). A transportable optical lattice clock with 7×10^{-17} uncertainty. *Phys. Rev. Lett.* 118: 073601-1-6.

97 Grotti, J., Koller, S., Vogt, S. et al. (2018). Geodesy and metrology with a transportable optical clock. *Nat. Phys.* 14: 437–441.

98 Margolis, H.S. (2009). Trapped ion optical clocks. *Eur. Phys. J. Spec. Top.* 172: 97–107.

99 Herschbach, N., Pyka, K., Kellr, J., and Mehlstäubler, T.E. (2012). Linear Paul trap design for an optical clock with Coulomb crystals. *Appl. Phys. B* 107: 891–906.

100 Keller, J., Kalincev, D., Burgermeister, T. et al. (2017). Optical Clocks Based on Linear Ion Chains with High Stability and Accuracy. ArXiv:1712.02335;

101 Schulte, M., Lörch, N., Leroux, I.D. et al. (2016). Quantum algorithmic readout in multi-ion clocks. *Phys. Rev. Lett.* 116: 013002-1-5.

102 Becker, T., van Zanthier, J., Nevsky, A.Y. et al. (2001). High-resolution spectroscopy of a single In^+ ion: progress towards an optical frequency standard. *Phys. Rev. A* 63: 051802–051805.

103 Berkeland, D.J., Miller, J.D., Bergquist, J.C. et al. (1998). Laser-cooled mercury-ion frequency standard. *Phys. Rev. Lett.* 80: 2089–2092.

104 Diddams, S.A., Udem, T., Bergquist, J.C. et al. (2001). An optical clock based on a single trapped $^{199}Hg^+$-ion. *Science* 293: 825–828.

105 Rosenband, T., Hume, D.B., Schmidt, P.O. et al. (2008). Frequency ratio of Al^+ and Hg^+ single-ion optical clocks; metrology at the 17th decimal place. *Science* 319 (5871): 1808–1812.

106 Margolis, H.S., Barwood, G.P., Huang, G. et al. (2004). Hertz-level measurement of the optical clock frequency in a single $^{88}Sr^+$ ion. *Science* 306: 1355–1358.

107 Madej, A.A., Dubé, P., Zhou, Z. et al. (2012). $^{88}Sr^+$ 445-THz single-ion reference at the 10^{-17} level via control and cancellation of systematic uncertainties and its measurement against the SI second. *Phys. Rev. Lett.* 109: 203002-1–203002-4.

108 Chwalla, M., Benhelm, J., Kim, K. et al. (2009). Absolute frequency measurement of the $^{40}Ca^+$ 4s $^2S_{1/2}$ -3d $2D_{5/2}$ clock transition. *Phys. Rev. Lett.* 102: 023002-1–023002-4.

109 Matsubara, K., Hachisu, H., Li, Y. et al. (2012). Direct comparison of a Ca^+ single-ion clock against a Sr lattice clock to verify the absolute frequency measurement. *Opt. Express* 20: 22034–22041.

110 Huang, Y., Liu, P., Bian, W. et al. (2014). Evaluation of the systematic shifts and absolute frequency measurement of a single Ca^+ ion frequency standard. *Appl. Phys. B* 114: 189–201.

111 Tamm, C., Engelke, D., and Buehner, V. (2000). Spectroscopy of the electric-quadrupole transition $^2S_{1/2}$ (F=0)$^{-2}D_{3/2}$ (F=2) in trapped $^{171}Yb^+$. *Phys. Rev. A* 61: 053405-1–053405-9.

112 Roberts, M., Taylor, P., Gateva-Kostova, S.V. et al. (1999). Measurement of the $^2S_{1/2}$ -$^2D_{5/2}$ clock transition in a single $^{171}Yb^+$ ion. *Phys. Rev. A* 60: 2867–2872.

113 Dehmelt, H. (1975). Proposed 1014 $\delta\nu/\nu$ laser fluorescence spectroscopy on Tl^+ mono-ion oscillator II (spontaneous quantum jumps). *Bull. Am. Phys. Soc.* 20: 60.

114 Tamm, C., Weyers, S., Lipphardt, B., and Peik, E. (2009). Stray-field-induced quadrupole shift and absolute frequency of the 688-THz $^{171}Yb^+$ single-ion optical frequency standard. *Phys. Rev. A* 80: 043403-1–043403-7.

115 Tamm, C., Huntemann, N., Lipphardt, B. et al. (2014). A Cs-based optical frequency measurement using cross-linked optical and microwave oscillators. *Phys. Rev. A* 89: 023820-1–023820-8.

116 Schneider, T., Peik, E., and Tamm, C. (2005). Sub-hertz optical frequency comparisons between two trapped $^{171}Yb^+$ ions. *Phys. Rev. Lett.* 94: 230801-1–230801-4.

117 Dzuba, V.A. and Flambaum, V.V. (2009). Atomic calculations and search for variation of the fine-structure constant in quasar absorption spectra. *Can. J. Phys.* 87 (1): 25–35.

118 Roberts, M., Taylor, P., Barwood, G.P. et al. (1997). Observation of an electric octupole transition in a single ion. *Phys. Rev. Lett.* 78: 1876–1879.

119 Yudin, V.I., Taichenachev, A.V., Oates, C.W. et al. (2010). Hyper-Ramsey spectroscopy of optical clock transitions. *Phys. Rev. A* 82: 011801-4.

120 Huntemann, N., Lipphardt, B., Okhapkin, M. et al. (2012). Generalized Ramsey excitation scheme with suppressed light shift. *Phys. Rev. Lett.* 109: 213002-1-5.

121 Sanner, C., Huntemann, N., Lange, R. et al. (2018). Autobalanced Ramsey spectroscopy. *Phys. Rev. Lett.* 120: 053602-1-6.

122 Huntemann, N., Sanner, C., Lipphardt, B. et al. (2016). Single-ion atomic clock with 3×10^{-18} systematic uncertainty. *Phys. Rev. Lett.* 116: 063001-1-5.

123 Huntemann, N., Okhapkin, M., Lipphardt, B. et al. (2012). High-accuracy optical clock based on the octupole transition in $^{171}Yb^{+}$. *Phys. Rev. Lett.* 108: 090801-1-5.

124 King, S.A., Godun, R.M., Webster, S.A. et al. (2012). Absolute frequency measurement of the $^{2}S_{1/2} - {}^{2}F_{7/2}$ electric octupole transition in a single ion of $^{171}Yb^{+}$ with 10^{-15} fractional uncertainty. *New J. Phys.* 14: 013045.

125 Sherstov, I., Okhapkin, M., Lipphardt, B. et al. (2010). Diode-laser system for high-resolution spectroscopy of the $^{2}S_{1/2} \rightarrow {}^{2}F_{7/2}$ octupole transition in $^{171}Yb^{+}$. *Phys. Rev. A* 81: 021805-1-5.

126 Yu, N., Dehmelt, H., and Nagourney, W. (1992). The $3^{1}S_{0}$-$3^{3}P_{0}$ transition in the aluminum isotope ion $^{26}Al^{+}$: a potentially superior passive laser frequency standard and spectrum analyzer. *Proc. Natl. Acad. Sci. U.S.A.* 89: 7289.

127 Rosenband, T., Schmidt, P.O., Hume, D.B. et al. (2007). Observation of the $^{1}S_{0} \rightarrow {}^{3}P_{0}$ clock transition in $^{27}Al^{+}$. *Phys. Rev. Lett.* 98: 22080-1-4.

128 Wübbena, J.B., Amairi, S., Mandel, O., and Schmidt, P.O. (2012). Sympathetic cooling of mixed-species two-ion crystals for precision spectroscopy. *Phys. Rev. A* 85: 043412-1-13.

129 Chou, C.W., Hume, D.B., Koelemeij, J.C.J. et al. (2013). Frequency comparison of two high-accuracy Al^{+} optical clocks. *Phys. Rev. Lett.* 104: 070802-1-4.

130 Chou, C.W., Hume, D.B., Rosenband, T., and Wineland, D.J. (2010). Optical clocks and relativity. *Science* 329: 1630–1633.

131 Blatt, S., Ludlow, A.D., Campbell, G.K. et al. (2008). New limits on coupling of fundamental constants to gravity using ^{87}Sr optical lattice clocks. *Phys. Rev. Lett.* 100: 140801-1–140801-4.

132 Bjerhammar, A. (1985). On a relativistic geodesy. *Bull. Géodé.* 59 (3): 207–220.

133 Peik, E. and Tamm, C. (2003). Nuclear laser spectroscopy of the 3.5 eV transition in Th-229. *Europhys. Lett.* 61 (2): 181–186.

134 Peik, E., Zimmermann, K., Okhapkin, M., and Tamm, C. (2009). Prospects for a nuclear optical frequency standard based on thorium-229. In: *Proceedings of the 7th Symposium on Frequency Standards and Metrology* (ed. L. Maleki), 532–538. World Scientific.

135 Campbell, C.J., Radnaev, A.G., Kuzmich, A. et al. (2012). Single-ion nuclear clock for metrology at the 19th decimal place. *Phys. Rev. Lett.* 108: 120802-1–120802-5.

136 Safronova, M. (2018). In search of the nuclear clock. *Nat. Phys.* 14: 198.

137 (a) Reich, C.W. and Helmer, R.G. (1990). Energy separation of the doublet of intrinsic states at the ground state of ^{229}Th. *Phys. Rev. Lett.* 64: 271–273. (b) Helmer, R.G. and Reich, C.W. (1994). An excited state of ^{229}Th at 3.5 eV. *Phys. Rev. C* 49: 1845.

138 Beck, B.R., Becker, J.A., Beiersdorfer, P. et al. (2007). Energy splitting of the ground state doublet in the nucleus ^{299}Th. *Phys. Rev. Lett.* 98: 142501-1-4.

139 von der Wense, L., Seiferle, B., Laatiaoui, M. et al. (2016). Direct detection of the ^{229}Th nuclear clock transition. *Nature* 533: 47–51.

140 Thielking, J., Okhapkin, M.V., Glowacki, P. et al. (2018). Laser spectroscopic characterization of the nuclear clock isomer ^{229m}Th. *Nature* 556: 321–325.

141 Flambaum, V.V. (2006). Enhanced effect of temporal variation of the fine structure constant and the strong interaction in ^{229}Th. *Phys. Rev. Lett.* 97: 092502-1–092502-3.

142 Kozlov, M.G., Safronova, M.S., López-Urrutia, J.R., and Schmidt, P.O. (2018). Highly Charged Ions: Optical Clocks and Applications in Fundamental Physics. ArXiv:1803.06532.

143 Berengut, J.C., Dzuba, V.A., and Flambaum, V.V. (2010). Enhanced laboratory sensitivity to variation of the fine-structure constant using highly charged ions. *Phys. Rev. Lett.* 105: 120801-1–120801-4.

144 Schiller, S. (2007). Hydrogenloke highly charged ions for tests of the time independence of fundamental constants. *Phys. Rev. Lett.* 98: 180801-1-4.

145 Windberger, A., Crespo López-Urrutia, J.R., Bekker, H. et al. (2015). Identification of the predicted 5s-4f level crossing optical lines with applications to metrology and searches for the variation of fundamental constants. *Phys. Rev. Lett.* 114: 150801-1-6.

146 Hanneke, D., Fogwell Hoogerheide, S., and Gabrielse, G. (2011). Cavity control of a single-electron quantum cyclotron: measuring the electron magnetic moment. *Phys. Rev. A* 83: 052122-1–052122-26.

147 Odom, B., Hanneke, D., D'Urso, B., and Gabrielse, G. (2006). New measurement of the electron magnetic moment using a one-electron quantum cyclotron. *Phys. Rev. Lett.* 97: 030801-1–030801-4.

148 Gabrielse, G., Hanneke, D., Kinoshita, T. et al. (2007). Erratum: new determination of the fine structure constant from the electron *g* value and QED [*Phys. Rev. Lett*. 97: 030802 (2006)]. *Phys. Rev. Lett.* 99: 039902-1-2.

149 Mohr, P.J., Newell, D.B., and Taylor, B.N. (2016). CODATA recommended values of the fundamental physical constants: 2014. *Rev. Mod. Phys.* 88: 035009-1-73.

150 Safronova, M.S., Budker, D., DeMille, D. et al. (2018). Search for new physics with atoms and molecules. *Rev. Mod. Phys.* 90: 025008-1-106.

151 Uzan, J.-P. (2003). The fundamental constants and their variation: observational and theoretical studies. *Rev. Mod. Phys.* 75: 403.

152 Karshenboim, S.G. and Peik, E. (eds.) (2004). *Astrophysics, Clocks and Fundamental Constants*, Lecture Notes on Physics, vol. 648. Berlin, Heidelberg: Springer-Verlag.

153 Webb, J.K., Murphy, M.T., Flambaum, V.V. et al. (2001). Further evidence for cosmological evolution of the fine structure constant. *Phys. Rev. Lett.* 87: 091301-1-4.

154 Srianand, R., Chand, H., Petitjean, P., and Aracil, B. (2004). Limits on the time variation of the electromagnetic fine-structure constant in the low energy limit from absorption lines in the spectra of distant quasars. *Phys. Rev. Lett.* 92: 121302-1-4.

155 Peik, E., Lipphardt, B., Schnatz, H. et al. (2004). Limit on the present temporal variation of the fine structure constant. *Phys. Rev. Lett.* 93: 170801-4.

156 Bize, S., Diddams, S.A., Tanaka, U. et al. (2003). Testing the stability of fundamental constants with the ^{199}Hg single-ion optical clock. *Phys. Rev. Lett.* 90: 150802-1-4.

157 Marion, H., Pereira Dos Santos, F., Abgrall, M. et al. (2003). Search for variations of fundamental constants using atomic fountain clocks. *Phys. Rev. Lett.* 90: 15080-1-4.

158 Fischer, M., Kolachevsky, N., Zimmermann, M. et al. (2004). New limits on the drift of fundamental constants from laboratory measurements. *Phys. Rev. Lett.* 92: 230802-1-4.

159 Fortier, T.M., Ashby, N., Bergquist, J.C. et al. (2007). Precision atomic spectroscopy for improved limits on variation of the fine structure constant and local position invariance. *Phys. Rev. Lett.* 98: 070801-4.

160 Le Targat, R., Lorini, L., Le Coq, Y. et al. (2013). Experimental realization of an optical second with strontium lattice clocks. *Nat. Commun.* 4: 2109-1-8.

161 Huntemann, N., Lipphardt, B., Tamm, C. et al. (2014). Improved limit on a temporal variation of m_p/m_e from comparisons of Yb^+ and Cs atomic clocks. *Phys. Rev. Lett.* 113: 210802-1-5.

162 Godun, R.M., Nisbet-Jones, P.B.R., Jones, M.J. et al. (2014). Frequency ratio of two optical clock transitions in $^{171}Yb^+$ and constraints on the time variation of fundamental constants. *Phys. Rev. Lett.* 113: 210801-1-5.

163 Karshenboim, S.G. and Peik, E. (2008). Astrophysics, atomic clocks and fundamental constants. *Eur. Phys. J. Spec. Top.* 163: 1–7.

164 Dzuba, V.A., Flambaum, V.V., and Webb, J.K. (1999). Calculations of the relativistic effects in many-electron atoms and space-time variation of fundamental constants. *Phys. Rev. A* 59: 230–237.

165 Dzuba, V.A., Flambaum, V.V., and Marchenko, M.V. (2003). Calculations of the relativistic effects in many-electron atoms and space-time variation of fundamental constants. *Phys. Rev. A* 68: 022506-1-5.

166 Ashby, N., Parker, T.E., and Patla, B.R. (2018). A null test of general relativity based on a long-term comparison of atomic transition frequencies. *Nat. Phys.* 14 (8): https://doi.org/10.1038/s41567-018-0156-2.

167 Cacciapuoti, L., Dimarcq, N., Santarelli, G. et al. (2007). Atomic clock ensemble in space: scientific objectives and mission status. *Nucl. Phys. B* 166: 303–306.

168 Gill, P. (2011). When should we change the definition of the second? *Philos. Trans. R. Soc. London, Ser. A* 369: 4109–4130.

169 Riehle, F. (2015). Towards a redefinition of the second based on optical atomic clocks. *C.R. Phys.* 16 (5): 506–515.

170 BIPM (2016). Strategy documents: CCTF strategy, www.bipm.org/en/committees/cc/cctf/strategy.html (accessed 03/2018).

171 Djerroud, K., Acef, O., Clairon, A. et al. (2010). Coherent optical link through the turbulent atmosphere. *Opt. Lett.* 35: 1479–1481.

172 Giorgetta, F.R., Swann, W.C., Sinclair, L.C. et al. (2013). Optical two-way time and frequency transfer over free space. *Nat. Photon.* 7: 434–438.

173 Droste, S., Ozimek, F., Udem, T. et al. (2013). Optical-frequency transfer over a single-span 1840 km fiber link. *Phys. Rev. Lett.* 111: 110801-1-5.

174 Delva, P., Lodewyck, J., Bilicki, S. et al. (2017). Test of special relativity using a fiber network of optical clocks. *Phys. Rev. Lett.* 118: 221102-1-6.

175 Planck, M. (1900). Zur Theorie des Gesetzes der Energieverteilung im Normalspektrum. *Verh. Dtsch. Phys. Ges.* 2: 237–245 (in German).

176 (a) Einstein, A. (1905). Über einen die Erzeugung und Verwandlung des Lichts betreffenden heuristischen Gesichtspunkt. *Ann. Phys.* 17: 132–149 (in German). (b) see also: Renn, J. (ed.) (2005). *Einstein's Annalen Papers. The Complete Collection*. Weinheim: Wiley-VCH.

177 Lewis, G.N. (1926). The conservation of photons. *Nature* 118: 874–875.

178 A critical discussion of the conception "photon" can be found in: Lamb, W.E. (1995). Anti-photon. *Appl. Phys. B* 60: 77–84.

179 (a) Glauber, R.J. (1963). The quantum theory of optical coherence. *Phys. Rev.* 130: 2529–2539. (b) Glauber, R.J. (1963). Coherent and incoherent states of the radiation field. *Phys. Rev.* 131: 2766–2788.

180 For further reading see e.g: Mandel, L. and Wolf, E. (1995). *Optical Coherence and Quantum Optics*. New York: Cambridge University Press.

181 Hanbury Brown, R. and Twiss, R.Q. (1956). Correlation between photons in two coherent beams of light. *Nature* 177: 27–29.

182 Hong, C.K., Ou, Z.Y., and Mandel, L. (1987). Measurement of subpicosecond time intervals between two photons by interference. *Phys. Rev. Lett.* 59: 2044–2046.

183 Martinelli, M. and Martelli, P. (2008). Laguerre mathematics in optical communications. *Opt. Photon. News* 19: 30–35.

184 Zou, X.T. and Mandel, L. (1990). Photon-antibunching and sub-Poissonian photon statistics. *Phys. Rev. A* 41: 475–476.

185 Boumester, D., Ekert, A., and Zeilinger, A. (eds.) (2000). *The Physics of Quantum Information*. Berlin: Springer-Verlag.

186 Zwinkels, J.C., Ikonen, E., Fox, N.P. et al. (2010). Photometry, radiometry and 'the candela': evolution in the classical and quantum world. *Metrologia* 47 (5): R15–R32.

187 Lounis, B. and Orrit, M. (2005). Single photon sources. *Rep. Prog. Phys.* 68: 1129–1179.

188 Grangier, P. (2005). Experiments with single photons. *Semin. Poincare* 2: 1–26.

189 Eisaman, M.D., Fan, J., Migdal, A., and Polyakov, S.V. (2011). Single-photon-sources and detectors. *Rev. Sci. Instrum.* 82: 071101-1-25.

190 Sergienko, A.V. (2001). *Proceedings of the International School of Physics "Enrico Fermi" Course CXLVI* (ed. T.J. Quinn, S. Leschiutta and P. Tavella), 715–746. Amsterdam: IOS Press.

191 Kimble, H.J., Dagenais, M., and Mandel, L. (1977). Photon antibunching in resonance fluorescence. *Phys. Rev. Lett.* 39: 691–695.

192 Diedrich, F. and Walther, H. (1987). Nonclassical radiation of a single stored ion. *Phys. Rev. Lett.* 58: 203–206.

193 De Martini, F., Giuseppe, G., and Marrocco, M. (1996). Single-mode generation of quantum photon states by excited single molecules in a microcavity trap. *Phys. Rev. Lett.* 76: 900–903.

194 Kitson, S., Jonsson, P., Rarity, J., and Tapster, P. (1998). Intensity fluctuation spectroscopy of small numbers of dye molecules in a microcavity. *Phys. Rev. A* 58: 620–627.

195 Brunel, C., Lounis, B., Tamarat, P., and Orrit, M. (1999). Triggered source of single photons based on controlled single molecule fluorescence. *Phys. Rev. Lett.* 83: 2722–2725.

196 Urban, E., Johnson, T.A., Hanage, T. et al. (2009). Observation of Rydberg blockade between two atoms. *Nat. Phys.* 5: 110–114.

197 Gaetan, A., Miroshnychenko, Y., Wilk, T. et al. (2009). Observation of collective excitation of two individual atoms in the Rydberg blockade regime. *Nat. Phys.* 5: 115–118.

198 Dudin, Y.O. and Kuzmich, A. (2012). Strongly interacting Rydberg excitations of a cold atom gas. *Science* 336: 887–889.

199 Loubser, J.H.N. and van Wyk, J.A. (1977). Electron spin resonance in annealed type 1b diamond. *Diamond Res.* 11: 4–7.

200 Loubser, J.H.N. and van Wyk, J.A. (1978). Electron spin resonance in the study of diamond. *Rep. Prog. Phys.* 41 (8): 1201–1249.

201 Fuchs, G.D., Dobrovitski, V.V., Hanson, R. et al. (2008). Excited-state spectroscopy using single spin manipulation in diamond. *Phys. Rev. Lett.* 101: 117601-1-4.

202 Kurtsiefer, C., Mayer, S., Zarda, P., and Weinfurter, H. (2000). Stable solid-state source of single photons. *Phys. Rev. Lett.* 85: 290–293.

203 Brouri, R., Beveratos, A., Poizat, J.-P., and Grangier, P. (2000). Photon anti-bunching in the fluorescence of individual color centers in diamond. *Opt. Lett.* 25: 1294–1296.

204 Schmunk, W., Rodenberger, M., Peters, S. et al. (2011). Radiometric calibration of single photon detectors by a single photon source based on NV-centers in diamond. *J. Mod. Opt.* 58: 1252.

205 Pezzagna, S., Rogalla, D., Wildanger, D. et al. (2011). Creation and nature of optical centres in diamond for single-photon emission—overview and critical remarks. *New J. Phys.* 13: 035024-1–035024-28.

206 Neu, E., Steinmetz, D., Riedrich-Möller, J. et al. (2011). Single photon emission from silicon-vacancy colour centres in chemical vapour deposition nano-diamonds on iridium. *New J. Phys.* 13: 025012-1-21.

207 Valgu, A., Porrovecchio, G., Chu, X.-L. et al. (2017). Experimental demonstration of a predictable single photon source with variable photon flux. *Metrologia* 54: 218–223.

208 Riedrich-Möller, J., Kipfstuhl, L., Hepp, C. et al. (2012). One- and two-dimensional photonic crystal microcavities in single crystal diamond. *Nat. Nanotechnol.* 7: 69.

209 Neu, E., Fischer, M., Gsell, S. et al. (2011). Fluorescence and polarization spectroscopy of single silicon vacancy centers in heteroepitaxial nanodiamonds on iridium. *Phys. Rev. B* 84: 205211-1–205211-8.

210 Marshall, G.D., Gaebel, T., Matthews, J.C.F. et al. (2011). Coherence properties of a single dipole emitter in diamond. *New J. Phys.* 13: 055016.

211 Aharonovich, I., Castelletto, S., Simpson, D.A. et al. (2009). Two-level ultrabright single photon emission from diamond nanocrystals. *Nano Lett.* 9: 3191–3195.

212 Aharonovich, I., Castelletto, S., Simpson, D.A. et al. (2010). Photophysics of chromium-related diamond single-photon emitters. *Phys. Rev. A* 81: 043813-1–043813-7.

213 Naydenov, B., Kolesov, R., Batalov, A. et al. (2009). Engineering single photon emitters by ion implantation in diamond. *Appl. Phys. Lett.* 95: 181109-1–181109-3.

214 Mizuochi, N., Makino, T., Kato, H. et al. (2012). Electrically driven single photon source at room temperature in diamond. *Nat. Photon.* 6: 299–303.

215 Jelezko, F. and Wrachtrup, J. (2012). Focus on diamond-based photonics and spintronics. *New J. Phys.* 14: 105024-1–105024-3.

216 Staudacher, T., Shi, F.S., Pezzagna, S. et al. (2013). Nuclear magnetic resonance spectroscopy on a (5-Nanometer) 3 sample volume. *Science* 339: 561–563.

217 Mamin, H.J., Kim, M., Sherwood, M.H. et al. (2013). Nanoscale nuclear magnetic resonance with a nitrogen-vacancy spin sensor. *Science* 339: 557–560.

218 Suter, D. and Jelezko, F. (2017). Single-spin magnetic resonance in the nitrogen-vacancy center of diamond. *Prog. Nucl. Magn. Reson. Spectrosc.* 98–99: 50–62.

219 Abe, E. and Sasaki, K. (2018). Tutorial: magnetic resonance with nitrogen-vacancy centers in diamond—microwave engineering, materials science, and magnetometry. *J. Appl. Phys.* 123: 161101-1-14.

220 Bimberg, D., Grundmann, M., and Ledentsov, N.N. (1998, Chichester). *Quantum Dot Heterostructures*. Wiley (1999).

221 Hawrylak, P. and Wojs, A. (1998). *Quantum Dots*. Berlin: Springer-Verlag.

222 Shields, A.J. (2007). Semiconductor quantum light sources. *Nat. Photon.* 1: 215–223.

223 Steffen, R., Forchel, A., Reinecke, T. et al. (1996). Single quantum dots as local probes of electronic properties of semiconductors. *Phys. Rev. B* 54: 1510–1513.

224 Brunner, K., Bockelmann, U., Abstreiter, G. et al. (1992). Photoluminescence from a single GaAs/AlGaAs quantum dot. *Phys. Rev. Lett.* 69: 3216–3219.

225 Stranski, I.N. and Krastanov, L. (1938). Zur Theorie der orientierten Ausscheidung von Ionenkristallen aufeinander. *Sitzungsber. Akad. Wiss. Wien Math.-Naturwiss.* 146: 797–810.

226 Jarjour, A.F., Taylor, R.A., Oliver, R.A. et al. (2007). Cavity-enhanced blue single-photon emission from a single InGaN/GaN quantum dot. *Appl. Phys. Lett.* 91: 052101-1–052101-3.

227 Dekel, E., Gershoni, D., Ehrenfeld, E. et al. (2000). Cascade evolution and radiative recombination of quantum dot multiexcitons studied by time-resolved spectroscopy. *Phys. Rev. B* 62: 11038–11045.

228 Finley, J.J., Fry, P.W., Ashmore, A.D. et al. (2001). Observation of multicharged excitons and biexcitons in a single InGaAs quantum dot. *Phys. Rev. B* 63: 161305-1-4.

229 Findeis, F., Zrenner, A., Böhm, G., and Abstreiter, G. (2000). Optical spectroscopy on a single InGaAs/GaAs quantum dot in the few-exciton limit. *Solid State Commun.* 114: 227–230.

230 Press, D., Götzinger, S., Reitzenstein, S. et al. (2007). Photon antibunching from a single quantum-dot-microcavity system in the strong coupling regime. *Phys. Rev. Lett.* 98: 117402-1-5.

231 Michler, P., Imamoglu, A., Mason, M.D. et al. (2000). Quantum correlation among photons from a single quantum dot at room temperature. *Nature* 406: 968–970.

232 Michler, P., Kiraz, A., Becher, C. et al. (2000). A quantum dot single-photon turnstile device. *Science* 290: 2282–2285.

233 Ward, M.B., Farrow, T., See, P. et al. (2007). Electrically driven telecommunication wavelength single-photon source. *Appl. Phys. Lett.* 90: 063512-1-3.

234 Imamoglu, A. and Yamamoto, Y. (1994). Turnstile device for heralded single photons: coulomb blockade of electron and hole tunneling in quantum confined p-i-n heterojunctions. *Phys. Rev. Lett.* 72: 210–213.

235 Benson, O., Satori, C., Pelton, M., and Yamamoto, Y. (2000). Regulated and entangled photons from a single quantum dot. *Phys. Rev. Lett.* 84: 2513–2516.

236 Kim, J., Benson, O., Kan, H., and Yamamoto, Y. (1999). A single-photon turnstile device. *Nature* 397: 500–503.

237 Hadfield, R.H. (2009). Single-photon detectors for optical quantum information applications. *Nat. Photon.* 3: 696–705.

238 Sappa, F., Cova, S., Ghioni, M. et al. (1996). Avalanche photodiodes and quenching circuits for single photon detection. *Appl. Opt.* 35: 1956–1976.

239 Castelletto, S.A., De Giovanni, I.P., Schettini, V., and Migdall, A.L. (2007). Reduced deadtime and higher rate photon-counting detection using a multiplexed detector array. *J. Mod. Opt.* 54: 337–352.

240 (a) Irwin, K.D. (1995). An application of electrothermal feedback for high resolution cryogenic particle detection. *Appl. Phys. Lett.* 66: 1998–2000. (b) Irwin, K.D., Nam, S.W., Cabrera, B. et al. (1995). A quasiparticle-trap-assisted transition-edge sensor for phonon-mediated particle detection. *Rev. Sci. Instrum.* 66: 5322–5326.

241 Lita, A.E., Miller, A.J., and Nam, S.W. (2008). Counting near-infrared single-photons with 95% efficiency. *Opt. Express* 16: 3032–3040.

242 Fukuda, D., Fujii, G., Numata, T. et al. (2009). Photon number resolving detection with high speed and high quantum efficiency. *Metrologia* 46: S288–S292.

243 Lita, A.E., Calkins, B., Pellochoud, L.A. et al. (2009). High-efficiency photon-number-resolving detectors based on hafnium transition-edge sensors. *AIP Conf. Proc.* 1185: 351–354.

244 Rajteri, M., Taralli, E., Portesi, C. et al. (2009). Photon-number discriminating superconducting transition-edge sensors. *Metrologia* 46: S283–S287.

245 Taralli, E., Portesi, C., Lolli, L. et al. (2010). Impedance measurements on a fast transition-edge sensor for optical and near-infrared range. *Supercond. Sci. Technol.* 23: 105012-1–105012-5.

246 Kück, S., Hofer, H., Peters, S., and Lopez, M. (2014). Detection efficiency calibration of silicon single photon avalanche diodes traceable to a national standard. *12th International Conference on New Developments and Applications in Optical Radiometry (NEWRAD 2014)*, Espoo, Finland (24–27 June 2014), 93. http://newrad2014.aalto.fi/Newrad2014_Proceedings.pdf (accessed 1 March 2019).

247 Müller, I., Klein, R., Hollandt, J. et al. (2012). Traceable calibration of Si avalanche photodiodes using synchrotron radiation. *Metrologia* 49: S152–S155.

248 López, M., Hofer, H., and Kück, S. (2015). Detection efficiency calibration of single-photon silicon avalanche photodiodes traceable using double attenuator technique. *J. Mod. Opt.* 62: 1732–1738.

249 Klein, R., Thornagel, R., and Ulm, G. (2010). From single photons to milliwatt radiation power. *Metrologia* 47: R33–R40.

250 Brida, G., Genovese, M., and Gramenga, M. (2006). Twin-photon techniques for photo-detector calibration. *Laser Phys. Lett.* 3: 115–123.

251 Polyakov, S.V., Ware, M., and Migdall, A. (2006). High accuracy calibration of photon-counting detectors. *Proc. SPIE* 6372: 63720J.

252 Rodiek, B., Lopez, M., Hofer, H. et al. (1917). Experimental realization of an absolute single-photon source based on a single nitrogen vacancy center in a nanodiamond. *Optica* 4 (1): 71–76.

253 (a) Lee, K.G., Chen, X.W., Eghlidi, H. et al. (2011). A planar dielectric antenna for directional single-photon emission and near-unity collection efficiency. *Nat. Photon.* 5: 166–169. (b) Chen, X.W., Götzinger, S., and Sandoghdar, V. (2011). 99% efficiency in collecting photons from a single emitter. *Opt. Lett.* 36: 3545–3547.

10

Outlook

Modern quantum science and technology are employed to link units to the defining constants of the present SI. The choice of defining constants as the foundation of the present SI, rather than explicitly defining base units, has created a unit system that is open to innovation. In the future, any newly discovered physical phenomenon can be used to realize an SI unit if it establishes a well-understood relation between a physical quantity and the defining constants of the SI. To illustrate the advantages of the present SI, we compare it once more to the previous SI, which was based on explicit definitions of the base units. Some of these definitions involved a specific subfield of physics, thereby excluding others. For example, the ampere definition was based on classical electrodynamics, excluding modern quantum physics from the realization of the electrical units in the previous SI.

The present SI also promotes innovative applications of quantum standards in industry. Quantum standards, such as Josephson voltage standards, provide an intrinsically accurate value of a physical quantity traceable to the SI if they are operated properly. Traceability to the SI is required by accreditation bodies. It is usually achieved by the calibration of industry instruments by accredited calibration laboratories or national metrology institutes. This procedure requires industry to interrupt the use of their instruments to send them out for calibration. The use of quantum standards reduces downtime and cost since they do not require calibration by accredited calibration laboratories or national metrology institutes. Only regular participation in comparison campaigns is required from industry to ensure proper operation of their standards. A remaining challenge for metrology is to bring a larger variety of quantum standards to the "workbench", that is, to make them fully accessible to all kind of users and sectors, including industrial production, health care, environmental protection, and finally regulators and standardization bodies.

First steps have been taken toward this goal. As we have discussed in Chapter 4, Josephson technology has considerably matured in recent years. Quantum voltmeters for the audio-frequency range have already been commercialized [1–3]. Josephson technology for more challenging voltage measurements and for other tasks in electrical metrology, for example, current measurements [4], can be expected to follow. In general, electrical quantum standards will find wider applications if they can be operated at higher temperatures. Further progress

The New International System of Units (SI): Quantum Metrology and Quantum Standards,
First Edition. Ernst O. Göbel and Uwe Siegner.
© 2019 Wiley-VCH Verlag GmbH & Co. KGaA. Published 2019 by Wiley-VCH Verlag GmbH & Co. KGaA.

in material science may enable this development, as discussed for the example of the quantum Hall effect in graphene in Section 5.5. Moreover, new material classes, such as topological insulators, may allow the operation of quantum Hall resistors at zero magnetic field, which would also relax the experimental requirements [5].

Beyond electrical metrology, first steps have been taken to construct a robust Kibble balance (see Section 7.3), which provides direct traceability to the defining constants for practical weighing applications over a mass range from 1 mg to 1 kg [6]. Moreover, at the time of writing, projects had been started to investigate the feasibility of practical absolute Johnson noise thermometers (see Section 8.1.5). In time and frequency metrology, chip-scale thermal atomic clocks based on microfabricated vapor cells are already commercially available [7]. Looking beyond the realization of the present SI second, engineering toward more practical optical clocks has started and a transportable strontium optical lattice clock was developed [8]. At the time of writing, work toward a robust single ytterbium ion clock was being pursued, which could be operated for several days without user interaction [9]. These examples show that practical quantum technology for measurements on the factory floor has immense potential encouraged by the innovative character of the present SI.

References

1 Lee, J., Behr, R., Palafox, L. et al. (2013). An ac quantum voltmeter based on a 10 V programmable Josephson array. *Metrologia* 50: 612–622.

2 Schubert, M., Starkloff, M., Lee, J. et al. (2015). An AC Josephson voltage standard up to the kilohertz range tested in a calibration laboratory. *IEEE Trans. Instrum. Meas.* 64: 1620–1626.

3 Schubert, M., Starkloff, M., Peiselt, K. et al. (2016). A dry-cooled AC quantum voltmeter. *Supercond. Sci. Technol.* 29: 105014 (8 pp).

4 Lee, J., Behr, R., Schumacher, B., et al. (2016). From AC quantum voltmeter to quantum calibrator. Conference on Precision Electromagnetic Measurements Digest 2016, Electronic ISBN 978-1-4673-9134-4, https://doi.org/10.1109/CPEM.2016.7540470.

5 Götz, M., Fijalkowski, K.M., Pesel, E. et al. (2018). Precision measurement of the quantized anomalous Hall resistance at zero magnetic field. *Appl. Phys. Lett.* 112: 072102 (5 pp).

6 Rothleitner, C., Schleichert, J., Rogge, N. et al. (2018). The Planck-Balance – using a fixed value of the Planck constant to calibrate E1/E2-weights. *Meas. Sci. Technol.* 29: 074003 (9 pp).

7 Kitching, J. (2018). Chip-scale atomic devices. *Appl. Phys. Rev.* 5: 031302 (38 pp).

8 Koller, S.B., Grotti, J., Voght, S. et al. (2017). A transportable optical lattice clock with 7×10^{-17} uncertainty. *Phys. Rev. Lett.* 118: 073601 (6 pp).

9 Opticlock (2018). Information on the BMBF project opticlock. http://www.opticlock.de/en/info (accessed 15 October 2018).

Index

The New International System of Units (SI): Quantum Metrology and Quantum Standards,
First Edition. Ernst O. Göbel and Uwe Siegner.
© 2019 Wiley-VCH Verlag GmbH & Co. KGaA. Published 2019 by Wiley-VCH Verlag GmbH & Co. KGaA.